

Monday Morning, October 18, 2010

Graphene Focus Topic

Room: Brazos - Session GR+SS+TF+EM-MoM

Epitaxial Graphene on SiC

Moderator: P.E. Sheehan, Naval Research Laboratory

8:20am **GR+SS+TF+EM-MoM1 Controlling Carriers in Graphene, G.G. Jernigan, P.E. Thompson, C.S. Hellberg, J.L. Tedesco, V.D. Wheeler, L.O. Nyakiti, P.M. Campbell, D.K. Gaskill**, Naval Research Laboratory

No technique for graphene synthesis yields controllably doped material. Measurements of carrier density and carrier type produce results that are dependent on extrinsic factors. For example, exfoliated graphene and metal-catalyzed graphene on SiO₂ often obtain carriers through unwanted charges in the oxide[1] or by gas adsorption[2] making graphene p-type. Similarly, epitaxial graphene on SiC should be n-type due to work function differences with the underlying SiC substrate[3]. Our recent measurements of graphene grown on Si-face SiC show that device processing steps can cause it to switch between carrier types. Additionally, we have found graphene grown on C-face SiC to be highly doped by Si impurities, which can produce either electrons or holes.

We have begun a series of investigations to impart properties after growth on epitaxial graphene formed on Si- and C-face SiC[4-5]. Substitutional incorporation of impurity atoms can lead to doping in a graphene sheet, if their concentration does not drastically affect the pi-network. This can be achieved by selective oxidation to remove C atoms from the graphene lattice and by molecular beam deposition (MBE) of dopants with controllable ultra-low fluxes to fill the C vacancies. It is important to note that Group III and V dopants can maintain the 2D geometry of the graphene sheet without producing an unsaturated bond (as they do when incorporated into the bulk of Si.) Thus, the extra p-orbital electrons from the Group V elements can be added to the graphene pi-network, or Group III elements can provide extra holes, without adversely affecting carrier mobility. Using MBE, we have substitutionally doped graphene with B and P. Ultraviolet photoelectron spectroscopy (UPS) is used to observe shifts in the Fermi level resulting from doping, and we have seen up to a 110 meV shift with 1% B in the lattice of graphene. Discussion of scanning tunneling microscopy (STM) observations of dopant placement and electrical properties will be presented. Density functional theory has been used to compute the density of states for the doped system in support of the STM and electrical measurements.

[1] S. S. Datta, D. R. Strachan, E. J. Mele, and A.T.C. Johnson, *Nano Lett.* 9 (2009) 7.

[2] Y. Dan, Y. Lu, N.J. Kybert, Z. Luo and A.T.C. Johnson, *Nano Lett.*, 9 (2009) 1472.

[3] T. Filleter, K. V. Emtsev, Th. Seyller, and R. Bennewitz, *Appl. Phys. Lett.* 93 (2008) 133117.

[4] G.G. Jernigan, et al., *Nano Lett.* 9, 2605 (2009).

[5] J.L. Tedesco, B.L. VanMil, R.L. Myers-Ward, J.M. McCrate, S.A. Kitt, P.M. Campbell, G.G. Jernigan, J.C. Culbertson, C.R. Eddy, Jr., and D.K. Gaskill, *Appl. Phys. Lett.*, 95, 122102 (2009).

8:40am **GR+SS+TF+EM-MoM2 The Role of Carbon Surface Diffusion on the Growth of Epitaxial Graphene on SiC, T. Ohta, N.C. Bartelt, S. Nie, K. Thürmer, G.L. Kellogg**, Sandia National Laboratories

Growth of high quality graphene films on SiC is regarded as one of the more viable pathways toward graphene-based electronics. Graphene films are readily formed on SiC by preferential sublimation of Si at elevated temperature. Little is known, however, about the atomistic processes of interrelated Si sublimation and graphene growth. We have observed the formation of graphene on SiC by Si sublimation using low energy electron microscopy, scanning tunneling microscopy, and atomic force microscopy. This work reveals unanticipated growth mechanisms, which depend strongly on the initial surface morphology. Carbon diffusion governs the spatial relationship between Si sublimation and graphene growth. Isolated bilayer SiC steps generate narrow ribbons of graphene by a distinctive cooperative process, whereas triple bilayer SiC steps allow large graphene sheets to grow by step flow. We demonstrate how graphene quality can be improved by controlling the initial surface morphology to avoid the instabilities inherent in diffusion-limited growth. This work is supported by the LDRD program at Sandia Labs and the US DOE Office of Basic Energy Sciences, Division of Materials Science and Engineering (DE-AC04-94AL85000), and was performed in part at CINT (DE-AC04-94AL85000). Sandia is a multiprogram laboratory operated by Sandia Corporation, a Lockheed Martin Co., for the U.S. DOE NNSA (DE-AC04-94AL85000).

9:00am **GR+SS+TF+EM-MoM3 Epitaxial Graphene on SiC(0001), T. Seyller**, Universität Erlangen, Germany **INVITED**

The properties of graphene, its fabrication, and its application are very active fields of research. The large carrier mobility and prospects for room-temperature ballistic transport raise hopes for application of graphene in electronic devices. Applications, however, demand growth methods suitable for producing graphene layers on a wafer scale. While this goal is impossible to reach with mechanical exfoliation, epitaxial graphene (EG) grown on the basal plane surfaces of silicon carbide (SiC) offers a much better prospective. In this talk I shall review studies of the structural, electronic, and transport properties of EG grown on SiC by solid-state decomposition at elevated temperatures. The first part describes a study of the electronic structure and structural properties of EG which can conveniently be determined using surface science techniques. In the second part I demonstrate how the growth of EG is improved by going from the traditional growth environment, namely ultrahigh vacuum, to an Argon atmosphere. The latter method leads to vastly improved EG films with properties similar to those of exfoliated graphene. Finally I shall discuss how the interface between SiC and graphene can be controlled by intercalation of foreign atoms.

9:40am **GR+SS+TF+EM-MoM5 Structural Defects in Epitaxial Graphene Layers Synthesized on 4H-SiC(000-1) Substrate - Transmission Electron Microscopy (TEM) Studies, J. Borysiuk**, University of Warsaw, Poland, **S.K. Krukowski**, Polish Academy of Sciences, Poland

Main structural defects in graphene layers, synthesized on the carbon-terminated face, i.e. SiC(000 $\bar{1}$) face of 4H-SiC substrate, are discussed. The discussed structures include in-plane edge dislocations, grain boundaries, puckers, etc. These defects are investigated using High Resolution Transmission Electron Microscopy (HRTEM), revealing their atomic arrangement. The mechanism of creation of such defects, in relation to the misalignment to the underlying crystallographic structure of the SiC substrate is elucidated. The relation between the SiC surface structure, including the presence of the single atomic steps, the sequences of atomic steps, and also the macrosteps, and the emergence of edge dislocations or boundaries between the regions having different crystallographic orientation in the graphene layers, is shown. In addition, the structures containing different stacking sequences of carbon atoms in the graphene layers are presented. The presented C-layers stacking includes AA, AB, ABC sequences, and also the stacking close to turbostratic stacking.

10:00am **GR+SS+TF+EM-MoM6 Controlling the Growth Rate of Graphene on Silicon Carbide, D.B. Torrance, D.L. Miller, M. Phillips, H. Tinkey, E. Green, P.N. First**, Georgia Institute of Technology

Controlled thermal decomposition of silicon carbide is so far the most effective method for growing high-quality graphene epitaxially and at the wafer scale. In this work we simultaneously study the graphenization of SiC(0001) and SiC(000 $\bar{1}$) as a function of temperature and buffer-gas pressure in a custom-built ultrahigh vacuum (UHV) induction furnace. The buffer gas is modeled as a homogeneous diffusion medium using kinetic theory. In-situ characterization by both Auger electron spectroscopy and low-energy electron diffraction (LEED) was used to determine the pressure- and temperature-dependent growth rate of graphene layers. Sample quality was further assessed ex-situ using a variety of techniques such as Raman spectroscopy and scanning tunneling microscopy.

10:40am **GR+SS+TF+EM-MoM8 Evidence of Screw Dislocations in Epitaxial Graphene Islands, J.K. Hite, J.C. Culbertson**, Naval Research Laboratory, **J.L. Tedesco**, National Institute of Standards and Technology, **M.E. Twigg, A.L. Friedman, P.M. Campbell, R.L. Myers-Ward, C.R. Eddy, Jr., D.K. Gaskill**, Naval Research Laboratory

Epitaxial graphene (EG) has lately garnered enormous interest, due to its high free-carrier mobility and compatibility with semiconductor processing. In fact, the first EG RF field effect transistor has been demonstrated.¹ However, the growth mechanism of this material is not well understood. Current RF device work has been on the Si polar face of (0001) semi-insulating SiC substrates as EG on this face mainly consists of 1 monolayer of graphene. In contrast, the C-face consists of a dozen or more graphene layers and has a rougher morphology. Yet, there is significant interest in obtaining few layer, smooth EG on the C-face of SiC due to its better electrical properties as compared to the Si-face. Recently, it was shown that C-face EG grown in Ar ambient slows the growth rate, and under certain conditions results in islanding of the graphene on the C-face.² These islands open the possibility of investigating the initial stages of graphene growth.

Electron channeling contrast imaging (ECCI) has previously been used to investigate threading dislocations in semiconductors such as GaN and SiC.^{3,4} In this work, ECCI is used for the first time to investigate graphene island morphology as a function of island size and growth conditions. Using this characterization tool, single threading screw dislocations (TSDs) have been found in the center of small EG islands (>20 μ m diameter). ECCI images confirm that these small graphene islands are forming in hexagonal recesses below the surface of the SiC substrate. For larger islands, the evidence of TSDs disappears suggesting that as the islands grow or coalesce to larger diameters either the TSD becomes buried or no longer contributes to growth. Once the islands become this large, the graphene begins to grow above the SiC surface, unlike the smaller islands. After removal of the EG by various methods, TSDs are still observed in the centers of the pits formed by the small island graphene growth. After some removal efforts, many pits retained small triangles of graphene around the TSD. These results are consistent with Raman and AFM maps of the islands that demonstrate that the centers of the islands are much deeper and the graphene thicker than the surrounding graphene. The evidence of TSDs in the centers of these C-face EG islands strongly suggests that these dislocations serve as nucleation sites for EG growth, where the TSD may provide an escape pathway for sublimated silicon atoms during the growth process.

¹J.S. Moon *et al.*, IEEE Electron Dev Lett **31**, 260, 2010

²J.L. Tedesco *et al.*, Appl Phys Lett, in press

³Y.N. Picard *et al.*, Scripta Materiala **61**, 773, 2009

⁴Y.N. Picard *et al.*, Appl Phys Lett **90**, 23401, 2007

11:00am **GR+SS+TF+EM-MoM9 Direct Measurement of the Energy Gaps Involved in the Lifting of the Valley and Spin Degeneracies in Epitaxial Graphene**, *Y.J. Song, A.F. Otte*, CNST/NIST; Maryland NanoCenter UMD, *D.B. Torrance, Y. Hu, P.N. First, W.A. de Heer*, Georgia Institute of Technology, *J.A. Stroscio*, CNST/NIST

Landau levels on epitaxially grown graphene were recently mapped both spatially and energetically using scanning tunneling spectroscopy in magnetic fields at 4 K [1]. In this talk we present new measurements, made at ≈ 10 mK, of all four electron states resulting from the lifting of the fourfold spin- and valley-degeneracy of the $N = 1$ Landau level in applied magnetic fields. We show that the energy splitting from the broken valley degeneracy is ten times larger than electron spin splitting in our samples. When the Fermi level lies inside the four-fold Landau manifold, significant electron correlation effects result in an enhanced valley splitting at even filling factors, and an enhanced electron spin splitting at odd filling factors. Most surprisingly, we observe new many body states with top-layer Landau level filling factors $7/2$, $9/2$, and $11/2$.

[1] David L. Miller, Kevin D. Kubista, Gregory M. Rutter, Ming Ruan, Walt A. de Heer, Phillip N. First, and Joseph A. Stroscio, Science **324**, 924-927 (2009).

11:20am **GR+SS+TF+EM-MoM10 Morphology of Epitaxial Graphene on SiC: Nano-Objects, Nano-Cracks, and Ribbons**, *S. Chiang*, Univ. of California at Davis, *N. Camara*, IMB-CNM-CSIC, Spain, *S. Vizzini, D. Martinotti*, CEA-Saclay, France, *H. Oughaddou*, Univ. de Cergy-Pontoise & CEA Saclay, France, *H. Enriquez*, Univ. de Paris-Sud/Orsay & CEA-Saclay, France, *Ph. Godignon*, IMB-CNM-CSIC, Spain, *J. Camassel*, GES, UMR-CNRS, France, *P. Soukiasian*, Univ. de Paris-Sud/Orsay & CEA-Saclay, France

We use scanning tunneling microscopy/spectroscopy (STM/STS) and low energy electron microscopy (LEEM) to investigate epitaxial graphene grown under vacuum on a 4H-SiC(000-1)-C-face substrate and self-organized parallel graphene ribbons grown in a furnace on a 6H-SiC(000-1) C-face sample covered by a graphite cap. On the vacuum grown graphene, we observed two types of nanostructures including nano-objects and nano-cracks. The results reveal that these nano-objects are located at the graphene/SiC interface leading to electronic interface states. Their height profiles suggest that these objects are made of packed carbon nanotubes confined vertically and forming mesas at the SiC surface. We also find nano-cracks covered by the graphene layer that, surprisingly, is not broken going deep into the crack, with no resulting electronic interface state. Therefore, unlike the above nano-objects, these cracks should not affect the carrier mobility. LEEM has been used to observe the formation of graphene ribbons grown on SiC in a furnace. The morphology and distribution of the ribbons has been examined, and their typical size is about 1 μ m wide and 10 μ m long.

Work supported by Agence National pour la Recherche (ANR) under GraphSiC program

Thin Film

Room: Ruidoso - Session TF+EM-MoM

Nanostructuring Thin Films

Moderator: A. Melechko, North Carolina State University

8:20am **TF+EM-MoM1 Nanostructured Magnetic Thin Film Heterostructures: Fabrication, Exchange Interactions and Tailored Anisotropies**, *K.M. Krishnan*, University of Washington **INVITED**

9:00am **TF+EM-MoM3 Self and Directed Assembly of Thin Metallic Films by Pulsed Laser Induced Dewetting**, *Y. Wu*, University of Tennessee, *J.D. Fowlkes*, Oak Ridge National Laboratory, *P.D. Rack*, University of Tennessee

The synthesis and assembly of functional metallic nanomaterials is critical for realizing many important applications of nanoscience and nanotechnology. In this study, we investigated thin film dewetting of metal films via pulsed nanosecond laser melting. We studied film instabilities induced by capillary forces and the subsequent mass transport which can lead to thin film break-up and subsequent nanoparticle formation. We have also explored the dewetting and nanopattern formation of nano-lithographically patterned thin films of various shapes to understand how various initial and boundary conditions can guide the assembly. In this presentation we will discuss the various spinodal and Rayleigh-Plateau instability mechanisms and the inertial, visco-inertial and viscous flow regimes involved in the thin metal film assembly. Finally we will discuss how nano-lithographically defined features can be used to direct the assembly of multi-functional nanoparticle ensembles.

9:20am **TF+EM-MoM4 Plasma-assisted Metallorganic Chemical Vapor Deposition of ZnO Nanostructures: Impact of Process Parameters on Dimensionality and Morphology**, *M. Bonvalot, G.M. Rosaz*, Ltm-Cnrs, Cea-Leti, France

ZnO is a II-VI semiconductor with a large band gap (3.4 eV) and excitonic binding energy (60 meV), which make it particularly attractive for a great diversity of potential emerging applications in the field of nanotechnologies (UV light emitters, laser diodes...). Several synthesis routes of ZnO nanostructure arrays have been reported in the literature, essentially on sapphire substrates. However, very few studies have been reported on growth of ZnO nanostructures on Si(111) substrates due to the difficulty of matching materials with different spatial symmetry group.

In this study, ZnO nanostructures have been prepared on Si(111) by plasma assisted pulsed injection MOCVD (metallorganic chemical vapor deposition). This technique of elaboration offers the advantage of large area growth and is compatible with existing semiconductor processing technologies. The key role of the plasma during material preparation is to allow lower substrate temperature (as low as 350°C), thus providing lower activation energies. It also allows in situ thermal treatment of substrates and prepared nanostructures. Moreover, the active chemical species of the plasma can help force in situ doping of the semiconducting nanostructure, which opens up a large spectrum of metastable phase formation possibilities.

We have investigated the effect of several process parameters (precursor flow rate, O₂/Ar partial pressure, plasma incident power) on the morphology of the produced nanostructures. Three growth regimes have been identified: 2 dimensional very fine grain thin films, ordered hexagonal shaped plates and oriented columnar grains with a very large density corresponding to nanowire growth. These results will be presented in the light of literature data [1, 2]. The transition between these three different growth regimes is induced by a careful adjustment of the substrate temperature and Ar/O₂ plasma flowrate. The role of these process parameters will be highlighted based on gas phase OES and SEM analyses, and the growth mechanism of densely packed 1D ZnO nanostructures will be presented.

[1] S. Agouram, J.A. Bastos-Segura and V. Munoz-Sanjos, [<http://www.sciencedirect.com/science/journal/07496036>] **42**, 140 (2007).

9:40am **TF+EM-MoM5 Self-assembled and Engineered Nanostructures in $\text{Hf}_{1-x}\text{Al}_x\text{N}/\text{MgO}(001)$ Single-Crystal Alloys: Effects on Physical Properties**, *B. Howe, E. Sammann, J.-G. Wen, M. Sardela, T. Spila, J. Greene*, University of Illinois at Urbana-Champaign, *L. Hultman*, Linköping University, Sweden, *I. Petrov*, University of Illinois at Urbana-Champaign

Transition metal nitrides (TMN) are well known to have a remarkable range of unique physical properties. One method used to further enhance the physical properties of many transition metal nitrides is to alloy them with a second, thermodynamically immiscible nitride. The most famous example is $\text{Ti}_{1-x}\text{Al}_x\text{N}$; many have reported drastically enhanced physical properties including super hardness, increased oxidation resistance, age-hardening behavior, and the formation nanoscale compositional modulations during film growth and post annealing experiments. However, very little has been reported on the ability to control this nanostructure, nor has the effect of these nanostructures on the physical properties of the films. We have chosen $\text{Hf}_{1-x}\text{Al}_x\text{N}$ as a model system to study the nanostructures of interest. We begin by reporting on the effects of nanostructure on the opto-electronic, thermal transport and elastic constant properties of $\text{Hf}_{1-x}\text{Al}_x\text{N}$ single crystal layers grown on $\text{MgO}(001)$ using ellipsometry, temperature dependent hall effect, and picosecond probe acoustic transport measurements, respectively. We continue by summarizing a systematic study into the effects of growth parameters (ion energy, E_i , ion-to-metal flux ratio, $J_{\text{ion}}/J_{\text{me}}$, and substrate temperature, T_s) on single crystal reactively sputtered $\text{Hf}_{0.7}\text{Al}_{0.3}\text{N}/\text{MgO}(001)$ layers in order to controllably manipulate the nanostructure and study its effects on the physical properties. Films are deposited from a Hf/Al 70/30 (at. %) target in 5% N_2/Ar mixtures while $J_{\text{ion}}/J_{\text{me}}$ is varied from 0.7 to 12.6, T_s from 400 to 700 °C, and E_i from 10 to 80 eV. $J_{\text{ion}}/J_{\text{me}}$ has a strong effect on the formation of 3D nanoscale (2-3nm) compositional modulations as indicated by HR-XRD and HR-TEM. Nanoindentation experiments reveal an increase in film hardness from 31.7 ± 0.6 GPa to 38.9 ± 0.6 GPa. E_i has a strong effect on the AlN incorporation probability, which can be adjusted between ~ 0 and 100% by varying the ion energy (E_i) incident at the growing film over a narrow range, 10-40 eV. Epitaxial film compositions vary from $x = 0.30$ with $E_i = 10$ eV, to 0.27 with $E_i = 20$ eV, 0.17 with $E_i = 30$ eV, and ≤ 0.002 with $E_i \geq 40$ eV. This extraordinary range in real-time manipulation of film chemistry during deposition is due to the efficient resputtering of Al atoms (27 amu) by Ar^+ ions (40 amu) backscattered from Hf atoms (178.5 amu). We demonstrate that this effect can be used to grow superlattices with abrupt interfaces at high deposition rates from a single target by switching E_i . We grew superlattices with bilayer thicknesses from 1-6nm and films exhibited an increase in hardness from 32.5 ± 0.9 GPa to 37.8 ± 1.2 GPa.

10:00am **TF+EM-MoM6 Lowering the Epitaxial Growth Temperature of Ge Quantum Dots on $\text{Si}(100)-(2 \times 1)$ by Electronic Excitation**, *A.O. Er, H. Elsayed-Ali*, Old Dominion University

Low temperature epitaxy is important for device fabrication because it can lead to suppressing the introduction of defects such as dislocations and stacking faults. The effect of laser-induced electronic excitations on the self-assembly of Ge quantum dots (QDs) on $\text{Si}(100)-(2 \times 1)$ grown by pulsed laser deposition is studied. The experiment was conducted in ultrahigh vacuum. A Q-switched Nd:YAG laser (wavelength $\lambda = 1064$ nm, 10 Hz repetition rate) was split into two beams; one used to ablate a Ge target while the other to electronically excite the substrate. In-situ reflection high-energy electron diffraction (RHEED), scanning tunneling microscopy (STM), and ex-situ atomic force microscopy (AFM) were used to study the morphology of the grown QDs. The dependence of the QD morphology on substrate temperature and ablation and excitation laser energy density was studied. Electronic excitation is shown to affect the surface morphology. For Ge coverage of 22 monolayer, it was observed that excitation laser reduces the epitaxial growth temperature to 250 °C. Applying excitation laser to the substrate during the growth changes the QD morphology and island density and improves the size uniformity of QDs at 390 °C. Applying the excitation laser during growth decreases the surface roughness at room temperature. RHEED recovery curves show that applying excitation laser increases the surface diffusion. A purely electronic mechanism of enhanced surface diffusion of the Ge adatoms due to a phonon-kick mechanism following two-hole localization could explain the results. Ongoing experiments using a femtosecond laser for excitation and in-situ STM for detection of the early stages of island nucleation will be presented.

10:40am **TF+EM-MoM8 Novel Nanoparticle and Thin film Growth Via Matrix Assisted Pulsed Laser Evaporation of Metal Based Acetates**, *M.A. Steiner, J.M. Fitz-Gerald*, University of Virginia

Until recently, the majority of research surrounding Matrix Assisted Pulsed Laser Evaporation (MAPLE) has been concentrated on preserving the

structure and properties of polymeric and biomaterials. Deviating from this course, novel research will be presented illustrating the feasibility of applying matrix-assisted processing to grow inorganic materials from precursor solutions in the form of complex nanoparticles and thin films. By replacing the preferentially absorbing matrix material with a transmitting solvent, laser energy is instead absorbed by a precursor solute which decomposes and is subsequently ejected onto the substrate in the form of nanoparticles. [1] [2] Acetates are a widely favored metallorganic precursor for thin film processing on various substrates because they decompose under ultraviolet irradiation. Results will be presented in the form of thin films and nanoparticle systems of Au-Ag-Pd, ZnO, and YBaCuO material systems.

[1] Allmond, C., Sellinger, A., Gogick, K., & Fitz-Gerald, J. (2007). Photochemical synthesis and deposition of noble metal nanoparticles. *Applied Physics A: Materials Science & Processing*, 86(4), 477-480

[2] Sellinger, A., Aburada, T., & Fitz-Gerald, J. (2008). Synthesis of multimetallic nanoparticles using a solution-based pulsed laser deposition approach. In *Proceedings of SPIE* (Vol. 7005, p. 700516)

11:00am **TF+EM-MoM9 Nanocomposite Vanadium Oxide Thin Films**, *B.D. Gauntt, M.W. Horn, O.M. Cabarcos, E.C. Dickey*, Penn State University

Thin film vanadium oxide is used as the active layer in un-cooled, infrared imaging devices based on microbolometer structures. In this type of imaging device, infrared radiation is detected via a temperature driven resistivity change in the active layer. Underlying readout circuitry and the need for increased detection sensitivity require low electrical resistivity material with high thermal coefficient of resistivity (TCR). Vanadium oxide thin films deposited via reactive pulsed direct current (DC) sputtering have properties in the range of interest with room temperature resistivity varying from 0.01 to 6×10^4 Ohm cm and TCR's varying from -0.1 to -4.2 %/°C. Films with resistivity in the range of interest (0.1 to 1.0 Ohm cm) contain the rocksalt structured FCC VO_x phase ($0.8 < x < 1.3$) accompanied by significant structural disorder, while those with greater resistivity are amorphous. The relationship between TCR and room temperature resistivity is exponential, and throughout the present series of films is fixed, i.e. a film with a given resistivity has a set TCR. Energy filtered electron diffraction patterns collected in the transmission electron microscope (TEM) reveal a diffuse scattering feature at low scattering angle for both amorphous and nanocrystalline films, suggesting that films containing nanocrystals also contain an amorphous phase. Raman spectroscopy results from amorphous films show a broad feature around ~ 890 cm^{-1} , while spectra from nanocrystalline films exhibit the "amorphous" feature and a second broad feature at ~ 300 cm^{-1} . The feature at ~ 300 cm^{-1} was the only feature present in the most crystalline of the films, suggesting it represents the disordered FCC VO_x phase. Film stoichiometry, as measured with Rutherford backscattering spectroscopy, puts the overall chemistry of the nanocrystalline films outside the FCC VO_x phase field, with many of the samples having a V:O ratio greater than 1.3. A pre-peak feature in the V-K edge was observed with X-ray absorption spectroscopy (XAS), and the intensity of the pre-peak, which is known to result from local octahedral disorder, increased with increasing oxygen content and correlates with diffraction observations of increasing disorder. The combined TEM, RBS, Raman, and XAS analyses suggest vanadium oxide films with properties in the range of interest for microbolometer-based devices consist of a two-phase material containing FCC VO_x nanocrystals embedded in an oxygen-rich amorphous matrix. Films lacking sufficient disorder have resistivity in the range of interest but insufficient TCR magnitude, suggesting the need for both the nano-crystalline phase and the amorphous matrix.

11:20am **TF+EM-MoM10 Titanium-doped Carbon-based Nanocomposite Coatings, Mechanical and Tribological Properties, Biocompatibility and Cell-Attachment Properties: Implications in Orthopedic Implants**, *P. Epaminonda*, University of Cyprus, *Y. Christou, A. Odysseos*, EPOS-IASIS R&D, Cyprus, *C. Rebholz, C. Tsotsos*, University of Cyprus

Stress shielding due to uneven load distributions at the bone-prosthesis interface affect joint prostheses and can lead to wear and loosening. Commonly used cobalt-chromium-molybdenum alloys can degrade during wear at an average rate of 0.02-0.06 mm/year. Other alloys such as titanium-aluminum-vanadium although biocompatible and highly corrosion resistant, exhibit relatively low mechanical properties and poor wear resistance. Nanocomposite nanocrystalline (nc-) $\text{Ti}(\text{N,C})$ / amorphous diamond-like-carbon (a-C:H) coatings exhibit high hardness (H), low friction coefficients, high wear resistance and resilience to substrate deformation thus making them promising candidates for prosthetic implant applications. In this work we investigate the influence of the microstructure of nc- $\text{Ti}(\text{N,C})$ /a-C:H coatings on the mechanical, tribological and biological

properties with the aim of using such materials not only as wear resistant films in biomedical implants, but also as a bioactive surface that can promote bone ingrowth at areas of medical implants, such as the femoral stem or the acetabular cell in hip replacement joints, that are in direct contact with bone. Approximately 2 μm thick, nc-Ti(N,C)/a-C:H coatings were deposited on Si wafer and implant alloy coupons using low temperature (~ 200 °C) DC reactive magnetron sputtering. The carbon content was varied from 41 to 57 at % and the obtained a-C:H phase ranged from 31 – 47 at. % in order to form the desired nanocomposite structure of 2-4 nm wide Ti(N,C) with 1 to 2 monolayer coverage of a-C:H. An increase in the amorphous phase results in a decrease in mechanical and a decline in tribological performance, however the change in structure and surface morphology at increased carbon content favours the bioactivity of the films. Coating chemical composition and microstructure was investigated by means of x-ray photoelectron spectroscopy (XPS), x-ray diffraction (XRD) and transmission electron microscopy (TEM). The mechanical and tribological properties of the films were determined using nanoindentation and nanotribo-scope methods. In order to assess the biocompatibility of nc-Ti(N,C)/a-C:H coatings and investigate their osteoblast - attachment properties and thus determine their efficacy as implant coatings, the osteoblastogenic osteosarcoma immortalised cell lines Saos-2 and Hos were seeded and allowed to grow on the coating surface. Cell attachment properties were assessed in terms of viability of seeded cells. Viable attached cells were quantified by a mitochondrial enzymatic activity-based colorimetric assay against cultures seeded on conventional tissue-culture treated plastic surface.

11:40am **TF+EM-MoM11 Magnetic Responsive Polymer Nanocomposites Thin Films: Synthesis, Characterization and Implementation in RF/Microwave Applications.** *C. Morales, J. Dewdney, S. Skidmore, S. Pal, K. Stojak, H. Srikanth, T. Weller, J. Wang,* University of South Florida

Newly-developed magnetic responsive polymer nanocomposites were elaborated using low complexity equipments and low-cost lab materials and apparatus. Sub-10nm CoFe₂O₄ and Fe₃O₄ nanoparticles with tightly controlled size distribution were synthesized using a chemical coprecipitation procedure, which involves Iron and Cobalt salts and oleic acid and oleylamine as surfactants. This polymer nanocomposite is dissolved in hexane together with calculated amount of surfactant-coated nanoparticles to obtain the polymer nanocomposites with uniform nanoparticle dispersion at desired concentration. Excellent dispersion of magnetic nanoparticles in the polymer matrix is very important for a low-loss material at microwave and RF frequencies, as it minimizes magnetic hysteresis losses by reducing magnetic coupling amongst particles. The amount and composition of all the constituent solvents is critically-controlled for the purpose of maintaining the desired viscosity to control the exact thickness of the thin film after solvent evaporation and the curing process.

The electrical microwave properties of Fe₃O₄-based polymer nanocomposites (e.g., permeability, permittivity and loss tangent) were tuned under externally-applied DC magnetic fields. In addition, two novel microstrip-based test structures were used to extract the complete set of microwave properties and their dependence on externally-applied magnetic field. The transmission of microwave signals through these structures is susceptible to variation in the dielectric/magnetic properties of the polymer nanocomposites, which facilitates the demonstration of the tunability and extraction of properties at different magnetic field strengths.

The required magnetic field is achievable by small commercial permanent magnets, which justifies the use of this new class of materials for implementation of practical microwave and RF devices and circuits. Magnetic polymer nanocomposites are very easy to process, which enables them to be employed in both PCB board and chip levels using conventional manufacturing processes. They exhibit unique and very attractive properties for many microwave applications that require tunability and flexible materials.

Thin Film

Room: Pecos - Session TF+EN-MoM

ALD: Energy Applications

Moderator: S.M. George, University of Colorado at Boulder

8:20am **TF+EN-MoM1 ALD Applications in Heterogeneous Catalysis.** *P.C. Stair,* Northwestern University & Argonne National Lab, *J. Lu,* Northwestern University, *H. Feng, J.E. Libera, J.W. Elam, M.J. Pellin,* Argonne National Laboratory, *H.-S. Kim,* Northwestern University
INVITED

Atomic Layer Deposition (ALD) has enormous potential for the synthesis of advanced heterogeneous catalysts with controlled composition and structure at the atomic scale. The ability of ALD to produce conformal oxide coatings on porous, high-surface area materials offers the possibility to provide completely new types of catalyst supports. At the same time ALD can achieve highly uniform catalytically active metal and oxide phases with (sub-) nanometer dimensions.

Vanadium oxide species supported on high surface area oxides are among the most important catalytic materials for the selective, oxidative conversion of hydrocarbons to useful chemicals. In our laboratory ALD has been used to synthesize both the catalytic vanadium oxide and the supporting oxide on both high surface powders and anodic aluminum oxide (AAO) nanoliths. These materials have been characterized by SEM, XRF, ICP, UV-Vis absorption spectroscopy, Raman spectroscopy and evaluated for the oxidative dehydrogenation (ODH) of cyclohexane.

More recently we have studied what we call “ABC-type” ALD in which metal nanoparticles and support materials are grown sequentially in each ALD cycle. This method makes possible metal deposition at lower temperatures than conventional AB-type ALD and exceptionally small particles, ca. 0.5 nm. Using additional ALD support layers at the conclusion of the growth, the metal particles are stabilized against sintering at high temperatures and reaction conditions.

9:00am **TF+EN-MoM3 Process and Materials Optimization for Ru/RuO₂ ALD using a Novel Cyclohexadienyl Precursor.** *K. Gregorczyk, L. Henn-Lecordier,* University of Maryland, *J. Gatineau, C. Dussarrat,* Air Liquide, *G.W. Rubloff,* University of Maryland

Ruthenium is of particular interest to the semiconductor industry and others due to its low bulk resistivity ($7\mu\Omega\text{ cm}$) and high work function (4.7eV). In addition, its complementary oxide, RuO₂, can exhibit high specific capacitance (up to 750 F/g) and conductivity ($80\text{--}100\mu\Omega\text{ cm}$), making it attractive for energy storage applications. We report results for Ru and RuO₂ ALD using a novel Ru cyclohexadienyl precursor and oxygen. This precursor is attractive because it is liquid at room temperature, stable in air and non-reactive with water, while its vapor pressure is similar to that of common ALD Ru precursors RuCp₂ and Ru(EtCp)₂, i.e., 0.1 Torr at 60°C and 1 Torr at 100°C. ALD Ru deposition was achieved in a wafer scale (100mm), cross-flow ALD reactor. Self-limiting ALD surface chemistry is observed between 250-300°C with a growth rate of $\sim 0.5\text{Å}/\text{cycle}$ and across-wafer uniformity >98%. Four point probe measurements show a low sheet resistance of $16\mu\Omega\text{ cm}$. Ru nucleation is improved compared to RuCp₂ and Ru(EtCp)₂ based processes, with no nucleation delay on SiO₂ or TiO₂, a slight delay on Si, and a significant delay on Al₂O₃. Growth rates are constant with the number of deposition cycles. Conformality studies were conducted using high aspect ratio anodic aluminum oxide (AAO) thin films, using a thin TiO₂ nucleation layer before Ru ALD. This Ru ALD process converts to a RuO₂ ALD process at higher oxygen partial pressure, with an oxide conductivity of $\sim 80\mu\Omega\text{ cm}$. Post-process thin film characterization using XRD, XPS and AFM will be also presented.

This work was supported by the US Department of Energy, Office of Basic Energy Sciences as part of an Energy Frontier Research Center.

9:20am **TF+EN-MoM4 Atomic Layer Deposition Enabled Metal-Insulator-Metal Tunnel Diode for Infrared Energy Rectifying System.** *I.-T. Wu,* University of South Florida, *N. Kislov,* NanoCVD Inc., *J. Wang,* University of South Florida

Amongst present-day renewable energy sources, solar cells have been widely considered as the most viable solution. However, the energy conversion efficiency for the solar cells is limited to 30% or below due to the device physics. Rectifying antenna (rectenna) is an ideal supplement that is able to efficiently capture the abundant infrared (IR) energy from the solar radiation in part due to IR antenna's inherent high efficiency. The rectenna system consists of two key elements: antenna and rectifying diode. The IR antenna captures the solar radiation within the wavelength of

interest to be delivered to the ultrafast diode that rectifies the received signal into usable DC power.

Rectennas operating at microwave frequencies with efficiency up to 85% has been routinely demonstrated. However, the key remaining challenge for the infrared counterparts can be ascribed to the insufficient cutoff frequency of the semiconductor-based diodes owing to their excessive depletion-induced capacitance. In order to obtain the desired response times less than 10-12seconds, metal-insulator-metal (MIM) tunnel diodes with junction area in the range of 100nm×100nm were implemented herein to enable the coveted terahertz frequencies due to the greatly reduced junction capacitance and ultrafast quantum tunneling.

In this work, MIM tunnel diodes with sub-micron sized junction have been mass produced using CMOS-compatible processes without the need for E-beam lithography or sophisticated chemical etching. Standard photolithography and atomic layer deposition (ALD) were used to allow formation of a micrometer-wide finger in the second metal layer separated from the electrode in the first metal layer by an ALD-deposited sidewall dielectric spacer, thus forming a nm-thick vertical tunnel junction. The nano-scale junction is defined by the width of the finger and the thickness of the electrode, while the junction thickness is controlled by the ALD process.

On par to nano-scale devices, MIM tunnel diodes with micron-scale self-aligned cross-fingers have been successfully developed. Through this process, we have investigated a wide variety of metal and insulator materials such as Au, Cu, Pt, Ni, Al, Al₂O₃, HfO₂ to advance the performance of the MIM diode with particular focus on its efficiency. Some preliminary DC and RF characterization have been carried out to study the device characteristics such as responsivity, nonlinearity and asymmetry of I-V, and frequency responses. Ongoing research for modeling of MIM tunneling diode based on measured S-parameter data and further reduction of the device junction area will be detailed in the final manuscripts.

9:40am **TF+EN-MoM5 New Semiconductor-Insulator-Semiconductor Solar Cell Concept based on Wet Chemically Etched Silicon Nanowires: Processing and Electro-Optical Properties, B. Hoffmann, V.A. Sivakov, G. Broenstrup, F. Talkenberg, Institute of Photonic Technology, Germany, S.H. Christiansen, Max Planck Institute for the Science of Light, Germany**

Silicon nanowire (SiNW) ensembles with vertical geometry have been realized using wet chemical etching of bulk silicon wafers (n-Si(100)) with an etching hard mask of silver nanoparticles that are deposited by wet chemical electroless deposition on silicon surfaces.

The new concept of the solar cell is based on the semiconductor-insulator-semiconductor (SIS) layer sequence produced by Atomic Layer Deposition (ALD). A thin tunnelling oxide (SiO₂, Al₂O₃) with a thickness of 5-20 Å and a 300 nm transparent conductive oxide (Al doped ZnO or In doped SnO₂) around 1D silicon nanostructures have been realized using Plasma Assisted ALD approach (Oxford Plasma, OpAL).

The first prototype reached an open-circuit voltage of 80mV and a short-circuit current density of 23mA/cm².

The influence of the thickness and chemical nature of the tunnelling oxide will be discussed. Back side contacts of Ti/Al or Ti/Ag were realized using sputtering. From literature it is known that the planar SIS solar cell can reach an energy conversion efficiency of approx 15%. Absorption of visible and infra-red light is significantly enhanced in nanowires compared to planar layers of identical thickness. Thus, wet chemically etched silicon nanowires have the potential for even higher energy conversion efficiencies compared to the planar SIS solar cells. The morphology, crystallographic and surface structure, optical and solar cell properties will be presented and discussed in details.

10:00am **TF+EN-MoM6 Ultrathin Al₂O₃ for c-Si Solar Cells: Differences in Passivation by Thermal and Plasma ALD-Synthesized Films, G. Dingemans, N.M. Terlinden, M.L.C. Adams, H.B. Profijt, M.M. Mandoc, M.C.M. van de Sanden, E.W.M.M. Kessels, Eindhoven University of Technology, Netherlands**

Ultrathin films of Al₂O₃ synthesized by ALD at low substrate temperatures (200 °C) have recently demonstrated their potential as surface passivation material in c-Si photovoltaics enabling solar cell efficiencies up to 23.4%. So far, the best results were obtained by plasma ALD Al₂O₃ but recently it was shown that similar excellent results can be obtained by thermal ALD [1]. For both methods, Al₂O₃ yield excellent lifetimes after annealing (at 400 °C) on both p- and n-type Si wafers with the best results corresponding to ultralow surface recombination velocities < 1 cm/s (for 3.5 Ohm cm n-

type c-Si). However, also several striking differences have been observed in terms of the underlying passivation mechanism as will be addressed in this contribution. From capacitance-voltage (C-V) measurements, corona charging experiments and optical second harmonic generation (SHG) it was found that Al₂O₃ deposited with thermal ALD contains a lower negative fixed charge density (~10¹² cm⁻²) than plasma ALD (> 5·10¹² cm⁻²). This indicates that field-effect passivation (i.e., shielding of one type of charge carriers from the surface) is less important for thermal ALD. On the other hand, it was observed that chemical passivation (i.e., reduction of interface defect states) is very important for both thermal and plasma ALD Al₂O₃. Relatively low interface defect densities *D_{it}* of <10¹¹ eV⁻¹ cm⁻² were found for both methods after anneal. However, for as-deposited Al₂O₃, the interface defect density (and correspondingly the surface recombination velocity) is significantly poorer for plasma ALD Al₂O₃ than for thermal ALD Al₂O₃. From vacuum ultraviolet (VUV) emission measurements, it has been found that the high *D_{it}* can be attributed to plasma radiation damage by photons with an photon energy of ~9.5 eV. Furthermore, it will be shown that the difference in importance of field-effect passivation explains several differences observed in the passivation performance for thermal and plasma ALD Al₂O₃ (e.g., the minimum thickness required for excellent passivation).

[1] G. Dingemans, M. C. M. van de Sanden, W. M. M. Kessels, *Electrochem. Solid-State Lett.*, 13, H76 (2010).

10:40am **TF+EN-MoM8 Cathodoluminescent and Photoluminescent Properties of Pulsed Laser Deposited Thin Phosphor Films, O.M. Nwaabiorwa*, P.D. Nsimama, J.J. Dolo, University of the Free State, South Africa, M.S. Dhlamini, University of the Free State and CSIR, South Africa, E. Coetsee, J.J. Terblans, H.C. Swart, University of the Free State, South Africa**

INVITED

Phosphors have many uses today, such as information display, medical imaging, and theft prevention. The phosphors are often used as powders, even though thin films offer higher resolution and better chemical stability. We have investigated the cathodoluminescent (CL) and photoluminescent (PL) properties of thin films of several phosphors (e.g. SrAl₂O₄:Eu²⁺, Dy³⁺; SiO₂:PbS; Gd₂O₂S:Tb³⁺; SiO₂:Ce³⁺, Tb³⁺ and Y₂SiO₅:Ce³⁺) that were ablation deposited onto Si (100) substrates using either conventional pulsed laser deposition (PLD) or pulsed reactive crossed beam laser ablation (PRCLA). Several deposition parameters were varied, including vacuum versus partial pressure of gas (O₂ or Ar), type of laser pulse, and substrate temperature using either a 307 nm XeCl or 248 nm KrF excimer laser. The CL spectrum and intensity were measured in vacuum from films irradiated with 2 keV electrons for a prolonged period of time, while PL data were collected in air under excitation by either a 325 nm HeCd laser or a monochromatized xenon lamp. Both the CL and PL intensities were strongly dependent on the deposition conditions and post-deposition annealing. Data from scanning electron microscopy (SEM) and atomic force microscopy (AFM) show that the major influence of the deposition conditions on the CL/PL intensity was through changes in the morphology and topography of the films, which affects light scattering and out-coupling. Finally, the CL intensity from the films decreased significantly during prolonged electron beam irradiation. The degraded CL intensity resulted from the formation of non-luminescent oxide layers on the film surfaces. The chemical composition and electronic states of the 'dead' layers were analyzed using x-ray photoelectron spectroscopy (XPS). The influence of the various deposition conditions on the luminescent intensities will be discussed. The mechanism leading to lower CL intensities will be concluded to be electron stimulated surface chemical reactions.

* Paul Holloway Award Winner

Thin Film

Room: Pecos - Session TF-MoA

Organic ALD

Moderator: G.N. Parsons, North Carolina State University

2:00pm **TF-MoA1 Inorganic/Organic Interface Structure on ALD Modified Polymer Fibers**, J.S. Jur, J.C. Spagnola, W.J. Sweet, B. Gong, Q. Peng, G.N. Parsons, North Carolina State University

Inorganic thin film growth by atomic layer deposition (ALD) on polymer fibers is shown to be significantly affected by the process conditions and materials. Transmission electron microscopy in combination with *in situ* quartz crystal microbalance analysis shows a strong influence on processing temperature and polymer backbone structure that can lead to varying types of interface modifications between the inorganic and organic polymer. Deposition on cellulose cotton shows conformal surface growth due to the presence of hydroxyl sites, resulting in conformal thin film growth. Polypropylene, which has no reactive sites, does allow for vapor phase diffusion of the ALD precursors, resulting in subsurface growth. The subsurface growth on polypropylene is significantly impeded at lower processing temperatures. The strong temperature dependence of interface modification is ascribed to a relatively large increase in bulk species diffusivity that occurs upon the temperature-driven free volume expansion of the polymer. The interface structure can significantly modify the physical properties of resulting inorganic-coated polymer fibers. For example, we measured the electrical properties of ALD ZnO coatings on polypropylene fiber mesh, and we find that modifying the polymer inorganic interface using low temperature ALD Al₂O₃ before ZnO ALD produces fibers with conductance that is increased by a factor >100x as compared to ZnO coated polypropylene without the interface pretreatment. For a range of polymer materials studied, we find distinct trends between polymer structure, ALD process conditions and resulting interface structure, and these results will be presented and discussed.

2:20pm **TF-MoA2 Molecular Layer Deposition of Hybrid Siloxane/Alumina Polymer Films**, A.I. Abdulagatov, B. Yoon, V.R. Anderson, Z.M. Gibbs, A.S. Cavanagh, S.M. George, University of Colorado at Boulder

Polydimethylsiloxane (PDMS) is an important polymer with excellent flexibility and low elastic modulus. The properties of PDMS are also tunable based on varying the cross-linking between the polymer chains. PDMS MLD was initially attempted using the sequential dosing of bis(dimethylamino)dimethylsilane or dimethylmethoxychlorosilane (DMMCS) and water at different temperatures. Unfortunately, the surface reactions appeared to terminate and no mass gain was measured after about 20 MLD cycles. After precursor dosing was stopped, the deposited film was observed to decrease in mass. This loss of mass is believed to be related to desorption of cyclic siloxanes from the PDMS MLD film. Cyclic siloxane desorption is entropically favored at longer PDMS chain lengths and higher temperatures and is facilitated by the high flexibility of the PDMS chains. To prevent desorption of the cyclic siloxanes, hybrid siloxane/alumina films were grown by mixing aluminum into the siloxane film using trimethylaluminum (TMA). The new hybrid MLD films contain [-Si(CH₃)₂-O-] units that are separated by [-Al-O-] linkages. The hybrid siloxane/alumina polymer films were grown using the precursor sequence: DMMCS; H₂O, TMA; and H₂O. Quartz crystal microbalance studies revealed linear growth with growth rates of ~22 ng/cm² at 200°C. FTIR vibrational studies revealed -Si(CH₃)₂OCH₃, -Si(CH₃)₂OH, -AlCH₃, and -AlOH surface species after the DMMCS; H₂O, TMA; and H₂O exposures, respectively. FTIR studies also observed self-limiting adsorption during the individual precursor exposures. X-ray reflectivity (XRR) measurements revealed a hybrid siloxane/alumina growth rate of ~1.0 Å/cycle at 200°C and a film density of ~2.3 g/cm³. Elemental analysis of films using X-ray photoelectron spectroscopy (XPS) indicated that the films were chlorine-free. Hybrid siloxane/alumina polymer films could be grown at temperatures as low as 120°C, and these films showed some chlorine impurities.

2:40pm **TF-MoA3 Quantum Chemical Simulations of ALD and MLD; Insights from Simulations**, C. Musgrave, University of Colorado at Boulder

INVITED

Ab Initio simulations have become widely used tools in the materials, surface science and chemistry communities for predicting molecular and materials properties and for studying atomistic processes. In this talk we will give an overview of how these methods can be used to understand ALD

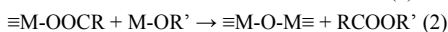
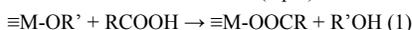
and MLD from an atomistic viewpoint and what you can learn from simulations. We will also discuss the limits of quantum chemistry and provide guidelines for those interested in using simulations to study ALD. Examples from our past and current work as well as that of others will be used to illustrate the application of these methods to surface reactions relevant to ALD and MLD. Examples include; the effect of using precursors with different ligands, including alkoxides, alkylamides and halogens, to deposit HfO₂ and Al₂O₃; the effect substrate type and functionalization on the initial ALD nucleation reactions; the ability to grow oxynitrides; and the use of simulations as a computational spectroscopy tool to compliment experiment in the determination of ALD intermediates and products.

3:40pm **TF-MoA6 Nonaqueous Sol-Gel Chemistry in Atomic Layer Deposition**, N. Pinna, University of Aveiro, Portugal and Seoul National University, Korea

INVITED

Nonaqueous sol-gel routes are elegant approaches for the synthesis of high quality metal oxide nanomaterials such as pure inorganic nanocrystals [1], ordered hybrid organic-inorganic materials [2] or thin films by atomic layer deposition (ALD) [3]. In this communication, after a short introduction to nonaqueous sol-gel chemistry we will focus on the ALD using nonaqueous sol-gel. In particular, the similarities and differences of the chemical processes taking place in solution and in ALD will be discussed through two examples of recent approaches of metal oxide film deposition

Our approach makes use of metal alkoxides and carboxylic acids as metal and oxygen source, respectively [4]. In the first step, it is expected that the reaction of surface alkoxide species with carboxylic acids leads to surface carboxylate species (eq. 1). In the second step an aprotic condensation reaction between surface carboxylate species and metal alkoxides leads to metal-oxide bonds formation (eq. 2).



This process enables the growth of metal oxides at temperatures as low as 50 °C on various supports.

A comparison of this nonaqueous sol-gel route to ALD approaches using ozone as oxygen source will be made. Although, from a first look it seems that the chemistry responsible for metal oxide formation is very different, this is certainly not the case. As a matter of fact it was recently reported that during the ALD of metal oxides, the exposure to ozone leads to formate, carbonate and hydroxyl groups on the surface [5-7]. According to Goldstein et al., a large amount of formate surface species were formed by the reaction of trimethylaluminum (TMA) and O₃ [5]. Therefore, the formation of surface carboxylic species upon reaction with ozone leads to similar surface states as in the case of reaction with carboxylic acids [4]. These findings will be used to discuss the chemical reactions responsible for the deposition of PbTiO_x using lead bis(3-N,N-dimethylamino-2-methyl-2-propoxide), titanium(IV) isopropoxide and a combination of water and ozone as oxygen sources as recently reported by Hyun Ju Lee et al. [8]

References:

- [1] Pinna, N. & Niederberger, M. *Angew. Chem. Int. Ed.*, **2008**, *47*, 5292
- [2] Pinna, N. *J. Mater. Chem.*, **2007**, *17*, 2769
- [3] Clavel, G. et al. *J. Mater. Chem.*, **2009**, *19*, 454
- [4] Rauwel, E. et al. *Angew. Chem., Int. Ed.*, **2008**, *47*, 3592
- [5] Goldstein, D. N. et al. *J. Phys. Chem. C*, **2008**, *112*, 19530
- [6] Rai, V. R.; Agarwal, *J. Phys. Chem. C*, **2008**, *112*, 9552
- [7] Kwon, J. et al. *Chem. Mater.*, **2008**, *20*, 3248
- [8] Lee, H. J. et al. *ECS Transactions*, **2009**, *19*, 829

4:20pm **TF-MoA8 Combined Atomic Layer Deposition and Molecular Layer Deposition for Encapsulation of Electrospun Nylon Nanofibers**, C. Oldham, B. Gong, J.C. Spagnola, North Carolina State University, K. Senecal, T. Godfrey, Natick Soldier RD&E Center, J.S. Jur, G.N. Parsons, North Carolina State University

Electrospun nanofibers are of interest for air filtration, thermal insulation, biochemical sensing, and a range of other applications. Nanofibers can be readily electrospun from polyamide-6 (PA-6) nylon, but nylon is highly susceptible to water uptake and rapid degradation when exposed to chemical reactants, including those used in ALD. The high surface area of nanofibers makes these issues more acute and difficult to manage. We have recently investigated the deposition of Al₂O₃ and ZnO on nylon nanofibers and found distinctly different results for these two material processes. Aluminum oxide ALD from trimethylaluminum and water resulted in significant fiber degradation, whereas fibers remained intact upon ALD using diethyl zinc and water. The ZnO coating was not sufficient, however,

to impede attack and degradation during subsequent exposure to Al₂O₃ ALD using TMA. We have recently explored a new MLD process in our lab using TMA and glycidol, where the resulting film is a hybrid organic-metal oxide polymer. This MLD coating onto a ZnO-coated nylon nanofiber results in only minimal reaction with the polymer under the ZnO. After 75 MLD cycles, exposing the nylon nanofibers to 25 cycles of trimethylaluminum/water results in no visible degradation, indicating successful encapsulation by the ZnO/MLD bilayer. We will present the chemistry associated with the reaction between the TMA and PA-6. Additionally, the surface chemistry of the PA-6 nanofibers after encapsulation, and the air stability of the hybrid organic-metal oxide coatings will be discussed.

4:40pm TF-MoA9 Structure and Properties of Ultra-High Molecular Weight PHEMA Synthesized Using Solvent-Free Initiated Chemical Vapor Deposition (iCVD), R.K. Bose, K.K.S. Lau, Drexel University

Initiated chemical vapor deposition (iCVD) is a low temperature variant of hot-wire chemical vapor deposition (HWCVD) which has been used to produce a wide variety of free radical polymers like fluoropolymers, acrylic polymers and silicone polymers without the use of solvents. An initiator is activated in the gas phase by a resistively heated filament array. The radicals thus generated undergo surface polymerization on a cooled substrate by attaching to multiple monomer units. In this work, we produced thin films of poly(2-hydroxyethyl methacrylate) (PHEMA), an important hydrogel, for potential biomaterials applications such as skin substitutes. Fourier transform infrared (FTIR) and nuclear magnetic resonance (NMR) spectroscopies showed that the chemistry of PHEMA obtained by iCVD synthesis matched closely to PHEMA obtained from solution synthesis. Deposition kinetics were tuned to achieve high deposition rates (~1.5 μm/min), which yielded mechanically robust ultra-high molecular weight polymer films. As a result, the films displayed a high degree of physical chain entanglement giving rise to high tensile modulus and storage modulus. This eliminates the need for chemical crosslinking, thus preserving maximum hydrophilicity for cell growth. The films showed good water transport and swellability. *In vitro* cytotoxicity studies of adult human dermal fibroblasts on PHEMA showed these films were non-cytotoxic and displayed viable cell adhesion. Non-specific protein adsorption was shown to be reduced compared to controls.

5:00pm TF-MoA10 Molecular Layer Deposition of Alucones Using Trimethylaluminum and Glycerol or Glycidol, R.A. Hall, B. Yoon, Y. Lee, S.M. George, University of Colorado at Boulder

Molecular layer deposition (MLD) can be used to grow hybrid organic-inorganic films using organic MLD and inorganic ALD precursors. The alucones are the most studied of these hybrid organic-inorganic films. Alucone MLD depends on the sequential, self-limiting reactions between trimethylaluminum (TMA) and various organic alcohols. In this work, alucone MLD was performed using glycerol, a sugar alcohol with three hydroxyl groups or glycidol, an alcohol molecule that contains an epoxide group. Both of these alcohols should promote cross-linking in the alucone film for enhanced film stability and film toughness.

Studies of alucone MLD using TMA and glycerol (GL) or glycidol (GLY) were performed using *in situ* quartz crystal microbalance (QCM), Fourier transform infrared (FTIR) and quadrupole mass spectrometry (QMS) techniques. The FTIR studies showed that the TMA and GL or GLY reactions were both self-limiting. For the TMA + GL reaction, the FTIR spectra observed the growth/loss of AlCH₃ and C-OH vibrations versus TMA/GL exposures. The mass gain measured by the QCM was 43 ng/cm²/cycle at 150°C. QMS confirmed the presence of TMA and GL parents and observed the CH₄ reaction products. *Ex situ* XRR measurements yielded a growth rate of 2.40 Å/cycle after 50 cycles at 150°C.

Alucone films grown using TMA and GL or GLY were more stable than alucone films grown using TMA and ethylene glycol. The instability of alucone films has been attributed to unreacted AlCH₃ species. To explore this issue, alucone films were grown using TMA, GL and H₂O exposures in an ABC sequence. QCM measurements showed that the mass gain increased to 56 ng/cm²/cycle for this ABC sequence at 150°C. In addition, the QMS observed CH₄ intensities during H₂O exposures that were ~1/4 the intensity observed during GL exposures. These results indicate that H₂O exposures can remove unreacted AlCH₃ species and increase the mass gain per cycle.

Tuesday Morning, October 19, 2010

Graphene Focus Topic

Room: Brazos - Session GR+TF-TuM

Characterization, Properties, and Applications

Moderator: M. Chhowalla, Rutgers University

8:00am GR+TF-TuM1 Near-field Scanning Microwave Microscopy of Few-Layer Graphene, N.G. Kalugin, New Mexico Tech

Near-field microwave microscopy can be used as an alternative to atomic-force microscopy or Raman microscopy in determination of graphene thickness. We evaluated the values of AC impedance for few layer graphene. The impedance of mono and few-layer graphene at 4GHz was found predominantly active. Near-field microwave microscopy allows simultaneous imaging of location, geometry, thickness, and distribution of electrical properties of graphene without device fabrication. Our results may be useful for design of future graphene-based microwave devices.

Sandia is a multiprogram laboratory operated by Sandia Corporation, a Lockheed Martin Company, for the

United States Department of Energy's National Nuclear Security Administration under contract DE-AC04 94AL85000.

8:20am GR+TF-TuM2 Molecular Simulation of the Indentation of Free-Standing Graphene Films in the Presence of Defects, J.D. Schall, R.V. Petrach, Oakland University

Recent experimental advances in the synthesis of graphene have enabled the construction of free-standing graphene-based "nanobridges" (for example: Shivaraman, Nanoletters, 9, 2009, 3100). This has allowed for the first time to probe the mechanical properties of this unique material directly through experiment. In the past, mechanical properties had been estimated theoretically via various molecular simulation techniques. With these new experimental advances, many new questions arise. To list a few: How do defects affect mechanical properties? How do molecular adsorbates modify these materials? Again, molecular simulation is expected to play a significant part in the future of graphene research. In this talk, results of simulated indentation of free-standing graphene films mimicking recent force-probe experiments will be presented. Simulations are conducted using Brenner's second generation reactive empirical bond order potential. This method allows for accurate determination of mechanical properties and chemical modification of the films. Using indentation and a simple force balance approach, the Young's modulus of a pristine free-standing graphene nano-bridge was estimated to be in excess of 1 Terapascal. Results from films with Stone-Wales defects, vacancies, and chemical adsorbates also will be presented.

8:40am GR+TF-TuM3 Mechanical Characterization of Freestanding Graphenoid Nanomembranes from Self-Assembled Monolayers, X. Zhang, C.T. Nottbohm, A. Turchanin, A. Beyer, A. Götzhäuser, Bielefeld University, Germany

We report on the fabrication and mechanical characterization of novel graphenoid nanomembranes with a thickness of approximately 1 nm. The nanomembranes are prepared from electron cross-linked aromatic self-assembled monolayers (SAMs). The membranes are then transferred to window-substrates (Si) for mechanical characterization. Bulge testing of such freestanding nanomembranes within an atomic force microscope is utilized to investigate their mechanical properties.

A series of biphenyl-based molecules were used to prepare the nanomembranes, such as carbonitrile-biphenyl-trimethoxysilyl (CBPS), biphenyl-thiol (BPT) and nitro-biphenyl-thiol (NBPT). Biphenyl-based nanomembranes have elastic moduli ranging from 6 to 12 GPa. They display outstanding performance in the ultimate tensile strength with values of 400 to 500 MPa, which is several times higher than the values of other carbon based membranes. Furthermore, annealing of the cross-linked nanomembranes in ultra high vacuum systematically increase of the Young's moduli from 10 GPa to ~45 GPa for an annealing temperature of ~1000 K. Strain relaxation lowers the residual strain from 0.9 % to ~0.35 % for temperatures of 800 K and above. This is caused by a structural transformation in which the nanomembrane is converted into nanocrystalline graphene.

9:00am GR+TF-TuM4 Chemical Vapour Deposition (CVD) Growth of Graphene on Copper, C. Mattevi, H.K. Kim, G. Eda, M. Chhowalla, Imperial College London, UK

Uniform large-scale fabrication of graphene thin films with controllable thickness represents a key challenge for integration of graphene into

practical electronic devices. Recently, graphene of high quality has been synthesized by chemical vapor deposition (CVD) on transition metal catalysts [1,2]. The graphene growth by CVD on polycrystalline copper [2] is particularly interesting because it allows single graphene layer over 95% of the surface and the residual 5% is covered by 2-3 layered graphene film. Hence, this is the first [2] reported reproducible method to synthesize uniform graphene thickness over large area. Then the as grown graphene can be transferred by different processes, onto a variety of substrates. An appealing challenge is to selectively obtain different graphene thicknesses over large area, to satisfy different applications. Here we report a detailed study of the multilayer graphene domains that appear in limited regions of the copper surface. The lateral size as well as the graphene thickness and stacking order, has been carefully investigated as a function of copper pre-treatment and growth parameters. In particular the role of the feed stock gas pressure and ratio between the etching gas (H₂) and the precursor (CH₄) has been demonstrated to affect the lateral size and the thickness. Optoelectronic properties of the transferred graphene films onto SiO₂ are also presented.

References

1. K. S. Kim, Y. Zhao, H. Jang, S. Y. Lee, J. M. Kim, K. S. Kim, J. H. Ahn, P. Kim, J. Y. Choi and B. H. Hong, *Nature* **457**, 706 (2009).
2. X. Li, W. Cai, J. An, S. Kim, J. Nah, D. Yang, R. Piner, A. Velamakanni, I. Jung, E. Tutuc, S. K. Banerjee, L. Colombo, and R. S. Ruoff, *Science* **324**, 1312 (2009).

9:20am GR+TF-TuM5 Structural and Electronic Properties of Graphene Synthesized by Chemical Vapor Deposition, Y. Chen, Purdue University

INVITED

We have studied the structural and electronic properties of large scale (up to several inches) graphitic and graphene thin films synthesized by chemical vapor deposition (CVD) on polycrystalline Ni_{1,2} and Cu₃ foils then transferred onto insulating substrates (SiO₂ on doped Si). For films grown on Ni_{1,2}, structural characterizations by atomic force microscopy (AFM), scanning tunneling microscopy (STM), *cross-sectional* transmission electron microscopy (XTEM)⁴ and spectroscopic Raman mapping confirm that such large scale graphitic thin films contain both thick graphite regions and thin regions of few layer graphene. The films also contain many wrinkles, with sharply-bent tip and dislocations revealed by XTEM, yielding insights on the growth and buckling processes of the film. Measurements on mm-scale back-gated transistor devices fabricated from the transferred film show ambipolar field effect with resistance modulation ~50% and carrier mobilities reaching ~2000 cm²/Vs. We also demonstrate quantum transport of carriers with phase coherence length over 0.2 μm from the observation of 2D weak localization in low temperature magneto-transport measurements. Our results show that despite the non-uniformity and surface roughness, such large-scale, flexible thin films can have electronic properties promising for device applications. For films grown on Cu₃, we show they consist dominantly of monolayer graphene as indicated by Raman mapping. STM imaging shows monolayer graphene lattice. Low temperature transport measurements are performed on micro devices fabricated from such CVD graphene, displaying ambipolar field effect (with on/off ratio ~5 and carrier mobilities up to ~3000 cm²/Vs) and "half-integer" quantum Hall effect, a hall-mark of intrinsic electronic properties of monolayer graphene. We also observe weak localization and extract information about phase coherence and scattering of carriers by disorder in the graphene. We have measured the thermal conductivity of suspended CVD graphene to be ~3000 W/m-K, comparable with that of exfoliated graphene, by combining electronic transport and Raman thermometry⁵. Finally, I will present some results on graphene layers grown by CVD directly on insulating substrates. Work in collaboration with Q. Yu, H. Cao, L. Jauregui, R. Colby, E. Stach, N. Guisinger and H. Li.

1. Q. Yu *et al.*, *Appl. Phys. Lett.* **93**, 113103 (2008)
2. H. Cao *et al.*, *J. Appl. Phys.* **107**, 044310 (2010)
3. H. Cao *et al.*, *Appl. Phys. Lett.* **96**, 122106 (2010)
4. R. Colby *et al.*, *Diamond Relat. Mater.* **19**, 143 (2010)
5. L. A. Jauregui *et al.*, *ECS Trans.* **28** (5), 73 (2010)

10:40am GR+TF-TuM9 Scanning Tunneling Spectroscopy of a Gated Single-Layer Graphene Device in the Quantum Hall Regime, S. Jung, G.M. Rutter, N.N. Klimov, D.B. Newell, N.B. Zhitenev, J.A. Stroscio, NIST

We have performed scanning tunneling spectroscopy (STS) measurements to investigate Dirac particle interactions and localization by local impurities in a gated single-layer exfoliated graphene device in the quantum Hall

regime at a temperature of 4.3 K. At the Dirac point, electron-hole puddles created by the disorder potential in SiO₂ substrate are observed at zero magnetic field. In an applied magnetic field, the carriers are condensed into well-resolved Landau levels (LLs), whose general evolution as a function of both charge density and magnetic field is well described by the context of 'massless' Dirac particles. Tunneling spectroscopy measurements as a function of magnetic field and applied gate potential are shown to give insight into the localization of carriers and their relation to the disorder potential. At low magnetic fields, tunneling spectra display long-range scattering features related to the graphene disorder potential variation. The disorder potential also determines the spatial distribution of LLs in higher magnetic fields. We observe that isolated compressible LL regions surrounded by incompressible strips behave like graphene quantum dots (QDs). Single-electron charging of the QDs is seen as four-fold Coulomb oscillations in individual dI/dV curves. These results show that the plane of the graphene 2DEG breaks into a checkerboard pattern of electron- or hole-rich QDs localized at either maxima or minima of the disorder potential.

11:00am **GR+TF-TuM10 Scanning Tunneling Spectroscopy of Gated Bilayer Graphene Device in the Quantum Hall Regime**, *N.N. Klimov*, CNST/EEEL/NIST and Maryland NanoCenter UMD, *G.M. Rutter*, CNST/NIST, *S. Jung*, CNST/NIST and Maryland NanoCenter UMD, *D.B. Newell*, EEEL/NIST, *N.B. Zhitenev*, *J.A. Stroscio*, CNST/NIST

It has been shown recently, both theoretically [1] and experimentally [2-3], that a bandgap can be opened and even tuned continuously in bilayer graphene (BLG) in the presence of a strong electrical field, which induces asymmetry of the electrostatic potential of the two graphene layers. This makes BLG an attractive material for future digital electronic applications, infrared nanophotonics, pseudospintronics, and terahertz technology. On the other hand a complete understanding of the physics of BLG and the effect of disorder on a microscopic scale is missing. In this work, we present local tunneling measurements of bilayer graphene exfoliated on SiO₂/Si using scanning tunneling spectroscopy at a temperature of 4.3 K. The graphene bilayer is probed with both the application of a perpendicular magnetic field and with an external gate voltage applied to the Si substrate. We study the effect of disorder potential induced by SiO₂/Si on the electronic properties of bilayer graphene. We find that disorder potential causes a bandgap opening in BLG, while a backgate voltage has a secondary effect on the density of states. We also find that the magnetic quantization of the carriers, evidenced by the formation of Landau levels (LL), does not obey the simple scaling of LL energy versus magnetic field for an ideal graphene bilayer.[4] The LL spectra are seen to vary greatly depending on the local potential variation and associated charge density. We have investigated these variations with detailed spectroscopic maps of the LL spectra as a function of energy, gate voltage, and local potential variation. We find the assignment of the spectral features to be much more complex than expected, and may require the introduction of an intrinsic electrical bias in the bilayer system. In this talk, we will discuss the possible theoretical models that may account for our observations.

[1] E. McCann, V. I. Fal'ko, *Phys. Rev. Lett.* **96**, 086805 (2006).

[2] J. B. Oostinga, *et. al.*, *Nature Mater.* **7**, 1510157 (2008).

[3] E. V. Castro *Phys. Rev. Lett.* **99**, 216802 (2007).

[4] E. A. Henriksen *et al.*, *Phys. Rev. Lett.* **100**, 087403 (2008).

11:20am **GR+TF-TuM11 Monolayer Graphene on 150mm Substrate**, *H.J. Chung*, *J. Heo*, *H. Yang*, *S.-H. Lee*, *S. Seo*, Samsung Advanced Institute of Technology, Korea

Monolayer graphene over a 150 mm substrate was fabricated using Cu-Ni multilayer growth substrates with Inductively Coupled Plasma-Enhanced Chemical Vapor Deposition (ICPCVD) over 700°C. It was confirmed with Raman spectroscopic mapping after metal etching and transfer process. Over 2000 FETs were fabricated on a 150 mm wafer and on-off ratio and Dirac shift were measured for each device and compared to ones from the graphene grown on Ni substrate. In addition, the result from SPM investigation will be presented.

11:40am **GR+TF-TuM12 Probing the Electronic Structure, Surface Chemistry, and Alignment of Graphene using Soft X-ray Absorption Spectroscopy**, *C. Jaye*, NIST, *V. Lee*, SUNY at Buffalo, *P. Lysaght*, SEMATECH, *S. Banerjee*, SUNY at Buffalo, *D.A. Fischer*, NIST

Graphene, a single layer of graphite packed in a honeycomb lattice, has been the subject of intense scientific research since its discovery in 2004 owing to its remarkable properties such as the half-integer quantum Hall effect, ballistic conduction, and the extremely high mobilities of its charge carriers. Graphene has numerous potential applications in the electronics industry including within ultra-high frequency transistors, electrical interconnects and as a replacement for indium-tin-oxide. Nevertheless, the fabrication of large-area graphene remains a challenge. We present

systematic studies of the electronic structure, defect density, and alignment of relatively large-area graphene thin films prepared by a) solution/sonochemical methods and b) chemical vapor deposition (CVD). The solution-chemistry-based approaches have the advantage of ease of scalability, making it an attractive approach for industry. We have been able to achieve the fabrication and transfer of large-area graphene films on both conductive and non-conductive substrates. The fabricated films have been characterized by Raman spectroscopy, near-edge X-ray absorption spectroscopy, and four-point-probe conductivity measurements. This battery of measurements allows evaluation of the role of different reducing agents in reducing graphene oxide to graphene. We have also performed systematic measurements of single- and few-layered graphene grown by CVD onto Cu and Ni substrates. X-ray absorption spectroscopy in particular provides strong evidence for substrate hybridization and rippling of graphene. The rippling of graphene induced during transfer to insulating substrates represents a formidable challenge that will need to be solved since corrugations and electronic asperities in graphene induce local scattering potentials. Finally, we will present some X-ray absorption spectroscopy imaging data showing local electronic asperities in graphene.

Thin Film

Room: Pecos - Session TF1-TuM

ALD: Dielectrics for Semiconductors

Moderator: H. Kim, Yonsei University, Korea

8:00am **TF1-TuM1 Feasibility of Wrinkle Free Graphene Process**,

B.H. Lee, *C.H. Cho*, *S.K. Lim*, *S.Y. Lee*, *H.J. Hwang*, *Y.-G. Lee*, *U.J. Jung*, *C.G. Kang*, Gwangju Institute of Science and Technology, Korea **INVITED**

Graphene is an attractive material for advanced device applications due to its excellent electrical conductivity. Up to now, the best quality graphene in terms of electrical properties are obtained only from the graphene mechanically exfoliated from a natural graphite. Other processes such as a thermal graphitization of SiC and a precipitated graphene from metal films super saturated with carbon atoms did generate a good quality graphene in terms of Raman analysis. However, the morphology of graphene shows a high density of physical defects such as micro size wrinkles, island growth etc. For practical application of nanoscale device fabrication, global size wrinkles should be eliminated like a flat silicon substrate. Major sources of global defects in graphene are 1) a mismatch of thermal expansion coefficient between the graphene and the growth templates (metal, SiC etc), 2) a preferential out-diffusion or adoption of carbon along the grain boundary of metal. In this talk, a novel process that can detour these problems and generate a wrinkle free graphene will be discussed.

8:40am **TF1-TuM3 The Effects of Interfacial Organic Layers on the Growth of Thin Al₂O₃, HfO₂ and TaN_x Films by Atomic Layer Deposition**, *K.J. Hughes*, *S. Issacson*, *J.R. Engstrom*, Cornell University

One of the most poorly understood aspects of atomic layer deposition involves the initial stages of growth. As growth via ALD is almost always conducted on a substrate of different composition that the film being grown on top of it, there are often issues related to what are the best ways to initiate growth. Over the past few years we have been examining the use of interfacial organic layers (IOLs) as way to tailor the nucleation and growth of ALD thin films. Here, unlike essentially all work we have reported previously, we have conducted ALD using a conventional hot wall, viscous flow-type reactor, operating at pressures of ~ 1-100 mTorr. We focus here on the growth of two oxides: the benchmark Al₂O₃ and high-k HfO₂, and one nitride, TaN_x. As to the IOLs we consider one vapor phase deposited self-assembled monolayer, perfluorooctyltrichlorosilane (FOTS), which is expected to provide no active sites for ALD growth. We also consider a solution phase deposited polymer, poly(ethylene imine) (PEI), which possesses a high density of -NH₂ groups expected to act as active sites for growth. Concerning the latter IOL, from synchrotron x-ray reflectivity we confirm that PEI forms a thin (~ 7 Å) smooth film on the substrates we have examined. For ALD growth of Al₂O₃ on both bare SiO₂, and SiO₂ treated with PEI we observe linear growth, and no detectable incubation period. Growth on FOTS/SiO₂ on the other hand clearly exhibits an incubation period of ~ 15 cycles. Thus, for Al₂O₃, growth on unmodified SiO₂ and SiO₂ modified with PEI are indistinguishable. In contrast, growth of both HfO₂ and TaN_x is definitely perturbed by the presence of the PEI interfacial organic layer: compared to growth on unmodified SiO₂, growth on PEI |SiO₂ exhibits an incubation period of ~ 10 cycles for HfO₂, and > 40 cycles for TaN_x. A common question is what is the fate of the IOL? Concerning the growth of Al₂O₃, from *ex situ* angle-resolved x-ray photoelectron spectroscopy (ARXPS) we find that the elemental species associated with

the IOL (F for FOTS, and N for PEI) are located at the IOL/Al₂O₃ interface, indicating the IOL has not migrated to the top surface during growth.

9:00am **TF1-TuM4 Property of Interfacial Layer Induced V_{FB} Shift in Al-related Gate Oxide Deposited by Remote Plasma Atomic Layer Deposition.** *H.T. Jeon, H. Kim, S. Woo, J. Lee, H. Lee,* Hanyang University, Republic of Korea

With the continuous dimensional scaling down of Si based devices has called for using high-k dielectrics to replace SiO₂ or nitrided SiO₂ as the gate oxide in CMOS devices. However, the uncontrollability of flatband voltage (V_{FB}) is still a crucial issue for CMOS devices with high-k gate dielectrics. This undesirably flatband voltage shift is highly related to the interfacial defects, such as interface defect density, fixed charge density and oxygen vacancy. Therefore, it is significant to understanding the physical and chemical properties of the interface regions.

To grow thin films with excellent properties, plasma-enhanced atomic layer deposition (ALD) has been widely used as a thin film deposition method. PEALD commonly produces better quality of films at lower growth temperatures than dose thermal ALD because the required activation energy is provided by a plasma source. Some processes require the presence of radicals to enhance chemical reactions without having to use ion bombardment, as it can cause plasma-induced damage. Remote plasma ALD (RPALD), wherein the plasma is created in a remote chamber using RF power, was developed to meet these processing demands. The radicals generated in the plasma enter into the process chamber for deposition.

In order to understand the interfacial influence on the V_{FB} shift in high-k based MOS structure, it is need to investigate the dependence of the V_{FB} shift on the properties of interfacial layer. In this paper, to modify the Si surface, N₂ plasma was treated on Si surface at RF powers of 100 W, 200 W and 300 W. The Al₂O₃ was deposited by remote plasma ALD at 250°C. The Pt/Al₂O₃/Si MOS structure was fabricated to investigate the impact of interfacial layer between Al₂O₃ and Si substrate on change in V_{FB}. In addition, plasma was monitored by optical emission spectroscopy (OES). The physical and chemical properties of high-k dielectric films and interfacial layer were examined by XPS and AES.

We found that the nitrogen content at Si substrate increased during N₂ plasma pre-treatment at high RF power which results in a negative shift of V_{FB}. Therefore, the properties of the interfacial layer which are critical in determining the V_{FB} are affected by N₂ plasma pre-treatment.

9:20am **TF1-TuM5 Atomic Layer Deposited Pb(Zr,Ti)O_x Films Composed as Ferroelectric and Multiferroic Materials.** *F. Zhang, T.E. Quickel, Y.-C. Perng, S. Tolbert, J.P. Chang,* University of California, Los Angeles

Atomic layer deposition (ALD) of complex oxides is a viable method to tailor the composition and microstructure of the resulting thin films, thereby generating multi-functionality that is needed in various device applications. Another desirable feature of ALD is its ability to uniformly and conformally coat complex surface structures of high aspect ratios, making it possible to interface distinct materials to form composite materials that may show exciting properties, such as multiferroic behavior.

In this work, lead zirconium titanate (PZT) films were synthesized by depositing PbO, ZrO₂ and TiO₂ ALD layers with a sequence of (Pb-O)-(Ti-O)-(Pb-O)-(Zr-O). The deposition rate for PZT was approximately 0.7nm/cycle-sequence. The as-deposited materials were amorphous but crystallized into perovskite structure upon annealing to 950°C. The polarization properties found in the P-V measurements including remanent polarization (P_r), saturation polarization (P_s), and coercive field (E_c) are promising and are strongly affected by the ALD sequence which dictates the composition and structuring of the resulting thin film.

One example of the advantages of ALD produced PZT can be seen in our work on composite multiferroic materials, which can be created by coupling together nanoscale ferroelectric and ferromagnetic materials. In this work, mesoporous cobalt ferrite (CFO) thin films formed by block-copolymer templating methods with pores 14 nm in diameter were used as the ferromagnetic framework. Ultra-thin ALD PZT films were used to create a uniform and conformal coating over and on all CFO pore spaces and generate a nano-structured PZT-CFO hybrid material, as confirmed by scanning electron microscope (SEM), transmission electron microscope (TEM), and ultraviolet photoelectron spectroscopy (UPS) measurements. Superconducting quantum interference device (SQUID) magnetometry is underway to assess the multiferroic properties of this PZT/CFO composite, including both in-plane and out-of-plane saturation magnetization measurements after electrical poling and polarization voltage (P-V) measurements.

9:40am **TF1-TuM6 Y₂O₃ Atomic Layer Deposition from a Novel Process and its Integration in a Gate First Approach for 0.8 nm Equivalent Oxide Thickness.** *C. Dubourdieu,* CNRS and IBM Research, *M.M. Frank, E. Cartier, J. Bruley, S.M. Rossnagel,* IBM T.J. Watson Research Center, *A. Kellock,* IBM Almaden Research Center, *V. Narayanan,* IBM T.J. Watson Research Center

A large part of the high-k dielectric stacks investigated for the replacement of the SiO₂ or Si₃O₄N gate oxide in metal-oxide-semiconductor (MOS) field-effect transistors consists of a Hf-based oxide or silicate deposited on top of an ultrathin interfacial SiO₂ layer. We report here the formation of yttrium lanthanum silicate in direct contact with silicon for the fabrication of MOS capacitors with a resulting highly competitive equivalent oxide thickness (EOT) of 0.8nm. Such a low EOT is remarkable as it is obtained with a non Hf-based dielectric and following a high-temperature gate first route. This result is achieved by integrating Y₂O₃ films grown on buffer layers by a novel atomic layer deposition process that combines an original yttrium precursor and an innovative liquid injection source.

The growth of Y₂O₃ thin films by ALD from Y(EtCp)₃ and water precursors will be presented. The yttrium precursor was introduced using a novel delivery scheme consisting of a pulsed injection system from Kemstream®. The control of the growth as a function of various process parameters (precursor supply time, water purging time, temperature) was investigated. Film stoichiometry was determined by Rutherford backscattering spectrometry. The reactivity of Y(EtCp)₃ with water and the frontiers between ALD and CVD regimes will be discussed.

We describe MOS capacitors prepared from ALD-Y₂O₃ thin films deposited onto Si(p-type)/SiO₂(0.8 nm)/La₂O₃ (1 nm) structures. The Y₂O₃ thickness ranges from 1.5 to 3.5 nm. The metal gate electrode consists of 10 nm TiN and implanted polysilicon on top. The complete stack undergoes a high-temperature RTA at 1000°C for 5 s under N₂ for dopant activation in the poly-Si, which simulates gate first process of CMOS transistor fabrication. Finally, a forming gas anneal is performed at 475°C. The stack microstructure and composition were studied by transmission electron microscopy, electron loss spectroscopy and energy dispersive x-ray spectrometry. Interdiffusion reactions occur between SiO₂, La₂O₃ and Y₂O₃ layers upon the RTA and result in an yttrium lanthanum silicate film in direct contact with Si. The elemental distribution within the silicate layer will be discussed. C-V and I-V were performed on 10x10 μm² size capacitors in a frequency range of 1 kHz up to 300 kHz. EOTs as low as 0.8 nm were obtained for stacks with initially 3 nm Y₂O₃ deposited films. The leakage current density for such stacks is of 2.1x10⁻³ A/cm² at -1V. The formation of silicate enables an appropriate V_{FB}, which is tunable for nFET and pFET. Results obtained for stacks prepared from different buffer layers such as Al₂O₃ and HfO₂ will also be discussed.

10:40am **TF1-TuM9 Direct Liquid Injection Chemical Vapor Deposition of Nickel Ferrite and Barium Titanate Thin Films.** *N. Li, A. Wang, A. Gupta, T.M. Klein,* University of Alabama

Multiferroic heterostructures, such as the ferromagnetic-ferroelectric bilayered structures, have attracted a lot of attention due to their potential application in multifunctional devices. The simultaneous tunability of magnetic and electric fields in such structures is very useful for microwave and millimeter wave planar devices such as tunable phase shifters, resonators and delay lines. Growth of high quality and thick (10μm-100μm) ferromagnetic and ferroelectric thin films is an essential step to obtain satisfactory final devices. In this work, the growth of single crystal nickel ferrite (NFO, ferromagnetic) and barium titanate (BTO, ferroelectric) thin films with high growth rate by direct liquid injection chemical vapor deposition is investigated. The liquid precursor source for injection was prepared by dissolving corresponding metalorganic precursors into a solvent. In our case, Ni(acac)₃•PMDTA adduct (acac=acetylacetonate, PMDTA= N,N,N',N',N"-pentamethyldiethylenetriamine) and Fe(acac)₃ were dissolved in toluene as NFO precursor solution; Ba(hfa)₂•tetraglyme adduct (hfa=hexafluoroacetylacetonate) and Ti(tmhd)₂(ipo)₂ (tmhd= 2,2,6,6-tetramethyl-3,5-heptanedionato, ipo=isopropoxide) were dissolved in toluene as the BTO precursor solution. The as-prepared metal organic precursor solution was fed into a commercial vaporizer system through a liquid mass flow controller (10g/h range). Epitaxial growth of NFO and BTO thin films on MgO(100) were observed using X-ray diffraction. X-ray photoelectron spectroscopy showed the existence of trace amount of fluorine on the BTO surface. Scanning electron microscopy and atomic force microscopy showed the grain sizes to be around 100nm and the surface roughness around 20nm. The growth rates of both the NFO and BTO thin films are in the range of 0.5~1 μm/h under our experimental conditions.

11:00am **TF1-TuM10 Structure-Property Relationship in high-k, ALD Al-doped TiO₂ Films using Raman Spectroscopy**, *L.C. Haspert, P. Banerjee, L. Henn-Lecordier, G.W. Rubloff*, University of Maryland

Thin film TiO₂ is a relatively high permittivity material with applications in electronic and energy devices. However, TiO₂ crystallizes easily, forming grain boundaries and creating current percolation pathways which increase leakage current and power consumption. Al-doped TiO₂ (ATO) increases the thermal stability of TiO₂, reducing leakage currents by suppressing phase transformation and limiting grain growth. To achieve the benefits of Al doping which retaining those of TiO₂, structure-property relationships must be optimized as a function of processing parameters.

Raman spectroscopy (RS), a highly sensitive technique for observing the evolution of nano-crystalline phases - their time evolution, volume fraction, defect states and stresses, is employed here to characterize ATO films grown by atomic layer deposition (ALD) and their correlation with electrical performance. 25nm TiO₂ thin films were deposited at 150°C in a Beneq TFS500 cross-flow ALD reactor by sequentially pulsing TDMAT and water precursors. Aluminum doping was controlled from 0 to 15 at% by introducing a single TMA / water pulse sequence at pre-determined intervals of multiple TDMAT/water pulse sequences during oxide growth, producing reproducible compositions estimated from their TiO₂ to Al₂O₃ pulse ratios. Following ALD the films were rapid thermal annealed (RTA) in an oxygen-rich environment ranging from 600°C to 1000°C from 5 to 300 sec.

The degree of crystallization was determined primarily through lineshape analysis of the Raman-active 144 cm⁻¹ frequency mode. RS (and XRD) detected only the TiO₂ anatase phase, even at annealing temperatures where rutile formation was expected. RS data clearly shows the crystallization of TiO₂ with thermal anneal and that the crystallization onset shifts to higher temperatures with Al-doping while producing smaller grains. Pure TiO₂ films show a dielectric constant of 28.5 with high leakage currents (up to 10⁻³ A/cm²). Annealed ATO films have a slightly lower dielectric constant (24) but leakage currents are dramatically reduced to ~ 1.0x10⁻⁷ A/cm². The clear correlation between the microstructure measured by RS and the electrical performance of ALD TiO₂ and ATO thin films shows that RS can be a rapid, valuable monitor of thin film material nanostructure for correlation and optimization with electrical properties.

This work was supported by Laboratory for Physical Science, UMD

11:20am **TF1-TuM11 In-situ XPS and Half-Cycle Studies of Atomic Layer Deposited Al₂O₃ on Group-III Nitride Substrate for MOS-HEMT Applications**, *P. Sivasubramani, T.J. Park, B.E. Coss, S. McDonnell, R.M. Wallace, J. Kim*, University of Texas at Dallas, *Y. Cao, D. Jena, H. Xing*, University of Notre Dame

Group-III nitride (III-N) technology has been widely used in optoelectronics, RF transistors and power switching due to a suitable bandgap, excellent transport properties, high breakdown field, low power losses, as well as the possibility of forming a heterojunction structure on low cost, large area substrate templates such as Si, sapphire, etc. [1] X-N alloy on Ga-N (where X = Ga, In, or Al) are expected to achieve high-speed switching performance due to a high carrier mobility of 2-D electron gas formed at the heterojunction interface. The introduction of a high-quality, ultrathin, atomic layer deposited (ALD) dielectric in between the metal and semiconductor has been shown to effectively decrease the diode leakage current without compromising the MOS-HEMT transfer characteristics. [2, 3] The evaluation of interfacial and bulk bonding configurations as a function of ALD dielectric growth parameters could provide valuable information for III-N device application. Therefore, in this work, we have investigated the growth, interfacial, and bulk properties of ALD Al₂O₃ dielectric on top of Ga-N on top of a low-cost sapphire template. Immediately after surface preparation, the samples were loaded in an ultra high vacuum (UHV) custom tool which has an integrated x-ray photoelectron spectroscopy (XPS), ALD, and a UHV transfer tube for in-situ analysis of ALD half-cycle reactions with the III-N substrate. The surfaces were pre-cleaned using atomic H cleaning and/or solvent-wet chemical cleaning. XPS of III-N substrates indicates that a small, higher oxidation state component, possibly a hydroxide or an oxynitride (e.g. Ga-O-N) exists on the as-grown surface. The hydroxide and residual carbon components on the clean substrate and during the half-cycle reactions are simultaneously monitored. Significant charging of the semiconductor during XPS is circumvented by using a doped substrate along with suitable charge references. ALD half-cycle studies of the TMA (tri-methyl aluminum)/water and TMA/O₃ reactions on the III-N surface will be presented. References: [1] Phys. Status Solidi C 6, No. 6, 1361 (2009) [2] Appl. Phys. Lett. 86, 063501 (2005) [3] IEDM09-15

11:40am **TF1-TuM12 Defect Mechanisms for Chlorosilane Based Self-Assembled Monolayers**, *S. Miller, A.J. Muscat*, University of Arizona

Self-aligning manufacturing processes could allow smaller device structures to be made as well as significantly reduce the number of manufacturing steps required. By utilizing selective chemistry it is possible to control where growth occurs for many different materials. Self assembled monolayers (SAMs), such as octadecyltrichlorosilane (OTS), have been used to inhibit the atomic layer deposition (ALD) of materials spanning from high-k dielectrics to metals such as Ir or Pt. By tailoring the selective chemistry, it is possible to chemically activate and deactivate the surface for multiple materials. SAMs such as 3-mercaptopropyltriethoxysilane have been used to attach a variety of nanoparticles where desired, and when combined with other SAMs such as OTS can prevent adsorption or deposition where undesired. Simple patterning techniques such as photolithography, AFM lithography, or electron lithography can be combined with selective chemistries to allow high resolution spatial control over the growth and deposition of materials. One limitation of this technology is the long time scales required to fully deactivate deposition using SAMs, which are on the order of 48 hours. Molecular defects such as water in the SAM, unblocked hydroxyl groups, exposed Si-O bonds, misaligned boundaries between forming SAM islands, or polymerized SAM molecules in the SAM layers also leads to an eventual failure point for deposition deactivation. We found that they can be largely eliminated by forming the SAM on a uniformly hydroxylated surface, using a chloroform rinse step, and removing any polymerized or physisorbed SAM molecules from the surface during SAM formation. Using TiCl₄ as a probe for defect sites, the level of each defect type has been determined. The number of defects sites on the surface on a typical OTS SAM is on the order of 10¹² molecules/cm². 1/3rd of the defects are associated with the physisorbed SAM molecules. Of the other 2/3^{ds} of SAM defects nearly half are unblocked hydroxyl groups while the other half are likely open Si-O bonds at grain boundaries. Water has been shown not to be a contributing cause for nucleation of deactivation failure. TiO₂ deposition from a TiCl₄ and H₂O ALD process at 170°C has been deactivated for at least 100 cycles after treating for only 4 hours in 10mM OTS in toluene solution, as long as the sample is removed every hour and rinsed. The extraction step removes unwanted SAM molecules and exposes open surface areas allowing for new SAM molecules to quickly fill the gaps. These improvements in both the quality and the time scale of SAM formation could it feasible to begin incorporating these technologies into manufacturing.

Thin Film

Room: Ruidoso - Session TF2-TuM

Nonvolatile Memory

Moderator: C. Vallee, Université Joseph Fourier, France

8:00am **TF2-TuM1 MRAM: A Practical Application of Spintronics**, *D.W. Abraham*, IBM **INVITED**

Magnetic random access memory (MRAM) is a new class of solid state memory which is based on the spin of the electron (as opposed to its charge). This technology is a relative newcomer to the constellation of non-volatile memories, and offers a unique combination of non-volatility, density and speed. I will review the scientific discoveries that enabled the first MRAM chips, and then will discuss several distinct generations of the technology which have evolved in the last decade, including both field-switched and spin-torque-switched devices. Finally I will describe promising new structures which are currently under development which exploit the separation of spin and charge to allow more reliable and lower power operation.

8:40am **TF2-TuM3 Bipolar Resistive Switching Characteristics of HfO_x with Anode-Interface HfAlO_x Layer**, *H.-C. Sohn, J.G. Kim, H.D. Na, K.-M. Lee, S.-H. Lee*, Yonsei University, Republic of Korea

In this work, we investigated the effect of anode-interface HfAlO_x layer on the resistance switching characteristics of ALD HfO_x films. HfAlO_x on TiN bottom electrode with the thickness and the cycle ratio of HfO₂ and Al₂O₃ was deposited and then HfO₂ thin film was grown by atomic layer deposition (ALD) process. The resistance switching behavior of the Pt/HfO₂/HfAlO_x/TiN MIM stack was characterized in conjunction with physical property such as chemical bonding of HfO_x and HfAlO_x. HfAlO_x layer with increasing the ratio of Al₂O₃ improved the endurance, the variance of V_{SET} and V_{RESET}, and the variance of R_{LRS} and R_{HRS}. Also, the resistances of LRS during first RESET processing were decreased with increasing the ratio of Al₂O₃ in HfAlO_x films. X-ray photoemission spectroscopy showed that the cycle ratio of Al₂O₃ in HfAlO_x layer caused an increase of metallic Hf (Hf⁰) concentration. It was considered that an

increase of metallic Hf (Hf^0) concentration is closely related to the migration of oxygen ions or vacancies at interface between transition metal oxide and TiN electrode, resulting in the enhanced endurance, the current level of LRS and HRS, and the narrowed distribution of V_{SET} & V_{RESET} and R_{LRS} & R_{HRS} .

9:00am **TF2-TuM4 Plasma Treatments of HfO₂ Resistive RAM**, C. Vallée, P. Gonon, Ujf - Ltm, France, C. Mannequin, T. Chevolleau, Ltm - Umr 5129 Cnrs, France, H. Grampeix, N. Rochat, C. Licitra, V. Jousseau, CEA-LETI-MINATEC, France

Resistive-switching Random Access Memories (RRAM) have attracted considerable attention in recent years for future non-volatile memory applications. This resistance switching can be based on a modification of the crystalline structure of a material (PCRAM, Phase Changed RAM). One can also exploits the resistive switching properties of some oxides (OxRRAM, Oxide Resistive RAM) which display a change in resistance upon application of a bias voltage. In this case, oxides materials are deposited in a metal-insulator-metal (MIM) structure. In the last years several different oxides have been studied such as metal oxides (NiO, TiO₂, ZrO₂, Cu_xO...) and perovskites (BaTiO₃, SrTiO₃...) [1]. Hafnium oxide (HfO₂) is among the oxides particularly desirable as far as integration and process compatibility are concerned since it has the advantage of being more mature from a technological point of view.

In this work, HfO₂ RRAM with different thicknesses of HfO₂ films (10 and 20 nm typically) are tested with and without plasma treatment. HfO₂ films are grown at 350°C by atomic layer deposition (ALD) using alternate cycles of H₂O and HfCl₄ precursors (1 Torr) on Pt and TiN electrode materials. It is known that oxygen vacancies are playing a critical role for resistive switching. Different solutions have been proposed to modify the oxygen vacancies concentration in the device: integration of a TiO_x/TiO₂ bilayer films [2], doping a ZrO₂ RRAM by metallic ions [3]. Here hydrogen-based plasma treatments are studied. Hence, several different hydrogen-based (NH₃) plasma annealing treatments of the HfO₂ dielectric are carried out in order to study the influence of the oxygen vacancies or defects on the subsequent switching behaviour before the deposition of the top electrode. The MIM structures are then electrically and physically characterized. I(V) curves are then recorded and switching parameters such the SET voltage are compared for MIM devices with and without plasma treatment. It is for example observed that a 1 min NH₃ plasma treatment of HfO₂ deposited on TiN improved the overall switching properties of the RRAM. The modifications of switching properties are correlated to chemical analysis results, mainly Angle-resolved X-ray Photoelectron Spectroscopy, Attenuated Total Reflexion (ATR) and Spectroscopic Ellipsometry (SE) up to 8 eV, with special attention devoted to metal/oxide interface investigations.

[1] A. Sawa, *Materials Today* **11** (6) (2008) 28

[2] J.J. Yang, et al, *Nature Nanotech.* **3** (2008) 429

[3] H. Zhang *et al*, *Appl. Phys. Lett.* **96** (2010) 123502

9:20am **TF2-TuM5 Growth of GeTe Films by MOCVD and PE-MOCVD for Phase Change Memory**, E. Gourvest, STMicroelectronics, France, C. Vallée, UJF - LTM, France, P. Michallon, CEA-LETI-MINATEC, France, J. Vitiello, Altatech Semiconductor, France, R. Blanc, CNRS-LTM, France, D. Jourde, CEA-LETI-MINATEC, France, S. Lhostis, STMicroelectronics, France, S. Maitrejean, CEA-LETI-MINATEC, France
Phase-Change Memory (PCM) is one of the promising candidates for next-generation nonvolatile memory thanks to their low cost, low programming voltage and their excellent scalability to the nanoscale cell size [1]. This technology is based on fast and reversible phase change effect in the chalcogenide materials but suffers of the inherent lack of amorphous state stability which affects archival life of the memory cell. This problem is critical for embedded applications where a high retention time at high working temperature is required. In this case, binary compound GeTe material has been shown to be a good candidate since a phase transition temperature higher than the usual Ge₂Sb₂Te₅ material has been found and 10 years-fail time at 105°C has been estimated [2]. Moreover the reduction of the current pulse needed to change material from crystal phase to amorphous phase implies the confinement of phase change materials at dimensions below 100 nm [3]. In this case the growth of GeTe materials by chemical vapour deposition (CVD) or Plasma Enhanced CVD is required in order to fill confined structures.

For this purpose, this work investigates the deposition of GeTe materials by a pulsed liquid injection Metal Organic CVD system allowing storing the precursor at ambient temperature. The deposition is made in a 200 nm MOCVD tool that can be assisted by a Low Frequency as well as Radio Frequency plasma. The liquid precursors are injected into a heated evaporator where flash evaporation occurs. A sequential injection leads to a precise control of the deposited material stoichiometry. Furthermore deposition in amorphous or crystalline state is performed by setting the

substrate temperature. This chamber is connected to a cluster tool which allows quasi in situ analysis of the deposited films crystalline state by Spectroscopic Ellipsometry (SE) and of the growth mechanisms by angle-resolved X-ray Photoelectron Spectroscopy (ARXPS). Impact of process parameters on the films properties are then evaluated in the MOCVD and PECVD mode. In the case of plasma assistance the impact of the Low to Radio Frequency ratio on the thin film deposition is also studied. Direct informations on Ge/Te ratio and carbon contamination are given by the plasma analysis thanks to optical emission spectrometry. In addition to the chemical and physical properties investigations, the phase change performances and the electrical properties of the deposited materials are evaluated.

[1] S. J. Hudgens, *J. Non-Crys. Solids*, **354**, 2748 (2008)

[2] L. Perniola *et al.*, *IEEE Electron Device Lett.*, **31**, 5 (2010), pp. 488-490.

[3] S. L. Cho *et al.*, *Symp. VLSI Tech. Dig.* (2005), p. 96

9:40am **TF2-TuM6 Effects of Halogenated Plasma Chemistries on Degradation of Magnetic Material Properties**, R.M. Martin, D.W. Abraham, E.A. Joseph, Y. Zhang, IBM T.J. Watson Research Center

Patterning of magnetic materials with plasma processes is an integral step in the fabrication of magnetic devices such as magnetic tunnel junctions (MTJs) for magnetoresistive random access memory (MRAM). Obtaining optimal device performance requires preservation of the magnetic material properties throughout the fabrication process, and thus places limitations on the process window (e.g. temperature, gas chemistry) for patterning devices. Due to this, the use of halogenated plasma chemistries, which are commonly used in reactive ion etching (RIE) processing, must be carefully employed when patterning MTJ devices, as they can significantly degrade magnetic properties during the etch. One method used to minimize magnetic degradation is the incorporation of metallic capping layers which potentially isolate the halogen etch chemistry from the critical magnetic layers. However, the optimal thickness and/or properties of these layers have yet to be fully explored. For example, when a Cl₂ based plasma is exposed to a 300 Å Ru capping layer, the magnetic moment/area of the underlying magnetic free layer is reduced 11% from 1.64 to 1.46×10⁻⁴ emu/cm². Therefore in this work, the effects of the plasma etch chemistry on magnetic materials is explored using various halogenated chemistries and capping layer materials to understand the mechanisms by which patterning of magnetic devices can be achieved without degradation of magnetic properties.

10:40am **TF2-TuM9 Phase Change Materials for Random Access Memories: Deposition, Characterization and Performance**, C. Wiemer, CNR-IMM, Italy **INVITED**

The optimization of phase change memory devices requires a compromise between reducing element sizes and maintaining data retention and reliability. The down-scaling of the memory cell size can be achieved only by a greater control of film deposition over non-planar structures than so far reached by physical vapor deposition techniques. A reduced cell size would allow lower programming currents, which lead to improved performances and lower costs. Metal organic chemical vapor deposition (MOCVD) is a very attractive method for growing layers because it enables the production of thin films with better conformality and composition control, including doping possibilities, and increased manufacturing throughput compared to sputtering techniques. Therefore, MOCVD is potentially attractive for the deposition of chalcogenide materials for phase change memory devices.

In this presentation recent advances in MOCVD of chalcogenide materials will be presented. Results will cover both the use of hot wire, liquid injection MOCVD and thermal, N₂ based, MOCVD. The MOCVD growth is optimized both on flat SiO₂/Si and patterned substrates. The deposition of Ge₂Sb₂Te₅ layers is achieved by thermal MOCVD thanks to the use of a thin seed layer of germanium. The obtained Ge-Sb-Te alloys exhibit up to 10 phase switching cycles upon laser irradiation. Better performances are achieved so far by hot wire MOCVD where the optical switching behavior is demonstrated to be comparable to the one of sputtered deposited Ge₂Sb₂Te₅ films of the same thickness. Moreover, prototype memory cells including Ge₂Sb₂Te₅ from hot wire MOCVD show promising performances.

Advances in material characterization will be also discussed. Since the switching of a memory device is driven by Joule heating, the exploration of new chalcogenide materials in terms of electrical performances cannot proceed without the knowledge of the thermal dependence of their fundamental properties, like thermal conductivity, electrical resistivity and crystallographic phase stability. The effect of reducing the cell size on the role played by the properties of the interfaces between the chalcogenide material and the other elements of the memory cell will be discussed. In particular, since most of the work performed in material characterization

proceeds on flat, polycrystalline layers, special attention is devoted to the effects of size, preferential orientation and thin interfacial layers on the quantification of thermal and electrical properties as a function of temperature.

11:20am **TF2-TuM11 Bipolar Switching Behaviors in TiN/HfO₂/Pt Systems for Nonvolatile Resistive Memory Applications**, *D.-H. Ko, D.S. Lee, Y.H. Sung*, Yonsei University, Republic of Korea

Resistive random access memory devices based on transition metal-oxides (TMO) have been considered as the most promising candidates for the next generation nonvolatile memories because of its simple structures and compositions, low voltage operation and process compatibility with CMOS.

In this presentation, stable bipolar resistive switching behaviors of TiN/HfO₂/Pt structures will be discussed for the first time. The HfO₂ films were grown by reactive sputter at room temperature using O₂ and Ar gas, and the subsequent heat treatment was performed in an ambient of O₂ at 300°C. TiN and Pt layers were used as the top and bottom electrode materials, respectively. For the characterization of stable bipolar resistive switching, current-voltage measurements were used in compliance with 1 mA. Excellent memory characteristics including low set/ reset voltages and long retention time were demonstrated without additional electroforming process. The bipolar resistive switching behavior can be explained by the formation of conductive path consisting of oxygen vacancies. We analyzed a composition and chemical bonding of HfO₂ by x-ray photoelectron spectroscopy. In addition, microstructures of the films were analyzed by transmission electron microscopy.

Tuesday Afternoon, October 19, 2010

Energy Frontiers Topical Conference

Room: Pecos - Session EN+TF-TuA

Thin Films for Photovoltaics

Moderator: L.W. Rieth, University of Utah

2:00pm EN+TF-TuA1 Ar/H₂ Plasma Treatment of a-Si:H Thin Films: On the Role of Atomic Hydrogen in μ -Si:H Thin-Film Deposition. A.C. Bronneberg, A.M. Creatore, M.C.M. van de Sanden, Eindhoven University of Technology, the Netherlands

The transition from amorphous (a-Si:H) to microcrystalline (μ -Si:H) silicon film growth has been ascribed to the interaction of atomic hydrogen with the (sub)surface of the growing film [1]. To gain more insight into the formation of microcrystalline silicon and to the role of atomic hydrogen, several studies have been dedicated to hydrogen treatment of a-Si:H films [2,3,4,5]. However, the observed film crystallization is often wrongly ascribed to the impinging hydrogen atoms. What tended to be overlooked, is that the counter electrode is covered with an a-Si:H film during the deposition step. Interaction of the H₂ plasma with the coated electrode will result in formation of molecules and radicals originating from silane [4]. Hence, the resulting plasma conditions are similar to those used for μ -Si:H, which explains the observed crystal formation.

Here, we show that this is not only true for direct plasmas, but that also in remote plasmas the reactor wall has big influences on the growth process. By using *in situ* spectroscopic ellipsometry and *ex situ* Raman spectroscopy, we show that H₂ plasma treatment of a-Si:H only results in the formation of crystals when there is a source of silicon-based molecules and radicals. Together with a plasma study, comprising mass spectrometry and ion probe measurements, we address the origin and kinetics of the crystal formation and discuss the implications for μ -Si:H growth.

1. A. Matsuda, Journal of Non-Crystalline Solids **338**, 1-12 (2004).
2. A. F. I. Morral, J. Bertomeu, and P. R. I. Cabarrocas, Materials Science and Engineering B-Solid State Materials for Advanced Technology **69**, 559-563 (2000).
3. A. F. I. Morral and P. R. I. Cabarrocas, Journal of Non-Crystalline Solids **299**, 196-200 (2002).
4. K. Saitoh, M. Kondo, M. Fukawa, T. Nishimiya, A. Matsuda, W. Futako, and I. Shimizu, Applied Physics Letters **71**, 3403-3405 (1997).
5. G. Dingemans, M. N. van den Donker, A. Gordijn, W. M. M. Kessels, and M. C. M. van de Sanden, Applied Physics Letters **91**, (2007).

2:20pm EN+TF-TuA2 Spectroscopic Analysis of the Role of Hydrogen in Amorphous Silicon. P. Schäfer, F. Nobis, O.D. Gordan, H. Kupfer, F. Richter, D.R.T. Zahn, Chemnitz University of Technology, Germany

Amorphous hydrogenated silicon (a-Si:H) is widely used in photovoltaic applications. The high absorption renders a-Si:H technically relevant especially for thin film solar cells. Despite lower efficiency, an amorphous silicon solar panel possesses the advantage of higher absorption rate and easier processing at lower production cost.

Here the focus lies on highly (p and n) doped amorphous silicon films. The samples are prepared using d.c.-pulsed magnetron sputtering of crystalline silicon targets. A controlled hydrogen flow is added to the sputtering plasma. Hydrogen in amorphous silicon is known to saturate dangling bonds and improves the short range atomic order [1]. To probe the influence of hydrogen in the sputtering process various spectroscopic techniques were applied for sample characterisation.

Raman spectroscopy is a technique sensitive to the morphological aspects of the film. The relaxation of quasi-momentum conservation in amorphous films results in drastically different spectra of amorphous and crystalline silicon. A broad band at ~ 485 cm⁻¹ appears instead of the sharp crystalline phonon feature at 520 cm⁻¹. Its shape and asymmetry unveils further information on the short range order like the average dispersion angle from tetrahedral conformation. With the help of Fourier transformed transmission infrared spectroscopy the concentration of hydrogen in the sample is studied. Vibrational hydrogen-silicon stretching modes in the region around 2000 cm⁻¹ are therefore assessed by a modified [2] Brodsky-Cardona-Cuomo approach [3]. Access to the optical constants n and k and therefore the complex dielectric function ϵ of the sputtered material is granted by variable angle spectroscopic ellipsometry. Thereby important parameters like the Tauc-Lorentz band gap which is mainly determined by interband gap defects are revealed. The combination of these spectroscopic techniques provides a detailed picture of morphological, electrical, and optical parameters of the system. An in depth discussion of the degree of structural

improvement, the decrease of interband gap defects, the saturation of hydrogen content, and evolution of optical properties in correlation with the hydrogen flow will be presented.

[1] R. A. Street, "Hydrogenated Amorphous Silicon", chapter 2.3, Cambridge University Press.

[2] A. A. Langford, M. L. Fleet, B. P. Nelson, W. A. Lanford, N. Maley: Phys. Rev. B **45** (1992) 13367.

[3] M. H. Brodsky, M. Cardona, J. J. Cuomo: Phys. Rev. B **16** (1977) 3556.

2:40pm EN+TF-TuA3 Improved Efficiency and Air Stability of Hybrid Thin Film Solar Cells with a ZnO Nanoparticle Layer. P.H. Holloway, L. Qian, J. Yang, R. Zhou, A. Tang, Y. Zheng, J. Xue, University of Florida
INVITED

4:00pm EN+TF-TuA7 Energy Band Alignments and Influence of Doping on Ga-doped ZnO, CuO and Si. S.Y. Chiam, S.J. Wang, J.S. Pan, L.M. Wong, Institute of Materials Research & Engineering, Singapore, W.K. Chim, National University of Singapore

It is important to investigate new materials for thin film solar cells for 2nd generation devices. Materials extraction cost and annual electricity production considerations highlighted several potential new materials including cuprous oxide (Cu₂O). In this work, we report on the growth of Cu₂O and highlighted the importance of the oxygen partial pressure during growth. Namely, the partial pressure of oxygen determines the transition of Cu₂O to CuO with increasing partial pressure. This is accomplished at a fixed total pressure as this may influence Cu₂O formation. We then discuss about the interface energy alignments, first between Cu₂O/ZnO and then ZnO/Si. The former is of importance as inorganic thin film p-n junction that is suitable for 2nd generation solar cell devices. For the latter case, we fabricated device structure on differently doped Si, to investigate influence on doping on the transport characteristics of the hetero- pn junction. It is found that forward bias characteristics for a heterojunction, is not critically dependant on the band offsets, but rather the build-in-field at the heterojunction. If the physics is considered from the point of view of quasi-fermi level separation during light illumination, this build-in-field will also determine the V_{oc}. In this sense, band offset measurements can only give an indication of the maximum limit of the V_{oc} for differently doped semiconductors (non-degenerate) heterojunction solar cells. In addition, we show that under illumination, the current conduction for the ZnO/Si at zero-bias is a "forward bias" current, unlike all homojunction devices. This can be understood with a detail examination of the energy band diagrams. This work shows the importance of using measured band offsets to aid in understanding the relative Fermi-level alignment instead of using bulk electron affinity values. The work also demonstrates a whole array of playground possible for thin film heterojunction of different materials to engineer an ideal junction for solar cell devices.

4:20pm EN+TF-TuA8 Growing Low-Dislocation-Density Ge on Si through Nanometer Sized Voids in Chemical Oxide and Subsequent Integration of III-V Films for Multijunction Solar Cells. D. Leonhardt, J.J. Sheng, University of New Mexico, J.G. Cederberg, M.S. Carroll, Sandia National Laboratories, M.J. Romero, National Renewable Energy Laboratory, S.M. Han, University of New Mexico

4:40pm EN+TF-TuA9 Optimizing Heterojunctions of ZnTe/ZnSe Solar Cells: Effect of Surface Treatment and Growth Conditions. F. Fang, B. McCandless, R. Opila, University of Delaware

II-VI direct band gap semiconductors are attractive for thin film solar cell (TFSC) applications owing to their potential flexibility in tunable optoelectronic properties and possible application in tandem cells for being band gap materials (E_g > 2 eV). For the n-ZnSe/p-ZnTe heterojunction solar cell, the defect states and electronic band alignment at the ZnSe/ZnTe interface are crucial for device performance. We have employed Al-K α X-ray photoelectron spectroscopy as well as synchrotron source ultra-violet photoelectron spectroscopy to study the surface chemical composition and electronic structures at heterojunction interface. Scanning electron microscopy (SEM) was used to study observe the film microstructure morphology of the interface.

We used two different deposition techniques: Close Space Sublimation (CCS), a low-cost deposition method already demonstrated for high efficiency and commercial CdTe TFSC, and conventional thermal evaporation. Our preliminary results indicated that surface oxides on CCS-grown ZnSe film formed once open to air, and a significant valence band offset induced by this oxide is observed which acts like additional energy

barrier for carrier transport, resulting in low open circuit voltage. Also, during sequential CSS deposition of the two stacking films, the covering ZnTe thin film layer growth damage the microstructure of the underlying ZnSe film, i.e., enlarged pores are observed in ZnSe films in the locations where partially covering ZnTe film was deposited. A degraded device performance is expected and low short circuit currents and fill factors of the cells are detected. By analogy to CdS/CdTe TFSC, we are aiming for close-packed column polycrystalline of ZnSe/ZnTe film growth. Therefore, we are exploring etching processes, annealing temperatures and ambient settings to optimize the growth conditions. Evaporation is under investigation, since we have the option of dual-sources in the self-designed chamber, sequential growth of ZnSe and ZnTe films without vacuum break is feasible. Film morphology as well as energy band alignment at the heterojunctions using evaporation growth is being studied.

5:00pm EN+TF-TuA10 Investigation of NbSe₂ as Potential High Work Function Back Contact for CdTe Solar Cells, M.A. Wolak, S. Gutmann, M.M. Beerbom, C.S. Ferekides, R. Schlaf, University of South Florida

The layered semi-metal NbSe₂ combines a chemically inert van der Waals surface with a high work function of about 5.8 eV. This motivated an investigation of NbSe₂ as Ohmic hole injection contact for CdTe solar cells. Current back contacts made from Cu suffer from interdiffusion issues leading to cell degradation. In the discussed experiments, the interface between NbSe₂ and CdTe was investigated using x-ray and ultraviolet photoemission spectroscopy (XPS, UPS). In these experiments CdTe and NbSe₂ thin films were grown in-situ in a vacuum chamber attached to the photoemission system. This enabled the investigation of the CdTe/NbSe₂ interface without interference by ambient contamination. After growth of a CdTe thin film, the NbSe₂ film was prepared in several steps. Photoemission spectroscopic characterization between each of the deposition steps allowed the observation of the formation of the band line-up at the interface. The results of the experiments indicate that an intermixed layer forms at the interface. This layer causes the formation of an interface dipole, preventing the formation of an Ohmic contact. A Schottky-type band line-up formed instead.

5:20pm EN+TF-TuA11 In-Rich InGa_{1-x}N Films for Efficient Photovoltaic Devices Grown by ENABLE, T.L. Williamson, M.A. Hoffbauer, Los Alamos National Laboratory, K.M. Yu, L.A. Reichertz, W. Walukiewicz, Lawrence Berkeley National Laboratory

The wide band gap tunability of In_xGa_{1-x}N thin films (0.7 eV to 3.4 eV, 1>x>0) makes them ideal for efficient photovoltaic (PV) devices. However, growing high-quality In-rich In_xGa_{1-x}N films with strong photoluminescence in the green-to-red portions of the visible spectrum has faced considerable challenges due to indium phase segregation and other materials issues. These challenges have precluded the growth of both In-rich InGa_{1-x}N and compositionally graded InGa_{1-x}N materials, and make it difficult to grow higher bandgap Ga-rich materials on top of lower bandgap In-rich materials. Overcoming these difficulties using conventional epitaxial techniques is challenging due to the low decomposition temperatures of In-rich materials (e.g. InN~550°C) and the relatively high growth temperatures for Ga-rich materials (e.g. GaN >800°C).

Energetic neutral atom beam lithography & epitaxy (ENABLE) is a low-temperature thin film growth technology recently developed at LANL that utilizes a collimated beam of energetic neutral N atoms (kinetic energies 0.5 to 5.0 eV) to react with evaporated Ga and In metals to grow InGa_{1-x}N. ENABLE is similar to MBE, but provides a much larger N atom flux and correspondingly high film growth rate. The high kinetic energy of the reactive N atoms substantially reduces the need for high substrate temperatures, making isothermal growth over the entire InGa_{1-x}N alloy composition range possible at rates of >3 microns/hr with no toxic precursors or waste products.

Data on film photoluminescence, crystallinity, electrical properties, doping, and electro-luminescence of In_xGa_{1-x}N, graded In_xGa_{1-x}N, and GaN films grown using ENABLE over the full composition range will be presented. ENABLE-grown In_xGa_{1-x}N films show strong photo- and electro-luminescence spanning the entire visible region of the spectrum, with reasonable carrier mobilities background carrier concentrations typically in the low 10¹⁷ range. Evidence for p-type doping of In-rich InGa_{1-x}N films and characterization of p/n junctions will be discussed along with the prospects for using ENABLE to fabricate efficient PV devices.

5:40pm EN+TF-TuA12 Copper Oxide Thin Films: Preparation and Modulation of Semiconducting Properties by Electrochemical Methods, F. Caballero-Briones, CICATA-IPN/Universitat de Barcelona, Spain, A. Palacios-Padrós, Instituto de Bioingeniería de Catalunya, Spain, F. Sanz, Instituto de Bioingeniería de Catalunya/CIBER-BBN, Spain

Copper oxide is a p-type semiconductor with a direct band gap of 2 eV, suitable for photovoltaic applications. In this work we present an

electrochemical method to prepare p-type semiconducting Cu₂O films around 100 nm thick with noticeable photocurrent response. The film properties were modulated by varying different conditions such as the time at a dissolution potential and the film doping with alkaline ions. The modification of the time of exposure to the dissolution potential allows the tailoring of the crystallinity, the band gap energy and the disorder parameter E₀ and also provided elements to outline the growth mechanism of the Cu₂O films that involve surface reaction, diffusion of oxygen species that react in the solid state accordingly to the point defect model, and heterogeneous deposition of Cu₂O from the Cu⁺ ions dissolved in a chemical bath-like fashion. On the other side, the study of the behavior of different alkaline metal ions (A: Li, Na, K, Cs) present in the electrolyte used to prepare the Cu₂O films lead to important results. It was observed that important amounts of the alkaline ion (around 1%) can be incorporated to the film and that are indeed electrically active impurities that modify the band gap energy probably by introducing states within the band gap in the case of Cs or by getting incorporated to the crystalline lattice for Na or Li. Changes in the optical absorption, thickness, density of carriers and in defects are related with the size of the employed ion. To complete the study, an electronic diagram of the Cu|Cu₂O|Electrolyte interface was prepared by using a combination of techniques including Electrochemical Impedance and Electrochemical Tunneling Spectroscopy/Microscopy.

Graphene Focus Topic

Room: Brazos - Session GR+TF-TuA

Graphene and 2D Nanostructures

Moderator: Y. Chen, Purdue University

2:00pm GR+TF-TuA1 Graphene and Its Progeny: from Fundamental Material Properties to Device Applications, A.W. Ghosh, University of Virginia

INVITED

The incredible material properties of graphene have spurred intense interest among chemists, physicists and engineers towards potentially exciting electronic applications. Much like nanotubes, graphene electrons have high mobilities due to the sharp curvature of their bands at the Gamma point that reduces their effective masses, as well as long scattering lengths due to symmetry selection rules among their pseudospin separated bands. However, a potential problem with graphene is its metallicity, which makes its ON-OFF ratio unacceptable for digital logic. Effort is under way to mitigate this by opening bandgaps through various chemical and electrostatic means. I will argue that any such band-gap opening leads to an inevitable reduction in mobility *even if we manage to do so without affecting its scattering length*. The trade-off arises from a fundamental asymptotic constraint on all graphitic materials (epitaxial graphene, strained graphene, nanoribbons, nanotubes, and bilayer graphene) that pins the high energy electrons away from the Gamma point to an ultimately linear dispersion. However, opening a bandgap by width confinement, e.g. in a nanoribbons, can provide distinct electrostatic if not material advantages. The presence of diffuse boundary conditions at the edges, along with strain and edge roughness, systematically erases any signs of chirality and metallicity in GNRs, making their widths the single arbiter of metallicity. This allows us to envisage wide-narrow-wide (WNW) nanoribbons monolithically patterned out of a single template into both switches and interconnects. The 2-D electrostatics of the source-drain contact edge capacitances improves the gate control, allowing the current to show a highly desirable saturation characteristic. Furthermore, the presence of C-C bonds at the channel-contact interface makes metal induced gap states relatively ineffective in pinning the bands, promoting Ohmic behavior. I will quantify the advantages and disadvantages of WNW devices, and compare with alternate GNR switches, such as utilizing electron focusing in p-n junctions.

2:40pm GR+TF-TuA3 Electronic Structure of Graphene/BN Heterojunctions formed by Graphene CVD: Doped Graphene, C. Bjelkevig, Z. Mi, University of North Texas, J. Xiao, P.A. Dowben, Nebraska Center for Nanostructures and Materials, S. Gaddam, S. Pokharel, J.A. Kelber, University of North Texas

Graphene has been grown by chemical vapor deposition of C₂H₄ on a monolayer of h-BN(0001) formed by atomic layer deposition (BCl₃, NH₃) on Ru(0001). AES, STM and LEED confirm a graphene-like overlayer, with near-zero DOS near the Fermi level, in registry with a BN R30(√3x√3) substrate. Raman spectra reveal graphene "G" and "2D" features with relative intensities indicative of single layer graphene. A large (350 cm⁻¹) redshift in the 2D feature relative to HOPG indicates significant BN-to-graphene charge transfer. The charge transfer is confirmed by photoemission/angle-resolved inverse photoemission spectroscopies

(PES/ARIPES), that demonstrate filling of the lowest unoccupied graphene state (π^*) near the Brillouin zone center. These results are in direct contrast to PES/ARIPES results for graphene/Cu, and reported results for graphene/SiC(0001), that show empty graphene π^* states. The data show that the BN layer acts as an n-type dopant for graphene. For the graphene/BN heterojunctions, the ARIPES-determined dispersion of the unoccupied graphene $\sigma^*(\Gamma_1^+)$ state yields an effective mass of $0.05 m_e$, in excellent agreement with reported transport measurements on graphene sheets, and indicating that BN doping does not fundamentally alter the graphene electronic structure. The direct growth of graphene on dielectric substrates, and the controlled exploitation of graphene/substrate heterojunction properties, are critical issues for practical device fabrication. The implications of direct CVD of undoped graphene and graphene/BN heterojunctions on high dielectric constant substrates for device applications will be discussed in light of recent results in our laboratories for graphene thermal and free radical-assisted CVD on OH-terminated MgO(111).

Acknowledgements: Work at UNT was supported by the Global Research Consortium of the Semiconductor Research Corporation through Task ID 1770.001, and through ONR under award no. N00014-08-1-1107 through a subcontract with Texas State University at San Marcos. Work at UNL was supported by the Defense Threat Reduction Agency (Grant No. HDTRA1-07-1-0008), and the NSF "QSPINS" MRSEC (DRM-0820521) at UNL. The authors also thank Luigi Colombo and Adam Pirkle for acquisition of the Raman spectra.

3:00pm GR+TF-TuA4 Electrical Transport in Graphenoid and Graphene Nanomembranes from Pyrolyzed Self-Assembled Monolayers, A. Turchanin, Univ. of Bielefeld, Germany, D.H. Weber, National Metrology Inst., Germany, M. Bünenfeld, Univ. of Bielefeld, Germany, J. Mayer, Ernst Ruska-Centre for Microscopy, Germany, C. Kisielowski, National Center for Electron Microscopy, T. Weimann, National Metrology Inst., Germany, A. Götzhäuser, Univ. of Bielefeld, Germany

Ultrathin carbon nanomembranes have recently attracted enormous interest. We report a molecular route to the fabrication of a monolayer or few layers of free-standing graphenoid and graphene nanomembranes based on molecular self-assembly, electron processing and pyrolysis. Aromatic biphenyl self-assembled monolayers (SAMs) are cross-linked by electron irradiation. The cross-linking results in mechanically stable graphenoid sheets with the thickness of a single molecule (~ 1 nm) and arbitrary sized. The graphenoid sheets can be lifted from their surface and transferred to another solid substrate or holey structures, where they become free-standing nanomembranes. Upon annealing (pyrolysis) up to 1300 K the molecular sheets transform into nanocrystalline graphene phase. This transformation is accompanied by a drop of the sheet resistivity from $\sim 10^8$ to ~ 10 k Ω /sq and a 2D insulator to metal transition. We characterize the insulator to metal transition by electrical transport measurements as well as by complementary spectroscopic and microscopic techniques. A plethora of applications of the suggested molecular route to free-standing ultrathin carbon materials is feasible that take advantage from the fact that the large scale fabrication, control over the thickness and nanostructuring are easily controlled.

[1] A. Turchanin, A. Beyer, C. T. Nottbohm, X. H. Zhang, R. Stosch, A. Sologubenko, J. Mayer, P. Hinze, T. Weimann, and A. Götzhäuser: One Nanometer Thin Carbon Nanosheets with Tunable Conductivity and Stiffness, *Adv. Mater.* 21, 1233-1237 (2009)

[2] A. Turchanin, D. Käfer, M. El-Desawy, C. Wöll, G. Witte, and A. Götzhäuser: Molecular Mechanisms of Electron-Induced Cross-Linking in Aromatic SAMs, *Langmuir* 25, 7342-7352 (2009).

[3] C. T. Nottbohm, A. Turchanin, A. Beyer, A. Götzhäuser: Direct e-beam writing of 1 nm thin carbon nanoribbons, *J. Vac. Sci. Technol. B* 27, 3059-3062 (2009).

4:00pm GR+TF-TuA7 From 2D to 1D - Supramolecular Architectures on Rippled Graphen, M. Roos, H.E. Hoster, R.J. Behm, Ulm University, Germany

Bis(terpyridine)derivatives (BTP) form highly ordered hydrogen-bonded 2D networks on solid surfaces.1-4 The preferred hydrogen bond configurations and thus the resulting structures are steered via the positions of the nitrogen atoms within the BTP molecules. Elaborate synthesis procedures allow varying these positions without altering the footprint shape of the molecules.1 On smooth surfaces like graphite or metal single crystals, the molecule-substrate interactions play a secondary role for the structures, mainly by determining the orientations of the molecules and thus of the ordered networks.2-4 In this contribution, we will demonstrate that more pronounced template effects arise for substrates where the molecule-substrate interaction laterally varies at nm-scales. As an example, we will show the ordering behaviour of two different types of BTP molecules on Graphene monolayers grown on Ru(0001). The moiré-type pattern of these surfaces has a periodicity of 3 nm, i.e., in the order of the BTP dimensions

and the network meshes they usually form. Submolecularly resolved STM images show that the BTP molecules are confined to the valleys of the graphene ripple structure. We will compare the resulting supramolecular 1D and 2D assemblies to the ordered 2D networks formed by the same molecules on smooth substrates, and we will discuss in how far the template effect can be quantitatively explained by a lateral modulation of the van der Waals interactions due to the height corrugation of the Graphene sheet.5

1 C. Meier et al., *J Phys Chem B* 109 (2005) 21015.

2 M. Roos et al., *Phys. Chem. Chem. Phys.* 9 (2007) 5672.

3 H. E. Hoster et al., *Langmuir* 23 (2007) 11570.

4 T. Waldmann et al., *ChemPhysChem* 11 (2010) 1513.5 W. Moritz et al., *Phys. Rev. Lett.* 104 (2010) 136102.

4:20pm GR+TF-TuA8 Understanding the Functionalization of Graphene by Electron-Beam Generated Plasmas, M. Baraket, S.G. Walton, E.H. Lock, J.A. Robinson, F.K. Perkins, Naval Research Laboratory

Graphene is a single monolayer thick carbon sheet with remarkably high electron mobility. Its unique structural and electronic properties make it an interesting material for nanoscale electronic and sensing devices. The addition of functionalities increases its reactivity toward certain materials and thus broadens its applications. One significant impediment to realizing the potential of graphene is the development of an industrially viable approach to producing precisely engineered functionalities over large areas. In this respect, plasmas are an ideal candidate but problems associated with the large fluxes of high-energy ions are a significant concern. Electron beam generated plasmas, characterized by low incident ion energies (< 5 eV), have been used to functionalize graphene without any damage [1]. We discuss the use of this system to controllably introducing oxygen, hydrogen, fluorine, nitrogen or ammine containing groups at different concentrations. The reversibility of the functionalization via low-temperature annealing will also be discussed. This work was supported by the Office of Naval Research. M.B. appreciates the support of the National Research Council.

[1] M. Baraket, S.G. Walton, E.H. Lock, J. T. Robinson, and F.K. Perkins. The functionalization of graphene using electron beam generated plasmas. *Applied Physics Letters* 96, 231501 (2010)

4:40pm GR+TF-TuA9 Chemically Tailoring Graphene via Organic Self-Assembled Monolayers, M.C. Hersam, Northwestern University INVITED

Chemically functionalized semiconductor surfaces have been widely explored due to their potential for enabling molecular electronic and sensing devices that are compatible with conventional microelectronic technology [1]. Thus far, the vast majority of work in this field has focused on established semiconductors including silicon, germanium, and gallium arsenide. Meanwhile, the condensed matter physics community has diverted substantial experimental and theoretical effort to graphene, an emerging electronic material with superlative carrier mobility and exotic charge transport phenomena such as the quantum Hall effect.

In an attempt to unify these two fields, we have been exploring strategies for forming and interrogating organic self-assembled monolayers on graphene surfaces. In particular, we have recently demonstrated that self-assembled monolayers of perylene-3,4,9,10-tetracarboxylic-dianhydride (PTCDA) can be formed on graphene surfaces via gas-phase deposition in ultra-high vacuum (UHV) environments at room temperature [2]. Molecular-scale resolution scanning tunneling microscopy (STM) images reveal long-range order in the PTCDA monolayers, while scanning tunneling spectroscopy (STS) measurements yield distinct electronic features associated with the PTCDA that are not observed on pristine graphene.

In addition to UHV STM characterization, this talk will summarize our most recent efforts to nanopattern self-assembled monolayers on graphene at the sub-10 nm scale. Nanopatterning chemically functionalized graphene presents opportunities for tailoring the electronic and chemical properties of graphene nanoribbons in addition to providing a molecular-scale resolution template for subsequent materials growth on graphene surfaces.

[1] M. A. Walsh and M. C. Hersam, "Atomic-scale templates patterned by ultrahigh vacuum scanning tunneling microscopy on silicon," *Annual Review of Physical Chemistry*, **60**, 193 (2009).

[2] Q. H. Wang and M. C. Hersam, "Room-temperature molecular-resolution characterization of self-assembled organic monolayers on epitaxial graphene," *Nature Chemistry*, **1**, 206 (2009).

5:20pm **GR+TF-TuA11 Stability of Continuous Graphene Sheet and Graphene Flake on the Si(111) Surface**, *B.B. Kappes, T.E. Davies*, Colorado School of Mines, *S. Jun*, University of Wyoming, *A.C.T. van Duin*, Penn State University, *C.V. Ciobanu*, Colorado School of Mines

While rapid use of carbon nanostructures in the silicon-based nanoelectronics industry will involve the direct integration of graphene with silicon chips, so far graphene has not been grown on pristine silicon surfaces because usual synthesis routes would likely lead to the formation of stable silicon carbide instead of the precipitation of carbon at the surface. Here we show that if graphene can be deposited on pristine Si(111) surfaces, then it forms moiré superstructures and binds strongly to the substrate over a wide range of in-plane orientations. The binding energies depend on the orientation of graphene as well as the strain applied to achieve commensurability with the substrate; the strongest binding estimated from density functional theory calculations is approximately 1.5 eV/carbon atom. Using molecular dynamics simulations based on bond-order and reactive force field interatomic potentials, we present evidence that graphene remains stable and bonded to the substrate for temperatures up to 80% of the substrate melting temperature. Bonding information, study of the local density of states, and simulated scanning tunneling microscopy show graphene on Si(111) is semiconducting, with a sizable number of carbon hybridized sp^3 and a bandgap affected by the orientation of graphene with respect to the substrate.

5:40pm **GR+TF-TuA12 Effect of Point-like Defects on the Atomic Structure and Electronic Properties of Graphene Supported on Amorphous SiO₂**, *K.E. Kweon, G.S. Hwang*, University of Texas at Austin
Graphene supported on the common gate dielectric, SiO₂, has been considered as a highly promising candidate for future electronics. Therefore, it is important to understand the interfacial interaction between graphene and SiO₂. Most of the existing theoretical studies have modeled the underlying SiO₂ surface using defective or H-terminated crystalline structures. However, the gate oxide is amorphous and possibly has a number of point-like defects, yet no detailed study has been undertaken on the defect effect. In this talk, based on first principles calculations we present how the SiO₂-graphene binding and consequent graphene electronic structure are influenced by the presence of point-like defects in not only SiO₂ surface but also graphene sheet. We considered six different surface defects on SiO₂: silyl radicals [(≡Si-O)₃Si•], oxy radicals [(≡Si-O)₃Si-O•], silylene center [(≡Si-O)₂Si:], silanone [(≡Si-O)₂Si=O], peroxide radicals [(≡Si-O)₃Si-O-O•], and dioxasilirane [(≡Si-O)₂Si <O₂], along with defective graphene that contains vacancies. This talk will mainly touch on the pathways and energetics of the defect-mediated graphene binding to SiO₂, and how the covalent graphene-SiO₂ binding affects the electronic properties of graphene.

Thin Film

Room: Ruidoso - Session TF-TuA

ALD/CVD: Surface Chemistry and Fundamentals

Moderator: S.M. Rossnagel, IBM Research

2:00pm **TF-TuA1 Studying Roll-to-Roll ALD Process Conditions Using a Moving Substrate Under a Gas Source Coating Head**, *R. Fitzpatrick, Z.M. Gibbs, S.M. George*, University of Colorado

Continuous roll-to-roll ALD processing is currently being developed for economical and efficient ALD on polymer and other flexible substrates. One of the key implementations of roll-to-roll ALD was introduced by Kodak (D. H. Levy et al., *Appl. Phys. Lett.* **92**, 192101(2008)). To understand the dependence of roll-to-roll ALD on process conditions, we have constructed a laboratory-scale apparatus featuring a fixed gas source coating head that sits in ambient above a moving substrate that is driven by a programmable stepper motor. The gas source coating head consists of a series of rectangular channels that spatially separate the ALD reactions. As the substrate moves under the gas source coating head, the channel sequence for each reactant is: precursor; exhaust; N₂ purge; and exhaust. The gas source head was built for 1.5 ALD cycles. Using Al₂O₃ ALD as a model system, the gas source head has the trimethylaluminum (TMA) channel sequence in the middle and the water channel sequence on each side of the TMA. This design allows for the deposition of two Al₂O₃ ALD cycles during one complete back-and-forth translation of the moving substrate. A low conductance gap between the precursor and exhaust channels allows for nearly "static" reactant exposures and prevents intermixing of the reactants. A higher conductance gap was machined into the gas source head between the exhaust and purge channels to create a

"high flow" entrainment region that further isolates the precursor channels. The spacing between the gas source head and substrate is fixed and can be controlled with micron precision. This new apparatus can test how roll-to-roll ALD depends on the gap spacing, substrate speed, gas flow rates, and pressure difference between reactant and purge channels. An understanding of these process parameters will be necessary for the successful implementation of continuous, large scale roll-to-roll ALD.

2:20pm **TF-TuA2 Reactive Intermediates during Atomic Layer Deposition of Aluminum Oxide from Ozone and an Oxygen Plasma**, *V.R. Rai*, Colorado School of Mines, *V. Vandalon*, Eindhoven University of Technology, Netherlands, *S. Agarwal*, Colorado School of Mines

In this presentation, the authors will elucidate the surface reaction mechanisms during the atomic layer deposition (ALD) of aluminum oxide from trimethyl aluminum (TMA) in conjunction with O₃ and an O₂ plasma. The deposition mechanism was explored over a substrate temperature range of 70–200 °C using in situ attenuated total reflection Fourier transform infrared spectroscopy. Our IR data show that both –OH groups and carbonates are formed on the surface during the oxidation cycle. Gas-phase IR data indicate that oxidizer-assisted combustion of methyl ligands in chemisorbed TMA produces CO₂ and H₂O, which react simultaneously on the Al₂O₃ surface to produce carbonates. The origin of the –OH groups was attributed to the reaction of the uncombusted methyl ligands with gas-phase H₂O. While the type of surface sites are common to both oxidizing agents, in the case of O₂-plasma-assisted ALD, surface carbonates are simply reactive intermediates, which completely decompose upon prolonged plasma exposure. The ratio of carbonates to –OH groups is strongly dependent on the oxidizing agent, and its dose in case of plasma-assisted ALD. Surface reactions such as chemisorption of TMA, formation of –OH groups and Al₂O₃ were pseudo first order. On the other hand, the kinetic behavior of the carbonates suggests a series reaction of the type, $A(CH_3) \rightarrow B(\text{carbonates}) \rightarrow C(Al_2O_3)$. Although carbonate sites contribute to Al₂O₃ growth, their contribution was determined to be insignificant.

2:40pm **TF-TuA3 Synthesis of Micro/Mesoporous Alumina Fibers by Gas Phase Infiltration of Polyesters with Trimethyl Aluminum and Water**, *B. Gong, Q. Peng, C. Devine, K. Lee, G.N. Parsons*, North Carolina State University

Preparation of inorganic micro/mesoporous materials has attracted considerable attention because of their function in catalytic, separations, and other applications. Although many approaches are known to synthesize porous materials, methods to form mesoporous materials with pre-determined shape and morphology are not readily known. Sub-surface deposition, recently observed during atomic layer deposition (ALD) on polymer substrates, provides a potential method to transform polymers from fully organic solids into organic-inorganic hybrid and micro/mesoporous materials. Moreover, the transformation allows polymers with well defined micro and nano-structure, such as polymer fiber matrices, to maintain their shape and structure to form new replica materials. In this presented work, we apply this process to synthesis of Al-O/organic hybrid micro fibers by gas phase infiltration of tri-methyl aluminum and water alternatively by polyesters, such as polybutylene terephthalate (PBT). Through in-situ infrared analysis, we show that TMA acts as a strong Lewis acid and attacks the nucleophilic ester groups in polyesters to insert Al-O bonds into the polymer chains. The organic components are removed by post annealing to produce a micro/mesoporous alumina fiber. Surface area, pore volume, and pore size distribution of the porous alumina fibers were tested by nitrogen adsorption/desorption experiments, and surface areas exceeding 400 m²/g were obtained. SEM was used to track the morphology change along the process, and cross-section TEM images of annealed samples confirmed the formation of porous structures.

3:00pm **TF-TuA4 Growth Rate Control in ALD by Surface Functionalization: Alkyl Alcohols on Metal Oxides**, *A. Yanguas-Gil, J.W. Elam*, Argonne National Laboratory

In this work we explore the effect that alkyl alcohols (ROH) have on the saturation growth rate during the ALD of metal oxides. The traditional dosing sequence for metal oxide ALD is: M/O/M/O... where M is the metal precursor and O is the oxygen source. We find that by dosing organic molecules prior to dosing the metal precursor (e.g. ROH/M/O...) we can modify the surface chemistry and control the saturation growth rate. We will present results describing the effect of alkyl alcohols (R=Me, Et, iPr, and Bu) using H₂O as the oxygen source and the metal precursors Ti(iPr)₄ for TiO₂ ALD, TMA for Al₂O₃ ALD, and DEZ for ZnO ALD. Furthermore, we demonstrate this effect in the ALD of doped metal oxides.

Our results show that the ROH/M/H₂O sequence causes a substantial reduction in the growth per cycle for all of the ALD systems studied. For instance, the growth per cycle reduces from 0.31 to 0.06 Å/cycle in the case

of TiO₂ ALD using MeOH/Ti(iPr)₄/H₂O, and from 1.2 to 0.4 Å/cycle in the case of Al₂O₃ ALD using MeOH/TMA/H₂O at 200°C.

Previous studies in the literature indicate that ROH reacts with basic sites on the metal oxide surface. Alcohol deprotonation followed by metal oxygen heterolytic bond formation leads to the formation of alkoxide functional groups bound to metal cations. To investigate this process, we performed *in situ* mass spectrometry and quartz crystal microbalance studies during the ROH/M/H₂O dosing sequence. We discovered that the ROH adsorbed on the surface desorbs intact as ROH during the subsequent water pulse, but no alcohol is released during the metal precursor pulse. Furthermore, the reduction of the growth rate per cycle is not affected by purge times, suggesting that the ROH molecules bond strongly to the metal oxide surface. Finally, no reduction in growth per cycle is observed using the dosing sequence: ROH/H₂O/TMA/H₂O. This finding suggests that the ROH and H₂O are able to displace one another, and signifies an almost complete elimination of the alkoxide groups during the water pulse. This observation agrees with the many reports of successful metal oxide ALD using metal alkoxide and water.

The ability to tune the saturation growth rate by modifying the surface chemistry can be of great utility for the ALD of doped materials where a homogenous distribution of dopants at a low concentration is desired.

4:00pm TF-TuA7 Waterless TiO₂ Atomic Layer Deposition using Titanium Tetrachloride and Titanium Tetraisopropoxide, V.R. Anderson, A.S. Cavanagh, A.I. Abdulagatov, Z.M. Gibbs, S.M. George, University of Colorado

Most processes for TiO₂ atomic layer deposition (ALD) utilize water or other oxidants that can oxidize some substrates of interest. To avoid this oxidation, waterless or oxidant-free surface chemistry can be used that involves titanium halides and titanium alkoxides. This waterless surface chemistry approach for metal oxide ALD was originally proposed by the University of Helsinki group (M. Ritala et al., *Science* **288**, 319 (2000)). In this study, TiO₂ ALD was accomplished using titanium tetrachloride (TiCl₄) and titanium tetraisopropoxide (TTIP). *In situ* Fourier transform infrared (FTIR) studies revealed that the mechanism for TiO₂ ALD using TiCl₄ and TTIP changed with temperature. At high temperatures between 250 and 300 °C, the isopropoxide species after TTIP exposures quickly underwent beta-hydride elimination to produce TiOH species on the surface. The observation of propene by quadrupole mass spectrometry confirmed the beta-hydride elimination reaction pathway. The TiCl₄ exposure then reacted with the TiOH species to deposit TiCl_x species on the surface. At low temperatures between 125 and 200 °C, the isopropoxide species remained after TTIP exposures to react with TiCl₄. However, this reaction was much less efficient than the reaction of TiCl₄ with TiOH species. Quartz crystal microbalance (QCM) studies were also used to monitor TiO₂ ALD at low and high temperatures. The QCM studies measured low TiO₂ growth rates of ~3 ng/cm² at a low temperature of 150°C. In contrast, much higher TiO₂ growth of ~15 ng/cm² were observed at a higher temperature of 250°C under similar reaction conditions. X-Ray reflectivity measurements determined that TiO₂ ALD using TiCl₄ and TTIP at 250°C produced a growth rate of 0.5-0.6 Å per cycle. X-Ray photoelectron studies also confirmed TiO₂ film growth with a chlorine contamination of less than 0.5 at%. This waterless TiO₂ ALD process using TiCl₄ and TTIP should be valuable for preventing substrate oxidation during TiO₂ ALD on oxygen-sensitive substrates such as cobalt.

4:20pm TF-TuA8 Growth Mechanism and Properties of Mg_xZn_(1-x)O Nanocomposites by Atomic Layer Deposition, Q. Peng, A.U. Mane, J.W. Elam, Argonne National Laboratory

Magnesium-zinc oxide (Mg_xZn_(1-x)O) ternary films are an interesting class of alloy materials in which the band gap can be tuned by adjusting the Mg doping concentration. Consequently, Mg_xZn_(1-x)O has been widely studied for application in the fields such as electronics, optics, photoelectronics, and solar cells. Mg_xZn_(1-x)O thin films have been fabricated through a variety of methods including chemical vapor deposition, physical vapor deposition, molecular beam deposition, and ALD. Although there have recently been a few reports describing ALD Mg_xZn_(1-x)O for application in photovoltaics, there has been no detailed study of the growth mechanism and properties of the ALD Mg_xZn_(1-x)O thin films.

In this work, the ALD Mg_xZn_(1-x)O was systematically explored with different doping concentration of Mg by using diethyl zinc (DEZ), bis-cyclopentadienyl-magnesium (Cp₂Mg) and H₂O as the precursors. The growth mechanism was investigated using quartz crystal microbalance and quadrupole mass spectrometry measurements. The growth rate of the Mg_xZn_(1-x)O alloy films was determined using spectroscopic ellipsometry. The crystal structures of the films before and after thermal treatment were analyzed using x-ray diffraction. In addition, the optical properties of the Mg_xZn_(1-x)O with different Mg concentrations were analyzed using UV-vis absorption spectroscopy and the electrical properties were evaluated using

mercury probe current-voltage measurements. The thermal stability of the conductivity and structure of the Mg_xZn_(1-x)O films were studied as well. The system will be compared with Al doped ZnO system fabricated by ALD, to illustrate the conduction mechanism in doped ZnO synthesized by ALD process.

4:40pm TF-TuA9 Nucleation and Growth of Conformal and Ultrathin Pt Films on Al₂O₃ and W Substrates Using Plasma Enhanced ALD, L. Baker, A.S. Cavanaugh, D. Seghete, S.M. George, University of Colorado, A.J.M. Mackus, E.W.M.M. Kessels, Eindhoven University of Technology, Netherlands, Z.Y. Liu, F.T. Wagner, General Motors Research & Development

Pt ALD using thermal chemistry has nucleation difficulties and leads to the deposition of Pt nanoclusters. In contrast, Pt ALD using O₂ plasma nucleates much more readily and spectroscopic ellipsometry (SE) studies are consistent with continuous Pt films (H.C.M. Knoops et al., *Electrochem. Solid-State Lett.* **12**, G34 (2009)). However, SE measurements alone were insufficient to characterize the early stages of the Pt ALD process. In this investigation, we have examined Pt ALD with MeCpPtMe₃ and O₂ plasma as the reactants using SE, X-ray reflectivity (XRR), X-ray photoelectron spectroscopy (XPS) and scanning electron microscopy (SEM) studies versus the number of ALD cycles. Analysis of the XRR and XPS results indicates that plasma Pt ALD on Al₂O₃ ALD substrates has a short nucleation delay. The nucleation delay is followed by a brief period of rapid Pt ALD film growth of 0.1 nm per cycle that is followed by a slower steady-state Pt ALD film growth of ~0.05 nm per cycle. During the Pt ALD nucleation and growth on the Al₂O₃ ALD substrate, SEM images show that the Pt film morphology evolves from isolated nanoclusters to worm-like nanostructures and finally to a conformal film at a Pt film thickness of approximately 7 nm. Nucleation and growth of Pt ALD on W ALD substrates led to very different results. In this case, a H₂ plasma was used instead of an O₂ plasma to prevent oxidation of the W ALD substrate. XRR and XPS studies revealed that Pt ALD with MeCpPtMe₃ and H₂ plasma as the reactants on W ALD substrates nucleated immediately and a continuous and conformal Pt ALD film was formed at a Pt ALD thickness of less than 5 nm. These results indicate that Pt ALD can be tuned to produce Pt nanoclusters or a continuous and conformal ultrathin Pt film using either thermal or plasma Pt ALD.

5:00pm TF-TuA10 Homogeneous Thermal Decomposition of Triethylaluminum: Effect of NH₃, J. Lee, T.J. Anderson, University of Florida

Thermal decomposition pathways of triethylaluminum ((C₂H₅)₃Al, TEAL) were investigated in a custom, up-flow, cold-wall CVD reactor. The extent of homogeneous decomposition of TEAL in N₂ as well as with added NH₃ was measured using *in situ* Raman spectroscopy measurement. The results of Density Functional Theory (DFT) calculations were used to assist in assignment of the observed Raman shifts to the decomposition products TEAL:NH₃, DEAlH, TEAl:NH₃, H₂N-AIH-NH-AIH₂, H₂Al-NH₂, MEAlH, MEAlH-AIH₂ and DEAl-AIH₂ as well as the estimating the rates of selected pathways. For the case of thermal decomposition of TEAL with N₂ carrier gas, the species H₂Al-NH₂ was observed. This is believed to result from the reaction of ammonia with the product of β-hydride elimination. This species is a possible reactant for AlN formation. Raman shifts of 600, 1989, 2025, 2580, 2835, 2849, 2900, 2918, 2939, and 3173 cm⁻¹ were recorded for TEAL in N₂, while shifts of 452, 1462, 1525, 1639, 2580, 2853, 2841, and 2849 cm⁻¹ were observed for a mixture of TEAL with ammonia in N₂. In addition, four vibrational bands (930, 965, 3230, and 3334 cm⁻¹) for ammonia were observed with high intensity. The temperature profile along the reactor centerline was measured and this was compared to the simulated results using a custom-FEM Galerkin method. DFT calculations using B3LYP/LanL2DZ level of theory were carried out to find the optimized geometry of each intermediate and transition structure and to calculate activation energy. This methodology, which uses the results from *in situ* Raman spectroscopy, DFT calculations, and FEM reactor modeling, is a powerful approach to understanding thermal decomposition mechanisms.

5:20pm TF-TuA11 Surface Reactions of TiCl₄ and Al(CH₃)₃ on GaAs(100), B. Granados, A.J. Muscat, University of Arizona

III-V materials have been considered as alternative channel materials for future high-speed low-power digital logic applications mainly because of their higher electron mobility compared to silicon. However, the integration of III-V materials into device structures faces multiple challenges due to the lack of a high quality native oxide and the high density of traps at metal-oxide interface, resulting in Fermi level pinning.

Most of the recent work on GaAs passivation has been done using atomic layer deposition (ALD) method. ALD offers precise control of film thickness, low processing temperatures, and excellent conformality. Additionally, a self-cleaning effect has been reported during Al₂O₃, HfO₂,

and TiO₂ ALD on GaAs leading to the reduction or removal of GaAs oxides. Understanding the surface reactions involved in this self-cleaning effect is important in order to improve the GaAs-oxide interface, while depositing high-k dielectric films using ALD.

In this study, the ALD of trimethylaluminum (TMA, Al(CH₃)₃) and titanium tetrachloride (TiCl₄) on hydrofluoric acid (HF) treated GaAs (100) samples was conducted to investigate the similarities and differences in the surface chemistry of these precursors. After aqueous HF etching and air re-oxidation, the oxides were composed of As₂O₃ and Ga₂O. Annealing the sample desorbed volatile compounds such as As₂O₃ from the surface resulting in an As-rich (2.7:1, As:Ga ratio) surface. The precursors, TiCl₄ and TMA, reacted with As and Ga oxides and completely removing them from the surface. This is the first time that a TiCl₄ self-cleaning effect on GaAs is reported. TMA, as expected, produced a film of Al₂O₃ (2.3 monolayers thick) on top of the GaAs surface when the reaction was performed at 170°C.

In contrast to TMA, the oxygen and titanium levels remained below the XPS detection limits with TiCl₄ exposures in the temperature range from 170°C to 230°C, while a 0.03 monolayer-thick film was deposited at temperatures ranging from 89°C to 170°C. XPS results showed that in the higher temperature range, TiCl₄ reacted with the GaAs oxides on the surface producing only volatile compounds, leading to a clean, sharp GaAs surface. The proposed mechanism consists of two processes: TiO₂ formation on the surface and in-situ etching of these TiO₂ islands by chlorine atoms from breakdown of the precursor. This novel GaAs oxide cleaning method produced an oxygen-free surface, which has potential applications for GaAs integration in microelectronics and optoelectronics devices.

5:40pm **TF-TuA12 Atomic Layer Deposition of Co-Al Films Studied by In-Situ Infrared Spectroscopy**, *J. Kwon, Y.J. Chabal*, University of Texas at Dallas, *J. Anthis, R. Kanjolia*, SAFC Hitech

Cobalt-aluminum alloys are of great interest due to their unique properties such as corrosion resistance, high thermal stability, and unusual magnetic properties. In a search for appropriate precursors, we have investigated the growth of Co-Al thin films by atomic layer deposition (ALD) using CCTBA (μ^2 -h²-(Buacetylene)dicobalthexacarbonyl) and DMAH (Dimethylaluminumhydride) on H-terminated Si(111) and on 2-nm TaN films. In-situ infrared absorbance spectra show that upon the first CCTBA pulse on H/Si(111), alkynes (C≡C triple bonds) bound to Co₂(CO)₆ are converted to a benzene ring, as evidenced by the ring C=C stretching mode at 1475 and 1610 cm⁻¹. This transformation is not completely unexpected because cobalt carbonyl complexes (Co_x(CO)_y) are used to catalyze cyclotrimerization reactions in organotransition-metal chemistry. IR spectra also show that the presence of hydrogen enhances the adsorption of carbonyl groups on the H/Si(111) surface. After the first CCTBA pulse which reacts almost completely with H-Si bonds (2083 cm⁻¹), the amount of adsorbed CO on the surface (1970 cm⁻¹) is found to decrease. The subsequent DMAH pulse is effective to remove the surface carbonyl groups, leaving Al-CH₃ and/or Al-H bonds on the surface. In contrast, the adsorption of carbonyl on a TaN surface where H is absent is negligible after the first CCTBA pulse.

In all cases, CH_x ligands are not removed during CCTBA or DMAH cycles, leading to accumulation of carbon species in the film. The growth of metallic Co-Al films is hindered due to Al-O bond formation during deposition. The source of oxygen is likely associated to a surface Fischer-Tropsch (FT) process. It appears that reaction of cobalt particles with hydrogen (originating from the DMAH precursor) generates water as a by-product through a FT-like process, thus forming Al-O bonds. This formation of Al-O bonds through a FT process is greatly suppressed (~50%) by annealing the sample to 300 °C in N₂ ambient before exposure to DMAH, which removes the carbonyl group from the surface and therefore the source of oxygen. Although the growth pattern is similar for both H/Si(111) and TaN substrates, a part of Ta atoms in the original TaN films are reduced to metallic Ta⁰ during growth, according to XPS Ta 4f core level spectrum after deposition of Co-Al(O_x) films.

Tuesday Afternoon Poster Sessions

Thin Film

Room: Southwest Exhibit Hall - Session TF-TuP

Thin Film Poster Session I

TF-TuP2 Electrical and Optical Properties of Very Thin Ag Films with Surface and Interface Nanolayers. *M. Kawamura, K. Nishida, R. Kiyono, Y. Abe, K. Sasaki*, Kitami Institute of Technology, Japan

We have attempted improvements of thermal stability of Ag thin films which are candidates of electrodes in various electronic devices. Consequently, we have found that an introduction of very thin (about 3 nm thick) Al oxide surface and interface layers was very effective. For example, we confirmed a high thermal stability up to 600 °C even the Ag layer thickness was reduced to 50 nm in Al/Ag/Al films.

In the present work, we have further reduced the thickness of Ag layer in Al/Ag/Al films to obtain high transparency and investigated possibility to apply them as transparent electrodes. As a result, the Ag layer thickness could be reduced to 10 nm in Al/Ag/Al films, keeping a low electrical resistivity. On the other hand, Ag single layers thinner than 14 nm were discontinuous state having a high electrical resistance. Transmittance above 70% was obtained for the Al/Ag(10nm)/Al films. In addition, the property change of the films was found to be very little even after keeping them in air at 60 °C for 300 hrs, or in pure water at room temperature for 200 hrs. Consequently, it is found that the Al/Ag/Al thin films have good properties as transparent conductive electrodes.

TF-TuP3 Synthesis and Characterization of Cubic BC₂N Deposited by Reactive Laser Deposition. *H.A. Castillo*, Universidad Nacional de Colombia Sede Manizales, Colombia, *J.M. Vélez*, Universidad Nacional de Colombia Sede Medellín, Colombia, *W.H. de la Cruz*, Universidad Nacional Autónoma de México

Boron carbide nitride is considered a very important material, used for industrial applications due to their high hardness. Cubic BC₂N films were synthesized in a laser ablation system using a target of B₄C with 99.9% wt. Films were grown on (111) silicon wafers in an ultra high vacuum system with a base pressure in a low 1×10^{-9} Torr range. Target ablation was performed by means of a KrF excimer laser ($\lambda=248$ nm). During the grown process, the substrate temperature was varied in order to identify the influence of this parameter in the structure, composition and morphology of the coating. The composition, bonding configuration was obtained by X-ray photoelectron (XPS) and the mechanical properties hardness and Young's modulus were determined using a Berkovich nanoindenter. Structural analyses with X-ray diffraction exhibited only 111, 200 and 220 lines of the cubic lattice.

TF-TuP4 Comprehensive Comparison of Electrical and Reliability Characteristics for Various Copper Barrier Films. *Y.J. Cheng, C.-T. Jung, J. Wu*, NCNU, Taiwan, Republic of China

The physical, electric and reliability characteristics of various Copper (Cu) barrier layers, including SiC, SiCN, SiCO, SiCNO, and SiN, were investigated. The reliability results associated with film characteristics were also reported in this work. The SiN film still shows the better Cu barrier performance, adhesion strength with Cu, and electromigration (EM) reliability, but its dielectric constant is too high. Nitrogen-doped or oxygen-doped silicon carbide barrier films (SiCN or SiCO) can reduce the dielectric constant, but show a traded-off reliability performance. A newly developed SiCNO film with doping nitrogen and oxygen can meet the better reliability (EM/SM) requirements at the same time, and has a comparable physical and electrical performance to the SiN film.

TF-TuP5 Growth of Silicon-Germanium-Carbon Alloys Using Modified Laser Ablation. *J.G. Quiñones Galván, F. de Moure Flores, A. Hernández Hernández, S. Cerón Gutiérrez, K. Nieto Zepeda, M.A. Meléndez Lira*, CINVESTAV-IPN, Mexico

Laser ablation technique allows depositing thin films with the same stoichiometry of the target material. The common use of solid targets is a limitation when there is a need to produce ternary alloys. In order to overcome that limitation we designed a modification of the laser ablation technique to employ powders as target.¹

The incorporation of carbon in a SiGe alloy is an alternative for achieving larger band gap and strain compensation. The main problem to control substitutional carbon concentration in SiGeC is the low solubility coefficient of carbon in silicon. Laser ablation technique allows exploring

deposition parameters far from the equilibrium that could improve the content of substitutional carbon.

In this work we present the growth and characterization of thin films of Si_{1-x-y}Ge_xC_y alloys in the compositions range $0.27 \leq x \leq 0.29$ and $0.01 \leq y \leq 0.03$ deposited at different temperatures using the Modified Laser Ablation technique.

The samples were characterized by scanning electron microscopy, atomic force microscopy, X ray diffraction, energy dispersive X-ray spectroscopy, Raman, photoluminescence and photoreflectance spectroscopies. Results indicate the modification of the electronic properties of the alloys depending on the carbon content.

¹ M. González-Alcudia, A. Márquez-Herrera, M. Zapata-Torres, M. Meléndez-Lira and O. Calzadilla-Amaya, Adv. in Tech. of Mat. And Mat. Proc. J. 9, 81 (2007).

TF-TuP6 Interface and Properties of ALD Ta₂O₅ Films on Si (100) and GaAs (100) Surfaces. *T. Gougousi, J.W. Lacin*, UMBC

Tantalum pentoxide (Ta₂O₅) films have been deposited using an Atomic Layer Deposition (ALD) process based on the reaction of pentakis dimethyl amido tantalum (PDMAT) and H₂O at 250°C. Films were deposited on native oxide Si(100) surfaces and native oxide and etched GaAs(100) surfaces. Linear growth at ~0.6 Å/cycle has been confirmed using spectroscopic ellipsometry. Atomic Force Microscopy indicates that the films are smooth and x-ray diffraction data indicate that the as-deposited films are amorphous, and begin to crystallize after anneals at 800°C (3 min, Ar). These observations are mirrored in the infrared spectra. Film composition has been studied using x-ray photoelectron spectroscopy (XPS) and it has been found that the films are slightly over oxidized. The interface of films deposited on native oxide and etched GaAs surfaces has also been studied using XPS and high resolution transmission electron microscopy. Data from both techniques indicate that an interface cleaning mechanism similar to that observed for other amide based ALD processes may be present.

TF-TuP7 The Mechanical Properties and Thermal Stability of CrZrSiN/AlN Multilayer Coatings Synthesized by Closed Field Unbalanced Magnetron Sputtering. *S. Lee*, Korea Aerospace University, Republic of Korea

In this work, for the high temperature applications, CrZrSiN/AlN multilayer coatings with various bilayer thicknesses (Λ) were synthesized using a closed-field unbalanced magnetron sputtering (CFUBMS) and their chemical composition, crystalline structure, morphology, mechanical properties, and thermal stability were characterized by glow discharge optical emission spectroscopy (GDOES), X-ray photoelectron spectroscopy (XPS), X-ray diffraction (XRD), scanning electron microscopy (SEM), atomic force microscopy (AFM), and nanoindentation. Also, the thermal stability of the CrZrSiN/AlN multilayer coatings was evaluated and compared with that of the CrZrSiN coatings by annealing the thin films at temperatures between 500 °C and 1200 °C for 30 min in air and under vacuum. The experimental results revealed that the hardness of the CrZrSiN/AlN coating was much superior to that of the CrZrSiN coating after annealing at various temperatures due to the presence of alternating AlN thin films. Furthermore, in the CrZrSiN/AlN coating with the bilayer thicknesses of 2.4 nm, the relatively high hardness of 28.3 GPa was maintained even after annealed at 1100 °C. The detailed experimental results will be presented.

TF-TuP8 First Reset Resistance Switching Characteristics with the Crystallinity of Ta₂O₅ Films. *H.-C. Sohn, H.D. Na, K.-M. Lee, J.G. Kim, S.-H. Lee*, Yonsei University, Republic of Korea

In this work, we investigated the effect of the crystallinity on the first reset resistance switching characteristics of Ta₂O₅ films. Ta₂O₅ films annealed by Rapid Temperature Process (RTP) at above 650 °C were changed from amorphous to poly-crystal structure. The post-annealing temperature of above 650 °C produced the resistance switching behavior of first reset process, indicating the disappearance of forming process due to high current level. For identifying the formation of local conductive path, the ratio of High Resistance States (HRS) and Low Resistance States (LRS) in 200 x 200 μm^2 pattern of Ta₂O₅ was measured with the regular interval of 25 points at read voltage of 0.2 V. The crystallinity of Ta₂O₅ films with the annealing temperature was measured by X-Ray Diffraction (XRD) and Transmission Electron Microscopy (TEM). TEM and Fast Fourier Transform (FFT) images showed the nano-crystal structure in local region of Ta₂O₅ film annealed at 650 °C. We expected that the local crystal structure in Ta₂O₅ films formed by RTP is expected to be closely related to the local conductive path.

TF-TuP9 Preparation and Characterization of Ta-doped Indium Tin Oxide Films Deposited by DC Magnetron Sputtering, S.M. Chung, J.H. Shin, W.-S. Cheong, C.-S. Hwang, S.H. Park, K.I. Cho, ETRI, Republic of Korea

Transparent conductive oxide (TCO) films have been widely used as transparent electrodes for various applications such as smart windows, flat panel display (FPD), touch panel, light-emitting diodes, optical wave guides, and solar cells. It is well known that the TCO films require the properties of wide band gap (>3.0eV), high conductivity, and high transmittance (>80%) in the visible range. Current applications of the TCO films emphasize minimizing resistivity. Among the technologies available for producing ITO films, DC magnetron sputtering can produce high quality films and be adapted to large-area coatings. In general, the characteristics of indium tin oxide (ITO) depend on its oxidation state and the content of impurities. The carrier concentration may also be modified by the dopant activation state because a donor atom can substitute the lattice site producing more than one free electron to increase conductivity. Ta also can be a donor because the indium is replaced by Ta in the In_2O_3 -matrix ITO film, which releases one free electron contributing the electrical conductivity.

In this work, ITO and ITO:Ta films were deposited on corning glass substrates by DC magnetron sputtering using ITO and Ta-doped ITO targets, respectively, at room temperature. Effects of Ta dopant on the structural and opto-electrical properties of the ITO films were investigated. The detailed results will be revealed in this presentation.

TF-TuP10 Deposition of Ga-doped ZnO Films by Atomic Layer Deposition Using Ozone as the Oxygen Source, H. Yuan, B. Luo, S.A. Campbell, W.L. Gladfelter, University of Minnesota

Gallium-doped ZnO (GZO) films were grown on Si and SiO_2/Si substrates at 250°C by atomic layer deposition using diethylzinc as zinc precursor and ozone as the oxygen source. Trimethylgallium were used as the dopant precursor, and two approaches to doping were studied. In one a nanolaminate was formed by interspersing a trimethylgallium/ozone cycle in between the diethylzinc/ozone cycles. The overall gallium concentration depended on the number of diethylzinc/ozone cycles. The second approach involved co-injection of both metal precursors in which their relative concentrations were controlled by adjusting the precursor vessel temperature. The influence of the deposition method on the composition, structural, electrical, and optical properties of the GZO thin films as a function of doping metal concentration will be reported. X-ray diffraction patterns showed all the samples were polycrystalline and exhibited (0001) preferential orientation. The carbon content of the films was below the detection limit of Auger electron spectrometry. The lowest resistivity ($4.7 \times 10^{-4} \Omega \cdot \text{cm}$) of the as-deposited films was obtained through use of the co-injection process. The average optical transmission was over 85 % in the range of 400-800 nm and the optical band gap increased with increasing doping in accordance with the Burstein-Moss effect. The effect of rapid thermal annealing will be presented.

TF-TuP11 Fabrication and Structural Analysis of W-Ti-O Thin Films, N.R. Kalidindi, S.K. Gullapalli, R.S. Vemuri, F.S. Manciu, K.B. Karuppanan, C.V. Ramana, University of Texas at El Paso

Semiconductor oxide based chemical sensors are widely used for detecting very small amounts of toxic gases. Tungsten (W) oxide thin films have been used for measuring small amounts of H_2S gas. The present work was performed on tungsten-titanium mixed oxide (W-Ti-O) thin films for application in H_2S sensors. W-Ti-O were deposited by r.f. magnetron sputtering from a W-Ti alloy target with 5 % (wt %) Ti. W-Ti-O films were grown at different substrate temperatures ranging from 30 to 500°C. All the films were grown with argon/oxygen ratio of 1:9. Structural characterization was performed using X-ray diffraction (XRD) and scanning electron microscopy (SEM) measurements. The results indicate that the W-Ti-O films grown up to the substrate temperature of 200°C were amorphous while films grown at 300-500 °C were crystalline. The peak broadening was found to increase with increase in substrate temperature from 300°C to 500°C due to the increase in disorder with the inclusion of Ti. XRD and SEM results confirm significant disordering at the Si-film interface at higher processing temperatures. Based on the results, which will be presented and discussed, the effect of substrate temperature on the microstructure of W-Ti-O films is established.

TF-TuP12 O K and Si (Ge) $L_{2,3}$ ($M_{2,3}$) Spectra of Non-Crystalline Plasma-Deposited Thin Film nc-SiO₂ and nc-GeO₂, D.J. Zeller, K. Wu, G. Lucovsky, North Carolina State University

Four-fold coordinated Si-atoms in nc-SiO₂ are bonded to two-fold coordinated O-atoms in a bent 3-atom group with Si 3d-associated T_{2g} symmetries on the Si-atoms [1]. These constrain the dihedral angles binding O-atoms, and contribute to medium range order (MRO) with

correlation a length of ~0.4 to 0.45 nm, and a coherence length of ~1 nm, each obtained from analysis of the first sharp diffraction peak in X-ray/electron diffraction [2]. Similar considerations apply to nc-GeO₂. Analysis of O K edge spectra for nc-SiO₂ reveals conduction band states with 3s-state symmetries at the band edge, and stronger 3d-state symmetries at higher energy. The s-state features define the respective band gaps of ~9 eV for nc-SiO₂, and ~6 eV for nc-GeO₂. In nc-SiO₂, the energy difference between band edge non-degenerate A_1 features, and the triply degenerate T_2 and doubly degenerate E d-state features is ~3 eV, whereas in c-Si it is smaller, ~1 eV. The relative energies of these features are the same as band edge features obtained from transmission and reflectivity studies in the visible and VUV where this d-state character was not previously recognized [3]. This correspondence derives from O 1s core hole localization, and a coherent process whereby these core states are filled by electrons from valence band O 2p p states. Additionally, there is a one-to-one correspondence between Si A_1 features and the Si T_{2g} features in the O K edge and the Si $L_{2,3}$ spectra of SiO₂. Studies of $L_{2,3}$ transitions by electron energy loss spectroscopy (EELS) did not detect the Si 3s features in the 100 to 104 eV regime of nc-SiO₂, or in the 98 to 100 eV regime of c-Si. Analysis of O K and $L_{2,3}$ spectra are based on the charge transfer multiplet (CTM) formalism [4]. The ground state is $\text{Si}2p^63d^1\bar{L} + \text{Si}2p^63s^0\bar{L}$, where \bar{L} describes a coherent process in which Si 1s core level holes are neutralized by electrons from the O 2p states. Ground states have 1A symmetries, excited states are $\text{Si}2p^53d^1\bar{L} + \text{Si}2p^53s^1\bar{L}$ with 1F and 1P symmetries, respectively. Degeneracies are lifted by different J values associated with the orbital angular momentum. Similar spectral features are observed for nc-plasma-deposited GeO₂, and these films exhibit the same correspondence between Ge 4s- and 4p-derived features in the O K edge and the Ge $M_{2,3}$ edge.

[1] Whitten J, et al., J. Vac. Sci. Technol. B 20, 1710 (2002).

[2] Lucovsky G, et al. physica status solidi (a) 207, 631 (2010).

[3] Laughlin RB, Phys. Rev. B 22, 3021 (1980).

[4] de Grott F, Kotani A. Core level spectroscopy of solids (Boca Raton, CRC Press, 2008).

TF-TuP13 High Temperature Oxidation Performance of Multilayered Al_xTi_{1-x}N/CrN Coatings, Y.Y. Chang, W.H. Wu, Mingdao University, Taiwan, Republic of China

The high temperature oxidation behavior of Al_xTi_{1-x}N and multilayered Al_xTi_{1-x}N/CrN coatings was studied. These coatings were synthesized by cathodic-arc evaporation with plasma enhanced duct equipment. Chromium and AlTi alloy (70/30 at. % ratio) cathodes were used for the deposition of Al_xTi_{1-x}N/CrN coatings. During the coating process of multilayered Al_xTi_{1-x}N/CrN, CrN was deposited as an interlayer. The multilayered structure was obtained by regulation of cathode power at a constant rotation speed of sample holders. The nanolayer thickness and alloy content of the deposited multilayered coating were correlated with the emission rate of alloy cathode materials. In this study, field emission scanning electron microscope (FESEM), and X-ray diffraction using glancing angle parallel beam geometries were used to characterize the microstructure of the deposited films. High resolution transmission electron microscope (HRTEM) was used for nanolayered structure analyses of the multilayered Al_xTi_{1-x}N/CrN coatings. For the high temperature oxidation test, the coated samples were annealed in the temperature range 700~1000 °C in air for 2 hours. After oxidation, the deposited Al_xTi_{1-x}N had completely transformed to TiO₂ and Al₂O₃ at 900 °C. Interestingly, the multilayered Al_xTi_{1-x}N/CrN possessed superior oxidation resistance than the graded Al_xTi_{1-x}N. The different oxidation mechanisms of Al_xTi_{1-x}N and multilayered Al_xTi_{1-x}N/CrN at high temperature are developed in this study.

TF-TuP14 Formation of Ti-Doped DLC Films by Inert-gas Ion Beam Assistance in a C₁₀H₈ Atmosphere, S. Narita, I. Takano, Kogakuin University, Japan

Diamond-like carbon (DLC) has the amorphous structure that is chiefly composed by graphite (sp^2) and disordered graphite (sp^3) state. Therefore mechanical properties of DLC generally show high hardness and low friction. DLC film has been prepared by various method of chemical vapor deposition (CVD) or physical vapor deposition (PVD) including the sputtering method. Commercial applications of DLC have been already performed as engine parts of an automobile or surface coating of a hard disk.

In this study, Ti-doped DLC films were formed using He⁺ or Ar⁺ ion beam assistance in a naphthalene (C₁₀H₈) atmosphere. The formation conditions of DLC film were changed with ion-beam accelerating voltage and current density. Ti doping was performed by using the electron-beam deposition method with Ti evaporation rate from 0.0 to 0.2 nm/sec. The mechanical properties of hardness and friction coefficient were determined using the dynamic micro knoop hardness tester and the ball-on-disk tribotester respectively. Atomic concentration and structure of the films were

investigated by X-ray photoelectron spectroscopy, X-ray diffraction and Raman spectroscopy.

The suitable mechanical property of DLC films was obtained by the condition with accelerating voltage of 5 kV at current density of 10 $\mu\text{A}/\text{cm}^2$. The maximum hardness was 5.37 GPa using Ar^+ ion beam, while the minimum friction coefficient was 0.117 using He^+ ion beam. It was clear that properties of DLC film was changed by ion species. In the case of Ar^+ ion beam, the higher hardness film contained much sp^3 state, while the film with lower friction coefficient contained much sp^2 state. From the other side the higher hardness film has a large crystal grain size as compared with the film with lower friction coefficient.

TF-TuP15 On the Optics of Thin Films Applied in Aerospace Telescope. *C.N. Hsiao, H.P. Chen, P.K. Chiu, Y.W. Lin, W.H. Cho, F.Z. Chen*, National Applied Research Laboratories, Taiwan, *D.P. Tsai*, National Taiwan University

Optical thin films designed for space grade multi-spectral assembly in CMOS sensor and reflective Ag mirror were deposited on radiation-resistant glass by ion-beam-assisted deposition for a Cassegrain-type aerospace telescope. The patterned multi-spectral assembly contained the blue, green, red, near infrared, and panchromatic multi layers high/low alternated dielectric band-pass filters arrays in a single chip which was fabricated by photolithography process. The corresponding properties of the films were investigated by in-situ optical monitoring, ellipsometry, spectrometry, and high-resolution transmission electron microscopy. It was found that the average transmittances are above 88% for the multi-spectral assembly, with a rejection transmittance below 1% in the spectral range of 350~1100 nm. The average reflectance of the Ag mirror (with a protective interference coating) is boosted above 99% in visible spectrum. The polarization sensitivity of the optical payload is below 5%. Furthermore, to estimate the optical stability of optical thin films for aerospace applications, a space environment that the satellite orbiting above the earth surface at an altitude near 900 kilometers were simulated by Co^{60} gamma (γ) radiation test (total dose effects) and thermal vacuum test (pressure below 10^{-7} Torr with thermal cycles). The optical stability of the films with the environmental test will be discussed.

TF-TuP16 Modification of Band Gap Structure of Cu-implanted TiO_2 Catalytic Thin Films by using Metal Plasma Ion Implantation Technique. *D.Y. Wang*, Mingdao University, Taiwan, *C.C. Yen, L.S. Chang*, National Chung Hsing University, Taiwan, *M.H. Shih*, Mingdao University, Taiwan, *H.C. Shih*, National Chung Hsing University, Taiwan

The anstaes TiO_2 thin film has long been identified as the potential photocatalytic materials for various industrial applications. The Cu-implanted TiO_2 catalytic films were prepared by the sol-gel process in conjunction with the metal plasma ion implantation (MPII) technique at an acceleration voltage of 20 keV with various ion dosages. The surface chemical states and compositions of Cu-implanted TiO_2 films were investigated by XPS. The optical band gap of the films was calculated by using Tauc formula. The photocatalytic activity was evaluated by the photodegradation of methylene blue (MB) under visible light irradiation. The correlation between the band gap structure and the photocatalytic behaviors of Cu-implanted TiO_2 were investigated. The electronic band structure and the location of Cu atom in anatase TiO_2 were studied by the first-principle calculations based on the density functional theory. The result demonstrated the dependence of the band gap structure on Cu dosage, which induced the formation of impurity energy levels in the band gap.

Keywords: TiO_2 , band structure, photocatalysis, MPII.

TF-TuP17 Nanofabrication of Insulated Scanning Probe Microscopy for Electromechanical Imaging in Liquid Solutions. *J.H. Noh*, University of Tennessee, *M. Nikiforov, S.V. Kalinin*, Oak Ridge National Laboratory, *A.A. Vertegel*, Clemson University, *P.D. Rack*, University of Tennessee at Knoxville; Oak Ridge National Laboratory

The fabrication and electrical and electromechanical characterization of insulated scanning probes have been demonstrated in liquid solutions. The silicon cantilevers were sequentially coated with chromium and silicon dioxide, and the silicon dioxide was selectively etched at tip apex using focused electron beam induced etching (FEBIE) with XeF_2 . The chromium layer acted not only as the conductive path from the tip, but also as an etch resistant layer. The relevant nanofabrication issues relative to the metallization and the insulator deposition process have been discussed. This insulated scanning probe fabrication process is compatible with any commercial AFM tip and can be used to easily tailor the scanning probe tip properties because FEBIE does not require lithography. The suitability of the fabricated probes is demonstrated and discussed by imaging of standard grid as well as piezoresponse force microscopy (PFM) and electrical measurements.

TF-TuP18 The Observation of Strain-Induced InN Nanorods Hetero-Epitaxially Grown by MOMBE. *F.-I. Lai, W.-T. Lin*, Yuan-Ze University, Taiwan, *W.-C. Chen, C.N. Hsiao*, National Applied Research Laboratories, Taiwan, *S.-Y. Kuo*, Chang Gung University, Taiwan, *H.C. Hsu*, National Cheng Kung University, Taiwan

In this study, we discussed the evolution of morphology and crystal structure of wurtzite indium nitride (InN) hetero-epitaxially grown on GaN/sapphire(0001) by metal-organic molecular beam epitaxy (MOMBE) system with growth temperature. In order to investigate the influences of growth temperature, the stoichiometry of In/N was identical ~1:1 during the InN growth. The optical and structural properties of InN films samples were characterized by temperature-dependence photoluminescence (PL), field-emission scanning electron microscopy (FE-SEM) and x-ray diffraction (XRD). With increasing growth temperature, the surface morphology of InN varied from 1-dimensional (1D) nanorods to 2-dimensional-films. XRD results reveal that the strain of InN were released while increasing growth temperature. The PL emission peaks of InN nanorods and films were about 0.77 eV and 0.83 eV, respectively. In addition, it is noteworthy that the interface between GaN and InN nanorods exist massif-like structure as growth at lower temperature. These observation implied that the formation of 1D InN nanorods was ascribed to the strain-induced mechanism and will be discussed in detail.

TF-TuP19 Protecting Polymers from the Natural Space Environment with Films Grown Using Atomic Layer Deposition. *M. Groner*, ALD NanoSolutions, Inc., *A.I. Abdulagatov, R. Fitzpatrick, S.M. George*, University of Colorado, *B. Wu, T. Minton*, Montana State University

Polymers used on spacecraft are subjected to various threats including hyperthermal oxygen atoms, UV and VUV photons, and ions. These threats can degrade the polymer and lead to static charge accumulation. Nanometer thick inorganic films grown by atomic layer deposition (ALD) can protect polymers including Kapton, Teflon, and PMMA. We are developing multifunctional multilayer ALD films incorporating Al_2O_3 layers for preventing oxygen atom erosion, TiO_2 to minimize UV/VUV radiation damage, and ZnO to dissipate static charge. Such ALD-coated polymeric films are currently being tested in low Earth orbit on the International Space Station on MISSE-7b. In the laboratory, we are further exploring the mechanisms of polymer degradation by atomic oxygen and VUV radiation, as well as the cracking of inorganic films on polymers resulting from different thermal expansion coefficients. Field emission scanning electron microscopy images and profilometry measurements revealed that Kapton H samples coated with 25 ALD cycles (~3 nm) of Al_2O_3 completely resisted atomic oxygen erosion. Quartz crystal microbalance measurements of TiO_2 films deposited on PMMA substrates with an Al_2O_3 interfacial adhesion layer showed that 100 cycles (~6.2 nm) of TiO_2 resisted PMMA degradation upon VUV exposure. Mass losses of VUV-exposed PMMA samples coated with similar overall bilayer thicknesses but different Al_2O_3 thicknesses were compared to decouple the role of the overall $\text{Al}_2\text{O}_3/\text{TiO}_2$ bilayer coating acting as a physical barrier from the role of TiO_2 acting as a VUV filter.

TF-TuP20 Effects of Pulse Frequency on the Structural, Electrical and Optical Properties of Al-doped ZnO Films by Pulsed dc Magnetron Sputtering. *C.T. Lee, B.H. Liou, W.H. Cho, C.N. Hsiao*, National Applied Research Laboratories, Taiwan, Republic of China, *K.S. Tang, C.C. Jaing*, Minghsin University of Science and Technology, Taiwan, Republic of China

The ZnO:Al (AZO) thin film was prepared on si and glass substrates at 200 °C by pulsed dc magnetron sputtering deposition. Effects of pulse frequency on the structural, electrical and optical properties of AZO films were investigated by field emission scanning electron microscopy, X-ray diffraction, Hall measurement and spectrometer. The columnar structures are observed by field emission scanning electron microscopy. X-ray diffraction analysis reveals that AZO films were polycrystalline and have preferred orientation along (002). The grain size and resistivity of AZO films were investigated as a function of pulse frequency (5-100 kHz). The maximum grain size and minimum sheet resistivity of AZO film with 20 kHz were 37.5 nm and 650 ohm/sqr, respectively. The average transmittance of AZO thin films was above 80% in the visible range. The presented results illustrate that the optimum properties of AZO films can be obtained at a pulsing frequency in the range of 5-100 kHz.

TF-TuP21 Fabrication of Cu-DLC Films by Cathodic arc Plasma Deposition. *J. Yun*, National Chung Hsing University, Taiwan, *S. Han*, National Taichung Institute of Technology, Taiwan

Copper-doped diamond-like carbon (Cu-DLC) films with varying Cu concentrations were deposited on 7050 aluminum alloy substrates using cathodic vacuum arc (CVA) system. Acetylene reactive gases were also activated at a pressure of 20 mTorr to 30 mTorr and a temperature fixed at 180 °C to provide the DLC. Structure, interface, and chemical bonding state

of the investigated film were analyzed by transmission electron microscope (TEM), FTIR spectra, and X-ray photoelectron spectroscopy (XPS). The Cu-DLC film deposited exhibited an amorphous structure, while different fracture feature and surface morphologies was observed in these carbon films prepared under various acetylene reactive gases pressure. With increasing acetylene reactive gases pressure, the friction coefficient of the thin films is lower than 0.21 and the residual stress between the DLC thin films and aluminum alloy substrates can be substantially decreased after the effective doping of Cu into the films, which implies that the Cu-DLC films are suitable to be used as a protective coating on aluminum alloys.

Wednesday Morning, October 20, 2010

Energy Frontiers Topical Conference

Room: Pecos - Session EN+TF-WeM

CIGS, CZTS and Chalcopyrite Films & Solar Cells

Moderator: E.S. Aydil, University of Minnesota

8:00am EN+TF-WeM1 **CIGS and CZTS Nanocrystal-Ink Solar Cells**,
H.W. Hillhouse, R. Agrawal, Q. Guo, G.M. Ford, Purdue University
INVITED

The development of suitable colloidal nanocrystal inks are a key step in the development of low-cost solar cells since they enable the use of fast and inexpensive coating processes such as spray coating and roll coating to form a thin film photoabsorbing layer. Chalcopyrite structure copper indium gallium diselenide (CIGSe) and stannite or kesterite copper zinc tin sulfides (CZTS) are key photoabsorbing materials for thin film solar cells due to their near ideal band gap and their serendipitous defect chemistry (CIGSe) and Earth abundance (CZTS). Although several methods have been reported that describe the synthesis of CIGSe and related nanocrystals, precise control of the composition for these ternary and quaternary compounds has been problematic [1]. We have reported the solution-phase synthesis of stoichiometric chalcopyrite structured CuInSe₂ nanocrystals [2], Cu(In,Ga)S₂ [3], and the very first synthesis of Cu₂ZnSnS₄ nanocrystals [4]. The syntheses proceed rapidly from elemental and halide reagents via a simple batch reaction without "hot injection" in a single component coordinating solvent. We have demonstrated the use of these nanocrystals for low-cost solar cells by fabricating devices without using any oxygen-free techniques (after NC synthesis) and employing a scalable roll coating method. The nanocrystal inks are first coated on a back contact (Mo coated sodalime glass in this case). The nanocrystal layer is then easily consolidated into large crystalline domains by a brief thermal treatment in a selenium rich atmosphere to prevent selenium loss or to replace sulfur with selenium. The fabricated cells are robust and increase in efficiency with time, exhibiting similar serendipitous defect chemistry as layers formed by vacuum co-evaporation. We have fabricated solar cells by roll coating CIGS or CZTS nanocrystal-inks over large areas. CIGS devices fabricated by roll coating over large areas with a device architecture of Mo/CIGS/CdS/i-ZnO/TiO₂/Ni/Al are (at the time of the abstract submission) 12.0% efficient under standard AM1.5G illumination. The presentation will focus on the key aspects of the nanocrystal synthesis, ink coating, nanocrystal consolidation, and device fabrication and characterization for both CIGS and CZTS solar cells.

[1] Hillhouse H.W. & Beard M.C., Current Opinion in Colloid & Interface Science, 14, 245 (2009).

[2] Guo, Q.J., Kim, S.J., Kar, M., Shafarman, W.N., Birkmire, R.W., Stach, E.A., Agrawal, R., Hillhouse, H.W., Nano Letters 8, 9, 2982 (2008).

[3] Guo, Q.J., Ford, G.M., Hillhouse, H.W., Agrawal, R., Nano Lett. 9, 8 3060 (2009).

[4] Guo, Q.J., Hillhouse, H.W., Agrawal, R., J. Am. Chem. Soc. 131, 11672 (2009).

8:40am EN+TF-WeM3 **Compositional (non)Uniformity and its Effect on CIGS Solar Cell Performance**, W. Li, S.R. Cohen, K. Gartsman, P. von Huth, R. Popovich-Biro, Weizmann Institute of Science, Israel, Th. Rissom, Helmholtz Zentrum Berlin, Germany, D. Cahen, Weizmann Institute of Science, Israel

CIGS is a promising material for solar cell applications. Uniformity of the polycrystalline composition and structure is an important factor in the solar cell performance. This work is an attempt to study CIGS (non)uniformity systematically as a function of depth, employing independent, complementary high resolution techniques which also reveal inter- and intra-grain compositional, structural, and electronic nonuniformities. In particular, thin cross-sections, prepared by field ion beam (FIB), were studied using TEM-based techniques to achieve higher spatial resolution of the composition than is normally possible. It was found that the Ga/In ratio in the devices drops initially with depth, then rises sharply again near the Mo contact. Furthermore, large variations of this ratio are observed from grain to grain. This variation is even observed within individual single crystal grains along their growth direction. Our measurements confirm the formation of a MoSe₂ phase at the Mo - CIGS interface. The lattice constant, measured by selected area diffraction (SAD), varies with the Ga composition, in agreement with Vegard's law. The extent of compositional variation was found to vary inversely with the temperature of sample preparation. Additionally, our measurements confirm the formation of a MoSe₂ phase at the Mo - CIGS interface.

A series of scanning probe (SPM)-based techniques, including scanning capacitance microscopy (SCM) and conducting probe atomic force microscopy (CP-AFM) were applied to correlate local device performance and doping concentration with the compositional (non)uniformity revealed in these TEM results and will be presented here.

This compositional non-uniformity may well be of relevance for the properties and performance of solar cells made with such films, and this issue will be addressed in the talk.

9:00am EN+TF-WeM4 **Combinatorial Cd_{1-x}Zn_xS Thin Films Deposited with a Continuous Flow Microreactor**, K.M. McPeak, Drexel University, H.P. Bui, T.P. Beebe, University of Delaware, J.B. Baxter, Drexel University

Chemical bath deposited CdS thin films are commonly used as buffer layers in CdTe and CIGS photovoltaics because they form a high quality *p-n* junction with the absorber. However, light absorption by the CdS reduces solar cell efficiency. Cd_{1-x}Zn_xS has a wider band gap than CdS, offering the potential to reduce deleterious absorption of light in the 300-550 nm range and improve current densities by over 2 mA/cm². To maximize energy conversion efficiency, the Cd_{1-x}Zn_xS should be a single-phase ternary alloy and the stoichiometry should be optimized to ideally position the conduction band edge for increased transmissivity while retaining good junction properties.

We report on chemical bath deposition of combinatorial Cd_{1-x}Zn_xS thin films using a continuous flow microreactor. The microreactor uses a sub-millimeter reaction channel, with the substrate acting as one reactor wall. The microreactor behaves like a plug flow reactor whereby the bath composition changes as flowing material is deposited on the substrate. While the bath composition changes with respect to position down the reaction channel, the composition at any position is time-invariant. The graded bath composition results in deposition of graded thin films whose stoichiometry and optoelectronic properties change significantly over length scales of millimeters to centimeters. Spatially resolved characterization of the substrate enables rapid and direct correlation of material properties to growth conditions, which is not possible with a batch reactor where bath composition changes with time.

Graded Cd_{1-x}Zn_xS films grown with 1:200 Cd:Zn bath composition at the inlet had composition that varied from x=0.0 to x=0.17 over a distance of 12 mm on a single substrate. Film stoichiometry was determined by x-ray photoelectron spectroscopy (XPS) mapping. Stoichiometry changes because of differences in speciation and reaction kinetics of the cation species as they flow down the channel. XPS and XRD confirm that CdZnS is a single phase material. Deep level emission in photoluminescence and XPS indicate that O and OH is also incorporated into the film and is bound to Zn, with amount increasing further down the reaction channel. The graded stoichiometry causes the absorption edge to blue-shift by over 80 nm, as determined by UV-vis transmission and reflectance measurements. Blue-shifting band edge and changes in defect density are also seen by photoluminescence. The continuous flow microreactor offers new potential for deposition of graded thin films that act as combinatorial libraries for high throughput screening and accelerated materials discovery.

9:20am EN+TF-WeM5 **A Chemical Bath Process for Depositing Cu₂ZnSnS₄ Photovoltaic Absorbers**, A. Wangperawong, J.S. King, S.M. Herron, B.P. Tran, K. Pangan-Okimoto, S.F. Bent, Stanford University

Inorganic thin film photovoltaics are an attractive technology for achieving large-scale deployment of inexpensive, stable, and efficient solar cells. However, current leading thin-film materials, such as CdTe and CIGS, face production limitations at a global scale as they contain both non-abundant and toxic elements. A material that has gained significant attention is Cu₂ZnSnS₄ (CZTS), which is not constrained by the drawbacks of CdTe and CIGS and has an ideal bandgap for a single junction photovoltaic device of 1.4-1.5 eV. Several groups have studied the fabrication of CZTS solar cells using a variety of methods ranging from sol-gel processing to sputter deposition, with a record efficiency of 9.6% recently reported. In the present work, we report an alternative water-based method for large area deposition of CZTS thin films that does not require expensive or complex equipment. Specifically, thin films of CZTS were fabricated on silicon, glass and molybdenum-coated substrates through a combination of chemical bath deposition, ion exchange and sulfurization heat treatment. The film composition could be controlled through a combination of number and length of chemical bath steps and ion exchange time. The resulting samples were analyzed by scanning electron microscopy (SEM), Auger electron spectroscopy (AES), X-ray diffraction (XRD), Raman spectroscopy, inductively-coupled plasma optical emission spectroscopy (ICP-OES), and diffuse reflectance absorption spectroscopy. XRD, Raman,

and UV-Vis optical spectra are consistent with the formation of CZTS. The results show that the process produces thin films of CZTS exhibiting uniform composition, well-defined crystal structure, and good optical properties with a bandgap of 1.45 eV. Complete solar cell devices made with chemical bath-deposited CZTS were fabricated. Measurements on these devices exhibit photovoltaic and rectifying behavior, and the results will be discussed.

9:40am **EN+TF-WeM6 Synthesis Routes for $\text{CuIn}_{1-x}\text{Ga}_x\text{Se}_2$ Thin Film Absorbers**, *R. Krishnan, T.B. Song, V.U. Chaudhari*, University of Florida, *E.A. Payzant*, Oak Ridge National Laboratory, *R. Noufi*, National Renewable Energy Laboratory, *T.J. Anderson*, University of Florida

Chalcopyrite $\text{Cu}(\text{In,Ga})\text{Se}_2$ is one of the most promising absorber materials for high efficiency thin film solar cells with reported conversion efficiency exceeding 20%. The National Solar Technology Roadmap for CIGS PV specifically calls for deposition rates of “30–40 $\mu\text{m}/\text{h}$ and <1 μm CIGS absorber thickness” by 2015. This is compared to the current estimate in the Roadmap of “5 $\mu\text{m}/\text{h}$ and 1.25–3 μm CIGS absorber thickness.” The comparison translates into a reduction of the absorber synthesis time from ~15 to 36 min to ~1.5 to 2 min. The challenge is to get high throughput and yield with columnar grain growth while retaining the high efficiency. In this work *in-situ* high temperature X-ray diffraction with and without selenium overpressure is used to determine absorber synthesis mechanisms for various precursors structures. Qualitative analysis of the data gives information on the reaction pathway and quantitative analysis of the data yields rate constants.

This presentation summarizes studies on the selenization of elemental stacked layers of copper, indium, gallium and selenium in two different configurations. In the first configuration (sample A), copper was first deposited on glass/Mo substrates, followed by gallium, indium and selenium. In the other configuration (sample B), gallium was first deposited followed by indium, copper and selenium. ICP results showed that both the samples were copper poor. Reaction pathways were followed with and without selenium overpressure and isothermal soaking experiments were performed to obtain the kinetic parameters using the Avrami growth model to reduce the data. The reaction pathways were similar for both the configurations, showing formation In, Cu_9Ga_4 , and Cu_2Se initially, followed by Se crystallization and formation of the intermediates In_3Se_3 , CuSe_2 , CuSe and CIS, and finally yielding product $\text{CuIn}_{1-x}\text{Ga}_x\text{Se}_2$. The value of x computed from Vegard's law yielded 0.35 for sample A and 0.37 for sample B. The activation energy computed from the Avrami model yielded 88.4(\pm 12) and 125.1(\pm 9) kJ/mole for samples A and B, respectively. The decrease in the local Avrami exponents (0.21–0.26) suggests the existence of an inhomogeneous distribution of nuclei during growth or interdiffusion of gallium and indium with simultaneous grain growth. Additional characterization such as SEM and TEM were performed to provide physical and compositional support of the pathway.

10:40am **EN+TF-WeM9 Atmospheric Processing Approaches to Low Cost Scalable Photovoltaics**, *M.F.A.M van Hest, A. Miedaner, C.J. Curtis, J. Leisch, P. Hersh*, National Renewable Energy Laboratory, *K. Steirer, R.M. Pasquarelli, J.A. Nekuda, R.P. O'Hayre*, Colorado School of Mines, **D.S. Ginley**, National Renewable Energy Laboratory **INVITED**

Solar photovoltaics are becoming an increasing part of the energy supply mix, however to have a really significant impact they must become cost competitive with more conventional energy sources. Direct write ink based methods could help toward this significant cost reduction. We are investigating solution precursors and ink based atmospheric deposition approaches to a variety of solar cell materials and processes. The first application we are studying is inkjet printing of contacts for photovoltaics in particular for Si solar cells. We have developed metal organic decomposition inks for silver, nickel, copper and aluminum for example. Conductivities close to that of bulk metals were obtained. The second application is the formation of the absorber layer in CuInSe_2 (CIS) based photovoltaics. CIS/CIGS is the most efficient thin film photovoltaic technology, but typically employ capital-intensive PVD materials deposition and subsequent selenization steps. Our approach uses liquid based precursors that can be inkjet printed and processed under atmospheric conditions. Various precursors were identified leading to In_2Se_3 , Cu_2Se and CuInSe_2 films without a selenization step on various substrates. Similar chemistries are applicable to copper zinc tin sulfide (CZTS) materials which are potentially more scalable. Details of film deposition and processing for these systems will be discussed. The third application is in the field of organic photovoltaics. Here inkjet printing is used to deposit the photoactive layer such as a polythiophene, for example P3HT, and the conducting contact layer such as PEDOT/PSS. Details will be shown on how solvents can influence the quality of the printed material. Direct write processing of these materials may be enabling for this technology leading to an all printed photovoltaics.

Graphene Focus Topic

Room: Brazos - Session GR+EM+MS+TF+MI-WeM

Graphene and Carbon-based Devices

Moderator: N.P. Guisinger, Argonne National Laboratory

8:00am **GR+EM+MS+TF+MI-WeM1 Epitaxial Graphene: Effects of Dielectric Overlayers and Device Design on FET Performance**, *M.J. Hollander, R. Cavalero, D. Snyder, M. LaBella, K. Trumbull, Z. Hughes, J. Robinson*, The Pennsylvania State University

The realization of a graphene-based electronic technology necessitates large-area graphene production, as well as the ability to integrate graphene with highly insulating films that act as the gate dielectric in field effect transistors (FETs). Graphene's two dimensional nature allows for phenomenal electronic properties and ultimate scalability, but also makes it susceptible to doping and scattering by charged impurities, dangling bonds, and other defects that may derive directly from choice in gate dielectric and deposition technique. The nature and extent of the effect of the dielectric over-layer on conduction within the graphene channel is of fundamental interest in designing and producing graphene based FETs. Atomic layer deposition (ALD) has proven to be an excellent technique toward the integration of dielectrics with graphene and provides a means to produce high quality films for gate dielectrics at temperatures below 300C, but requires the use of a thin nucleation layer to promote complete coverage and to protect the graphene.

We present results on graphene FETs utilizing various gate dielectrics and various nucleation layers. Graphene was grown epitaxially on 100 mm SiC wafers and processed using standard photolithographic techniques. Al_2O_3 and HfO_2 gate dielectrics were investigated using SiO_2 , TiO_2 , and Al_2O_3 nucleation layers in various combinations. We show that choice of gate dielectric and nucleation layer can have a dramatic effect on transistor performance and charge carrier mobility. Saturation current, transconductance, and device hysteresis were examined in the fabricated FETs while charge carrier mobility and charge carrier density within the epitaxial graphene were evaluated using Van der Pauw structures. Graphene FETs utilizing Al_2O_3 and SiO_2 seeded dielectrics exhibit the best performance while TiO_2 seeded and unseeded devices exhibit large gate leakage currents resulting in non-functioning FETs. Additionally we provide evidence that the choice of dielectric and seed can significantly impact the Dirac point (minimum conduction), amount of hysteresis, and on/off ratio of the graphene FETs. Trends in saturation current, and transconductance appear to be independent of nucleation layer and gate dielectric choice, indicating that conduction through the channel may be limited by mechanisms independent of the nucleation layer and gate dielectric.

In addition to the aforementioned performance metrics, FET performance after continued application of high electric fields across the channel will be reported. Finally, we examine how choice of channel length and width, along with transistor design, effect performance.

8:20am **GR+EM+MS+TF+MI-WeM2 Graphene Oxide on Patterned Self-Assembly Monolayer for Cancer Marker Detection**, *D.-J. Kim, C.Y. Jung, O.J. Yoon, N.-E. Lee*, Sungkyunkwan University, Republic of Korea, *J.-S. Park*, Korea Electronics Technology Institute, Republic of Korea

Graphene, two-dimensional sheet of sp^2 -hybridized carbon atom, has received much attention in recent years for many applications such as energy storage and conversion, batteries, fuel cells, optoelectronic device, field-effect transistors, electromechanical resonators, chemical sensors, and biotechnologies. Oxidized form of graphene, graphene oxide, which has functional groups of epoxide, carbonyls, hydroxide, and phenol groups at both sides can also provide various functionalities for biomedical applications because the high densities of defective sites can provide many active sites for electron transfer to biological species, similarly to graphene. In this study, we demonstrate the graphene oxide based immunosensor for cancer marker detection. Graphene oxide pattern was formed selectively on self-assembly monolayer (SAM) pattern formed by using inkjet printing. The hydroxyl terminated ITO electrode was first selectively functionalized by the amine ($-\text{NH}_2$) group by inkjet printing of SAM, and the graphene oxide flakes were adsorbed selectively on the SAM pattern. After immobilization of monoclonal antibody to PSA (prostate specific antigen) which is the biomarker in prostate cancer, the electrochemical performance of immunosensor was evaluated by varying the concentration of PSA-ACT (prostate specific antigen/ α 1-antichymotrypsin) complex. And the PSA polyclonal antibody conjugated with gold nanoparticles was applied to amplification of electrochemical signal because the attachment of nanoparticles onto electrodes drastically enhances the conductivity and electron transfer from the redox analytes. The results showed that graphene oxide based immunosensor can be possibly applied to the delicate diagnosis

of various disease markers as well as PSA at the extremely low level and with ultra-high sensitivity.

8:40am **GR+EM+MS+TF+MI-WeM3 Spintronics in Graphene Based Nanostructures**, *J. Fernández-Rossier*, Universidad de Alicante, Spain
INVITED

Spintronics in graphene has received attention from two complementary points of view. On one side, the small spin orbit coupling and nuclear spin density suggest that graphene should have very long spin relaxation and decoherence times, which would make it suitable for long distance spin transport and, eventually, for spin-based quantum computing. Although small, spin orbit interaction turns graphene into a spin hall insulator, at very small temperatures, so that the edges of graphene should carry spontaneous spin currents. Independently of the above, the zigzag edges of graphene nanostructures, like graphene ribbons and islands, are predicted to present ferromagnetic spin order due to electron electron coupling. In this talk I will discuss the properties of graphene nanostructures when both the spin-orbit coupling and the Coulomb interactions are included. I will show how the combined action of spontaneous spin order and spin orbit coupling results in persistent charge currents flow in the edges of a variety of graphene nanostructures.

9:20am **GR+EM+MS+TF+MI-WeM5 CVD Gate Dielectrics and Bandgap Engineering of Graphene Layers**, *W.J. Zhu, D. Neumayer, V. Perebeinos, P. Avouris*, IBM T.J. Watson Research Center

Graphene is very promising for electronic devices, particularly for analogue high frequency devices due to its high intrinsic mobility. One challenge in graphene devices is the formation of gate dielectrics on graphene due to its hydrophobic nature. We found a new CVD gate insulator that provides uniform coverage on graphene while preserving the channel mobility, thus making it a very promising gate dielectric for graphene devices. We also studied the channel resistance and the modification of the band structure as a function of the vertical electric field near the Dirac (neutrality) points in the fabricated top-gated graphene devices. We found that as the vertical field increases, in bi- and tri-layer graphenes, the band-gap increases, while in multi-layer graphene, the band-overlap increases. The values of band-gap/overlap in bi-, tri- and multi-layer graphenes were estimated using a simple model which takes into account the variations of the surface electrostatic potential at the Dirac/neutrality point.

9:40am **GR+EM+MS+TF+MI-WeM6 Characterization of Devices Fabricated from Electrostatically Transferred Graphene: Comparison with Epitaxial based Devices**, *S.W. Howell, L.B. Biedermann, T. Ohta, T.E. Beechem, W. Pan, A.J. Ross, D.C. Trotter*, Sandia National Laboratories

In this paper, we present our recent advancements in electrostatically transferring epitaxial graphene (EG) from SiC(0001) and SiC(000-1) to arbitrary glass substrates (including Pyrex). We will compare the electronic properties of electrostatically transferred EG and nominally-equivalent as-grown EG on SiC. These properties are measured using magnetoresistive, four-probe, and field effect transistor geometries. We feel this is a potential enabling technology for integration of graphene with structured and electronically-active substrates, such as MEMS and CMOS.

CVD-grown graphene on Cu has attracted wide interest since it can be readily transferred to arbitrary substrates. However, CVD-grown graphene has been shown to have lower mobilities and smaller domain sizes than EG. EG is difficult to transfer to arbitrary substrates. Currently two techniques exist to transfer EG – a gold/polymer film handle and thermal tape exfoliation [1,2]. While transfer is possible with these techniques, problems exist including contamination and damage, as measured by Raman spectroscopy.

To overcome the issues with the above mentioned transfer techniques, we have developed a technique capable of electrostatically transferring both patterned and chip-scale regions of EG to arbitrary glass substrates. We start with high-quality graphene (mobility 14,000 cm²/Vs and domains >100 um²) grown using an Ar-mediated approach [3,4]. In electrostatic graphene transfer, a large electric field is applied between the donor graphene sample (anode) and the acceptor insulating substrate (cathode). This strong electrostatic force deposits graphene on the insulating surface. Electrostatic transfer of EG is a clean technique which, unlike other EG transfer methods, does not contaminate the graphene with adhesive residue or gold contaminants. Both few-layer graphene from SiC(000-1) and monolayer graphene from SiC(0001) have been transferred using this technique.

Our initial attempts at EG transfer have been extensively characterized with Raman spectroscopy and atomic force microscopy. Raman spectroscopy shows that the inherent strain in EG has been partially relaxed. Furthermore, a defect peak (D peak) is frequently not seen in the transferred graphene indicating that the procedure does not significantly damage the graphene film.

Sandia is a multiprogram laboratory operated by Sandia Corporation, a Lockheed Martin Company, for the United States Department of Energy under contract DE-AC04-94AL85000.

- [1] D. Lee *et al.* *Nano Lett.* **8**, 4320 (2008)
- [2] S. Unarunotai *et al.* *APL* **95**, 202101 (2009)
- [3] W. Pan *et al.* submitted to *APL* (2010)
- [4] K. Emtsev *et al.* *Nature Mat.* **8**, 203 (2009)

10:40am **GR+EM+MS+TF+MI-WeM9 Electron Transport in Dual-Gated Mono- and Bilayer Graphene Devices with High-k Dielectrics**, *E. Tutuc, S. Kim, B. Fallah, K. Lee, J. Nah, S.K. Banerjee*, The University of Texas at Austin, *L. Colombo*, Texas Instruments, Inc.
INVITED

A key issue for graphene-based devices is the deposition of thin high-k dielectric layers combined with a minimum electron mobility degradation. Here we examine the carrier transport in mono and bilayer graphene field-effect transistors with top Al₂O₃ and HfO₂ dielectrics. The high-k dielectric films are grown by atomic layer deposition (ALD), and using a 1nm-thick Al interfacial layer in order to create intentional nucleation centers for the ALD. We show that this deposition technique allows the realization of high mobility graphene devices with aggressively scaled top dielectrics. We investigate the carrier mobility dependence on dielectric thickness and temperature in mono-layer graphene field-effect transistors with high-k dielectrics. The electron transport in dual-gated graphene bilayers with Al₂O₃ top dielectric reveals an interesting band-gap energy dependence on transverse electric field and perpendicular magnetic field in this system.

11:20am **GR+EM+MS+TF+MI-WeM11 In-situ X-ray Photoelectron Spectroscopy Studies of Ozone-based ALD Al₂O₃ Dielectrics on Graphite and Graphene**, *A. Pirkle, S. McDonnell*, University of Texas at Dallas, *L. Colombo*, Texas Instruments, Inc., *R.M. Wallace*, University of Texas at Dallas

Thin Film

Room: Dona Ana - Session TF+EM-WeM

High K Dielectrics for Si Electronics

Moderator: S. Gupta, University of Alabama

8:00am **TF+EM-WeM1 Moore's Law - From Simple Scaling to Integrating New Materials and Introducing New Device Architectures**, *R. Hendel*, Periodic Structures Inc.
INVITED

Moore's Law has been the driver for semiconductor integrated circuits over more than 40 years. Relentless scaling of dimensions switching provided increasing functionality and performance, resulting in leading edge single chips today that incorporate more than 1 Billion transistors.

All attempts on predicting the end of Moore's Law have been futile – innovations have always allowed continued scaling at reduced cost. However, while Moore's Law appears to be a continuous curve, we rarely reflect on the underlying changes that had to occur to enable this rate of progress. These changes comprised device architecture, the introduction of new materials and break-through processes.

Since Moore's Law describes a learning curve for which cost reduction is central, process simplicity frequently won out over performance advantages if the latter came at high cost. Self-aligned implanted poly-gate over the early metal gate structures is a prime example. Aggressive reduction in the cost per function also provided performance benefits: Smaller transistors switched faster and used less power to do so – truly a win-win situation.

Key innovations along this path were:

- The switch from thermal diffusion doping to implant
- The introduction of CMP, which was key in increasing the number of metal layers that could be integrated.
- The introduction of high-k dielectrics in conjunction with metal gates which addressed the critical gate leakage problem and will allow the introduction of new and better performing channel materials.

Compared to the past, the future will require even more innovation along three potential directions:

- Continuous improvements of current methodologies along existing technologies, consisting of solid engineering and hard work.

Innovations pursued in this category are: highly regular layouts, new channel materials in conjunction with modified hi-k/MG (yet planar) structures.

- Significant changes to traditional device structures and processes.

An example of innovations pursued in this category is the FinFET, which presents significant challenges in materials and processes that must be resolved before introduction into the manufacturing cycle.

· Radical new structures and approaches resulting in major deviation from today's mainstream technologies.

An example is new fundamental circuit components such as the Memristor or new approaches available if considering device operations at cryogenic temperatures (which may be feasible for server farms), allowing the exploration of concepts such as superinsulators.

This presentation will highlight the state-of-the-art in process technology and discuss challenges that require attention and timely solutions.

8:40am TF+EM-WeM3 Non-destructive Depth Profiles of Hafnium Silicate Films by Angle-Resolved and Variable-Kinetic Energy XPS, C. Weiland, N. Lorenz, R. Oplla, University of Delaware

High dielectric constant, or high-k films are currently being employed in semiconductor devices. Hafnium silicate ($\text{Hf}_x\text{Si}_{1-x}\text{O}_2$) films are a promising material system for such applications, as they combine the high dielectric constant of HfO_2 with the high stability against crystallization of SiO_2 . The $\text{Hf}_x\text{Si}_{1-x}\text{O}_2/\text{Si}$ interface must be defect free as defects at this interface can create charge centers which decrease channel mobility. Atomic layer deposition (ALD) is frequently used to deposit high-k films, and provides excellent thickness control and conformality by reacting only one saturating layer of reactant at a time. This work focuses on studying the composition and interface quality of $\text{Hf}_x\text{Si}_{1-x}\text{O}_2$ films deposited by ALD using novel silicon precursors and water as the oxidizer. Films are analyzed using non-destructive depth profiles by angle-resolved and variable-kinetic energy X-ray photoelectron spectroscopy (ARXPS, VKE-XPS). In ARXPS, the effective probe depth is varied by changing the takeoff angle between surface and detector. As a complementary technique, VKE-XPS provides depth profiles by adjusting the incident X-ray energy, and thus the corresponding inelastic mean free path of the photoemitted electrons. VKE-XPS also allows the ability to probe deeper into films than conventional lab-based sources, providing the possibility of analyzing thicker films or entire gate stacks. Using these techniques, we have studied the composition and interface quality of $\text{Hf}_x\text{Si}_{1-x}\text{O}_2$ films deposited using various Si precursors. The presence of charge at the interface manifests itself as shifts in the energy of the photoelectron peaks. Using this data, we can determine charge at the high-k/silicon interface as well as measure band offsets.

9:20am TF+EM-WeM5 Study of SiO_2 and SiN_x Passivation of HfInZnO Oxide Semiconductor Thin Film Transistor, J.C. Lee, E.H. Lee, J.G. Chung, B. Anass, J.H. Lee, J.S. Park, M.K. Ryu, Samsung Advanced Institute of Technology, Korea

ZnO based oxide semiconductor is a promising material for thin film transistor which has transparent, high electric mobility, and the advantage of low temperature process. Several kinds of ZnO based oxide semiconductors (InZnO , GaInZnO , HfInZnO , etc.) have been adapted to the active material of thin film transistor. However most of ZnO based oxide semiconductors have very sensitive property to ambient environment. It is essential to prevent the penetration of moisture into ZnO based oxide thin film transistor (TFT). In the purpose of preventing moisture penetration and/or protecting damage from TFT processes, SiN_x or SiO_2 passivation layer is used frequently.

In this study, we investigated the interface reactions between amorphous HfInZnO (Hf:In:Zn= 10:35:55, 40nm thickness) oxide semiconductor active layer and the passivation layer of SiN_x or SiO_2 (20 nm thickness). TEM, XPS and SIMS were used to investigate the interface reactions such as atomic diffusion, reduction of HfInZnO, chemical state, microstructure.

According to experimental results, a SiO_2 phase and Indium metallic state were observed at the interface between SiN_x and HfInZnO active layer. On the other hand, there was not observed Indium metallic state at the interfaces between SiO_2 and HfInZnO layers. In the case of SiN_x passivation, it is considered that some Si took oxygen from Indium oxide in HfInZnO and oxidized to SiO_2 . And some of Indium oxide reduced to metallic Indium at the interface. Indium diffusions from HfInZnO layers into passivation layers were observed at the both of SiN_x and SiO_2 samples. In the case of SiN_x passivation, it was a little bit higher diffusion than that of SiO_2 passivation. The low binding energy shift was observed at the Zn_{2p} XPS spectra at the both samples. However, there was no distinct difference at the Hf_{4d} spectra.

If there is metallic Indium between passivation and HfInZnO active layers, the metallic Indium may influence the conductance of active layer. The threshold voltage (V_{th}) shift of thin film transistor (TFT) could be affected by the change of conductance of active layer.

We observed that the V_{th} negative shift of the TFT used SiN_x passivation was higher than that of SiO_2 passivation. It may be due to the existence of metallic Indium at the interface.

In this report, it will be described the relationships between interface reactions and the property of HfInZnO oxide TFT in detail.

9:40am TF+EM-WeM6 Capacitance-Voltage (C-V) and X-ray Photoelectron Spectroscopy (XPS) Study of the Effect of a La_2O_3 Layer in the $\text{TiN}/\text{HfO}_2/\text{SiO}_2/\text{p-Si}$ Stack, E.J. Bersch, M. Di, University at Albany, S.A. Consiglio, R.D. Clark, G.J. Leusink, Tokyo Electron America Inc., A.C. Diebold, University at Albany

There has been much attention paid recently to the lowering of the threshold voltage (V_t) that is accomplished by including an additional ultrathin (~5-10 Å) oxide layer in the high-k/metal gate metal oxide semiconductor field effect transistor (MOSFET) gate stack. We have investigated the $\text{TiN}/\text{HfO}_2/\text{La}_2\text{O}_3/\text{SiO}_2/\text{p-Si}$ stack, where the La_2O_3 layer is the so-called V_t -shift layer. For several variations of this stack, where both the thickness and the position of the La_2O_3 layer were systematically varied, we measured two quantities directly related to the V_t , the flatband voltage (V_{fb}) and the Si band bending. The V_{fb} was measured using capacitance-voltage (C-V) measurements on stacks with 500 Å TiN layers, and the Si band bending was measured on sister wafers with 30 Å TiN layers. For a set of samples where the thickness of the La_2O_3 between the HfO_2 and SiO_2 layers was varied, we observed that the V_{fb} and Si band bending both become more negative as the thickness of the La_2O_3 was increased. For a set of samples where position of the La_2O_3 within the HfO_2 layer was varied, we observed that the V_{fb} and Si band bending became less negative as the amount of HfO_2 between the La_2O_3 and the SiO_2 was increased. These observations support the proposition that there is a dipole at the $\text{La}_2\text{O}_3/\text{SiO}_2$ interface which affects the Si band bending, as has been reported in the literature.^{1,2} We have also observed that there is a difference in the V_{fb} and Si band bending in $\text{TiN}/\text{HfO}_2/\text{La}_2\text{O}_3/\text{SiO}_2/\text{p-Si}$ stacks with thermally grown and chemically grown SiO_2 layers. Results of this study as well as one where the thickness of thermally grown SiO_2 layers was varied will be presented, and its implications on the theory of the interface dipole will be discussed.

1. K. Kita, et al., *Appl. Phys. Lett.*, 94, 132902 (2009).
2. P.D. Kirsch, et al., *Appl. Phys. Lett.*, 92, 092901 (2008).

10:40am TF+EM-WeM9 Modification of Defect-State Concentrations with Vacuum Ultraviolet and Ultraviolet Irradiation of Hafnium-Oxide Dielectric Layers, H. Ren, University of Wisconsin-Madison, S.-L. Cheng, Y. Nishi, Stanford University, J.L. Shohet, University of Wisconsin-Madison

The effects of 7.2 eV vacuum ultraviolet (VUV) and 4.9 eV ultraviolet (UV) irradiation on a 20 nm HfO_2 layer atomic layer deposited (ALD) on (100) Si substrate are explored with electron-spin resonance (ESR). Silicon dangling-bond defect concentrations (P_b centers) and positively charged oxygen vacancies (E' centers) were measured with g-factor fitting. The concentrations of the defect states are presented. VUV irradiation increases the level of $Pb0$ and $Pb1$ states, while UV decreases the level of $Pb0$ and $Pb1$ states, but increases the level of E' states significantly. [i] [#_edn1] In addition, rapid thermal annealing (RTA) mitigates the effects of both VUV and UV irradiation. Surface-potential measurements with a Kelvin probe show that electron photoemission process dominate VUV irradiation. On the other hand, electrons are transferred from E' states to the silicon substrate during UV irradiation. At the same time, electrons are photo-injected into the dielectric layer from the substrate. Furthermore, VUV spectroscopy measurements show that the Fermi level for E' defect states is around 4.7 eV, which is within the bandgap of the dielectric layer. Also, previous work [ii] [#_edn2] shows that the E' states, as oxygen-interstitial defects (OID), are located within the HfO_2 layer. We conclude that VUV irradiation modifies the concentrations of the silicon dangling-bond defect states and UV irradiation can be a potential source for positively charge oxygen vacancies during the processing.

Work Supported by the Semiconductor Research Corporation under contract 2008-KJ-1781

- [i] [#_ednref] H. Ren, S.L. Cheng, Y. Nishi and J.L. Shohet, *Applied Physics Letters* (to be published)
- [ii] [#_ednref][ii] J.L. Lauer, J.L. Shohet and Y.Nishi, *Applied Physics Letters* 94, 162907 (2009)

11:00am **TF+EM-WeM10 Plasma Enhanced Atomic Layer Deposition of Ruthenium Ultra-Thin Films for Advanced Metallization.** *J. Swerts, S. Armini, L. Carbonell, D.A. Annelies, F.A. Alexis, S. Mertens, T. Witters, M. Shaekers, Z. Tökei, G. Beyer, IMEC, Belgium, V. Gravey, A. Cockburn, K. Shah, J. Aubuchon, Applied Materials Inc., S. Van Elshocht, IMEC, Belgium*

Electrochemical deposition of Cu for interconnect metallization traditionally uses Physical Vapor Deposition (PVD) of a Cu seed layer on top of a PVD Ta/TaN barrier to conduct the current. However, the limitations of PVD in respect of step coverage compromise its use in future technology nodes. Atomic Layer Deposition (ALD) for barrier deposition combined with seedless Cu electroplating is one of the metallization routes explored for sub-25 nm line widths. However, compatibility with seedless electroplating seriously limits the choice of materials. Among the different candidates, Ru-based layers have been identified as very promising.

We report the growth and scalability of Ru films by plasma-enhanced ALD (PE-ALD) from MethylCyclopentadienylPyrrolylRuthenium (MeCpPyRu) and N_2/NH_3 plasma. The layers were deposited using a 300 mm showerhead type reactor (AMAT) with direct plasma capability. The substrate temperature during deposition was 330°C. The Ru growth per cycle was 0.04 nm. As substrates we used Si wafers with 100-300 nm SiO_2 on which a thin TaN or TiN layer was deposited by ALD or PVD.

The metal nitride is needed as a growth enabler since Rutherford backscattering spectrometry (RBS) showed that only $1E14$ Ru atoms/cm², i.e. less than a monolayer, were deposited on SiO_2 after 120 PE-ALD cycles. The minimal thickness of the metal nitride to enable Ru growth has been determined to be as low as 0.7-0.8 nm which is promising for scaling. Growth studies on scaled and thick ALD TiN or TaN still showed a limited growth inhibition during the first 40 cycles followed by a linear growth behavior. Static time-of-flight secondary ion mass spectroscopy (TOFSIMS) suggests Ru layer closure for a film thickness around 2 nm.

Atomic force microscopy revealed that the root mean square roughness values were below 0.4 nm for film thicknesses up to 20 nm. X-ray diffraction showed that the Ru layers have a hexagonal structure. The density of the Ru layer was 11.75 g/cm³ as derived from X-ray reflectivity and RBS. Elastic recoil detection analysis and TOFSIMS indicate that the N, O, C-levels in the bulk Ru layers were $\ll 1\%$. Surface analysis by static TOFSIMS showed the presence of organic contamination identified as MeCp ligands from the Ru precursor. In contrast, the Pyrrolyl ligand was not observed. A post deposition thermal treatment of the Ru film removes the ligand organic contamination. The impact of this surface contamination on the seedless Cu electroplating efficiency will be discussed. Finally, the step coverage of TiN/Ru and TaN/Ru stacks in narrow lines (65-15 nm width) was evaluated by transmission electron microscopy.

11:20am **TF+EM-WeM11 Effects of Hydrogen Plasma Pretreatment on Superconformal Gap-Filling of Cu-Al Alloy.** *H.K. Moon, N.-E. Lee, Sungkyunkwan University, Republic of Korea*

As the feature of microelectronic interconnects has continued to shrink, Cu resistivity is expected to increase at the nanoscale due to increased surface and grain boundary scattering of electrons. To prevent increase of the resistivity in nanoscale interconnects, alloying Cu with other metal elements such as Al, Mn, and Ag is being considered to increase the mean free path of the drifting electrons. The formation of Al alloy with a slight amount of Cu broadly studied in the past. The investigation of Cu alloy with a very small Al fraction, by contrast, recently started. The formation of Cu-Al alloy is limited in wet chemical bath and was mainly conducted for fundamental studies by sputtering or evaporation system. However, these deposition methods have a limitation in production environment due to poor step coverage in nanoscale Cu metallization. In this work, gap-filling of Cu-Al alloy was conducted by cyclic MOCVD (metal organic chemical vapor deposition), followed by thermal annealing for alloying, which prevented an unwanted chemical reaction between Cu and Al precursors and hydrogen in the gas phase. To fill the Cu-Al alloy into sub-100nm trench without overhang and void formation, furthermore, hydrogen plasma pretreatment of the trench pattern with Ru barrier layer was introduced in order to suppress of Cu nucleation and growth near the entrance area of the nanoscale trench by minimizing adsorption of metal precursors. As a result, superconformal gap-fill of Cu-Al alloy could be achieved successfully in the 40-nm trench with an aspect ratio of 4. Examined morphology, microstructure, chemical composition, and electrical properties of superfilled Cu-Al alloy will be discussed in detail.

11:40am **TF+EM-WeM12 Depth Resolved Cathodoluminescence Spectroscopy of Amorphous High- k Dielectric $LaLuO_3$.** *S. Shen, Ohio State University, Y. Liu, R.G. Gordon, Harvard University, L.J. Brillson, Ohio State University*

We have used depth-resolved cathodoluminescence spectroscopy (DRCLS) to measure the native point defects and reaction-induced defects within

ultrathin $LaLuO_3$ dielectric films. The rare earth oxide $LaLuO_3$ is gaining much attention because of its high dielectric constant (28 ~ 32) and its potential application to replace SiO_2 as a gate dielectric for Si microelectronics, requiring both sub-nanometer thick gate oxide layers and low leakage currents. $LaLuO_3$ deposited by atomic layer deposition (ALD) provides films with high crystallization temperature and relatively high conduction band offset, but they have non-negligible leakage currents that are attributed to electronic trap states in the band gap. Annealing can partially reduce these traps but can also induce diffusion/reaction at the $LaLuO_3$ interfaces. We used DRCLS to determine the changes in defect levels of WN/20 nm $LaLuO_3/Si$ gate structures as a function of annealing and the introduction of an Al_2O_3 diffusion barrier at the Si interface. A 10 nm WN/20nm $LaLuO_3/Si$ structure as-grown exhibits defect emissions at 2.4, 3.2, 3.8, 4.2 and 4.7 eV as well as a 5.48 eV band gap. With 300°C cyclic annealing, 10 nm WN/20nm $LaLuO_3/Si$, the band gap emission is absent and high energy emissions at 4.2 and 4.7 eV shift to 3.8 eV. A 10 nm WN/20nm $LaLuO_3/0.4$ nm Al_2O_3/Si interlayer structure exhibits negligible difference from the interlayer-free stack without anneal. However, with annealing, the WN/20nm $LaLuO_3/0.4$ nm Al_2O_3/Si defects at high energy and the band gap remain unchanged while the lower energy defects are suppressed. The 5.48 eV band gap emission agrees with an internal photoemission gap of 5.3 eV measured previously. The 4.2 and 4.7 eV emissions are consistent with weighted density function approximation calculations showing two oxygen-vacancy-related states at similar energies near the $LaLuO_3$ conduction band edge. The DRCLS-measured degradation of optical features with annealing of the interlayer-free structure is attributed to Si diffusion and reaction with $LaLuO_3$ as observed by cross sectional TEM. This degradation is suppressed with the Al_2O_3 barrier layer. Furthermore, the annealing of the interlayer structure reduces all the low energy defect emissions. Finally, the highest lying state at 4.7 eV above the valence band (0.78 eV below the conduction band) agrees reasonably well with the 0.6-0.7 eV electrical measurements of leakage current. These results highlight the importance of annealing with a diffusion barrier at the Si interface to suppress defects within $LaLuO_3$ without Si reaction at the $LaLuO_3$ interface.

Thin Film

Room: San Miquel - Session TF+SE-WeM

Glancing Angle Deposition (GLAD) I

Moderator: T. Karabacak, University of Arkansas at Little Rock

8:00am **TF+SE-WeM1 Soft Nanostructured Films for Biomedical Applications.** *M.C. Demirel, Pennsylvania State University INVITED*

Anisotropic textured surfaces represent key structural components utilized by various animals and plants to gain a competitive advantage for survival. For example, a closer look at complex structures in insect wings and lizard toes reveal organized structured features at the microscopic scale. These structures are composed of millions of aligned columns per square millimeter, which create novel anisotropic properties. We have demonstrated that these structures can be fabricated synthetically by an oblique angle polymerization (OAP) method. OAP allows us to tune the chemical properties of nanostructured surfaces and film morphology to control the physicochemical properties of the resulting films, such as hydrophobicity, porosity, electrochemistry, chemical reactivity, surface energy and crystallinity. In this talk, we will describe unique anisotropic physicochemical properties (i.e. morphing/folding, wetting, and friction) of well-ordered arrays of nano-rods/tubes, which mimic biological structures at the microscopic scale. We will also present results concerning the use of these films for biomedical and biosensors applications.

8:40am **TF+SE-WeM3 Growth Temperature Controlled Morphology of Ge Nanocolumns.** *C. Khare, J. Bauer, J.W. Gerlach, Leibniz Institute of Surface Modification (IOM), Germany, B. Fuhrmann, Martin-Luther-University Halle, Germany, T. Höche, B. Rauschenbach, Leibniz Institute of Surface Modification (IOM), Germany*

Germanium films with manifold nanostructures are grown by ion beam sputter glancing angle deposition (GLAD). Morphological shape variations were introduced through variation of the substrate temperature (T_s) and differently patterned silicon substrates. Pre-patterned substrates served as seeds for growing structures assisting the formation of a periodic nanostructure array. Nanocolumns grown on a bare Si(100) substrate demonstrated an altered morphology that can be controlled by the substrate temperature. At elevated substrate temperature ($T_s / T_M > 0.3$), surface diffusion-driven mass transport as a result of increased adatom mobility augmented fibrous-columnar and intra-columnar growth. Further increment

of the substrate temperature ($T_s / T_M > 0.45$) exhibited column merging and column broadening. Additionally, significant changes in the overall film thickness representing changes in the film porosity were observed. Similar merging and broadening characteristics were also exhibited on SiO₂ nanosphere templated substrates. For the films deposited at elevated substrate temperatures, XRD measurements showed the growth of polycrystalline films. TEM analysis confirmed the growth of large crystallites at elevated substrate temperatures. Thus, growth of Ge nanostructures with tailored morphology can be grown by substrate pre-patterning and by utilizing substrate temperature induced effects.

9:00am TF+SE-WeM4 Glancing Angle Deposited Platinum Nanorod Arrays with Enhanced Electrochemical Activity for Oxygen Reduction Reaction in PEM Fuel Cells, W.J. Khudhayer, A.U. Shaikh, T. Karabacak, University of Arkansas at Little Rock

In this work, we have investigated the electrochemical properties of vertically aligned, single-layer, low loading, carbon-free and single crystal Pt nanorod arrays as a potential cathode material in polymer electrolyte (PEM) fuel cells. These nanorods of different lengths in the range of 20-600 nm were produced by glancing angle deposition (GLAD) technique with Pt loading values of 0.016-0.5 mg/cm². Electrodes of conventional carbon supported Pt nanoparticles (Pt/C) were also prepared for comparison with Pt nanorods for their electrochemical properties. Scanning electron microscopy (SEM) and X-ray diffraction (XRD) were utilized to study the morphology and crystallography of Pt nanorods. SEM and XRD results reveal that Pt nanorods are well-isolated, vertically aligned, and single-crystal with atomically sharp tips. The single-crystal property allows enhanced electrochemical activity and reduced surface oxidation, while the isolated nature of the rods in lateral directions can provide a channeled porosity for effective transportation of gases in a PEM fuel cell. The electrochemical activity of Pt nanorods as well as Pt/C was evaluated using cyclic voltammetry (CV). CV results show that Pt nanorod electrocatalysts reduce oxygen to water at a more positive potential than Pt/C, indicating that our catalyst has a lower oxygen overpotential due to the enhanced electrode porosity, single-crystal property, and the dominance of the preferred crystal orientation for oxygen reduction reaction (ORR). In addition, a series of CV scans show that our catalyst is more stable than Pt/C in the acidic environment. Finally, in order to get a fair comparison for high surface area catalysts, detailed thin-film rotating disk electrode measurements at room temperature were performed on 200 nm long Pt nanorods as well as Pt/C for comparison to calculate the most important kinetics parameters (Tafel slopes, exchange current density, Pt mass-specific activity and area-specific activity), which are the accepted measures of true catalysts activity towards ORR. These results reveal the enhanced mechanism and kinetics of ORR on Pt nanorods compared to Pt/C.

9:20am TF+SE-WeM5 Hydrogen Storage Properties of Magnesium Nanotrees by Glancing Angle, M.F. Cansizoglu, T. Karabacak, University of Arkansas at Little Rock

Among many solid state materials for hydrogen storage, magnesium hydride (MgH₂) combines a hydrogen capacity of 7.6 wt % with the benefit of the low cost of production and abundance. The main difficulties for implementing MgH₂ are slow absorption/desorption kinetics and high reactivity towards air and oxygen, which are also common issues in most lightweight metal hydrides. Previously, improvements in hydrogen storage and release properties have been reported by using nanostructured magnesium that can be obtained through various fabrication methods including ball-milling, mechanical alloying, and vapor transport. In this study, we investigate the hydrogen absorption and desorption properties of magnesium "nanotrees" fabricated by glancing angle deposition (GLAD) technique, and also conventional Mg thin films deposited at normal incidence. Mg nanotrees are about 15 μm long, 10 μm wide, and incorporate "nanoleaves" of about 20 nm in thickness and 1,2 μm in lateral width. A quartz crystal microbalance (QCM) gas absorption/desorption measurement system has been used for our hydrogen storage studies. Nanostructured and thin film Mg have been deposited directly on the surface of the gold coated unpolished quartz crystal samples. QCM hydrogen storage experiments have been performed at temperatures ranging between 100-300oC, and at H₂ pressures of 10 and 30 bars. QCM measurements revealed that Mg nanotrees have better storage characteristics compared to Mg thin films. They can reach hydrogen storage values of about 4.80 wt% at 100oC, and up to about 6.71 wt% (which is close to the theoretical maximum storage value of Mg) at temperatures lower than 150oC. The significant enhancement in hydrogen absorption properties of Mg nanotrees is believed to originate from novel physical properties of their nanoleaves. These structures are very thin (~20 nm) and both surfaces are exposed to hydrogen enhancing the diffusion of hydrogen together with a decreased diffusion length. In addition, nanostructured Mg have been observed to be quite resistant to surface oxidation, which is believed to be due to the single crystal property of the Mg nanoleaves.

9:40am TF+SE-WeM6 Fabricating Crystalline ZnO Nanorods by Glancing Angle Deposition, J.M. LaForge, M.T. Taschuk, M.J. Brett, University of Alberta, Canada

Zinc oxide possesses a combination of properties, including semiconductor electronic behaviour, optical transparency, and piezoelectricity, that make it an interesting candidate for energy scavenging, photovoltaics, and chemical sensing applications (1, 2). Several unique nanostructures may be formed with ZnO, with a variety of growth methods that exploit the difference in surface energy between the low-index crystal faces of the wurtzite ZnO crystal leading to preferential growth along the c-axis.

Glancing angle deposition (GLAD) is assumed to operate effectively under conditions of limited surface diffusion so that growth occurs from geometric shadowing of an incoming particle flux. While amorphous GLAD films are typical, there are numerous crystalline films reported in the literature, including ZnO (3). This suggests that in certain material systems growth kinetics play a role in GLAD growth. However, the conditions under which GLAD produces crystalline films has not been thoroughly investigated or explained.

We have selected ZnO to investigate these issues for two reasons: first, the technological applications outlined above, and second, to explore the material growth properties which can produce crystalline structures. This makes it an ideal candidate for studying nanostructure morphology and crystal properties as a function of process parameters, including deposition rate, pitch and throw distance. Optimal growth conditions for zinc oxide nanorod films occurred for pitch values in the vicinity of 1 nm to 10 nm. Study of the post aspect ratio and areal post density suggests that typical GLAD growth occurs for deposition rates <0.005 nm sec⁻¹ and that growth kinetics begin to contribute significantly at deposition rates >0.01 nm sec⁻¹. Films deposited at pitch values between 0.001 nm to 6.5 μm are crystalline and textured, and greater texturing is achieved for conditions of decreased surface diffusion.

- (1) Wang, Z. L. *Journal of Physics: Condensed Matter*. **2004**, *16*, R829-R858.
- (2) Ye, C.; Fang, X.; Hao, Y.; Teng, X.; Zhang, L. *The Journal of Physical Chemistry. B*. **2005**, *109*, 19758-65.
- (3) Teki, R.; Parker, T.; Li, H.; Koratkar, N.; Lu, T.-M.; Lee, S. *Thin Solid Films*. **2008**, *516*, 4993-4996.

10:40am TF+SE-WeM9 Optical, Magnetic, Magneto-Optical and Electrochemical Properties of Sculptured Thin Films, E.B. Schubert, D. Schmidt, T. Hofmann, A.C. Kjerstad, E. Montgomery, S. Schöche, M. Schubert, University of Nebraska - Lincoln

Bottom-up and self-organized three-dimensional (3D) structure design on the nanoscale opens a new field in nanostructure based thin film engineering with a broad range of practical applications for sensors, optical coatings, photovoltaic devices or biomaterials, for example. Sculptured thin films (STF's) belong to this group of thin films and current research creates exciting new knowledge about the unique material properties that are related to shape, dimension, and distribution of the nanostructures within the thin film ensemble. The following paper presents new sculptured thin film properties obtained from material analysis using optical, magnetic, magneto-optical and electrochemical characterization techniques. [1-5] Material properties have been quantified from model analysis and results from our investigations lead to original device designs for applications such as highly-sensitive mass balances, subwavelength antireflection coatings, magneto-optical memory and chemical sensors.

- [1] E. Schubert, Contributions to Plasma Physics **47**, 545 (2007).
- [2] D. Schmidt, B. Booso, T. Hofmann, E. Schubert, A. Sarangan, and M. Schubert, Appl. Phys. Lett. **94**, 011914 (2009).
- [3] D. Schmidt, B. Booso, T. Hofmann, E. Schubert, A. Sarangan, and M. Schubert, Opt. Lett. **34**, 992 (2009).
- [4] D. Schmidt, A. C. Kjerstad, T. Hofmann, R. Skomski, E. Schubert, and M. Schubert, J. Appl. Phys. **105**, 113508 (2009).
- [5] D. Schmidt, T. Hofmann, E. Schubert, and M. Schubert, Appl. Phys. Lett. **96**, 091906 (2010).

11:00am TF+SE-WeM10 Stress Behavior of Obliquely Sputtered Ta Films on Glass Substrates, S.U. Jen, P.H. Chiang, Academia Sinica, Taiwan, Republic of China

Ta films were obliquely deposited on glass substrates by magnetron sputtering method using the parameters: deposition angle $\alpha = 60^\circ$; deposition temperature $T_s = 298, 373, 473, \text{ and } 573 \text{ K}$; Ar working gas pressure $P_{AR} = 2, 7.5, \text{ and } 15 \text{ mTorr}$; film thickness $t_f = 100 \text{ nm}$. From X-ray diffraction, atomic force microscopy, cross-section transmission electron microscopy, and Auger depth profile analysis, we conclude that: [1] the axis of each columnar grain is inclined at an angle $\beta \approx 35^\circ$ with respect to the film normal; [2] in-plane grain aggregates show some vestiges of the chain-

like structure, whose long axis is perpendicular to the plane of incidence (i.e. the transverse or width direction of the sample); [3] oxygen atoms are found inside the film; especially located in the columnar gaps (or microvoids) between neighboring grains. The stress of each film was measured via Stoney equation. The main results in regard to the stress behavior of this series of Ta films are summarized below: [a] the intrinsic stress S_i is always tensile and dominant over the thermal stress S_T ; [b] the total stress is anisotropic with the longitudinal stress being larger than the transverse stress; [c] as T_s increases, S_i becomes less tensile. Result [a] is reasonable because Ta is a high melting point material.¹ Especially, in the oblique-deposition case, the formation of gaps becomes more obvious. Hence, much larger tensile stress (than in the normal-deposition case) arises from the attractive interaction of oxygen atoms across the gaps. Result [b] is a consequence of the self shadowing effect, which is already manifested in the conclusion [2] above. Result [c] is due to the fact that as T_s is higher, there is a structure transition from zone I to zone T, and oxygen atoms are less likely to be incorporated into the film.

¹ G. Guisbiers, O. Van Overschelde, M. Wautelet, *Acta Materialia* 55, 3541(2007).

11:20am **TF+SE-WeM11 Role of Columnar Nanostructures on Static and Dynamic Wetting Properties of Silver Film**, *D. Singh, J. Singh*, IIT Delhi, India

The study of wetting has always been a very active field of research. In recent years, the interest in this field is stimulated by nanoengineering the surface to meet the requirements of various biological, chemical and industrial applications by modifying their wetting properties. In the present study, we have investigated the effect of silver nanocolumns on the static as well as dynamic wettability of surface. The nanocolumns of about 400 nm length and 150 nm diameter ($\alpha = 85^\circ$) were grown by oblique angle deposition method over the Si(100) substrate. The effect of these nanocolumns on static wetting behavior was studied by performing sessile drop contact angle measurements using de-ionized water. A significant enhancement in the hydrophobicity of silver surface with contact angle value of 108° was observed (see supplement file, Fig. 1). To ensure that the observed changes in wetting behavior are due to the influence of nanocolumns, the measurements were carried out for different surface features ranging from plane to nanocolumnar film (grown for $\alpha = 0^\circ, 65^\circ, 75^\circ$ and 85° , see SEM images in supplement file, Fig.2). Contact angle was observed to increase gradually from 94° to 96° with increase in oblique angle (α) from 0° to 75° . A drastic increase in contact angle was observed for nanocolumnar surface grown at $\alpha = 85^\circ$. For these silver samples the rms (root mean square) surface roughness was found to follow almost the same pattern as that of contact angle with α , suggesting the dependence of wettability on surface roughness. The observed results were explained following the Cassie-Baxter model considering the silver nanocolumns to form a silver-air composite surface. To investigate the effect of nanocolumns on dynamic wetting property, the contact angle measurements for higher sample surface temperature ($T_s = 80^\circ\text{C}$) were performed and the rate of change of contact angle of water drop for an interval of 10 sec was measured. This transition rate of contact angle values was found to increase drastically for the nanocolumnar surface (see the supplement file, Fig.3). It shows that the nanocolumnar growth affects not only the static contact angle by making the surface hydrophobic but also greatly influences the surface temperature dependent dynamic wetting behavior of water drop. This study provides a basic understanding of the wetting behavior of nanocolumnar surface as well as shows the possibility to tune the surface wettability for meeting the requirements of various industrial applications.

Thin Film

Room: Ruidoso - Session TF-WeM

ALD: Nanostructure, Magnetics and Biological Applications

Moderator: E.W.M.M. Kessels, Eindhoven University of Technology, the Netherlands

8:00am **TF-WeM1 Magnetic Nano-Objects Based on Atomic Layer Deposition: Switching Modes in Nanotubes and Core-Shell Nanowires**, *J. Bachmann, K. Nielsch*, University of Hamburg, Germany **INVITED**
Atomic layer deposition (ALD) is uniquely suited to the conformal deposition of magnetic thin films in pore structures of high aspect ratio, while offering precise tuning of the layer thickness and high uniformity. Combining one or several layers of ALD with self-ordered porous anodic alumina membranes used as templates yields arrays of magnetic nanotubes with diameters tunable between 20 and 200 nm, wall thicknesses from 2 to

40 nm, and lengths set anywhere between 0.1 and 100 microns. The magnetic properties of such nanotubes strongly depend on their geometry, as evidenced on the ensemble and single-object levels by SQUID and MOKE magnetometries, respectively. The structural parameters can be chosen so as to favor a certain mechanism of magnetization reversal or another.

Further structural complexity can be created by introducing additional preparative steps. Interference lithography can be exploited for sculpting tubes with controlled modulations in diameter. Electrodeposition enables us to synthesize wires in which a core and a shell of two distinct magnetic materials are separated by a non-magnetic spacer layer. In those cases, the geometric parameters are still accurately controlled and tunable. The particular geometric characteristics of the system directly transpire into their magnetic properties: diameter modulations may hinder the propagation of magnetic domain boundaries, whereas core-shell structures may give rise to two distinct magnetic reversal events.

8:40am **TF-WeM3 Structural and Magnetic Properties of Anatase Mn-doped TiO₂ Film Synthesized by Atomic Layer Deposition**, *M.C.K. Sellers, E.G. Seebauer*, University of Illinois at Urbana-Champaign

Transition metal doped semiconductors exhibiting room temperature ferromagnetism are intensely investigated for spintronics applications. Devices leveraging the spin-dependent effects of these materials would allow for increased data processing speeds, decreased power consumption, and improved integration densities in comparison to standard charge-based electronics. In the past ten years, experimental and computational studies have demonstrated room temperature ferromagnetism (RTFM) for several TiO₂-based dilute magnetic semiconductors (DMSs) namely TiO₂ doped with Mn, Cr, Fe, and Co. Most DMS TiO₂ films are synthesized via sol-gel, pulsed laser deposition (PLD), and plasma-assisted molecular beam epitaxy (PAMBE). Atomic layer deposition (ALD) of DMS TiO₂ has never been demonstrated, although this method has been used to deposit Mn-doped ZnO with DMS properties. ALD circumvents complications with solvent and byproduct removal and with calcination-induced shrinkage that arise during sol-gel synthesis. PLD and PAMBE are ill-suited to the high throughput requirements of commercial manufacturing. In addition, PLD can result in high particulate composition and uneven coverage, while PAMBE films suffer from thickness-dependent morphologies. ALD avoids such problems. The present work involves the synthesis of Mn-doped anatase TiO₂ (0 to 5 at% Mn) thin films on Si(100) via ALD at 200°C and 400°C. Ti(OCH(CH₃)₂)₄ and H₂O are utilized as ALD precursors and Mn(DPM)₃ as a dopant source. The effect of substrate temperature, number of cycles, precursor and oxidant injection times, purge time, and distance between sample and delivery tube on film thickness and uniformity have been investigated. X-ray photoelectron spectroscopy measurements indicate that Mn is successfully doped in the TiO₂ matrix and reveal information about film composition and elemental chemical states. Microstructure, crystallinity, bulk density, and roughness were investigated with scanning electron microscopy, x-ray diffraction, and x-ray reflectivity. SQUID magnetometry was used as a probe of RTFM; the bulk density, microstructure, and magnetic moment of the TiO₂ vary with the concentration of Mn. The results provide insight into the properties of DMS TiO₂ synthesized via ALD and underscore the advantages of the technique - precise thickness, compositional control, and higher process throughput - in comparison to alternative techniques of DMS growth.

9:00am **TF-WeM4 Fabrication of Refractory Nanoporous Structures by ALD of Tungsten on High Surface Area Silica Aerogels**, *A.U. Mane, Argonne National Laboratory, U. Sampathkumaran, T. Owen, R. Winter, Innosense LLC, J. Nolen, J. Greene, J.W. Elam*, Argonne National Laboratory

Refractory nanoporous materials with high porosity could serve as efficient catchers for the fast release of unstable nuclei in rare isotope accelerators. The unique, self-limiting capability of atomic layer deposition (ALD) offers an attractive synthetic route for fabricating refractory nanoporous materials. Here we demonstrated a method using high surface area silica aerogel monoliths as templates for the growth of conformal thin films by ALD. Static mode ALD of W using Si₂H₆ and WF₆ at 200°C was employed to coat the inner surfaces of the low density, nanoporous silica aerogel monoliths. To facilitate nucleation and improve adhesion of the ALD W, the aerogels were coated with 2Å Al₂O₃ using alternating exposures to Al(CH₃)₃ and H₂O prior to the W ALD. After coating, scanning electron microscopy revealed a porous microstructure in which the ALD W completely encapsulates the silica aerogel. The porosity of the aerogels was preserved during the first ~10 W ALD cycles allowing the density to be controlled by adjusting the number of W ALD cycles and values as high as 5 g/cc were obtained. BET surface area measurements revealed a gradual decrease in the surface area of the silica aerogel with increasing numbers of W ALD cycles consistent with a gradual filling of the aerogel voids. Next, we heated the W-coated aerogels to 1500°C in an inert atmosphere and

observed that they maintained their integrity and porosity with almost no loss in density. These results are very encouraging for the deployment of these materials as isotope catchers.

9:20am TF-WeM5 Nucleation and Ultra-Thin Film Formation during ALD on Multiwall Carbon Nanotubes, C. Devine, J.S. Jur, C. Oldham, J. Bonner, G.N. Parsons, North Carolina State University

Atomic layer deposition is widely studied as a means to coat and encapsulate polymers to impede diffusion of water, oxygen or other species. ALD is also a viable means to coat and surface functionalize carbon nanotubes and other nanostructured materials. Previous work suggests that ALD nucleation proceeds differently on single and multiwalled carbon nanotubes, where the more defective nature of multiwalled tubes allows more rapid nucleation and film growth. In this work, we are interested in using ALD to encapsulate multiwall carbon nanotubes with as thin a layer as possible, to modify the chemical signature of the nanotubes while maintaining their advantageous mechanical and physical properties. Our motivation for this work is to explore means to alter potential toxic inhalation effects that carbon nanotubes may present, for example, in manufacturing facilities producing nanotube-based products. We have worked with multiwall nanotubes from Helix Materials Solutions as well as from Mitsui. The Mitsui tubes are 30-50 nm in diameter and contain many concentric nanotubes. TEM analysis shows that ALD using TMA/water at 90 °C proceeds slowly at first, producing isolated nuclei for the first 15 cycles. Films are smoother after 25 cycles, and continuous film coatings are observed after 80 cycles, corresponding to film thickness of 3.8 nm. After complete film coverage, the film growth rate increases to values close to that expected for TMA/water at this process temperature. We will present results regarding how these coatings affect physical properties of the nanotubes, including surface wetting, as well as possible new means to coat large numbers of nanotubes in a conventional viscous flow reactor system.

9:40am TF-WeM6 Chemical Vapor Deposition of Sandwiched Antibacterial Layers, F. Schamberger, T.H. Huber, G. Franz, Hochschule Muenchen, Germany

To deposit organic polymers on three-dimensional, even rugged surfaces, (pe)cvd is the method of choice. Thickness and film quality are mainly controlled by the number density of the precursors and their mixing ratio which determine the equilibrium of polymerization between reactions in the gas phase at high densities or at the surface for low densities. In most cases, MFCs can be used. Since MFCs can be heated only up to about 80 °C, precursors with low vapor pressure cannot be discharged into the reactor by this method, and the flow is mainly controlled by vapor pressure which limits the controlled deposition of thin layers.

We have recorded the vapor pressure curves for diparylene N and diparylene C applying a dynamic and a static method, resp. [1], and correlated flow and deposition rate with vapor pressure. To meet the demands for exact layer thickness even for values below 1 µm, an almost digital grow method is required. We introduce such a simple, low-cost method for the coating of antibacterial layers which have been deposited by subsequent wet chemical methods and galvanic plating. For very thin layers, the increase in pinhole density with shrinking film thickness has been investigated as functions of total pressure and process time by qualitative visual inspection (sem) and quantitative measurements by comparing the permeability of thin films against water vapor and oxygen. For swiss cheese layers, the antibacterial film below is but partly protected, however, the antibacterial action can be prolonged over years. Eventually, the change in mechanism from polymerization at the surface to volume polymerization has been investigated by varying the doping levels of the ambient gas (argon or oxygen), and has been correlated in-situ by mass spectrometry and ex-post to some film properties; among them are surface roughness and surface energy and the refraction index as well as the ir spectrum which has been modeled for the dimeric and the polymeric species applying a Gaussian method.

[1] Council Regulation (EC) No 440/2008 of 30 May 2008 laying down test methods pursuant to Regulation (EC) No 1907/2006 of the European Parliament and of the Council on the Registration, Evaluation, Authorisation and Restriction of Chemicals (REACH) (Text with EEA relevance), Official Journal L 142 , 31/05/2008 P. 0001 - 0739

10:40am TF-WeM9 ALD for Nano and Micro Electro-Mechanical Systems, V.M. Bright, University of Colorado at Boulder INVITED

Atomic Layer Deposition (ALD) can be effectively used to deposit custom-designed, multi-material layers with atomic resolution on any micro- or nano-scale device surfaces. The nano-scale ALD coating can protect the devices from electrical short, charge accumulation, moisture-induced adhesion, wear, corrosion, creep, fatigue or anodic oxidation during prototyping or long-term product life. ALD films for N/MEMS achieve these goals similar to what CVD Si₃N₄ has been for CMOS. As MEMS

scales further shrink toward nano-electro-mechanical systems (NEMS), ALD processes offer a new strategy for depositing conformal and precise films that may have important applications as a novel dielectric, a sacrificial layer for gap control in nanofabrication, or as a structural layer for NEMS realization.

ALD relies on sequential, self-limiting surface reactions to deposit ultra thin, conformal films. The following characteristics of ALD films and processes make them flexible and multifunctional, and represent their appeal for N/MEMS: ALD film thicknesses can be precisely deposited from a few Å to hundreds of nm; ALD films can be deposited at temperatures ranging from 33°C to over 200°C; ALD films are pinhole-free, dense, smooth and highly conformal; ALD films can be deposited on silicon, polysilicon, silicon nitride, metals, polymers, and ceramics; ALD films can be conformally deposited on any size or shape device or any substrate; ALD can coat high surface area to volume ratio structures with complex geometries; ALD can deposit dielectric or conductive layers; ALD can deposit hydrophobic or hydrophilic layers covalently bonded to the surface; ALD can deposit on lithographically defined selective areas; ALD films can be micromachined to create nano-scale gaps and free standing structures; ALD coating process' deposition rate can be high, e.g. 0.5 nm/min at 177°C for Al₂O₃.

These ALD techniques for N/MEMS, pioneered at the University of Colorado – Boulder, represent breakthrough in nano-scale processes that can be used to fabricate custom-designed, multi-material layers with atomic resolution. The ALD processes developed are proven, mature, and are available to serve the N/MEMS community.

References

- S. George, et al, *J. Physical Chem.*, **100**, 13121 (1996).
- N. Hoivik, et al, *Sensors and Actuators A*, **103**, 100 (2003).
- C. Herrmann, et al, *J. Micromech. Microeng.*, **15**, 984 (2005).
- C. Stampfer, et al, *Nano Letters*, **6** (2), 233, (2006).
- T. Helbling, et al, *Nanotech.*, **20**, 434010 (10pp), (2009).
- D. Seghete, et al, *Sensors and Actuators A*, **155**, 8, (2009).
- B.D. Davidson, et al, *Sensors and Actuators A*, on line.

11:20am TF-WeM11 Understanding Plasma Enhanced Chemical Vapor Deposition for the Production of Composite Nanomaterials with Biomedical Applications, J.C. Shearer, E.R. Fisher, Colorado State University

Fe₂O₃ and other magnetic nanoparticles are becoming key components of both chemical and biological applications, including drug delivery schemes and magnetic resonance imaging contrast agents. Nanoparticles coated with organic and inorganic films have distinct properties and enhanced functionalities over those of uncoated nanoparticles. Plasma-enhanced chemical vapor deposition (PECVD) was employed to conformally coat Fe₂O₃ with SiO₂ or polyallyl alcohol films, thereby creating composite nanomaterials. Comparisons will be made between composite nanoparticles created with an in-house atmospheric pressure plasma system and similar composite materials created in a traditional low-pressure PECVD system. In other studies, surface sites were activated with O₂ and Ar plasmas to plasma graft SiO₂ and polyallyl alcohol monolayer films onto the nanoparticles. Compositional and morphological data demonstrate that conformal SiO₂ and polyallyl alcohol coatings were achieved and that the use of PECVD methods allowed specific tailoring of the film structure, composition, and growth characteristics. The performance of the composite materials was explored through dispersion, UV-vis spectroscopy, and chemical functionalization studies. Further insight into the deposition process is provided by actinometric optical emission spectroscopy (AOES) and laser induced fluorescence spectroscopy (LIF), which allow characterization of the gas-phase species and their energetics (i.e. internal and kinetic energies) for each system. Preliminary data from our Imaging of Radicals Interacting with Surfaces (IRIS) technique provides additional information on the molecular-level chemistry that occurs at the interface between gaseous plasma species and nanoparticle substrates.

Wednesday Afternoon, October 20, 2010

Advanced Surface Engineering

Room: San Miguel - Session SE+TF-WeA

Glancing Angle Deposition (GLAD) II

Moderator: K. Robbie, Queen's University, Canada

2:40pm SE+TF-WeA3 Nanorods by Extreme Shadowing: New Pictures and New Physics, *D. Gall*, Rensselaer Polytechnic Institute
INVITED

Glancing angle deposition (GLAD) uses an oblique deposition angle to exacerbate atomic shadowing during physical vapor deposition to create underdense layers consisting of nanorods with engineered shapes and three-dimensional composition variations. This growth process is intrinsically chaotic. However, initial substrate patterning combined with temporal changes in the deposition fluxes yield surprisingly regular nanostructure arrays. The questions about the theoretical minimum feature size as well as rod branching, merging, and broadening is discussed by presenting statistical morphology data from various metals deposited over a large temperature range. The rod width follows a power law scaling where the growth exponent depends linearly on the island nucleation length scale, but exhibits a discontinuity at 20% of the melting point, associated with a transition from a 2D to a 3D island growth mode. Different metals show excellent quantitative agreement when scaled to the melting point, yielding a single homologous activation energy of 2.46 for surface diffusion on curved nanorod growth fronts, applicable to all metallic systems at all temperatures. The onset of bulk diffusion near 50% of the melting point during such growth under exacerbated shadowing conditions leads to a direct transition from an underdense (zone I) structure to a dense (zone III) structure. Applications include nanostructured fuel cell electrodes, active components of nano pressure sensors, and lubricant transport channels for high-temperature self-lubrication.

4:00pm SE+TF-WeA7 Quasi-periodic Pattern Formation on Columnar Thin Films by Ion Beam Erosion at Oblique Incidence, *M. Suzuki, H. Moriwaka, K. Nakajima, K. Kimura*, Kyoto University, Japan

It is well known that obliquely deposited thin films show various shape related properties due to not only their complex columnar shapes but also their unique surface morphology. For example we have succeeded to prepare in-line aligned noble metal nanorod arrays on a template layer with anisotropic surface roughness originating from the bundled columns created by serial-bideposition technique (SBD)¹. Our nanorod arrays show the excellent surface enhanced Raman scattering properties. However, it is difficult to avoid the irregularities in size and shapes of the columns in the obliquely deposited thin films. On the other hand, recently, much attention has been paid on the pattern formation by ion beam erosion (IBE) at oblique incidence. When the flat surface is irradiated with the ion beam, quasi-periodic ripple patterns are self-organized. These ripple patterns seem to be more regular than the morphology found in the obliquely deposited thin films. However, the ripples in IBE surface are too gentle to use their functionalities or to use them as a template for the shadowing growth. In this work, we tried to reduce the irregularities of columnar shapes of obliquely deposited thin films by IBE.

Layers of Ge with an anisotropic surface morphology were prepared by SBD technique on a Si substrate. During the SBD, the deposition angle for Ge measured from the surface normal was fixed at an angle of 82°, while the azimuthal angle was changed rapidly by 180° with each deposition of an approximately 10 nm thick layer. After 15 cycles of SBD, Ge layers with an thickness of 300 nm were obtained. The surface of the Ge layer was irradiated with Xe⁺ ions of 5 keV up to the fluence of 0.5, 1.5, 3.0×10¹⁶ ions/cm² at an angle of incidence of 45° or 70°. The planes of incidence of Ge vapor and Xe⁺ ions are perpendicular to each other.

The average aspect ratio of the surface corrugation is 1.4 for the non-irradiated Ge films and significantly increases with increase of fluence. At the fluence of 3.0×10¹⁶ ions/cm², the aspect ratio reaches 7 mainly due to the elongation of the surface corrugation along the incident direction of the ion beam. The width of the surface corrugation is wider for 45° incidence than 70° incidence. Remarkably, distinct periodicity is found in the autocorrelation images of the SEM of the surface. These results are understood in terms of the directive sputtering toward the forward direction of the ion beam and the redeposition of the sputtered atoms, and are characteristic for the ion beam erosion of the porous materials.

1. M. Suzuki, et al., Appl. Phys. Lett., **88**, 203121 (2006).

4:20pm SE+TF-WeA8 Shadowing Effect of Patterned Seeds in Glancing Angle Deposition, *D. Soma, D.-X. Ye*, Virginia Commonwealth University

Glancing angle deposition (GLAD) technique has been developed by several groups including us in the past few years to produce three-dimensional nanostructures of a large variety of material. This technique combines oblique angle deposition with substrate manipulations in a physical vapor deposition system. The shadowing effect is the dominant growth mechanism resulting in the formation of various nanostructure arrays by programming the substrate rotation in polar and/or azimuthal direction. On patterned seeds, the shadowing effect strongly depends on the geometric parameters of the seed arrays, i.e. the aspect ratio of individual seeds, and the separation and arrangement of the seeds. In this talk, we will study those geometric parameters using a (2+1)-dimensional Monte Carlo simulation. In our simulation, we couple the shadowing effect and ballistic aggregation with rotating oblique incident particles. The uniformity of the nanostructures grown on the seeds will be investigated. The results of this study will provide a guideline for the design of seeds to achieve uniform size nanostructures by using GLAD.

4:40pm SE+TF-WeA9 Control of Phase Formation in Metal Oxide GLAD Films, *R.T. Tucker*, University of Alberta, Canada, *A.E. Schoeller, M.D. Fleischauer*, NRC - National Institute for Nanotechnology, Canada, *M.J. Brett*, University of Alberta, Canada

Glancing angle deposition (GLAD) has found application in a wide range of fields requiring porous, high surface area thin films, including sensors, optics, and energy devices. [1] This diversity is due in large part to the wide range of compatible materials, including metals, semiconductors, and organic compounds. Metal oxides are of particular interest for energy storage and conversion applications since they can be tuned for a combination of transparency, electrical conductivity, and chemical and thermal stability. Achieving the desired stoichiometric phase is essential for controlling desirable metal oxide properties. Here we discuss the challenges associated with achieving phase control in porous GLAD films.

Metal oxide GLAD films typically deposit in an amorphous state, so post-deposition processing is one route used to access a particular crystallinity and stoichiometry. Thermal annealing conditions depend on the desired phase: anatase TiO₂ readily forms at a few hundred degrees Celsius in air; Ti₄O₇ generally requires longer anneals at high temperatures (1000 °C) in a reducing atmosphere (eg. H₂ in carrier gas). [2] Annealing temperature, duration, and environment (e.g. oxidizing vs. reducing atmosphere) can all have an impact on film morphology, since coalescence or softening of structures is greatly enhanced at temperatures near the melting point of the metal oxide. Both the porosity of the film and the strength of the reducing atmosphere affect the extent of oxygen removal and morphology changes at relatively high temperatures, while still allowing access to a wide range of compositions (e.g. Ti_nO_{2n-1}, n = 2 - 9), phases (e.g. monoclinic, tetragonal, or orthogonal Nb₂O₅) and the associated optical, electronic, and thermal properties.

We will present methods to retain the porosity and structure of GLAD thin films while achieving desired stoichiometry and phase via post-deposition annealing, with a specific focus on phase and crystallinity characterization using x-ray diffraction. We will attempt to correlate results from the Ti-O and Nb-O systems with results from other systems of interest (e.g. W-WO₃) [3] as part of a better understanding of phase formation in porous thin films.

[1] M.M. Hawkeye and M.J. Brett, J. Vac. Sci. & Tech. A, **25**, 1317 (2007).

[2] J.R. Smith *et al.*, J. Appl. Electrochem., **28**, 1021 (1998).

[3] D. Deniz *et al.*, Thin Solid Films, **518**, 4095 (2010).

We thank NSERC, iCORE, Micralyne, and the National Research Council - Technology Development Program for financial support.

5:00pm SE+TF-WeA10 A Fan-Shadowing Model in Oblique Angle Deposition, *B. Tanto*, Rensselaer Polytechnic Institute, *G.A. Ten Eyck*, Sandia National Laboratories, *T.-M. Lu*, Rensselaer Polytechnic Institute

Recently oblique angle deposition has been used in a wide range of important, unique applications. The column angle of the obliquely deposited columnar structures is an important parameter that determines their mechanical, optical, and chemical properties. Unfortunately this angle can be greatly affected by materials and processing conditions which are too complex to model and predict. Existing models such as the tangent rule and cosine rule are independent of materials and processing conditions and therefore in general have a limited ability to predict the column angle. We present a semi empirical model that includes the effects of materials and processing conditions. We show that our model is able to accurately predict

column angle analytically for a wide range of obliquely deposited amorphous Ge for two different sets of processing conditions. We also show how this model can be used to predict other useful quantities, such as porosity and column width.

The model uses the fact that the deposition on a line (or wire) results in a fan structure due to a self-shadowing effect with a fan angle that depends on materials and processing conditions. We first show how columnar structures can be generated by analytically applying global shadowing between the fan structures growing on adjacent lines. The columnar structures obtained possess geometrical properties (such as column width and column merging) that are consistent with columnar structures observed in experiment and simulation. We show how the exact shape and time evolution of the columnar structure can be calculated based on the knowledge of the fan shape. Once the exact shape of the columnar structure is known, various useful quantities can also be obtained: column angle, porosity, and column width. We experimentally verified our model by depositing amorphous Ge on line seeded substrate and on a flat substrate. The model agrees with experiments done on both substrates.

Finally, we describe relatively simple experimental setups that can be used for fast and convenient measurement of the fan geometry at various processing conditions, such as flux rates and temperatures. These fan geometry data obtained on normal incident flux can then be used to predict the columnar structure geometries for the whole range of incident flux angles and for all the various processing conditions.

5:20pm SE+TF-WeA11 Investigation of the Nanorod-Structuring Threshold in Glancing Angle Deposition (GLAD), D. Deniz, R.J. Lad, University of Maine

Thin films of tin (Sn), aluminum (Al), gold (Au), ruthenium (Ru), tungsten (W), ruthenium dioxide (RuO₂), tin dioxide (SnO₂) and tungsten trioxide (WO₃) were grown by glancing angle deposition (GLAD) to determine whether a nanostructuring threshold condition can be quantified as a function of both substrate temperature and melting point of the material. Films were grown using both DC and pulsed DC magnetron sputtering with continuous substrate rotation over the temperature range from 18 – 800°C. Film morphologies, structures, and compositions were characterized by high resolution scanning electron microscopy (SEM), X-ray diffraction (XRD) and X-ray photoelectron spectroscopy (XPS). Films were also grown in non-GLAD configurations for comparison. For the elemental metals, it is found that nanorod-structuring occurs for materials with melting points higher than that of Al (660°C) when films are grown at room temperature with a relatively small rotation rate of ~5 rpm. For the oxide materials, our results indicate that a critical substrate temperature (TS) to melting point (TM) ratio exists, above which GLAD nanorod-structuring becomes ineffective because the adatom mobilities become large enough for non-kinetically limited film nucleation and growth processes to occur, similar to those operative in a non-GLAD growth configuration.

Thin Film

Room: Pecos - Session TF-WeA

Thin Films: Growth and Characterization

Moderator: N.P. Guisinger, Argonne National Laboratory

2:00pm TF-WeA1 Growth and Characterization of Thin Films for Organic Electronics Applications, D.J. Gaspar, L. Wang, Z.H. Zhu, M.H. Engelhard, B.J. Tarasevich, J.S. Swensen, R.E. Williford, M.E. Gross, W.D. Bennett, D.W. Matson, Pacific Northwest National Laboratory INVITED

There are two basic ways of generating organic thin films for electronics applications – vacuum-based processes and solution processes (each with many variations). Each has advantages and disadvantages in film purity, morphology, deposition rate, process control, molecular design and materials choices. This presentation will describe the deposition, characterization and performance of organic thin films deposited using variants of both methods for organic light emitting diodes (OLEDs), organic thin film transistors (OTFTs), and other applications utilizing electroactive organic thin films. Specific advantages in film purity and access to different classes of materials are discussed. Surface characterization using time of flight secondary ion mass spectrometry (TOF-SIMS), X-ray photoelectron spectroscopy (XPS), atomic force microscopy (AFM) and conductive AFM), ellipsometry and Fourier transform infrared spectroscopy (FTIR) are used to characterize thin films, highlighting the challenges in characterizing these often sensitive and usually amorphous films, as well as need to develop a solid experimental understanding of the composition and structure of thin films deposited for organic electronics applications to understand performance.

2:40pm TF-WeA3 Bio Modification of Titanium Surfaces with Grafted Sodium Styrene Sulfonate Thin Films, G. Zorn, D.G. Castner, University of Washington

3:00pm TF-WeA4 Probing Stability of the Molecule-Substrate Interface in Self-Assembled Monolayers by Ion-Beam-Induced Desorption, P. Cyganik, Jagiellonian University, Poland, S. Wyczawska, F. Vervaecke, E. Vandeweert, P. Lievens, Catholic University Leuven, Belgium

Due to the ease of preparation and their relatively high stability, self-assembled monolayers (SAMs) are very promising candidates to be used in the development of micro- and nano-structured materials. With numerous detailed studies available nowadays for SAMs, the identification of SAMs adsorption geometry and stability of molecule-substrate interface still remains controversial and rather difficult to access experimentally. In this presentation we report experiments on ion-induced desorption and resonance enhanced ionization mass spectrometry of SAMs on Au(111) substrate.¹ Although ion-induced desorption is commonly considered as a very invasive process when used for probing monomolecular films, our experiments demonstrate that this method can be successfully applied to monitor fine changes in the molecule-substrate interface stability of model SAMs systems based on thiols (CH₃-C₆H₄-C₆H₄-(CH₂)_n-S-Au(111), n = 2-6) and selenols (BPnSe, CH₃-C₆H₄-C₆H₄-(CH₂)_n-Se-Au(111), n = 2-6). Current desorption experiments will be discussed together with recent microscopic² and spectroscopic³ analysis of the molecular structure and stability of these SAMs. We demonstrate that lower or higher ion-induced bond scission efficiency can be correlated with, respectively, higher or lower chemical stability of particular chemical bonds. Thus, a new method for probing the stability of the substrate-SAM interface can be proposed.

References

- (1) S. Wyczawska, F. Vervaecke, et al. *in preparation*.
- (2) P. Cyganik, K. Szelagowska-Kunstman, et al. *J. Phys. Chem. C* **2008**, *112*, 15466.
- (3) K. Szelagowska-Kunstman, P. Cyganik, et al. *Phys. Chem. Chem. Phys.* **2010**, *12*, 4400.

4:00pm TF-WeA7 Benzene Adsorption on Self-Assembled Monolayers, S.J. Sibener, H. Yuan, D.R. Killelea, K.D. Gibson, The University of Chicago

Non-dissociative deposition of gas-phase species onto surfaces of alkanethiol self-assembled monolayers (SAMs) allows creation of new types of multi-component nanoscale materials. Systems such as these have garnered much attention due to their central role as model systems for studies of orientation-controlled adsorption and non-dissociative attachment of functional molecules on organic surfaces of technological importance, including molecular electronics.

Benzene (C₆H₆), perdeuterobenzene (C₆D₆) or a 50:50 mixture of these two isotopologues were deposited on SAM surfaces using a supersonic molecular beam. Supersonic molecular beam techniques permitted precise control over the dynamics of the deposition process by changes in the incident reagent's translational energy (E_{trans}) and incident angle. The results presented here highlight the role these dynamical variables play in the adsorption, desorption and conformation of the resultant multilayer molecular film. A combination of *in-situ* infrared reflection absorption spectroscopy (FT-IRAS) and mass spectrometry was used to determine the surface coverage, molecular orientation and the sticking coefficient as a function of the surface coverage of the benzene molecules deposited on SAM surfaces. The interaction between adsorbates and the SAM substrate was also investigated by varying the SAM chain length and whether the SAM contains an odd or even number of carbon atoms. These results were compared to analogous results from adsorption on clean Au surfaces.

The results of these experiments uncovered the details of the adsorption process. The effects of E_{trans} and substrate temperature on sticking show the central role dynamics plays in the physisorption of molecules on surfaces. Most significantly, the sticking of gas-phase benzene was found to have a novel dependence on surface coverage, and non-Langmuirian uptake was observed.

4:20pm TF-WeA8 Ex and In Situ Analysis of the Growth of Ultrathin Organic Films from Ethanol Solutions, T. Hauffman, E. Tourwé, A. Hubin, H. Terryn, Vrije Universiteit Brussel, Belgium

In order to form stable self-assembling organic monolayers on numerous substrates, dipping deposition from organic solvents is a widespread technique. However, it is rarely investigated what is the influence of the solvent on the substrate and the molecules which are supposed to be deposited. In this study we present the self assembly of phosphonic acids from an ethanolic solution on aqueous based pretreated aluminium oxides. Following the deposition behavior with XPS and AFM throughout

deposition time, it was concluded that the nature of the deposition is random and fluctuating. In order to understand better what is going on, the deposition was followed in situ with odd random phase multisine impedance spectroscopy. This technique gives the opportunity to follow the behavior of the organic molecules as well as the behavior of the buried substrate. It was observed that ethanol adheres on the surfaces, changing the water based chemistry which was obtained through the pretreatment. Furthermore, a competition between the adsorption of the phosphonic acids and ethanol was seen, explaining the non-stable behavior previously analysed with XPS and AFM.

This statement was proven by characterizing ethanol-stabilised aluminium oxide samples during different immersion times. Although here no monolayer was formed, the trend observed corresponded with continuous organic layer growth.

4:40pm TF-WeA9 Effect of Deposition Pressure on the Structural, Optical and Electrical Characteristics of Y_2O_3 Thin Films by Reactive Magnetron Sputtering. *V.H. Mudavakkat, K.B. Karuppanan, C.V. Ramana*, University of Texas at El Paso

Significant research efforts have been directed in recent years on the growth of Y_2O_3 films because of their interesting physical, electronic, and optical properties. The diverse range of potential applications of Y_2O_3 films includes storage capacitors, random access memory (RAM) and metal-insulator-semiconductor (MIS) devices, protective and antireflective coatings for IR detectors, and optical filters. In the present work, Y_2O_3 films have been produced by the magnetron sputter-deposition. The effect of pressure on the structure, optical and electrical properties of Y_2O_3 films has been investigated. The rate of deposition found to be significantly influenced by the overall pressure during deposition. Optical characterization carried out using transmittance analysis indicate that the samples at lower deposition rates showed weaker absorption in comparison to the samples with higher deposition rates. X-ray diffraction (XRD) showed that the as-is deposited films at room-temperature exhibit [111] oriented cubic structure. Electrical characterization indicate that films are insulating with a very high resistivity. The capacitance-voltage characteristics are also obtained for Y_2O_3 films. The results will be presented and discussed.

5:00pm TF-WeA10 Effect of Partial Pressure on Structural and Optical Properties of WO_3 Thin Films. *R.S. Vemuri, S.K. Gullapalli, R.V. Chintalapalle*, University of Texas at El Paso

Tungsten oxide (WO_3) is a wide band gap semiconductor (~ 3.2 eV), which exhibits excellent properties suitable for the development of integrated chemical sensors and electrochromics. N-type conductivity coupled with selectivity and sensitivity to certain type of chemicals make WO_3 thin films interesting for NO_x and H_2S sensors. The present work was performed to understand the effect of oxygen partial pressure on the microstructure, optical and electrical properties of WO_3 thin films and optimize the conditions to produce materials suitable for sensor applications. WO_3 thin films were produced by the reactive RF magnetron sputtering. The films were grown at various reactive gas pressures (2.3 – 5.6 mTorr) by changing the oxygen flow rate while keeping the deposition temperature fixed at 400°C. Optical spectroscopy analysis of the grown films indicates that optical properties are sensitive to the oxygen partial pressure. The spectral transmission of the films increased with the increase in oxygen concentration. The band gap of these films was found to be increasing from 2.6 eV to 3.25 eV with increasing oxygen pressure. Electrical conductivity $\{\sim 10^{-2} (\Omega\text{-cm})^{-1}\}$ measurements indicate that there is a correlation between the growth conditions, optical and electrical properties.

5:20pm TF-WeA11 Effects of Deposition Temperature on Al doped ZnO Thin Film for Solar Cells by dc Magnetron Sputtering. *W. Yang, J. Joo*, Kunsan National University, Republic of Korea, *S.M. Rosnagel*, IBM Research

Aluminum-doped zinc oxide films (AZO) were deposited on soda-lime glass substrates by dc magnetron sputtering for solar cell application. The resistivity and average transmittance were improved from $2.3 \times 10^{-3} \Omega\text{-cm}$ to $3.3 \times 10^{-4} \Omega\text{-cm}$ and from 77.3% to 86% at high deposition temperatures compared to films at room temperature. The mobility and carrier concentration increased, and the crystallinity and grain size also increased at high temperature during deposition. By post deposition annealing at 400°C for very short time duration, the resistivity and transmittance of room temperature films were improved up to $4.8 \times 10^{-4} \Omega\text{-cm}$ and 90.5%. But we found the improved properties have no relation with the structural properties: crystallinity and grain size evaluated by XRD and SEM. The surface roughness of AZO films at high deposition temperature increased to 14 nm by larger grain size, but that by post deposition annealing needs an etching process due to no change of roughness.

5:40pm TF-WeA12 Influence of Growth Rate on the Epitaxial Orientation and Crystalline Quality of CeO_2 Thin Films Grown on $Al_2O_3(0001)$ by Oxygen Plasma-Assisted Molecular Beam Epitaxy. *M. Nandasiri, S. Kuchihbatla, P. Nachimuthu, T. Varga, V. Shutthanandan, W. Jiang, S. Thevuthasan*, Pacific Northwest National Laboratory, *S. Seal*, University of Central Florida, *A. Kayani*, Western Michigan University

Cerium oxide thin films were grown on $Al_2O_3(0001)$ substrates with different growth rates (1-10 Å/min) by oxygen plasma-assisted molecular beam epitaxy (OPA-MBE). The growth rate induced epitaxial orientations and crystalline quality of CeO_2 thin films were studied by in-situ reflection high-energy electron diffraction (RHEED), ex-situ atomic force microscopy (AFM), and high-resolution x-ray diffraction (HRXRD) techniques. CeO_2 grows as three-dimensional (3-D) islands and two-dimensional (2-D) layers at growth-rates of 1-7 Å/min and ≥ 9 Å/min, respectively. The average surface roughness of 5-10 Å shows high-quality surfaces of CeO_2 thin films. The formation of epitaxial $CeO_2(100)$ and $CeO_2(111)$ thin films occurs at growth rates of 1 Å/min and ≥ 9 Å/min, respectively. Glancing incidence XRD measurements have indicated that the films grown at intermediate growth rates (2-7 Å/min) consist of some polycrystalline CeO_2 along with $CeO_2(100)$. The thin film grown at 1 Å/min showed six in-plane domains, characteristic of well-aligned $CeO_2(100)$ crystallites. All six of the repeating rectangle units of O atoms from the oxygen sub-lattice in $Al_2O_3(0001)$ that bind to Ce atoms are nonequivalent which produces six in-plane domains. This also minimizes the lattice mismatch between the thin film and the substrate leading to well-aligned $CeO_2(100)$ crystallites. When increasing the growth rate from 1 Å/min to 2-7 Å/min, the lack of sufficient time to stabilize the Ce atoms on all the rectangle units of O atoms from oxygen sub-lattice in $Al_2O_3(0001)$ results in poorly-aligned $CeO_2(100)$ crystallites that start to coexist along with well-aligned crystallites. Furthermore, the content of the poorly-aligned $CeO_2(100)$ crystallites increases with increasing growth rate up to 7 Å/min, and three out of six in-plane domains gradually decrease and eventually disappear. At growth rates ≥ 9 Å/min, $CeO_2(111)$ film with single in-plane domain was identified. In order to accommodate the $CeO_2(111)$ unit on top of the $Al_2O_3(0001)$, the cerium sub-lattice undergoes compression in all three axes by $\sim 24\%$ resulting in poorly-aligned $CeO_2(111)$ crystallites. The formation of $CeO_2(100)$ 3D-islands at growth rates of 1-7 Å/min is a kinetically-driven process unlike at growth rates ≥ 9 Å/min which result in an energetically and thermodynamically more stable $CeO_2(111)$ surface.

Thursday Morning, October 21, 2010

Graphene Focus Topic

Room: Brazos - Session GR+AS+TF-ThM

Graphene Synthesis on Metals

Moderator: A.W. Ghosh, University of Virginia

8:00am **GR+AS+TF-ThM1 Contrast Behavior of Carbon Adatom Diffusion and Nucleation in the Initial Stage of Graphene Epitaxial Growth on Stepped Metal Surfaces**, *H. Chen, W. Zhu*, University of Tennessee at Knoxville; Oak Ridge National Laboratory, *Z. Zhang*, Oak Ridge National Laboratory; University of Tennessee at Knoxville

Using first-principles calculations within density functional theory, we study the energetics and kinetics of carbon adatom diffusion and nucleation on three stepped metal surfaces: Ir(111), Ru(0001) and Cu(111). We find that on the flat surfaces, two carbon atoms repel each other on Ir(111) and Ru(0001), while they prefer to form a dimer on Cu(111). Moreover, the step edges on Ir and Ru surfaces cannot effectively trap single carbon adatoms either, whereas it is strongly favorable to form carbon dimers at the step edges. The different behaviors are attributed to the competition between C-C bonding and different types of C-metal bonding, and the picture is generalized to other C-on-metal systems with predicted results. These findings provide an insight into the understanding of experimentally observed carbon nucleation in the initial stage of graphene epitaxial growth on metal surfaces.

8:20am **GR+AS+TF-ThM2 Density and Height Distribution of Ru and Bimetallic Pt/Ru Nanoclusters Self-Assembled on Ru(0001) Supported Monolayer Graphene**, *A.K. Engstfeld, S. Beckord, H.E. Hoster, R.J. Behm*, Ulm University, Germany

The Moiré-type nm-scale patterns of graphene monolayers on metal single crystals were recently shown to allow facile fabrication of ordered arrays of virtually monodisperse metal nanoclusters by simple metal vapour deposition in UHV [1-3]. In view of a potential utilization as model systems in electrocatalysis, we have tested the possibility of preparing Ru and bimetallic PtRu clusters by an analogous procedure. This included an extended study on the growth behaviour of the pure Ru clusters. Statistically evaluated STM images indicate that density and height distribution of Ru clusters are largely independent from the evaporation rate at room temperature. Lower/higher cluster densities along with larger/smaller cluster sizes were only achieved by higher/lower substrate temperatures during evaporation. For a given temperature, the lateral density of Ru clusters is higher than that of Pt clusters. Hence, the fabrication of bimetallic clusters can be performed more reliably when Ru is deposited first. We discuss in how far the found growth behaviour can be understood using classic nucleation theory.

8:40am **GR+AS+TF-ThM3 From Perfect Graphene to Cluster Superlattices**, *T. Michely*, University of Cologne, Germany **INVITED**

Through pyrolysis of hydrocarbons on noble metal surfaces monolayer graphite – graphene – is readily formed. Using scanning tunneling microscopy (STM) and low energy electron microscopy (LEEM) we investigate the temperature dependent growth and the nature of point and line defects in the graphene layer on Ir(111). We identify heptagon-pentagon pairs of carbon atom rings to accommodate for slight misalignments of graphene domains, and wrinkles in the graphene layer for the mismatch in thermal expansion of graphene and Ir. After a systematic optimization of the growth procedure we obtain a single sheet of well oriented graphene on Ir(111) with a minimum of point and line defects.

Angle resolved photo emission finds graphene on Ir(111) to be only marginally doped and to display the characteristic Dirac cone at the K-point of the graphene Brillouin zone. The absence of hybridization of Ir and graphene states is consistent with the weak graphene - Ir interaction, as inferred from the large graphene - substrate separation as measured by the X-ray standing wave method and calculated by density functional theory including van der Waals interactions. The moiré resulting from the incommensurate epitaxy of graphene on Ir(111) gives rise to a large graphene supercell. In the graphene electronic structure it is reflected by the opening of minigaps at the boundaries of the induced mini-Brillouin zone.

The graphene moiré with Ir(111) is an active template allowing one to grow superlattices of metal clusters (Ir, Pt, Au, W, Fe, Re, Co, etc), spatially and thermally stable below 450 K. The graphene moiré enables also patterned adsorption of molecules and the template effect is not limited to the Ir(111) substrate. Based on STM and XPS measurements as well as density functional theory calculations it is proposed that at geometrically defined locations within the supercell and if sandwiched between substrate and

cluster metal the graphene rehybridizes from sp^2 graphitelike to sp^3 diamondlike bonding, resulting in strong covalent bonds between metal and graphene. The relevance of the graphene template effect for nanocatalysis, nanomagnetism and electrochemistry will be outlined.

9:20am **GR+AS+TF-ThM5 Graphene on Pd(111): In situ Low-Energy Electron Microscopy Studies of Growth Kinetics and Structure – Work Function Relationship**, *S. Kodambaka, Y. Murata*, University of California Los Angeles, *E. Starodub, N.C. Bartelt, K.F. McCarty*, Sandia National Laboratories

Using *in situ* low-energy electron microscopy, we investigate the dynamics of graphene layer formation and the relationship between domain structure and its work function on Pd(111). We observe, in real time, the nucleation and growth of graphene islands during cooling via surface segregation of C atoms from the Pd bulk. Interestingly, we observe rapid motion of Pd substrate surface steps during graphene growth. Using low-energy electron diffraction, we identify at least five different orientations (domains) of monolayer graphene islands on the surface. We determine their relative orientations with respect to the substrate as approximately 2° , 6° , 11° , 19° , and 26° . We measured electron reflectivity (image intensity) values for each of the domains as a function of incident electron energy. From this data, we extracted the work functions of graphene domains which are found to vary with the domain orientation. Our results suggest that the substrate-graphene interactions influence the growth kinetics as well as the electronic structure of graphene.

9:40am **GR+AS+TF-ThM6 Second-Layer Graphene on Ir(111) – Relating Growth Mechanism to Physical and Electronic Structure**, *S. Nie*, Sandia National Labs, *A.L. Walter*, Lawrence Berkeley National Lab and Fritz-Haber-Institut der Max-Planck-Gesellschaft, Germany, *E. Starodub, K.F. McCarty, K. Thürmer*, Sandia National Labs, *K. Horn*, Fritz-Haber-Institut der Max-Planck-Gesellschaft, Germany, *A. Bostwick*, Lawrence Berkeley National Lab, *N.C. Bartelt*, Sandia National Labs, *E. Rotenberg*, Lawrence Berkeley National Lab

An interesting question is how the second layer of graphene grows on transition-metal substrates. First-layer graphene on Ir(111) [1] exists with four discrete in-plane orientations relative to substrate directions [2]. Thus, this system offers potential to better understand the relationship between second-layer growth and first-layer structure. We use low-energy electron microscope (LEEM) to characterize where the second-layer graphene forms on Ir(111) covered by domains of differently oriented first-layer graphene. We find that the second layer does not grow easily where the lattice of the first-layer graphene is aligned with the lattice of the substrate. Instead the second-layer graphene forms most easily where the first-layer graphene is rotated, by 30° , for example. Angle-resolved photoemission spectroscopy (ARPES) confirms this strong preference. So how does the orientation of the first layer control the growth of the second layer? ARPES and Raman spectroscopy provide insight, revealing that the rotated variants of first-layer graphene are even less strongly bound to the substrate than the more abundant, non-rotated variant [3]. This information suggests the following growth mechanism. Carbon atoms segregating from the substrate build up in concentration under the first layer. The second layer nucleates and grows where it is easier to debond the first layer from the substrate, that is, under the rotated first-layer domains. Electron diffraction also reveals that the second graphene layers are usually but not always aligned with the first-formed layer. Finally, we will discuss the doping of the different types of second-layer graphene, as revealed by ARPES.

This work was supported by the Office of Basic Energy Sciences of the US DOE under Contracts No. DE-AC04-94AL85000 (SNL) and No. DE-AC02-05CH11231 (LBL).

[1] A. T. N'Diaye, J. Coraux, T. N. Plasa, C. Busse, and T. Michely, *New J. Phys.* 10, 16 (2008).

[2] E. Loginaova, S. Nie, K. Thürmer, K., N. C. Bartelt, and K. F. McCarty, *Phys. Rev. B* 80, 085430 (2009).

[3] I. Pletikovic, M. Kralj, P. Pervan, R. Brako, J. Coraux, A. T. N'Diaye, C. Busse, and T. Michely, *Phys. Rev. Lett.* 102, 056808 (2009).

10:40am **GR+AS+TF-ThM9 Graphene on Transition Metals – Growth and Interfacial Processing**, *P. Sutter, E. Sutter*, Brookhaven National Laboratory **INVITED**

Graphene has been used to explore the fascinating properties of two-dimensional sp^2 bonded carbon, and shows great promise for applications. A key bottleneck lies in synthesizing the required starting material: structurally perfect, macroscopically large graphene sheets with uniform thickness, into which active device structures can be patterned.

Epitaxial growth on transition metals has recently become one of the most promising methods for large-scale graphene synthesis. Here we discuss the fundamental mechanisms of graphene growth on ruthenium [1] and platinum [2], both single crystals and polycrystalline thin films, studied by a combination of *in-situ* surface microscopy methods. Real-time observations by low-energy electron microscopy (LEEM) show that epitaxy on Ru(0001) produces arrays of macroscopic monolayer graphene domains, whose coalescence is followed by the formation of large bilayer areas in a controlled layer-by-layer fashion. LEEM imaging together with diffraction, selected-area angle resolved photoemission spectroscopy (micro-ARPES), and scanning tunneling microscopy provide unique insight into the interaction between graphene and transition metal substrates, key to the synthesis of high-quality graphene [2, 3].

Beyond large-scale synthesis, potential applications of graphene will require novel approaches to processing and functionalization. We will highlight experiments by real-time surface microscopy to understand chemical reactions at graphene-metal interfaces, which may become part of novel processing strategies for graphene devices.

Work performed under the auspices of the U.S. Department of Energy under contract No. DE-AC02 98CH1-886.

- [1] P. Sutter, J.I. Flege, and E. Sutter, *Nat. Mater.* **7**, 406 (2008).
- [2] P. Sutter, J.T. Sadowski, and E. Sutter, *Phys. Rev. B* **80**, 245411 (2009).
- [3] P. Sutter, M.S. Hybertsen, J.T. Sadowski, and E. Sutter, *Nano Lett.* **9**, 2654 (2009).

11:20am **GR+AS+TF-ThM11 Real-time Analysis of Graphene Growth on Polycrystalline Copper Foils**, *J.M. Wofford*, University of California at Berkeley and Lawrence Berkeley National Lab, *S. Nie, N.C. Bartelt, K.F. McCarty*, Sandia National Laboratories, *O. Dubon*, University of California at Berkeley and Lawrence Berkeley National Lab

Despite the potentially significant technological impact of graphene synthesis on Cu, little is understood about both the growth kinetics of this system and the morphology of the resulting heterostructure. We use low-energy electron microscopy (LEEM) to observe directly the UHV growth of graphene on polycrystalline Cu foils by the electron-beam evaporation of carbon. The temperatures required to synthesize highly ordered graphene simultaneously induce significant Cu sublimation and step flow, leading to a dynamic growth surface. As a result a complex interdependence develops between the graphene growth behavior and Cu surface morphology, with the graphene islands limiting Cu step mobility, and Cu step bunching distorting the propagation of the graphene growth front. This interplay becomes increasingly dramatic over time as the inhomogeneous sublimation of Cu leads to considerable surface roughening. In addition, the graphene islands are not compact in shape. Instead, the islands are ramified, consisting of several distinct lobes extending from a common nucleation site. Diffraction analysis reveals that each constituent lobe has a different in-plane orientation relative to the copper grain below and that the growth velocity of a given lobe depends strongly on its orientation relative to the underlying Cu at the growth front. We will describe the relationship between the orientation-dependent growth velocity and the local atomic geometry at the edge of the graphene sheet. Finally, the implications of this unexpected nucleation and growth mechanism on the formation of high-quality graphene films on Cu foils are evaluated.

Work at Sandia was supported by the Office of Basic Energy Sciences, Division of Materials Sciences, U. S. Department of Energy under Contract No. DE-AC04-94AL85000. Work at LBNL was supported by the Director, Office of Science, Office of Basic Energy Sciences, Division of Materials Sciences and Engineering, of the U.S. Department of Energy under Contract No. DE-AC02-05CH11231. JMW acknowledges the support from an NSF fellowship.

11:40am **GR+AS+TF-ThM12 Moiré Superstructures of Graphene on Faceted Nickel Islands**, *Y. Murata*, University of California Los Angeles, *V. Petrova*, University of Illinois at Urbana-Champaign, *B.B. Kappes, A. Ebnommasir*, Colorado School of Mines, *I. Petrov*, University of Illinois at Urbana-Champaign, *Y.-H. Xie*, University of California Los Angeles, *C.V. Ciobanu*, Colorado School of Mines, *S. Kodambaka*, University of California Los Angeles

Using scanning tunneling microscopy and spectroscopy, in combination with density functional theory (DFT), we investigated the morphology and electronic structure of monolayer graphene grown on the (111) and (110) facets of three-dimensional nickel islands on highly oriented pyrolytic graphite substrate. We observed hexagonal and stripe moiré patterns with periodicities of 22 Å and 12 Å, respectively, on (111) and (110) facets of the Ni islands. Graphene domains are also observed to grow, as single crystals, across adjacent facets and over facet boundaries. We suggest that the unexpected observation of moiré patterns of graphene on lattice-matched Ni(111) and the formation of single-crystalline domains across

different surface orientations are a consequence of the kinetic limitations of growth, rather than of the strength of the C-Ni interactions. Scanning tunneling spectroscopy data indicate that the graphene layers are metallic on both Ni(111) and Ni(110), in agreement with the DFT calculations. We attribute this behavior to strong hybridization between the *d*-bands on Ni and the *p* bands of carbon. Our findings point to the possibility of preparing large-area epitaxial graphene layers even on polycrystalline Ni substrates.

Magnetic Interfaces and Nanostructures

Room: Zuni - Session MI+TF-ThM

Magnetic Nanostructures, Thin Films and Heterostructures

Moderator: C. Clavero, College of William & Mary

8:00am **MI+TF-ThM1 AC Susceptibility of Ni Bars with Magnetic Single Domain**, *X.G. Zhang, I.I. Kravchenko, S.T. Retterer, J.F. Wendelken, Z. Gai*, Oak Ridge National Laboratory

For thin films, the generalized Curie-Weiss law extends the power law scaling well above T_c by replacing the linear reduced temperature t_L by a nonlinear reduced temperature $t_{NL}=1-T_c/T$. The film thickness d and temperature T are usually not independent variables in the scaling. Using the nonlinear reduced temperature, the power law scaling was shown to be accurate over the entire paramagnetic regime [1-3]. However, at low temperature, thermally activated domain wall motion is expected to contribute significantly to the temperature dependence of magnetic properties, therefore the scaling law is generally believed not to extend far below T_c . Such belief was contradicted by a very recent experiment [4] that showed a surprising power law scaling for the in-plane susceptibility of sputtered Ni films deposited on silicon for the entire temperature range between zero and T_c . In addition, thickness and temperature dependence are completely decoupled. This scaling result implies that even in the ferromagnetic regime, there is no domain wall motion contribution to the low field susceptibility [4]. To clarify the role of domain wall motion, arrays of single domain Ni microstructures are studied experimentally and theoretically. We will show the results of the AC susceptibility measurements of Ni microstructures with magnetic single domain, in which the contributions of domain wall motion and spin fluctuation to the susceptibility are separated.

This research at Oak Ridge National Laboratory's Center for Nanophase Materials Sciences was sponsored by the Scientific User Facilities Division, Office of Basic Energy Sciences, U.S. Department of Energy.

- [1] H. Lutz, P. Scobisria, J. E. Crow, and T. Mihalism, *Phys.Rev. B* **18**, 3600 (1978).
- [2] M. Fahnle and J. Souletie, *J. Phys.c* **17**, L469 (1984).
- [3] A. S. Arrott, *Phys. Rev. B* **31**, 2851 (1985).
- [4] X. H. Song, X.-G. Zhang, J. Fan, Y. R. Jin, S. K. Su, and D. L. Zhang, *Phys. Rev. B* **77**, 092408 (2008).

8:20am **MI+TF-ThM2 Deuterium Absorption in Co/Pd Multilayers**, *K. Munbodh, F.A. Perez, D. Lederman*, West Virginia University, *M. Zhernenkov, M. Fitzsimmons*, Los Alamos National Laboratory

The absorbed concentration of deuterium was calculated in Co/Pd multilayers at standard temperature and pressure using in-situ neutron reflectometry. The out-of-plane film expansion and deuterium concentration-depth profiles were determined from the fitting of the neutron reflectivity data. The measurements demonstrated that deuterium is absorbed in all the Pd layers. However, the concentration of the hydrogen varies with Pd layer thickness. Polarized neutron reflectometry with applied field of 6.5 kOe in the plane of the sample was performed and the detailed magnetic depth profile was established. These results showed an overall increase in magnetization upon deuterium absorption.

8:40am **MI+TF-ThM3 Correlated Structural and Magnetic Studies of Capping and Seed Layer Dependent Epitaxial FePd Thin Films**, *L. Wang, J.R. Skuza*, College of William & Mary, *T. Mewes*, University of Alabama, *C. Clavero, R.A. Lukaszew*, College of William & Mary

FePd binary alloys can form a chemically ordered phase ($L1_0$) that exhibits interesting properties such as high perpendicular magnetic anisotropy (PMA). This property has drawn great attention for many technological applications such as ultrahigh density magnetic recording media and spin transfer torque random access memory (STT-RAM). We investigate the influence of different capping layers (Au, Pd and V and compare with an insulating capping layer such as MgO) on the magnetic properties, particularly the magnetic anisotropy and damping, of highly anisotropic $L1_0$

FePd films which were grown onto MgO (001) substrates using magnetron sputtering in an ultra-high vacuum deposition system. We use x-ray diffraction techniques to study the chemical ordering of the films, and vibrating sample magnetometry (VSM), magnetic force microscopy (MFM) and ferromagnetic resonance (FMR) to investigate the magnetic properties. Our aim is to investigate and tailor the structural and magnetic properties of highly ordered FePd thin films with strong PMA via adequate choice of capping and seed layer materials.

We thank W. Chen and S. A. Wolf for their collaboration. Funding for this project was obtained from NSF grants DMR 0804243 and DMR 0605661 and a Cottrell Scholar Award from the Research Corporation.

9:00am **MI+TF-ThM4 Microstructural, Magnetic Anisotropy, and Magnetic Domain Structure Correlations in $L1_0$ Ordered Thin Films**, *J.R. Skuza, L. Wang, College of William & Mary, W. Chen, J. Lu, University of Virginia, T. Mewes, University of Alabama, C. Clavero, R.A. Lukaszew, College of William & Mary*

9:20am **MI+TF-ThM5 Correlating Microstructure with Magnetic Properties Variation in Patterned Magnetic Nanostructures with Transmission Electron Microscopy**, *J.W. Lau, National Institute of Standards and Technology* **INVITED**

Patterned magnetic nanostructures are keystone components in technologies such as hard drive media, sensors, and the magnetoresistive device variants (read-head, random access memory, logic). During manufacturing, different processes produce defects that are the source of variations in magnetic properties in magnetic nanostructures. One example is the Co/Pd nanodot array, interesting for its potential in realizing the bit-patterned media data storage platform. We showed that grains of a particular orientation formed during the film deposition can act as trigger sites for magnetization reversal. Therefore, the ease of switching a particular nanodot among millions of nominally identical nanodots depends on the random presence of trigger grains within it. When considered as an ensemble, the nanodot array will exhibit a switching field distribution; this is the superposition of the individual switching fields unique to each nanodot. In general, switching field distribution and other magnetic property variations in patterned magnetic nanostructures can present major problems for devices development where uniform magnetic performances are required.

The fact that magnetic phenomena in patterned magnetic nanostructures, whether it be magnetization reversal or magnetoresistance, are always observed as distributions means that it is important to identify the root causes to these distributions. An essential aspect to furthering the progress in developing magnetic nanostructure devices is therefore, to correlate nanostructure, defects and interfaces, and chemical composition to magnetic behaviors on the nanoscale. To this end, one of our main focuses is in developing ways to measure variations in magnetic properties using transmission electron microscopy (TEM). TEM is one of the few tools that can provide structural, chemical and magnetic information all at the same time.

In this presentation, I will highlight specific examples of measurements developed for patterned magnetic nanostructures using a TEM. The first example is the microstructure correlation to the switching field distribution in Co/Pd nanodots, described earlier. The second example is a set of *in situ* tunneling measurements where we succeeded in measuring unique energy barrier height and tunneling magnetoresistance (TMR) on fully functional nano-magnetic tunnel junctions (MTJ) built as a TEM sample. Finally, I will show how single nanostructure magnetometry can be achieved within a TEM.

10:40am **MI+TF-ThM9 Partial Perpendicular Anisotropy of CoFeB with Vanadium Capping**, *A. Natarajathinam, Z.R. Tadisina, S. Gupta, University of Alabama*

Magnetic tunnel junctions with vanadium-based capping layers on top of the CoFeB free layer have been studied. The interest in the effect of capping on the free layer originated from reports⁽¹⁾ that cap layers influence the crystallization of the CoFeB free layer through diffusion of the B into the cap, as well as induce a partial perpendicular magnetic anisotropy (PPMA or PPA) in the free layer^(2,3). Different cap layers differently accelerate the diffusion of the B from the free layer. In this study, we have sputter-deposited V/Ru and V/Ta capping layers on CoFeB and subsequently characterized these films by magnetometry and ferromagnetic resonance (FMR). We have found that V/Ru and V/Ta capping of CoFeB induces partial perpendicular anisotropy (PPA) in CoFeB, as well as reduces the Gilbert damping parameter, confirming results reported by other researchers⁽⁴⁾. The origin of this PPA is believed to be caused by the interface anisotropy between the free layer and the capping layer. The effect of post-deposition annealing, CoFeB thickness, and doping of CoFeB with vanadium on the anisotropy and damping of these V/Ru and V/Ta capped samples has been studied for the free layers. Doping CoFeB with vanadium

greatly reduces the $4\pi M_s$ and $4\pi M_{eff}$ values, resulting in an effective increase in the PPA, as well as the damping parameter. X-ray magnetic circular dichroism (XMCD) has also been performed on a series of V-doped films over a range of V concentrations. Magnetic tunnel junctions were fabricated to study device properties of the V-capped and V-doped films. The mechanisms for increasing TMR in these types of pMTJ's will be discussed.

This work is supported by the U.S. Department of Defense DARPA-MTO STT-RAM Universal Memory contract, and Grandis Inc., Milpitas, CA.

1. T. Miyajima, T. Ibusuki, S. Umehara, M. Sato, S. Eguchi, M. Tsukada, and Y. Kataoka, *Appl. Phys. Lett.* **94**, 122501 (2009).

2. E. Chen, D. Apalkov, Z. Diao, A. Driskill-Smith, D. Druist, D. Lottis, V. Nikitin, X. Tang, S. Watts, S. Wang, S. A. Wolf, A. W. Ghosh, J. W. Lu, S. J. Poon, M. Stan, W. H. Butler, S. Gupta, C. K. A. Mewes, T. Mewes, and P. B. Visscher, (invited paper), *IEEE Trans. Magn.* **46**, 1 (2010).

3. S. M. Watts, X. Tang, Z. Diao, D. Apalkov, D. Druist, E. Chen, V. Nikitin "Low switching current in conventional in-plane STT-RAM structure with partial perpendicular anisotropy", *Digest FV-11, 11th Joint MMM-Intermag Conference, Washington, DC* (2010).

4. D. Worledge, D. Abraham, S. Brown, M. Gaidis, G. Hu, C. Long, J. Nowak, E. O'Sullivan, R. Robertazzi, J. Sun, P. Trouilloud, *11th Joint MMM-Intermag Conference, Washington, D. C.* (2010).

11:00am **MI+TF-ThM10 Magnetic Properties of $Fe_xNi_{1-x}Fe/Co$ Bilayers**, *F.A. Perez, D. Lederman, West Virginia University*

$Fe_xNi_{1-x}Fe/Co$ bilayers were deposited on single-crystal MgF_2 (110) substrates via molecular-beam epitaxy. The RHEED patterns were used to characterize the surface crystallinity during growth. The high angle x-ray diffraction (XRD) allowed establishing epitaxial growth directions and in- and out-of-plane crystallinity coherences. The x-ray reflectivity (XRR) patterns were used to establish the layer thicknesses and the interface roughness parameters. The Fe-concentration was estimated from XRD lattice parameters and the XRR fittings and it was according with that from XPS analysis. The magnetic anisotropies of the Co layer were measured via standard magnetometry measurements.

11:20am **MI+TF-ThM11 Electrical Properties of Ni,Fe_2O_3 and $NiO,Fe_{1.925}Sm_{0.075}O_3$ Thin Films**, *K.B. Karuppanan, University of Texas at El Paso, M. Garimalla, IIT Madras, India, C.V. Ramana, University of Texas at El Paso*

Nickel ferrite is one of the most versatile and technologically important ferrite materials because of its high Curie temperature, high saturation magnetization, low conductivity and thus lower eddy current losses, high electrochemical stability, catalytic behavior. The focus of the present work was to grow Ni,Fe_2O_3 and $NiO,Fe_{1.925}Sm_{0.075}O_3$ thin films by RF magnetron sputtering and study their structural and electrical properties. Ni,Fe_2O_3 and $NiO,Fe_{1.925}Sm_{0.075}O_3$ films were grown by sputtering the bulk NiO,Fe_2O_3 and $NiO,Fe_{1.925}Sm_{0.075}O_3$ targets prepared by solid state chemical reaction. The results indicate that the as-grown films were amorphous. Samples annealed at 1073 K were crystalline. DC electrical conductivity measurements performed in the temperature range 60-300 K indicate the insulating behavior of the materials. The room-temperature conductivity of the $NiO,Fe_{1.925}Sm_{0.075}O_3$ film is less than that of pure Ni ferrite film. Analysis of the conductivity indicates that the small polaron and variable-range-hopping (VRH) mechanisms are operative in 180-300 K and 60-180 K temperature regions, respectively. Frequency variation of the electrical resistivity measurements in the range 1 kHz - 13 MHz indicate that the resistivity decreases with increasing frequency. The mean relaxation time and spreading factor values were found to be larger for the $NiO,Fe_{1.925}Sm_{0.075}O_3$ film which could be due to the fact that larger Sm^{3+} ion leads to increased bond distance.

11:40am **MI+TF-ThM12 Structural, Transport and Magnetic Properties of $SrSn_{0.95}Fe_{0.05}O_3$ Thin Films**, *G. Prathiba, IIT Madras, India, S. Venkatesh, Tata Institute of Fundamental Research (TIFR), India, N. Harish Kumar, IIT Madras, India*

Transparent magnetic semiconductors are potential materials for multifunctional magneto-opto-electronic devices. Wide band gap oxides are the best candidates for transparent semiconductors. Following the prediction of Dietl et al.,¹ on possible ferromagnetic ordering in wide band gap semiconductors doped with magnetic elements, the focus was on oxide dilute magnetic semiconductors. $SrSnO_3$ is a wide band gap material with a direct band gap of 4.27 eV. At room temperature it crystallizes in perovskite orthorhombic structure. The electrical resistivity of $SrSnO_3$ on forming solid solution with $SrFeO_3$ decreases. $SrSn_{0.95}Fe_{0.05}O_3$ thin films were prepared by RF magnetron sputtering on oxidized silicon (100) substrates at room temperature. The films were annealed at 1073 K for two hours. The as deposited films were found to be amorphous whereas the annealed films

were polycrystalline in nature. The surface morphology of the films studied using Atomic Force Microscopy (AFM) showed low roughness value (Root mean square value of surface roughness – 2.02 nm). The resistivity of the film was measured using two probe method in the temperature range 200 to 300 K. The variation of resistivity with temperature exhibits semiconducting behaviour. Using Arrhenius plot [$\rho = \rho_0 \exp(E/kT)$] the activation energy was found to be 0.39 eV. The magnetic measurements done using Superconducting Quantum Interference Device (SQUID) magnetometer showed ferromagnetic ordering below 20 K.

Reference:

¹T. Dietl, H. Ohno, F. Matsukura, J. Cibert and D. Ferrand, *Science*, 287 (2000) 1018

Thin Film

Room: Ruidoso - Session TF-ThM

Modeling and Analysis of Thin Films

Moderator: S.B. Sinnott, University of Florida

8:00am **TF-ThM1 Thermodynamics of Clustering and Magnetism in $Ti_{1-x}Al_xN$ and $Ti_{1-x}Cr_xN$ Thin Film Materials from First-Principles**, B. Alling, I.A. Abrikosov, L. Hultman, Linköping University, Sweden

Multinary nitride materials are widely used as coatings for wear protection of cutting tools, e.g. TiAlN, as well as in thin film electronic applications. One important aspect of the success of TiAlN is a composition dependent thermodynamically driven age-hardening process through spinodal decomposition into TiN and cubic AlN at cutting tool operational temperatures. To understand this phenomena and to be able to tailor optimal compositions for different applications, we perform a thorough theoretical thermodynamics investigation based on first principles calculations.

By mapping the complete quantum mechanical complexity of the system onto a generalized Ising Hamiltonian for the configuration of Ti and Al atoms, we are able both to predict thermodynamics using accurate Monte Carlo simulations and achieve a deeper understanding of the interactions governing the system.

One physical property that is difficult to find in nitrides and which disfavors the usage of the materials class in spintronics, is room temperature ferromagnetism. TiCrN is one of the rare nitride systems where strong ferromagnetism is seen. We use our methodological framework to analyze and explain why the magnetic interactions that favor anti-ferromagnetism in pure CrN is changed in the TiCrN solid solution, as well as the intricate dependence of the Curie temperature on the CrN content.

8:20am **TF-ThM2 Electronic Mechanism for Toughness Enhancement in $V_xM_{1-x}N$ Thin Films**, D.G. Sangiovanni, V. Chirita, L. Hultman, Linköping University, Sweden

We use Density Functional Theory (DFT) calculations in the generalized gradient approximation (GGA) to predict the properties of a number of novel V-M-N thin films in the B1 (NaCl) structure. The new compounds are obtained by alloying VN with Nb, Mo and W, in concentrations of 50 %. We evaluate the elastic moduli and constants of these ternaries and perform a detailed analysis of their electronic structure. These results are compared with the corresponding properties of typical binaries such as TiN and VN. Our calculations show that the new ternaries have hardness comparable with TiN and VN, and significantly, a resolute ductile behavior. This unique combination of hardness/ductility, which is in contrast to the hardness/brittleness relationship typically found in hard coatings, equates to significantly increased toughness, as confirmed by the stress-strain relationship we obtain for all these compounds. The electronic structure results presented herein reveal a layered charge density, consisting in alternating high and low electron density regions, similar to that recently reported for Ti-Mo/W-N thin films [1]. To fully understand the mechanism responsible for this interleaved arrangement of electrons, we carry out crystal orbital overlap population (COOP) and electron localization function (ELF) calculations, and succeed to energetically resolve the bonding/antibonding contributions, of the first and second neighbors, to the chemical bonds in these compounds. Based on the results of this analysis, we find that the electronic mechanism responsible for the observed toughness enhancement in these compounds is rooted in the increased metal-metal (second neighbors) interaction of $d-t_{2g}$ orbitals.

[1] D.G. Sangiovanni, V. Chirita and L. Hultman, *Phys. Rev. B* **81**, 104107 (2010)

8:40am **TF-ThM3 2010 Gaede-Langmuir Award Lecture- X-ray Absorption Spectroscopy and Many Electron Theory Applied to O-vacancy State Differences between (i) Non-crystalline SiO_2 and (ii) Nano-crystalline HfO_2 Thin Films**, G. Lucovsky*, North Carolina State University **INVITED**

Correlated atomic positions of Si-atoms bonded to 2-fold coordinated O-atoms are determined by Si $3d$ -derived T_{2g} states on these atoms [1]. These states constrain dihedral angles contributing to medium range order with correlation lengths of ~0.4 and 0.45 nm, and, a coherence length of ~1 nm, each obtained from the first sharp diffraction peak in X-ray diffraction [2]. O K edge soft X-ray SiO_2 spectra reveal conduction band edge states with singly degenerate A_1 symmetry, and stronger doubly and triply degenerate E and T_2 d -state beginning at energies ~3 eV higher. This difference is smaller in c-Si, ~1 eV. Analysis of O K and $L_{2,3}$ spectra are based on a charge transfer multiplet many electron theory [3]. Energy differences are the same for band edge features obtained from transmission/reflectivity studies in the visible/VUV where the d -state character was not previously recognized [4]. The correspondence derives from O 1s core hole localization, and a coherent process in which 1s core holes are filled by electrons from valence band O 2p p states, accounting for the one-to-one correspondence between sequenced features in the O K edge, and in the Si $L_{2,3}$ spectrum of SiO_2 . $L_{2,3}$ spectra, studied by electron energy loss spectroscopy (EELS), have not detected the weaker Si A_1 features in the 100 to 104 eV regime of SiO_2 , or 98 to 100 eV regime of c-Si. The O K edge X-ray spectra of transition metal elemental and complex oxides are qualitatively different with either doubly or triply degenerate d -state derived spectral features at the band edge. This results in significant quantitative differences in (i) the high-spin excited d -states of O-atom vacancy occupied d^2 states, and (ii) the negative ion electronically active d -state traps populated by charge injection. O-vacancy states in SiO_2 are close to mid-gap, and do not contribute to gate stack tunneling processes. This explains the order of magnitude higher interfacial trap densities, d_{it} , and trap-assisted tunneling in HfO_2 gate stacks. It also accounts for significant differences in radiation hardness. XAS spectra are presented for the first time for remote plasma deposited GeO_2 . These deposited films display significantly different O K edge spectra than those obtained by oxidation of Ge; more importantly A_1 , and E and T_{2g} features stronger and narrower than those of SiO_2 . Electrical data for deposited GeO_2 dielectrics on Si and Ge substrates are compared for the first time with SiO_2 test devices on the same substrates.

[1] Whitten J, et al., *J. Vac. Sci. Technol. B* 20, 1710 (2002).

[2] Lucovsky G, et al. *physica status solidi (a)* 207, 631 (2010).

[3] de Groot F, Kotani A. *Core level spectroscopy of solids* (Boca Raton, CRC, 2008).

[4] Laughlin RB, *Phys. Rev. B* 22, 3021 (1980).

9:20am **TF-ThM5 New Parameterization of the Modified Embedded Atom Potential for Large Scale Simulations of TiN Thin Films Growth**, D.G. Sangiovanni, V. Chirita, L. Hultman, Linköping University, Sweden

Classical Molecular Dynamics (MD) has become an indispensable tool in thin films modeling, as it allows the study of systems and phenomena reaching far beyond the inherent limitations of ab-initio and/or Density Functional Theory (DFT) methods. Generally, the range of systems to which the method can be applied has typically been limited to materials characterized by single-type bonding, such as ionic, covalent or metallic. This situation has been considerably improved in the last decade within the formalism of the Modified Embedded Atom Method (MEAM), which allows the treatment of mixed-type bonding materials, and in recent years, a number of studies have been devoted to MD simulations of important model systems such as TiN. Nevertheless, the very few MEAM parameterizations for TiN reported thus far are able to reasonably reproduce bulk, as well as some surface properties of this material. However, if meaningful MD simulations of TiN thin films growth are to be performed, a number of critical nucleation and diffusion phenomena have to be accounted for besides basic bulk/surface properties. Herein, we propose a new parameterization of the MEAM interaction potential for TiN, which in addition to correctly predicting bulk and surface properties, reproduces the experimentally observed trends in the diffusion of single species (Ti, N) and Ti-N dimers, on the most representative steps/surfaces for TiN growth, the (100) and (111) respectively. Our estimations of activation energies for diffusion and Ehrlich-Schwoebel (ES) step-edge barriers are in good agreement with previous ab-initio calculations and experimental observations. Consequently, this new MEAM parameterization has the potential to adequately account for most essential processes during the initial stages of TiN nucleation, which, as it is well known, dramatically

* Gaede Langmuir Award Winner

affect the growth mode and properties of thin films in laboratory and computer experiments.

9:40am **TF-ThM6 DSMC Modeling of Metal Vapor Flow in Vacuum in Application to Thin-Film Depositions**, V. Ayyaswamy, A. Alexeenko, Purdue University

Electron beam assisted physical vapor deposition (EBPVD) is widely used in a number of vacuum material processing applications for deposition of thin films of metals. The properties of these thin films including thickness uniformity, growth rates and other material properties are dependent, to a great extent, on the geometric configuration of the deposition source and electron gun power. A complete understanding of the deposition process requires the ability to accurately simulate the vapor flow that varies from highly collisional in regions near the source to being free-molecular near the substrate location. The direct simulation Monte Carlo technique, which is by far the most powerful technique to simulate such flows rapidly expanding into vacuum, requires an accurate molecular model for the interaction between the metal vapor atoms. A molecular model has been formulated [1] for the interaction of Cu atoms and validated with experimental data for electron-beam deposition of copper. The main goal of this work is to formulate molecular models for common metal vapors including Gold, Titanium, Nickel, and Aluminium and validate them with experimental data[2,3] for thin-film growth rates at various evaporation rates. The ability to accurately model deposition processes of thin films of metals would greatly assist in the design and control of such vacuum deposition systems and processes.

References

- [1] A. Venkatraman and A.A. Alexeenko, "DSMC Modeling of E-beam Metal Deposition", J. Vac. Sci. & Tech. A, July 2010 (*accepted*).
- [2] D. Chaleix, P. Choquet, A. Bessaudou, L. Frugier, and J. Machet, "A spatial distribution study of a beam vapour emitted by electron-beam-heated evaporation sources", J. Phys. D: Appl. Phys. 29(1996) 218-224.
- [3] K.B. Thakur and G.K.Sahu, "Spatial distribution of copper vapour flux during strip electron beam vaporation", J. Phys. D: Appl. Phys. 35(2002) 1812-1820.

Thursday Afternoon, October 21, 2010

Spectroscopic Ellipsometry Focus Topic

Room: Cochiti - Session EL+AS+EM+MS+TF-ThA

Spectroscopic Ellipsometry

Moderator: A.M. Creatore, Eindhoven University of Technology, the Netherlands

2:00pm **EL+AS+EM+MS+TF-ThA1 Developments in Spectroscopic Ellipsometry for Characterization of Organic and Inorganic Surfaces, Interfaces and Complex Layered Materials, M. Schubert**, University of Nebraska - Lincoln **INVITED**

In this paper we will review new developments in Spectroscopic Ellipsometry for characterization of organic and inorganic surfaces, interfaces and complex layered materials. Ellipsometry has matured over the past two decades with instrumentation and methodology capable of addressing today's and tomorrow's challenges in materials characterization and metrology. Ellipsometry measures the general state of polarization of light reflected or transmitted from samples. Owing to its nondestructive and generally applicable concept of investigating light emerging from specimens under investigations, and owing to its extreme accuracy and precision, ellipsometry has paved the way for almost all our modern technologies, continues to enable next-generation devices in electronics and optoelectronics, and emerges into fields of chemical, biochemical and biological platform technologies. Originating from the identification that the information carried upon the polarization within a light beam emerging from surfaces is extremely sensitive to mono and submonolayer characteristics, ellipsometry started decades ago pioneering development of microprocessors and electronic devices, which still today are based on planar thin film technology. Without ellipsometry, today's computation and information technology would be still in its infancy. In this paper, emerging developments and applications for metrology of optical and electrical properties of semiconductors and nanostructures by Terahertz Magneto-optic generalized ellipsometry, also referred to as the Optical Hall effect, will be highlighted. Examples will include state-of-the-art nitride semiconductor device structures and epitaxial graphene, candidates for tomorrow's next-generation devices. Likewise, new approaches for characterizing precise structural, magnetic and optical properties of three-dimensional nanostructure hybrid materials will be discussed. Examples will describe how ellipsometry characterization enables understanding and tailoring of electromagnetic properties of materials created by human intelligence, rather than by nature. New horizons are being explored currently by combining ellipsometry with independent surface sensitive techniques, such as acoustic Quartz-Crystal microbalance techniques. Combinations allow for identification of new information not accessible otherwise. Examples include observation of in-situ formation of self-assembled monolayers, protein adsorption onto sensitized surfaces, and formation of micelle-assisted bilayer configurations. Prospects, challenges and future developments will be reviewed from today's perspective.

2:40pm **EL+AS+EM+MS+TF-ThA3 Characterizing the Adsorption – Desorption Behavior of Organic Molecules Within Thin Mesoporous Carbon Composite Films using Spectroscopic Ellipsometry, B.D. Vogt, L.Y. Song, M.Z. Dai**, Arizona State University

Porous carbon materials are commonly utilized as adsorbants (i.e. activated carbon) and as catalyst supports. Direct templated synthetic routes to form ordered mesoporous carbons have recently been developed. By utilizing these concepts, mesoporous carbon composite films containing metal oxides can be synthesized. As a wide range of metal oxides can be utilized, these materials could be utilized in chemical sensing applications or as catalysts in fuel cell membranes. For both of these applications, the porous material will be exposed to organic vapors (such as ethanol in fuel cells). The condensation and evaporation of organic vapors from these materials is therefore an important consideration for their ultimate utilization in these applications. In-situ spectroscopic ellipsometry measurements of the mesoporous films exposed to controlled vapor pressures of organic vapors such as toluene, hexane and ethanol are utilized to understand the adsorption-desorption behavior of these films. Activated desorption of all three compounds is observed for pure carbon films, but addition of a small fraction of metal oxide enables the organics to be desorbed for the porous framework. These adsorption-desorption isotherms can also be utilized to estimate the pore size distribution and porosity of these films.

3:00pm **EL+AS+EM+MS+TF-ThA4 Mueller-Matrix Ellipsometry Studies of Chirality in Chitin-Based Structures and Thin Films of Al_{1-x}In_xN, K. Järrendahl, H. Arwin, R. Magnusson, P. Sandström, C.-L. Hsiao, J. Landin, S. Vallykh, J. Birch**, Linköping University, Sweden

A limited number of natural structures are known to reflect light that has circular or near circular polarization. This is for instance, the case for some scarab beetles where it is suggested that the polarization is caused by chiral structures in the form of helicoids in the cuticles. In this study, Mueller-matrix spectroscopic ellipsometry is applied in the spectral range of 250 to 1000 nm to investigate optical response and structures of the cuticle of various scarab beetles of the Cetoniinae subfamily. We will present our measurements showing how the polarization changes with wavelength as well as incidence angle and specify the conditions for when the reflected light is circularly left- or right-polarized. In most cases the reflected light is left-polarized as described by negative values of the M41 Mueller matrix element. For *Cetonia aurata*, a green beetle with metallic appearance, this is clearly seen in a rather narrow spectral range (470-550 nm). For other beetles (*Potosia cuprea* and *Licola lugubris*) similar polarization behavior is observed but the polarization features occur in a broader spectral region. We will show that there are even beetles (e.g. *Plusiotis argentiola*) reflecting both left- (M41 < 0) and right-polarized light (M41 > 0) in different parts of the spectral region. The Mueller data, including observations of the degree of polarization, are used to obtain structural and optical parameters from model calculations.

Our attempts to fabricate artificial structures with similar polarization properties will also be presented. Al_{1-x}In_xN thin films were grown on sapphire substrates by magnetron sputtering of indium and aluminum in a nitride atmosphere. Utilization of different seed layers and a substrate rotation gave chiral structures constituted by layers with a compositional gradient. Mueller-matrix results from these structures will be compared with the results from the natural structures. The Mueller data is also in this case very rich on information. In the initial steps to model these samples a similar approach as for the natural structures has been employed. Similarities and differences of the natural and artificial polarization response will be discussed in detail.

3:40pm **EL+AS+EM+MS+TF-ThA6 Mueller Polarimetry as a Tool for the Evaluation of the Diffraction Grating Profile Asymmetry, T. Novikova, P. Bulkin, LPICM, CNRS, Ecole Polytechnique, France, V. Popov, Moscow State University, Russia, A. De Martino, LPICM, CNRS, Ecole Polytechnique, France**

Mueller polarimetry in conical diffraction has proved to be a powerful optical technique for the metrological characterization of diffraction gratings. It was already shown that the shape of grating profile can be successfully reconstructed via appropriate optical modeling using full Mueller matrix measurements [1]. We also demonstrated that this approach can be of particular interest in microelectronics technology for the detection of overlay errors, which frequently result from the alignment deficiencies in lithography [2]. In some cases the asymmetrical distortion of grating profile can be induced by the etch process, or even be intentional, like in blazed gratings fabrication. For these applications a technique that allows for fast non-contact evaluation of the profile asymmetry may be of great value.

We studied the Mueller matrix spectra of symmetrical [3] and asymmetrical photoresist diffraction gratings on chromium using MM16 spectroscopic polarimeter, commercially produced by Horiba Jobin-Yvon, in the most general geometry of conical diffraction. At this configuration the 0th order cross-polarization complex reflection coefficients are antisymmetrical ($r_{sp}^0 = -r_{ps}^0$), provided that the grating is composed of only reciprocal materials and is invariant under the rotation by 180° about the normal incidence [4]. It leads to the following relations between the elements of 2x2 off-diagonal blocks of Mueller matrix: $M_{ij} = \pm M_{ji}$.

The lack of rotational symmetry violates the electromagnetic reciprocity theorem for the 0th-order diffraction on the asymmetrical gratings and, consequently, breaks the symmetry of the off-diagonal blocks of Mueller matrix ($|M_{ij}|$ is not equal to $|M_{ji}|$). This property of Mueller matrix of asymmetrical gratings was experimentally observed and numerically modeled at any illumination condition with exception of planar and pure conical mounting. We showed that the non-reciprocity in diffraction gratings can be used for the unambiguous detection of the grating profile asymmetry. The optimal choice of measurement configuration, i.e. azimuthal and polar angles considerably increases the sensitivity of the above mentioned technique.

References:

[1] T. Novikova, A. De Martino, S. Ben Hatit, and B. Drévilion, Appl. Opt. **45**, 3688 (2006).

- [2] T. Novikova, A. De Martino, R. Ossikovski and B. Drévilion, *Europ. Phys. J. Appl. Phys.* **31**, 63 (2005).
- [3] T. Novikova, A. De Martino, P. Bulkin, Q. Nguyen, B. Drévilion, V. Popov, and A. Chumakov, *Opt. Express* **15**, 2033 (2007).
- [4] L. Li, *Opt. Soc. Am. A* **17**, 881 (2000).

4:00pm EL+AS+EM+MS+TF-ThA7 Monitoring Ultra-Thin Organic Film Growth, In-Situ, with Combined Quartz Crystal Microbalance and Spectroscopic Ellipsometry, K.B. Rodenhausen, B.A. Duensing, A.K. Pannier, M. Schubert, University of Nebraska-Lincoln, M. Solinsky, The Procter & Gamble Company, T.E. Tiwald, J. A. Woollam Co., Inc.

We report a combinatorial approach to study ultra-thin organic films. This novel technique consists of *in-situ* spectroscopic ellipsometry and quartz crystal microbalance methods. In contrast to the quartz crystal microbalance, which is sensitive to the total mass attached to the surface, including the trapped solvent, spectroscopic ellipsometry only measures the amount of adsorbent on the surface. We also introduce a new "virtual separation approach" ($2\pi nd/\lambda \ll 1$) of analysis for the ellipsometry measurements. By using these two techniques in tandem, we are able to determine the thickness and solvent fraction of viscoelastic thin films.

We investigate cetyltrimethylammonium bromide (CTAB) thin films deposited onto a gold-coated quartz crystal as a model system. CTAB grown from a 2.5 mM solution demonstrates several phases in porosity evolution, including a temporary hold in water fraction as the film is rinsed off the substrate with water; these effects may be related to the structure of a CTAB bilayer.

In addition, a variety of self-assembled monolayers (SAMs) of alkanethiols on gold-coated quartz crystals are used as model biomaterials to determine the water fraction of an adsorbed prion layer. The porosity information distinguishes the proteins' conformation, dictated by the defined surface chemistries of the SAMs.

4:20pm EL+AS+EM+MS+TF-ThA8 Ellipsometric Studies of Electronically Coupled PbSe and PbS Quantum Dot Thin Films, S.G. Choi, National Renewable Energy Laboratory, O.E. Semonin, University of Colorado, J.M. Luther, M.C. Beard, A.G. Norman, National Renewable Energy Laboratory, Z. Lin, Colorado School of Mines, A. Franceschetti, National Renewable Energy Laboratory, M.T. Lusk, Colorado School of Mines, A.J. Nozik, National Renewable Energy Laboratory

Discovery of multiple exciton generation from colloidal suspensions of semiconductor quantum dots (QDs) has generated growing interests in realization of high-efficiency QD-based solar cells. Among a number of semiconductor QDs explored up to date, lead chalcogenides such as PbSe and PbS have been of great interest as a result of their wide tuning range of bandgap energy, abundance of materials, and large exciton Bohr radius.

In this presentation, I discuss optical properties of electronically coupled PbSe and PbS QD thin films. A series of QD multilayer thin films were prepared by a layer-by-layer dip-coating method onto glass substrates. Diameter of the QDs varies from 3.2 to 7.2 nm and from 3.5 to 8.3 nm for PbSe and PbS, respectively. Room-temperature pseudo-optical functions of the samples were measured by a rotating compensator-type, variable-angle spectroscopic ellipsometer. Transmittance data were also acquired in a normal-incidence configuration.

First, I determined refractive index $N = n + ik$ of the QD films using the B-spline basis functions within the multilayer model (ambient/surface roughness/QD film/substrate). We use the N obtained as the input parameters for modeling the internal quantum efficiency of the QD-based solar cell devices. Then, I extracted dielectric function $\epsilon = \epsilon_1 + i\epsilon_2$ for the ensemble of electronically coupled QDs using the Maxwell-Garnett effective medium approximations. The ϵ spectra show the first exciton peaks, and the E_1 and E_2 critical-point (CP) structures whose energies are higher than the corresponding bulk values probably due to the quantum confinement effects. This abstract is subject to government rights.

4:40pm EL+AS+EM+MS+TF-ThA9 In-situ Temperature Measurements by Spectroscopic Ellipsometry: Application to a-Si based Thin Films, D. Daineka, LPICM, CNRS, Ecole Polytechnique, France, V. Suendo, Institut Teknologi Bandung, Indonesia, P. Roca i Cabarrocas, LPICM, CNRS, Ecole Polytechnique, France

Accurate measurement of the substrate temperature is of crucial importance in many semiconductor technologies such as plasma enhanced chemical vapor deposition (PECVD). Traditional tools, both thermocouples and pyrometers, are not always reliable for in situ measurements in vacuum when the substrate can be out of thermal equilibrium. On the other hand, non-contacting optical methods allow to determine the surface temperature with great accuracy, provided the temperature dependence of optical constants for the studied material is known. Since recently, spectroscopic ellipsometers are widely available and often installed on the research

deposition systems, which provides an opportunity to use them for temperature monitoring. We have studied the optical functions of amorphous silicon based thin films with spectroscopic ellipsometry in the temperature range from 290 to 520 K. The experimental data were modeled using Tauc-Lorentz dispersion law for amorphous materials. We have found that the temperature coefficients of Tauc-Lorentz parameters, such as the optical gap, are rather close for a few different materials. That similarity suggests that these values can be used to determine the surface temperature for a broad range of amorphous silicon based materials with a good accuracy. Practical examples of using spectroscopic ellipsometry for temperature measurements in the low pressure PECVD environment are given.

5:00pm EL+AS+EM+MS+TF-ThA10 Real Time Spectroscopic Ellipsometry Studies of Amorphous and Nanocrystalline Si_{1-x}Ge_x:H Thin Films for Microbolometer Applications, D.B. Saint John, H.-B. Shin, M.-Y. Lee, E.C. Dickey, T.N. Jackson, N.J. Podraza, Penn State University

Hydrogenated amorphous and nanocrystalline silicon (a/nc-Si:H), germanium (a/nc-Ge:H), and their alloys have been used and continue to be assessed for use in uncooled infrared microbolometer applications. These materials may be deposited as uniform layers using equipment common to the manufacturing of displays and photovoltaics and are thus more amenable to manufacturing considerations than the ion beam deposited vanadium oxide films used in most commercial microbolometers. Real optimization of material in the a/nc-Si_{1-x}Ge_x:H system for use in these devices requires a better understanding of the relationship between the key electrical properties of interest including resistivity (ρ), temperature coefficient of resistance (TCR), and the 1/f noise character as a function of the degree of order and composition of the films. Si_{1-x}Ge_x:H thin films were deposited using plasma enhanced chemical vapor deposition using SiH₄, GeH₄, and H₂ at variable H₂- dilution. These films have been monitored using in situ real time spectroscopic ellipsometry (RTSE) over a spectral range from 0.75 to 5.15 eV during deposition to detect changes in the film thickness and optical properties in the form of the complex dielectric function spectra ($\epsilon = \epsilon_1 + i\epsilon_2$) as a function of deposition time. From the RTSE measurements and analysis it is possible to determine the structure of the material as amorphous, nanocrystalline, or mixed-phase and track the evolution of nanocrystallinity as a depth profile into the film. Ex situ Fourier transform infrared spectroscopic ellipsometry measurements over a spectral range from 0.05 to 0.75 eV were also performed to augment the complex dielectric function spectra and study absorption features relating to bonding. For electrical measurements, contacts were deposited in an isolated transfer length pattern for measurement of resistivity and TCR, while resistors with different volumes were made for volume normalization of the 1/f noise measurements. The TCR was measured from 20°C to 55°C. This study explores correlations between the electrical and optical properties of a-Si_{1-x}Ge_x:H and nc-Si_{1-x}Ge_x:H as functions of film processing conditions, resultant composition, and order. a-Si_{1-x}Ge_x:H films were prepared as a function of germanium content and hydrogen dilution to identify the impact that germanium and improved order at higher hydrogen dilution conditions have on the electrical properties (ρ , TCR, 1/f noise). The impact on the electrical properties due to the incorporation of small fractions of nanocrystallites are explored using mixed-phase (a+nc)-Ge:H films with nanocrystallite profiles guided by depth profile studies.

5:20pm EL+AS+EM+MS+TF-ThA11 Roll-to-Roll Fabrication of Thin Film Si:H Solar Cells: Real Time Monitoring and Post Deposition Mapping by Spectroscopic Ellipsometry, L.R. Dahal, Z. Huang, D. Attygalle, M.N. Sestak, C. Salupo, S.X. Marsillac, R.W. Collins, University of Toledo

Real time spectroscopic ellipsometry (RTSE) has been used to monitor the roll-to-roll deposition of thin film Si:H n-i-p solar cells on flexible plastic substrates coated with a Ag/ZnO back-reflector. In this process, the RTSE monitoring position is located directly above the ZnO sputtering target (i.e., at the closest target-substrate separation). RTSE data collection is initiated before the plasma is ignited so that ZnO nucleation can be observed. The film thickness increases with time until a steady state is reached, after which the bulk layer thickness at the monitoring point is constant with time. This occurs when the elapsed deposition time equals the time required for the moving substrate to travel from the leading edge of the deposition zone to the monitoring point. Although a constant substrate speed is selected such that the final film thickness is achieved in the time required to move through the entire deposition zone, this speed does not allow study of film growth that occurs after the substrate passes the monitoring point. To solve this problem, the substrate speed is reduced only in the early stage of growth such that the final film thickness of interest is reached at the monitoring point. In this way, RTSE can be used to analyze the entire layer on an initial length of the roll before the full length of the roll is processed. The thickness evolution of ZnO in the case of both normal and reduced

speeds shows good agreement with a simple inverse square variation of the deposition flux from the target to the flexible substrate.

After cell deposition, spectroscopic ellipsometry (SE) has also been applied for large area mapping of the completed 15 cm wide roll, at up to 1.5 m long sections at a time. Key information such as critical point, oscillator amplitudes, band gap energies, and widths have been extracted from which material density, composition, grain structure, disorder, and defect density can be determined. In this paper, optical mapping was applied for the intrinsic absorber layer in a full device a-Si:H solar cell structure. The results clearly show the degree to which thickness uniformity of the absorber layer depends on the gas flow and the electrode configuration. Also, by parameterizing the optical functions of the intrinsic absorber layer using single Lorentz oscillator modified by a low energy absorption cut-off, a map of its band gap and oscillator width can be deduced. Such an SE application is ideal for evaluation of uniformity in bulk thickness d_b , surface roughness thickness d_s , index of refraction, and extinction coefficient (n , k); the critical parameters for fabricating uniform and high efficiency solar modules.

Energy Frontiers Topical Conference Room: Mesilla - Session EN+SS+TF-ThA

Transparent Conductors

Moderator: S. Gupta, University of Alabama

2:00pm EN+SS+TF-ThA1 **Synthesis of ZnO:F by DC Reactive Magnetron Sputtering**, X. Noirfalise, University of Mons, Belgium, T. Godfroid, Matera Nova, Belgium, G. Guisbiers, IEMN Lille, France, R. Snyders, University of Mons, Belgium

Nowadays, numerous applications in the electronics and/or optoelectronics field need transparent thin films presenting a good electrical conductivity. The transparent conductive oxides (TCO) which reveal a large band gap and a good electrical conductivity fulfil these requirements. Recently, due to the significant increase of the demand, the prize of the most employed TCO, namely indium tin oxide (ITO) has strongly increased. Therefore, an alternative to this material becomes necessary. Among all the candidates, ZnO:F and Cd₂SnO₄ present the best performance in term of transparency and electrical conductivity. For obvious environmental reasons the latter cannot be considered. Therefore, ZnO:F is identified as the best candidate to replace ITO in TCO applications.

The most employed techniques for the synthesis of ZnO:F are Chemical Vapor Deposition and Spray Pyrolysis which both require organometallic precursor and high temperature processing. Another drawback of these technologies is the low chemical purity of the synthesized films because of the presence of the precursor decomposition products. At the contrary, reactive magnetron sputtering is an environmentally friendly technology allowing the synthesis of thin films with very fine control of the chemistry. Therefore, the aim of this works is to study the reactive magnetron sputtering of ZnO:F.

Thin films were prepared by DC reactive sputtering using a zinc target in an Ar/O₂/F₂ mixture. In a first attempts, ZnO films have been synthesized in order to optimize the matrix properties in terms of crystallinity and transparency. The studied parameters were the DC power (P_{DC}), the total pressure (P_{Tot}) and the O₂ flow (f_{O_2}). Our data reveal that the ZnO films presenting the best features are prepared for $P_{DC} = 70$ W, $P_{Tot} = 30$ mTorr and $f_{O_2} = 3$ sccm.

The second step was to introduce fluorine in this matrix. Therefore, we have studied the crystallographic, chemical, electrical and optical properties of the deposited films as a function of the fluorine content. In our deposition window, all films present a high transmission in the visible (> 80%). Our XRD data reveal decrease of the crystallite size with the increase of the fluorine content. Above a fluorine concentration of 2-3%, the ZnO:F crystallinity decreases. Our XPS and XRD data suggest that F atoms substitute O atoms in the ZnO structure. Finally, the electrical properties have been investigated by Hall effect measurements. For the optimal synthesis conditions (~ 2% of fluorine in the film), a charge carrier density of $\sim 10^{20}$ cm⁻³, an electrical resistivity of 10^{-2} Ω.cm and charge mobility of about 4 cm²/V.sec have been measured.

2:20pm EN+SS+TF-ThA2 **Relationship Between Resistivity Stability and Structure of Transparent Conducting Impurity-doped ZnO Thin Films**, J.-I. Nomoto, T. Hirano, T. Miyata, O. Ueda, T. Minami, Kanazawa Institute of Technology, Japan

Recently reported results show that the resistivity stability for moisture-resistance and heat-resistance tests in transparent conducting impurity-doped ZnO thin films prepared on low temperature glass substrates is

considerably affected by the film thickness as well as the kind and content of doped impurity. In this paper, we discuss the relationship between the obtainable resistivity stability and the structure in Al-, Ga- and B-doped ZnO (AZO, GZO and BZO) thin films prepared with a thickness in the range from 30 to 3000 nm by various deposition methods. Transparent conducting AZO, GZO and BZO thin films were prepared on glass substrates at 200°C by dc or rf magnetron sputtering, vacuum arc plasma evaporation and pulsed laser depositions. The resulting film structures were evaluated using a scanning electron microscope (SEM), an atomic force microscope (AFM) and a transmission electron microscope (TEM). The surface morphology of the impurity-doped ZnO films was found to change significantly after exposure to a highly moist environment (air at 85% relative humidity and 85°C) for 1000 h, as evidenced from AFM and SEM images; although the resistivity stability in these tests tended to improve with increasing impurity-doped ZnO thin film thickness, the effect was considerably dependent on the kind of doped impurity. In contrast, the surface morphology changed only slightly even after exposure to an oxidizing atmosphere (air at a temperature of 200°C) for 1000 h. The resistivity stability in the heat-resistance tests was found to depend significantly on whether the testing temperature was lower or higher than approximately 300°C. The amount of resistivity increase in the moisture-resistance and heat-resistance tests was found to correlate with the structure of the impurity-doped ZnO thin films, as evidenced from TEM images. The variation exhibited in the resistivity stability in these resistance tests is mainly attributed to micro-structural differences associated with the crystallinity of the deposited impurity-doped ZnO thin films.

2:40pm EN+SS+TF-ThA3 **Bulk and Surface Physics of Indium Oxide Thin Films Grown on Cubic Zirconia by O-plasma Assisted Molecular Beam Epitaxy**, R.G. Egdell, University of Oxford, UK **INVITED**

Tin doped indium oxide (In₂O₃) aka ITO is one of the most important transparent conducting oxides, yet it is only recently that many fundamental aspects the bulk and surface physics of indium oxide itself and of ITO have been addressed [1-3]. We have an ongoing programme concerned with growth of In₂O₃ on Y-stabilised ZrO₂ by oxygen plasma assisted molecular beam epitaxy and will review our most recent work in this area. Issues that will be addressed include the following:

The influence of surface energies and strain on the growth of In₂O₃ on low index zirconia surfaces. Mechanisms for relief of strain, including crystallographic tilting and development of nanostructures during high temperature MBE growth.

The influence of strain on the optical properties of ultrathin In₂O₃ films.

Surface structure and surface physics of In₂O₃ and ITO surfaces, including development of electron accumulation layers for material with low bulk doping levels.

References

- 1 P D C King *et al.*, Physical Review Letters 2008 **101** 116808
- 2 A Walsh *et al.*, Physical Review Letters 2008 **100** 167402/1-4
- 3 K H L Zhang *et al.*, Chemistry of Materials 2009 **21** 4353-4355

3:40pm EN+SS+TF-ThA6 **Recent Developments in Transparent Conducting Oxides for Thin-Film Solar Cells**, J. Burst, M. Scott, T. Gessert, National Renewable Energy Laboratory, S. Weiss, B. Rogers, Vanderbilt University, T. Coutts, Timothy J. Coutts Consulting, Inc

Transparent conducting oxides (TCOs) are utilized in all thin-film solar cells. Their function is to reduce electrical losses associated with collection of photogenerated current. However, they exhibit optical and electrical losses of their own and many researchers have tried to reduce these losses either by adjusting deposition conditions, post-deposition annealing, or by using completely novel materials. In our own work, we have shown that it is important to develop TCOs with high free-carrier mobility rather than high concentrations, which causes increased optical losses. Our latest results suggest significant gains in the performance of thin-film solar cells may be made via relatively minimal changes to the TCOs.

We have shown that the properties of transparent conducting oxides (TCOs) can be improved by doping them with approximately 1 atomic % cations whose oxides exhibit high dielectric permittivity. Our experiments have shown that TCOs doped with "high permittivity" cations have increased permittivity compared to the undoped TCO. Also, for similar carrier concentrations and mobilities, the doped TCOs have free-carrier absorption bands shifted to longer wavelengths (1500 nm doped v. 1300 nm undoped), thereby reducing optical losses compared to the undoped TCO. These observations are consistent with predictions based on the Drude free-electron model. In addition, there is evidence that the increased permittivity helps screen scattering centers, thereby leading to enhanced mobility. We will demonstrate that increasing film permittivity reduces optical losses in several standard TCO materials (ZnO, SnO₂, and In₂O₃). Film resistivity as low as 6×10^{-2} Ω.cm (corresponding to a sheet resistance of about 1 Ω/ sq

for a film 500 nm thick) has been achieved without compromising the high optical transmittance. The study has also indicated that TCO films with additions that alter permittivity appear to be less sensitive to variation in deposition ambient and temperature. Although this insight will clearly assist development of future TCO materials, we believe the results are even more relevant to present TCOs that may embody industrial advantages but remain limited by low mobility. *This abstract is subject to government rights.*

4:00pm **EN+SS+TF-ThA7 The Study of AZO/Au/AZO as a Transparent Electrode for Organic Light Emitting Diodes, J.H. Park,** Hanyang University, Republic of Korea

4:20pm **EN+SS+TF-ThA8 Origin of the Distribution of Electrical Properties of ITO Sputtered Films on Substrate, Y. Hoshi, Y. Yasuda,** Tokyo Polytechnic University, Japan, *H. Shimizu,* Niigata University, Japan
The ITO films deposited by magnetron sputtering and facing target sputtering at low substrate temperature have quite different distributions of film properties. However, their origin was still not clear. In this paper, we clarify the origin of the different distributions between the sputtering methods, and will propose a sputtering method to deposit the ITO films with good uniformity.

In the deposition of ITO films by a conventional planar magnetron sputtering, the films deposited at the center of the substrate have higher oxygen content than the films deposited at the end of the substrate. It should be noted that the film deposited by a facing target sputtering has much lower oxygen content than the films deposited by conventional planar magnetron sputtering. As a result, the ITO films with poor transparency were always obtained by the sputtering in pure Ar gas, when a Facing Target Sputtering system was used.

These phenomena can be explained by the following model; When sputter-deposition of ITO films was performed at a low temperature, only oxygen atoms produced by the sputter-emission from the target surface promote the oxidation of indium atoms on the film surface. In other words, oxygen molecules cannot oxidize the indium atoms at a low temperature.

In addition, oxygen atoms sputter-emitted from the target have different angular distributions than indium atoms have. That is, the emission ratio of oxygen atoms to indium atoms sputter-emitted from the target surface changes depending on the emission angle and gradually decreases with an increase of the emission angle. This phenomenon mainly causes the distribution of the properties of ITO films on the substrate, although bombardment of high energy negative oxygen ions also affects the distribution of film properties in planar magnetron sputtering.

In order to deposit uniform film on the substrate, compensation of the angular distribution in the emission ratio of oxygen atoms to indium atoms is necessary. Use of two sputtering sources arranged like a facing target sputtering system is one of the solutions to compensate the distribution and obtain the films with more excellent uniformity.

4:40pm **EN+SS+TF-ThA9 Deposition of Al-doped ZnO by Atomic Layer Deposition Using Ozone as the Oxygen Source, W.L. Gladfelter,** *H. Yuan, B. Luo, S.A. Campbell,* University of Minnesota

Transparent conducting oxide (TCO) films are used in many photovoltaic and optoelectronic devices. The need to deposit conformal films at relatively low temperature has raised interest in atomic layer deposition (ALD). Literature reports establish that n-doped zinc oxide has been deposited by ALD using water as the source of oxygen and aluminum or gallium as the dopant. The interest in replacing water with ozone has led to many new ALD routes to metal oxide films, including ZnO. In this presentation we will describe an effective ALD route to Al-doped ZnO. Aluminum-doped ZnO (AZO) films were grown on Si and SiO₂/Si substrates in the temperature range from 150 - 300°C using diethylzinc as the zinc precursor and ozone as the oxygen source. Trimethylaluminum was used as the aluminum precursor. Two approaches to doping were studied. In one a nanolaminate was formed by interspersing a trimethylaluminum/ozone cycle in between the diethylzinc/ozone cycles. The overall aluminum concentration depended on the number of diethylzinc/ozone cycles. The second approach involved co-injection of both metal precursors in which their relative concentrations were controlled by adjusting the precursor vessel temperature. The influence of the deposition method on the composition, structural, electrical, and optical properties of the AZO films as a function of doping metal concentration will be reported. X-ray diffraction patterns showed all the samples were polycrystalline and exhibited preferential (0001) orientation. The (0002) reflection for AZO films shifted in opposite directions depending on the deposition method. The carbon content of the films was below the detection limit of Auger electron spectrometry. The lowest resistivity ($6 \times 10^{-4} \Omega \cdot \text{cm}$) of the AZO films was obtained using the co-injection process. The average optical transmission was over 85 % in the range of 400-800 nm and the optical band gap increased with increasing doping in accordance with

Burstein-Moss effect. The resistivity of AZO films grown by the co-injection method decreased to $3 \times 10^{-4} \Omega \cdot \text{cm}$ after rapid thermal annealing (RTA) in an Ar atmosphere.

5:00pm **EN+SS+TF-ThA10 Atomic Layer Deposited (ALD) Al-doped ZnO Films for Transparent Conductor Applications, P. Banerjee,** University of Maryland, *W.-J. Lee, G.-Y. Bae,* Dong-Eui University, Republic of Korea, *S.-B. Lee, G.W. Rubloff,* University of Maryland

Among various materials for thin film transparent conductor applications, Al-doped ZnO (AZO) is a particularly attractive material because of its excellent properties, such as higher thermal stability, good resistance against damage by hydrogen plasma and potentially, low cost compared to indium tin oxide (ITO). Of the various available deposition techniques, Atomic layer deposition (ALD) provides superb control at the nanoscale for thickness, uniformity, conformality and Al doping of AZO films. This is particularly attractive for use in nanostructures, as well as in more conventional applications such as liquid crystal displays.

We report here results for structural, optical and electrical properties of ultrathin ALD AZO films as a function of at% Al. AZO films of ~ 100nm thickness were deposited on quartz substrates at 150C using a commercial BENEQ TFS 500 reactor using diethyl zinc (DEZ) and H₂O as precursors for ZnO, and trimethyl aluminum (TMA) and H₂O as precursors for Al₂O₃. Al-doping was incorporated in a film by introducing a single cycle of TMA-H₂O after fixed cycles of DEZ-H₂O pulses. This 'super' cycle was repeated until the desired thickness was achieved. Al-doping was varied from 0.0at% to 24.5at%, on various samples, as determined by EDX. In addition, XRD, AFM, UV-Vis spectroscopy and temperature-dependent (80K-340K) Hall measurements were carried out to understand the structural, optical and electrical properties in these films.

Strong texture effects were observed in the AZO films on the quartz substrates as the films preferentially crystallized along the [100] direction. This texturing effect is different from the [002] normally reported for AZO films deposited using established methods other than ALD. Crystallinity and electrical conductivity peaked at 3at% Al, consistent with previous published work. AFM results show a dramatic drop in surface roughness with Al doping. Optical transmittances of over 80% were obtained for all films in the visible region.

Calculation of lattice parameter constants from XRD data and analysis within the framework of the Burstein-Moss effect, reveal that AZO films act as substitutionally doped films for Al doping less than ~7.3at%. Beyond this value of doping, phase segregation and possible formation of a low conductivity phase cause a reduction in the concentration and mobility of free carriers and hence a degradation of the electrical properties.

5:20pm **EN+SS+TF-ThA11 Silicon-Titanium Oxides as Transparent Conductors for Photovoltaic Applications, J. Chivers, T. Vandervelde,** Tufts University

We report on the use of Earth-abundant silicon-dioxide and titanium-dioxide as a transparent conducting oxide (TCO) and antireflective (AR) coating. TCOs are a critical component in modern photovoltaic devices, used as a front-side contact that won't block incident light. At present, many TCOs require rare-Earth materials (e.g. Indium), which is problematic for large-scale manufacturing. The abundant, well characterized materials used here can be integrated into an existing product line quickly and cheaply. The varied band gap and index of refraction conditions inherent in the SiTiO₂ system allow controlled variation of material properties during monolithic growth. Some TCOs may also act as an AR coating, further increasing light absorption. The ideal AR coating would gradually change from the index of refraction of air to that of the underlying semiconductor. Most AR coatings used today make this transition in a small number of steps, which limits their efficacy. In this work, we investigate deposition processes that slowly grade the index of refraction while maintaining conductivity and transparency.

Graphene Focus Topic

Room: Brazos - Session GR+AS+TF+MI-ThA

Graphene: Surface Characterization

Moderator: P. Sutter, Brookhaven National Laboratory

2:00pm **GR+AS+TF+MI-ThA1 Scanning Tunneling Microscopy and Spectroscopy of Impurities on a Gated Graphene Device, R.T. Decker,** *V.W. Brar, M.H. Soloman, Y.C. Wang, A. Zettl, M.F. Crommie,* University of California Berkeley

INVITED

Understanding the scattering properties of electrons in graphene is important for controlling the behavior of different graphene nanostructure-

based devices. Here we report a scanning tunneling microscopy (STM) and spectroscopy (STS) study of impurities on a single monolayer of graphene. In our experiments the graphene is placed on a layer of insulating SiO₂ that sits above a doped silicon back-gate electrode. We will discuss our observations of the electronic local density of states of impurities, as well as how these properties respond to electrical gating of the graphene monolayer with respect to the silicon back-gate electrode.

In particular, we will show that the combination of the back-gate voltage and the STM tip-gating effect allows the controlled ionization of the impurity when the resonance sweeps through the Fermi energy. The influence of this induced Coulomb potential on the electrons in graphene in the vicinity of the impurity will be discussed.

2:40pm GR+AS+TF+MI-ThA3 Graphene Defect States in a Magnetic Field Studied by Scanning Tunneling Spectroscopy, K.D. Kubista, D.L. Miller, M. Ruan, W.A. de Heer, P.N. First, Georgia Institute of Technology, G.M. Rutter, J.A. Stroscio, National Institute of Standards and Technology

3:00pm GR+AS+TF+MI-ThA4 Atomic-Scale Maps of Quantum Hall States in Epitaxial Graphene, D.L. Miller, K.D. Kubista, Georgia Institute of Technology, G.M. Rutter, National Institute of Standards and Technology, M. Ruan, W.A. de Heer, P.N. First, Georgia Institute of Technology, J.A. Stroscio, National Institute of Standards and Technology

When a perpendicular magnetic field is applied to a graphene sheet, the resulting eigenenergies (Landau Levels or LLs) have a nonlinear energy distribution that includes a four-fold degenerate zero-energy state (LL₀). Maps of the energy-resolved local density of states (LDOS) acquired via cryogenic scanning tunneling spectroscopy (STS) provide atomic-scale imaging of the LL spatial distribution. Focusing on LL₀, we use STS maps to image the *localized* and *extended* quantum Hall states. Unexpectedly, we find atomic-scale variations of the LDOS above a critical magnetic field. We attribute this to an energy gap in LL₀ and show how it depends on the local A-B lattice symmetry. The gap is observed only within patches of at least a few magnetic lengths in size, which forces the splitting to "turn off" below the critical field. This behavior implies a breaking of the local sublattice symmetry imposed by moiré layer stacking.

3:40pm GR+AS+TF+MI-ThA6 Imperfect Graphene: Point Defects, Edges, Dislocations and Grain Boundaries, O.V. Yazyev, University of California, Berkeley **INVITED**

In two dimensions, properties of materials can be heavily affected by defects. In this talk, I will review our recent efforts directed towards understanding various types of structural irregularities in graphene.

Firstly, I will present the results of theoretical studies of the magnetism induced by point defects and edges in graphene and graphite. We show that in graphene single-atom defects such as vacancies and hydrogen chemisorption induce the spin-polarized defect states [1, 2]. The coupling between the magnetic moments is either ferromagnetic or antiferromagnetic, depending on whether the defects correspond to the same or to different sublattices of the graphene lattice, respectively. These results are able to clarify some experimental observations of high-temperature ferromagnetism in proton-irradiated graphite. Similarly, zigzag edges of graphene are predicted to induce spin-polarized edge states which can serve as a basis for novel spintronic devices. We address the question of the spin correlation length at finite temperatures in this one-dimensional magnetic system and establish the limitations of the proposed spintronic devices [3].

Then, I will talk about our latest results on dislocations and grain boundaries in graphene [4], topological defects which are still not well understood despite the growing number of experimental observations. We introduce a general approach for constructing dislocations in graphene characterized by arbitrary Burgers vectors as well as grain boundaries, covering the whole range of possible misorientation angles. By using ab initio calculations we investigate thermodynamic, electronic and transport properties of grain boundaries, finding energetically favorable large-angle symmetric configurations, strong tendency towards out-of-plane deformation in the small-angle regimes, pronounced effects on the electronic structure, and two distinct behaviors in the electronic transport [5] - either perfect reflection or high transparency for low-energy charge carriers depending on the grain boundary structure. Our results show that dislocations and grain boundaries are important intrinsic defects in graphene which may be used for engineering graphene-based functional devices.

[1] O. V. Yazyev and L. Helm, Phys. Rev. B 75, 125408 (2007).

[2] O. V. Yazyev, Phys. Rev. Lett. 101, 037203 (2008).

[3] O. V. Yazyev and M. I. Katsnelson, Phys. Rev. Lett. 100, 047209 (2008).

[4] O. V. Yazyev and S. G. Louie, arXiv:1004.2031 (2010).

[5] O. V. Yazyev and S. G. Louie, submitted.

4:20pm GR+AS+TF+MI-ThA8 Spectroscopic Ellipsometry for Thickness Measurement and Optical Dispersion Modeling of CVD-Grown Graphene, F.J. Nelson, V.K. Kamineni, A.C. Diebold, The University at Albany-SUNY

Graphene has attracted much research over the past several years due to its electrical and mechanical properties. It is a prime candidate for electronic and optoelectronic devices, yet much of the research has utilized the exfoliation, or "scotch-tape" technique of sample preparation. More scalable growth methods have been investigated, such as the thermal decomposition of SiC, and the resulting graphene films have properties dependent on their fabrication parameters. One potentially scalable technique is that of hydrocarbon gas-based CVD onto metallic substrates. Here, we report on the ellipsometric measurement of Few-Layer-Graphene (FLG) grown on copper foils and subsequently transferred to a different substrate (i.e. glass). One of the challenges with development of a dispersion model for FLG is that the CVD graphene has many "grains" inside the measured area while previous reports of exfoliated graphene were done on single crystal samples. The work explores finding an average thickness, as well as the optical dispersion modeling, of the graphene layers on different substrates, such as SiO₂/Si and glass slides.

Thin Film

Room: Ruidoso - Session TF-ThA

Multifunctional Thin Films and Characterization

Moderator: J.M. Fitz-Gerald, University of Virginia

2:00pm TF-ThA1 Structural and Dielectric Properties of Epitaxial BiFeO₃:BiMnO₃ Nanocomposite Films on Flexible Hastelloy, J. Xiong, J. Zhai, V. Matias, G. Zou, M. Zhuo, Y. Zhang, D.T. Trugman, Los Alamos National Laboratory, B. Tao, Y. Li, University of Electronic Science and Technology of China, J. Driscoll, University of Cambridge, UK, Q. Jia, Los Alamos National Laboratory

Growth of multifunctional thin films on flexible substrates is of great technological significance since such a platform is needed for the fabrication of flexible electronics. In this study, we report the growth of nanocomposite (BiFeO₃)_{0.5}:(BiMnO₃)_{0.5} [BFO:BMO] films on polycrystalline hastelloy. To grow epitaxial BFO:BMO films on polycrystalline substrates, we have used a template consisting of biaxially aligned TiN seed layer deposited by ion-beam-assisted deposited (IBAD) and a La_{0.7}Sr_{0.3}MnO₃ (LSMO) buffer layer deposited by pulsed laser deposition. It should be noted that LSMO is used not only as a buffer layer but also as the bottom electrode of the nanocomposite dielectric films. Microstructural characterization by X-ray diffraction and transmission electron microscopy showed that the nanocomposite thin films were epitaxy with orientation relations of (001)_{BFO:BMO}||[(001)_{LSMO}||[(001)_{TiN} and [100]_{BFO:BMO}||[100]_{LSMO}||[100]_{TiN}. Electrical measurements indicated good dielectric and ferroelectric properties which are comparable to that reported for ferroelectric films on single crystal substrates.

2:20pm TF-ThA2 Comparison of Ion Beam and Magnetron Sputtered Vanadium Oxide Thin Films, O.M. Cabarcos, B.D. Gauntt, J. Li, The Pennsylvania State University, S. Antrazi, 4Wave Inc., E.C. Dickey, D.L. Allara, M.W. Horn, The Pennsylvania State University

Uncooled Infrared (IR) focal plane arrays are an enabling technology for both military and commercial high sensitivity night vision cameras. The IR imaging is accomplished using MEMS microbolometers fabricated on read-out integrated circuits (ROIC's) and depends critically on the material used to absorb the incoming IR radiation. A typical detector works by monitoring changes in the electrical resistance of the detector material as it absorbs the radiation. Thus, suitable detector materials must exhibit a large temperature coefficient of resistance (TCR) and low noise characteristics to efficiently detect IR photons while also maintaining compatibility with standard IC processing. The most commonly used material in uncooled infrared imaging detectors is vanadium oxide deposited by reactive ion beam sputtering. Here we present a comparison of vanadium oxide thin films grown via reactive ion beam sputtering to films grown using reactive pulsed DC magnetron sputtering. Films deposited using both methods were optically and structurally characterized using Raman spectroscopy, transmission electron microscopy, atomic force microscopy, grazing incidence X-ray diffraction and Rutherford backscattering spectroscopy. Electrical properties of the films were also measured and were found to be very sensitive to the deposition conditions used. The ion beam sputtered films were determined to contain twinned FCC VOx nanocrystals with sub-nanometer scale twin spacing, in the form of large 10-20 nm wide columnar/conical grains. In contrast, the magnetron sputtered films consisted of equiax grains of FCC VOx (5-10 nm) encapsulated in an amorphous matrix. Subtle differences in

composition and structure could also be determined from the Raman spectra of the films. These differences in microstructure and composition were then correlated to the measured resistivities and TCRs of the films.

2:40pm TF-ThA3 Mapping Li-ion Diffusion on the Nanoscale in Thin Film Battery Materials, S.V. Kalinin, Oak Ridge National Laboratory INVITED

The electrochemical energy storage systems based on Li-based insertion and reconstitution chemistries are a vital aspect of energy technologies. Despite the wealth of device-level and atomistic studies, little is known on the mesoscopic mechanisms of ion diffusion and electronic transport on the level of grain clusters, individual grains, and extended defects.

The development of the capability for probing ion transport on the nanometer scale is a key to deciphering complex interplay between structure, functionality, and performance in these systems. Here we demonstrate how Scanning Probe Microscopy can be utilized to measure Li-ion mobility based on the strong strain-bias coupling in the system when local Li concentrations are changed by electrical fields. The imaging capability, as well as time- and voltage spectroscopies analogous to traditional current based electrochemical characterization methods are developed. The reversible intercalation of Li and mapping electrochemical activity in LiCoO₂ is demonstrated, illustrating higher Li diffusivity at non-basal planes and grain boundaries. In Si-anode device structure, the direct mapping of Li diffusion at extended defects and evolution of Li-activity with charge state is explored. The electrical field-dependence of Li mobility is studied to determine the critical bias required for the onset of electrochemical transformation, potentially allowing reaction and diffusion processes in the battery system to be separated at each location. The Scanning Probe Microscopy measurements are compared with classical characterization methods such as cyclic voltammetry and electrochemical impedance spectroscopy. The prospects of Scanning Probe Microscopy for battery characterization are discussed.

This material is based upon work supported as part of the Fluid Interface Reactions, Structures and Transport (FIRST) Center, an Energy Frontier Research Center funded by the U.S. Department of Energy, Office of Science, Office of Basic Energy Sciences under Award Number ERKCC61. Part of work is performed as a user proposal in the Center for Nanophase Materials Sciences at ORNL.

3:40pm TF-ThA6 Composition and Intermixing at the LaAlO₃/SrTiO₃ Interface by Rutherford Backscattering Spectrometry, S.V. Shuthanandan, A. Cohen, L. Qiao, S.A. Chambers, Pacific Northwest National Laboratory

There is a strong and growing interest in complex oxide interfaces because of the wide range of functional properties exhibited. It is well known that the LaAlO₃/SrTiO₃ (LAO)/STO interface exhibits novel electronic conductivity when grown in certain ways. LAO and STO are both band insulators in the bulk, but their interface exhibits n-type electrical conductivity when LAO is grown on TiO₂-terminated STO. Rutherford backscattering spectrometry (RBS) was used to determine interface composition in several pulsed laser deposition (PLD) grown LAO/STO samples prepared at leading laboratories. RBS data collected on these samples clearly show that La diffuses deep into the STO substrate. The clear presence of a shoulder between the low energy side of the La peak and the high energy side of the Sr peak suggests La indiffusion, although this shoulder could also be caused by pulse pile up in the detector, straggling, and/or multiple/dual scattering effects. Therefore, RBS data were taken as a function of beam current, incident beam energy, and film thickness to determine if this shoulder is due to these artifacts, or La indiffusion. It was determined that none of the aforementioned artifacts occur, thereby implicating La indiffusion. The presence of substitutional La at Sr sites in the substrate provides a plausible explanation for the observed n-type conductivity, as La is a shallow donor in STO.

4:00pm TF-ThA7 Low Work Function CsI Coatings for Enhanced Field Emission Properties, P.T. Murray, University of Dayton, T.C. Back, S.B. Fairchild, Air Force Research Laboratory

The use of CsI coatings on graphite fiber cathodes has been shown to reduce the field strength required for field emission from approximately 10⁷ V/cm to 250 V/cm. Interestingly, the mechanism for enhanced field emission is poorly understood. We have explored the enhancement mechanism by using simulated cathode structures consisting of CsI films deposited (by thermal evaporation and by pulsed laser deposition) onto graphite and Si surfaces; the films were characterized by x-ray photoelectron, Auger electron, ultraviolet photoelectron, and electron energy loss spectroscopy. Two aspects of the enhancement mechanism have been explored. The first, cathode conditioning, was addressed by characterizing the surfaces of CsI-coated cathodes and (stainless steel) anodes before and after conditioning. The results allow us to assess the

change in cathode surface chemistry as well as the extent to which material is transferred between electrodes during conditioning. The second aspect concerns the reported observation that CsI coated cathodes, after use, exhibit the disappearance of I and the appearance of a coating that appears to have wetted the cathode surface. We hypothesize that I depletion leaves behind a film of Cs which, with its low melting point, will flow during cathode operation. To test this hypothesis, we have characterized I depletion from CsI by carrying out electron and photon stimulated desorption from CsI surfaces. The talk will conclude with a discussion of our findings and their relevance to the enhancement mechanism.

4:20pm TF-ThA8 Characterization of SiO₂ Thin Films Prepared by Pulsed Electron Deposition, V.C. Rincon, S. Kotru, H.V. Nampoore, M. Chen, R.M. Frazier, The University of Alabama

Pulsed Electron Deposition (PED) is an ablation-based physical vapor deposition technique similar to Laser Deposition (PLD), where electrons are used as the ablation source. Silicon dioxide is a material which is extensively used by the microelectronic industry and also finds various applications as insulators, protective layers, antireflection coatings etc. There are many different techniques as thermal oxidation of silicon, low pressure chemical vapor deposition (LPCVD), plasma enhanced chemical vapor deposition (PECVD), to grow SiO₂. This work presents growth of thin films of SiO₂ deposited on Si (100) using PED. Films were deposited at oxygen pressure of 4.1mTorr and a pulse frequency of 3 Hz. Substrate temperature was varied from RT- 850 °C, along with varying the source's voltage in the range of 18-12 KV. Characterization tools such as ellipsometry, FTIR and AFM were employed to study the dependence of optical constants and roughness on the quality of SiO₂ films.

4:40pm TF-ThA9 Growth and Characterization Studies of CdS_{1-x}Se_x (0.0 ≤ x ≤ 1.0) Alloy Thin Films by Spray Pyrolysis, E. Masumdar, Rajarshi Shahu Mahavidyalaya, India

The n-CdS_{1-x}Se_x thin films of variable composition have been deposited on amorphous glass and FTO coated glass substrates by simple and cost effective spray pyrolysis technique. The various deposition parameters have been optimized by using photoelectrochemical technique. The structural, surface morphological, compositional, optical and electrical properties have been studied. The X-ray diffraction studies indicated that all the films are polycrystalline in nature with hexagonal structure irrespective of the composition. The lattice parameter 'a' and 'c' varies from 4.1034 to 4.2615 Å and 6.6664 to 6.9243 Å respectively with change in composition parameter from x = 0.0 to x = 1.0. Polycrystalline texture with nearly smooth surface and clearly defined grains has been observed for all samples from scanning electron microscopy (SEM). EDAX studies confirmed that CdS_{1-x}Se_x films have approximately same stoichiometry both initially and finally. The absorption coefficient 'α' is of the order of 10⁴ cm⁻¹. The optical absorption studies reveal that direct allowed transition with band gap energy between 2.44 and 1.74 eV. It is found that resistivity of the films decreased with increase in 'x' up to 0.8 and further it increases for x = 1.0. Semi-conducting behavior has been observed from resistivity measurements.

Key words: X-ray diffraction; Cadmium compounds; Semiconducting II-VI materials; Optical Properties; Electrical properties.

Corresponding author. Tel.: +919421363009; E-mail address: emasumdar@yahoo.com

5:00pm TF-ThA10 In situ Stoichiometry Control using Reflection-High-Energy-Electron-Diffraction Generated X-rays, C. Keenan, S. Chandril, West Virginia University, T.H. Myers, Texas State University - San Marcos, D. Lederman, West Virginia University

One major challenge in the stoichiometric growth of complex oxides, such as YMnO₃, is the control of the relative compositions of the constituent materials. Desirable properties of oxide materials, such as ferroelectricity, are highly dependent upon material stoichiometry, making stoichiometry control an important issue. While RHEED (Reflection High Energy Electron Diffraction) analysis is typically used as a qualitative tool, RHEED generated x-rays can be used to give quantitative compositional information. The relative compositions of Y and Mn in MBE grown YMnO₃ samples were studied using the grazing exit x-rays generated by RHEED electrons. Comparing the results with RBS characterization suggested that the technique has the potential for real-time compositional analysis.

This work was funded by the Office of Naval Research (Grant N00014-02-1-0974), the Air Force Office of Scientific Research (MURI grant F49620-03-1-0330), and the National Science Foundation (CIAM-DMR grant 0502825).

Spectroscopic Ellipsometry Focus Topic

Room: Southwest Exhibit Hall - Session

EL+AS+EM+MS+TF-ThP

Spectroscopic Ellipsometry Focus Topic Poster Session

EL+AS+EM+MS+TF-ThP1 Temperature Dependence of the Dielectric Function of AlSb Measured by Spectroscopic Ellipsometry, J.J. Yoon, Y.W. Jung, J.S. Byun, S.Y. Hwang, Y.D. Kim, Kyung Hee University, Republic of Korea, **S.H. Shin, S.Y. Kim, J.D. Song,** Korea Institute of Science and Technology, Republic of Korea

AlSb is a promising material for applications in heterostructure devices such as long-wavelength detectors, quantum-well lasers, and laser diodes. However, to understand and properly design these devices, information about its electronic properties and its dielectric function $\epsilon = \epsilon_1 + i\epsilon_2$ is needed. While room-temperature ϵ data for AlSb exist, very little information is available about its behavior at elevated temperatures. Here, we report pseudodielectric function data $\langle\epsilon\rangle$ from 300 to 800 K and from 0.7 to 5.0 eV, determined by spectroscopic ellipsometry. The samples were 1.5 μm thick layers grown on GaAs (001) substrates by molecular beam epitaxy (MBE). This thickness significantly exceeds the critical value for AlSb, so the layers are fully relaxed. The MBE station features an integrated spectroscopic ellipsometer and strain-free windows, thereby allowing ϵ data to be obtained without exposing the samples to air. For AlSb this is critical, because the removal of its oxides is not feasible owing to its reactivity. As a result of these precautions and the method by which these $\langle\epsilon\rangle$ data were obtained, we consider them to be the most accurate representation of ϵ to date. We also analyzed these data for critical-point (CP) parameters by fitting numerically calculated second energy derivatives of to standard analytic CP lineshape expressions. A parametric model was used, which describes dielectric functions by a combination of energy-bounded polynomials and poles, and encodes information in terms of amplitudes, critical-point energies, and broadening parameters. The reconstructed spectra are in excellent agreement with the data. We use these parameters to obtain information about the individual oscillators, including phonon effects, and interpolate them to obtain an analytic representation of the dielectric response of AlSb as a function of temperature. We expect these results to be an important database supporting engineering design, device technologies, and in-situ monitoring and control of device fabrication.

EL+AS+EM+MS+TF-ThP2 Optical Properties and Humidity Effects on Thin Films of Micro Fibrillated Cellulose Studied by Spectroscopic Ellipsometry, H. Arwin, E. Antunez de Mayolo, Linköping University, Sweden, **M. Eita,** Royal Institute of Technology (KTH), Sweden, **H. Granberg,** Innventia Ab, Sweden, **L. Wågberg,** Royal Institute of Technology (KTH), Sweden

High quality micro fibrillated cellulose (MFC) prepared from wood fibers can be used to prepare thin films on solid substrates by a layer-by-layer deposition technique. In applications MFC layers can be used alone or as a constituent in functional coatings, where the MFC can make a significant contribution to mechanical properties of the coating. Examples of potential applications are sensor layers, decorative coatings or mirrors. Here the optical properties in terms of the refractive index of MFC are studied with *in situ* spectroscopic ellipsometry (SE) and the effects on thickness and index due to humidity are investigated.

Films of MFC and polyethyleneimine (PEI) in the thickness range 30 - 300 nm are deposited on silicon substrates. Such MFC/PEI samples are exposed to water vapor in nitrogen (0-90% RH) and the ellipsometric response are measured *in situ* in the spectral range 245 - 1700 nm at an angle of incidence of 70 degrees using a dual-rotating compensator ellipsometer. From the SE-data the MFC/PEI film thickness and layer index are modeled.

Due to water exposure, the thickness of an MFC/PEI film is found to increase up to 15% or more, whereas the refractive index decreases. The effects are fully reversible and the dynamics of these changes are monitored with SE and are discussed.

EL+AS+EM+MS+TF-ThP3 Spectroscopic Ellipsometry and X-ray Photoelectron Spectroscopy of La₂O₃ Thin Films Deposited by Reactive Magnetron Sputtering, V. Atuchin, Institute of Semiconductor Physics, Russia, **A.V. Kalinkin,** Boreskov Institute of Catalysis, Russia, **V.A. Kochubey, V.N. Kruchinin,** Institute of Semiconductor Physics, Russia, **R.S. Vemuri, C.V. Ramana,** University of Texas at El Paso

Lanthanum trioxide (La₂O₃) is one among the most promising high- k dielectric materials to replace SiO₂ and Si₃N₄ in advanced metal-oxide-

semiconductor devices in gate stack. La₂O₃ can be prepared by various techniques but the film properties are strongly dependent on the fabrication conditions. Reactive magnetron sputtering deposition is widely used for the preparation of high quality transition multivalent metal oxide films with reproducible parameters and controlled thickness. The technique is preferred since it usually offers a high deposition rate for oxide films and a possibility to control the chemical composition of the film by reactive atmosphere in vacuum chamber. The aim of the present study is to understand the surface structure and evaluate the optical parameters of La₂O₃ films deposited on Si substrates by magnetron sputtering. La₂O₃ thin films were deposited onto Si(100) substrates in an argon/oxygen atmosphere using a high purity La target (99.9%). Structural parameters of the films were estimated by reflective high energy electron diffraction (RHEED) method at electron energy of 50 keV. All the films show no diffraction pattern indicating their amorphous nature in the near surface layers. Chemical state examined by the X-ray photoelectron spectroscopy (XPS), SPECS device, monochromatic Al K α radiation (1486.6 eV) before and after Ar⁺ (2.5 keV, 2 min) sputtering indicates the stoichiometric film formation. Chemical nature of the species was identified with using binding energy (BE) difference parameter $DLA = BE(\text{La } 3d_{5/2}) - BE(\text{O } 1s)$ [1]. Optical parameters of the films were measured with spectroscopic ellipsometry (SE) using a Spectroscan ellipsometer in the spectral range of 250 nm < λ < 1100 nm at the incidence angle of 70°. The La₂O₃ films with thickness 500-850 nm were transparent over the spectral range and dispersion relations of refractive index n were well derived using a model of (air)/(single homogeneous layer)/(Si substrate). The curves $n(\lambda)$ were approximated by Cauchy polynomials. Good relation between experimental points and theoretical curves confirms applicability of this simple model for the films. The optical parameters of La₂O₃ defined with SE are related to film bulk and are insensitive to top surface effects induced by hydration or carbonate formation. These parameters will be used as a basis for SE evaluation of nanometric lanthanum oxide films with thickness below 10 nm.

1.V.V. Atuchin, T.A. Gavrilova, J.-C. Grivel, V.G. Kesler, Electronic structure of layered ferroelectric high- k titanate La₂Ti₂O₇, J. Phys. D: Appl. Phys. 42 (2009) 035305.

EL+AS+EM+MS+TF-ThP4 Analysis of Anomalous Film Growth when Yttrium Oxide Thin Films are Exposed to 7.2eV Light, D. Mortensen, D.D. Allred, Brigham Young University

We have recently found that exposure of reactively sputtered yttrium oxide thin films to 7.2 eV photons in air produces a dramatic (factor of 4) increase in the films' thickness. This result was completely unexpected, Y₂O₃ is exceptional stable, and demanded further investigation. This is particularly important since yttria and neighboring metal oxides such as ZrO₂ have been considered, and HfO₂ is being used, as components in gate oxides for silicon devices. The excimer lamp used for the study was of the type used in cleaning the surfaces of silicon wafers in the semiconductor industry. It is vital to understand how metal oxides might swell during cleaning.

We have experimentally observed the following:

1. The film-thickness increase is linear with exposure time up to a point.
2. Over a factor of four increase in film thicknesses, as measured by spectroscopic ellipsometry, has been observed. E.g., film which was about 20 nm thick as deposited reached a thickness of about 100nm.
3. When the yttrium oxide sample is placed in a furnace the changes rendered to the yttrium oxide sample are reversed.
4. A film placed in a plasma cleaner does not show this increase.
5. These effects are noticeably absent under the same conditions for a silicon wafer.
6. The refractive index of the film decreased with exposure time, suggesting the film could becoming more porous, though effective media optical models were unsuccessful in modeling the optical properties.

In addition to ellipsometry the films were studied by XPS and STEM.

EL+AS+EM+MS+TF-ThP5 In-Situ Spectroscopic Ellipsometry of Lithium Ion Intercalation in GLAD Three-Dimensional Nanostructured Thin Films, E. Montgomery, M. Schubert, E.B. Schubert, T. Hofmann, D. Schmidt, University of Nebraska - Lincoln, R.A. May, University of Texas at Austin

Lithium intercalation in thin nanostructured and bulk films from metals and semiconductors has been studied using in-situ spectroscopic ellipsometry. Nanostructured thin films have a large surface area, and the stress caused by the intercalation of lithium is reduced in comparison to continuous films. The films are deposited using electron beam evaporation at a glancing angle or Glancing Angle Deposition (GLAD).

The charge capacity of the films can be observed as a change of index of refraction using ellipsometry. We will study intercalation as a function of structure geometry in chiral and achiral 3D GLAD thin films deposited from different metals onto silicon and other dielectric substrates. We report the anisotropic dielectric functions of the 3D nanostructures and their changes as a function of intercalation time and period.

EL+AS+EM+MS+TF-ThP6 Multi Phase Model Generation of Reflection Anisotropy Spectra of Copper Phthalocyanine Films on Vicinal Silicon Substrates, F. Seidel, L. Ding, O.D. Gordan, D.R.T. Zahn, Chemnitz University of Technology, Germany

In this work the in-plane anisotropy of copper phthalocyanine (CuPc) thin films grown on vicinal silicon substrates is explained by simulating Reflection Anisotropy Spectroscopy (RAS). In RAS the complex difference in reflection along two perpendicular directions is measured at an incidence angle close to 0° . While RAS has strong similarities with another polarisation related measurement technique, Spectroscopic Ellipsometry (SE), simulations of RA spectra using a similar mathematical formalism like in SE is not common.

One difference is that in SE the measurements are usually performed at an incidence angle close to the Brewster angle, where the difference between s and p reflected polarisation is maximal. However due to the similarities between the two techniques the evaluation of RA spectra can be performed in a similar way like for SE after some simple mathematical transformations. This is particularly useful when thickness induced interference can lead to incorrect interpretations of RA spectra. Therefore in this work we show that the RA spectra evaluation of CuPc layer with increasing thickness is mainly given by the optical interference effect and not by a change in the optical anisotropy of the film.

Thin Film

Room: Southwest Exhibit Hall - Session TF-ThP

Thin Film Poster Session II

TF-ThP1 Effects of Substrate Temperature on the Microstructure and Mechanical Properties of Multi-Element (TiVCrZrTa)N Coatings, M.H. Shiao, National Applied Research Laboratories, Taiwan, Republic of China, C.C. Jaing, K.S. Tang, Minghsin University of Science and Technology, Taiwan, Republic of China, C.T. Lee, C.Y. Su, Instrument Technology Research Center, Taiwan, Republic of China, Z.C. Chang, National Chin-Yi University of Technology, Taiwan, Republic of China, C.N. Hsiao, National Applied Research Laboratories, Taiwan, Republic of China

Multi-element nitride thin films of TiVCrZrTa high-entropy alloy were prepared by reactive RF magnetron sputtering technique with different substrate temperatures ranging from 25 °C to 400 °C. The microstructure and mechanical properties of the deposited nitride thin films were investigated by scanning electron microscope (SEM), atomic force microscope (AFM), transmission electron microscope (TEM), X-ray diffraction (XRD), nanoindenter, and phase shifting interferometry techniques. SEM and TEM results show that (TiVCrZrTa)N thin films exhibit a columnar structure. XRD and TEM diffraction results show a face-centered-cubic structure, and the intensity of (111) and (200) peaks increases with substrate temperatures in X-ray diffraction result. AFM measurements show the surface roughness of TiVCrZrTa nitride thin films increases slightly from 2.9 to 3.5 nm. Furthermore, the residual stress of (TiVCrZrTa)N thin films presents compressive stress and increases from 1.5 to 1.9 GPa with increasing substrate temperatures. The hardness and elastic modulus of TiVCrZrTa nitride thin films are approximate 26.5 and 240 GPa respectively, independent of the substrate temperatures.

TF-ThP2 Pulsed DC Magnetron Sputtered Nickel Thin Films: A Study of Stress, Density and Electronic Properties, E.D. Jones Jr., D.P. Adams, M.A. Rodriguez, Sandia National Laboratories

TF-ThP3 Photoluminescence Characterization using Hanle Effect in Al_{0.3}Ga_{0.7}As/GaAs Quantum Wells Grown on Processed Surfaces, J. Hernández-Rosas, C. Mejía-García, IPN, Mexico, A. Winter, Universität Bayreuth, Germany, M. López-López, IPN, Mexico, A. Gilinsky, Institute of Semiconductor Physics SB RAS, Russia, H. Pascher, Universität Bayreuth, Germany

In this work, we report the photoluminescence spectroscopy using Hanle effect of a series of quantum well (QW) structures of Al_{0.3}Ga_{0.7}As/GaAs grown by molecular beam epitaxy, which were prepared using different processing of the GaAs buffer layer surface. Each sample consists of three QW's with thicknesses of 7, 5, and 3 nm, respectively. The characterization by photoluminescence spectroscopy was done using several fixed wavelength lasers with circularly polarized excitation at 1.6 K. By means of Hanle effect the interband lifetime τ and the spin lifetime τ_s of the electrons were determined. A polarization change was observed if the photon energy of the exciting light exceeds the difference between the spin orbit band and the conduction band. The intensity of the inverse circular polarization seems to be increased in the samples with better quality. Interband transitions associated to the QW's were calculated using the effective mass approximation method in order to verify the experimental results.

TF-ThP4 Electrical Characterization of GLAD Thin Films, A. Lalany, R.T. Tucker, University of Alberta, Canada, M.D. Fleischauer, National Institute for Nanotechnology (NRC Canada), M.J. Brett, University of Alberta, Canada

Glancing Angle Deposition (GLAD)¹ thin films are increasingly used in optical and sensor devices that benefit from the unique refractive properties or ultra-high surface area. Extending the use of GLAD films to energy devices, epitomised by the fields of photovoltaics² and fuel cell catalysis³, increases the complexity in desired film requirements. High electrical conductivity along the length of GLAD structures - normal to the substrate plane - is necessary in order to exploit the high surface area of GLAD films in electronic devices. To date, GLAD has been applied to a variety of metals and conductive oxides⁴⁻⁶, and preliminary trends outline a relationship between the angle of incident flux, film density and in-plane resistivity. More specifically, it has been found that as the oblique deposition angle increases, the in-plane resistivity also increases. This relationship has been attributed to a decrease in film density resulting in diminished conductive pathways. Electrical anisotropy has also been observed, with differing in-plane resistivity for parallel and perpendicular directions with respect to the nanocolumns formed.⁴⁻⁶ A thorough study of both in-plane and through-post conductivity as a function of film composition, morphology, porosity, and crystallinity / phase is required to understand the complex interplay between film morphology and corresponding electrical properties. Quantifying differences between vertical and lateral-plane characteristics of GLAD films requires expanding on established techniques for in-plane measurements (which largely neglect morphological effects) and tailoring techniques to apply directly to GLAD films. It has been found that external boundaries begin to dominate standard bulk scattering mechanisms as film thickness decreases, resulting in an inverse relationship between film thickness and resistivity.⁷ Subsequently, the extensive boundaries present in GLAD films between and within individual features can result in complex electrical behaviour. We will quantify the variations in both in-plane and through-post conductivity through the use of direct and indirect experimental approaches, and relate the results to deposition parameters suitable for forming GLAD films of desirable conductivity.

[1] M.M. Haweye *et al.*, *J. Vac. Sci. Technol. A*, **25**, 1317, (2007).

[2] N. Li *et al.*, *Appl. Phys. Lett.*, **95**, 123309, (2009).

[3] A. Bonakdarpour *et al.*, *Appl. Catal. A.*, **349**, 110 (2008).

[4] J. Lintymer *et al.*, *Surf. & Coat. Tech.* **174-175**, 316, (2003).

[5] K.D. Harris *et al.*, *Adv. Funct. Mater.*, **18**, 2147, (2008).

[6] D. Vick *et al.*, *J. Vac. Sci. Technol. A*, **24**, 156, (2006).

[7] A.F. Mayada, M. Shatzkes, *Phys. Rev. B*, **1**, 1382 (1970).

TF-ThP5 Atomic Layer Deposition of Titanium Nitride Using Titanium Tetrachloride and Hydrazine, D. Seghete, A.I. Abdulgatov, V.R. Anderson, A.S. Cavanagh, W. Wang, S.M. George, University of Colorado at Boulder

The atomic layer deposition (ALD) of high quality metal nitrides at low process temperatures has remained a challenge. The use of organometallic precursors to reduce the deposition temperature can lead to carbon incorporation and poor electrical performance. One possibility is to use

halide precursors together with hydrazine instead of ammonia for the ALD of metal nitrides. Thermochemical calculations indicate that heats of reaction are more favorable and reaction temperatures should be lower with hydrazine. In this work, TiN ALD was performed using titanium tetrachloride (TiCl_4) and hydrazine (N_2H_4). *In situ* quartz crystal microbalance (QCM) measurements revealed a TiN ALD growth rate of 16 ng/cm^2 at 225°C. The TiCl_4 and N_2H_4 reactions were both observed to be self-limiting. At higher temperatures, TiN ALD is difficult to examine using the QCM because of thermal stability issues. X-ray diffraction (XRD) and X-ray reflectivity (XRR) studies revealed that TiN ALD deposited at 275°C resulted in the purest cubic polycrystalline TiN film. TiN ALD at 275°C also displayed the highest growth rate of 0.36 Å/cycle and a film density of 4.7 g/cm^3 . Fourier transform infrared (FTIR) studies of the TiCl_4 and N_2H_4 reactions at 275°C observed that primary ($-\text{NH}_2$) and secondary ($-\text{NH}$) amines are formed after hydrazine exposures. The FTIR spectra contained no evidence of any chlorine-containing salt on the surface. Elemental analysis of the TiN ALD grown at 275°C revealed no chlorine impurities within the X-ray photoelectron (XPS) instrument detection limit of 1 at%. However, oxygen was present at 14 at% that is attributed to oxidation after exposure to air. The use of hydrazine should facilitate the deposition of TiN ALD films at process temperatures <300°C.

TF-ThP6 Understanding Some Pitfalls and Loopholes in Routine Characterization and Metrology of Thin Films for Solar Cells, M. Scott, J. Burst, T. Gessert, National Renewable Energy Laboratory

We show that even the more ordinary metrology tools routinely used to evaluate thin films demonstrate some subtle, and some not so subtle, pitfalls which may lead to unexpected, and perhaps unnoticed, error in the measurement. In the extreme case, of course, one may altogether get the “wrong” answer. We focus on some of the primary tools used in the evaluation of thin films for photovoltaic applications. Empirical results from commercially available spectrophotometer, Hall, profilometer and other characterization tools are presented. We show, for example, that the commonly presented, but often unnoticed and not discussed, mismatch in reflectance data at the detector changeover (~800 nm) is readily explained and satisfactorily eliminated.

TF-ThP7 Deposition of Relatively Thin Highly C-axis Oriented AlN Films for High Frequency Electro-Acoustic Devices, V. Felmetser, P. Laptev, OEM Group Inc.

Thin film bulk acoustic resonators (FBAR) and bulk acoustic wave (BAW) filters based on piezoelectric aluminum nitride (AlN) thin films are widely employed for different wireless applications. As the resonance frequency of the resonator is determined by the thickness of the AlN layer, there is essential interest of using ultra-thin 100-200 nm films to extend the current technology from 1-2 to 5-10 GHz range. Reactive magnetron sputtering is a method of choice enabling formation of the films with a high degree of c-axis texture; however it is challenging to deposit such thin films with acceptable piezoelectric coefficients due to their drastically downward crystallinity compared to 500-2000 nm thick films required for lower frequency devices.

In this study, we use reactive sputtering technology with a dual cathode ac powered S-Gun magnetron [1]. The quality of the c-axis crystal orientation is characterized by the full width at half maximum (FWHM) of the AlN (0002) X-ray diffraction peak. AlN films deposited by the S-Gun on low-doped Si wafers exhibit a strong crystal orientation, which is improved with increasing film thickness. It is more sophisticated to achieve the same crystal orientation when the film is deposited on a metal bottom electrode, as it is required for the FBAR and BAW devices. Therefore, formation of well-textured underlying electrodes is essential, especially if the AlN films are relatively thin.

The crystal orientation of common electrode metals and alloys deposited on Si, SiO_2 , SiC, and diamond-like substrates is greatly enhanced by depositing a thin AlN seed layer underneath the metal. In the paper, we will discuss the critical conditions and process steps required for producing ultra-thin highly textured AlN films. For this purpose, we have developed a two-step sputter deposition process enabling better conditions for AlN nucleation. After preliminary rf plasma treatment of the substrate surface, the first 20-50 nm thick AlN layer is deposited at elevated temperature with higher nitrogen concentration in Ar- N_2 gas mixture, stimulating growth of higher quality columnar grains with the increase of AlN film thickness.

The results obtained for 100 and 200 nm thick AlN films deposited onto different metal electrodes (Mo, Cr, Ir) are presented in the paper.

The sputter technology has demonstrated high efficiency in producing very thin (100 nm) AlN films exhibiting superior crystallinity with FWHM < 2.5° on Mo electrode, which is equal to or even better than the value for the deposition on Si substrates.

[1] V. V. Felmetser, P. N. Laptev, and S. M. Tanner, *Surf. & Coat. Technol.*, 204 (2009) 840-844.

TF-ThP8 Properties of Transparent Conducting Sn-doped In_2O_3 Films Deposited by Pulsed Electron Deposition, M. Chen, V.C. Rincon, H.V. Nampoori, R.M. Frazier, S. Kotru, The University of Alabama

Sn-doped In_2O_3 (ITO) thin films find wide applications as an electrode material for photovoltaic devices. Optical transparency, electrical properties and surface roughness are the major parameters which need to be optimized for obtained device quality films for such applications. In the present work 100 nm thick ITO films were deposited on quartz substrates at room temperature using a vapor deposition technique, where a pulsed electron beam was used to ablate the target material. A series of films were deposited by varying the oxygen pressure in chamber during growth from 3.1mTorr to 20mTorr. Various characterization techniques were applied: x-ray diffraction, atomic force microscopy, four-point probe, Hall analysis, and Spectrophotometry were used to investigate the structure, surface morphology, electrical, and optical properties of these films. The best samples had a film resistivity of $6.8\text{E}^{-4}\text{ohm}\cdot\text{cm}$, and an average transmittance of 80% in the visible spectrum. The influence of post annealing on the film properties was also presented.

TF-ThP9 Synthesis and Characterization of Molybdenum Oxynitride Thin Films, J.Y. Park, Y.C. Kang, Pukyong National University, Republic of Korea

Molybdenum oxynitride films were deposited on the p-type Si(100) substrate using radio frequency (r.f.) magnetron sputtering technique at different nitrogen gas ratio from 0 to 100%. Molybdenum oxynitride films were investigated by atomic force microscopy (AFM), X-ray diffraction (XRD), scanning electron microscopy (SEM), spectroscopic ellipsometry (SE), and X-ray photoelectron spectroscopy (XPS).

The roughness of molybdenum oxynitride films were slightly increased up to 13% of nitrogen gas ratio then decreased significantly. XRD results show that the crystal structure was metallic Mo(110) at the 0% of nitrogen gas ratio. The thickness of molybdenum oxynitride films was decreased to 70 nm from 800 nm with increasing nitrogen gas ratio. The thickness deduced from SE experiment was well consistent with the result of SEM and band gap was calculated using extinction coefficient values obtained by SE. The high resolution XP spectra of Mo 3d, O 1s, and N 1s were deconvoluted to get more chemical information and valence band maximum was determined with valence band region XP spectra of molybdenum oxynitride thin films.

TF-ThP10 Effects of Non-Uniformity for GaN Deposition by the Structure of Gas Inlet in MOCVD, W. Yang, K. Hong, J. Joo, Kunsan National University, Republic of Korea, S. Lee, T. Lee, JUSUNG Engineering, Republic of Korea

GaN deposition equipment and processes for white LED (Light Emitting Diode) at MOCVD (Metalorganic Chemical Vapor Deposition) were numerically modeled to analyze the effects of reactive gas introduction strategy. The source gases, TMGa and NH_3 , were injected from shower head on the top of chamber, and the carrier gases, H_2 or N_2 , were introduced from two types of structure: vertical injection and horizontal injection. Wafers are setting on the holder at a radial distance of between 100 mm and 150 mm. The non-uniformity of deposition rate for vertical injection and horizontal injection was 1.9 % and 2.8 %, respectively. And In case of using the N_2 carrier gas instead of H_2 , the uniform deposition zone was increased by 20%.

TF-ThP11 In Search of New Multiferroics: Thin Film Synthesis and Characterization of Titanates of the MTiO_3 (M=Ni, Fe, Mn, Co) Family, R. Sanghavi, T. Varga, T. Droubay, P. Nachimuthu, V. Shuthanandan, S. Thevuthasan, Pacific Northwest National Laboratory

Today's challenge in multiferroics is to identify materials in which polarization and magnetization – normally considered contraindicated properties are strongly coupled. Recent theory calculations predicted that the family of compounds MTiO_3 (M = Mn, Fe, Ni), in a certain polymorphic structure (acentric $R3c$), are promising candidates where a polar lattice distortion can induce weak ferromagnetism (WFM). Guided by these insights, a phase of FeTiO_3 has been prepared more recently, which exhibits both ferroelectricity (FE) and WFM. However, the possible coupling between its polarization and WFM remains to be demonstrated. This demonstration may require the use of aligned single crystals to show that the magnetic and polar domains can be switched in concert. Results of the synthesis of the thin films of structurally analogous MTiO_3 compounds, and their characterization with a focus on the possible coupling between FE and WFM are reported. This fundamental study can be used to develop functional magnetic devices such as bio-sensors in which the magnetization can be controlled by electric field

TF-ThP12 Properties of ALD Al₂O₃ Protective Coatings. *P.J. Evans*, Australian Nuclear Science and Technology Organisation, *Y. Murai*, Nagaoka University of Technology, Japan, *M. Lindsay, J. Davis, G. Triani*, Australian Nuclear Science and Technology Organisation

TF-ThP13 Temperature Uniformity Issues of Inductive Heating in MOCVD Systems to Fabricate MQW White LEDs. *K. Hong, W. Yang, J. Joo*, Kunsan National University, Republic of Korea

Deposition temperature uniformity of GaN based MQW (multiple quantum well) layers is an important key which affects the wavelength uniformity of white LEDs. Two types of heater were tested: a resistive and inductive heater. Varying the gap between the heater and the susceptor, temperature uniformity was assessed by infra-red images for both cases of a static and a rotating susceptor. The best non-uniformity of resistive heater was obtained at 3 mm gap, 6.2%. Rotating the susceptor at 2.5 rpm over the induction heater gave 4.3% of temperature non-uniformity. Temperature distribution of the graphite susceptor over the induction heater was numerically modelled and agreed with experimental results.

TF-ThP14 Investigation on the Electrical and Optical Properties of ZnO:Al Thin Films by RF Magnetron Sputtering and Annealing. *C.T. Lee, B.H. Liou, D.R. Liou, C.N. Hsiao*, Instrument Technology Research Center, Taiwan, Republic of China

ZnO:Al (AZO) thin film was prepared on glass substrate with various substrate temperatures by RF magnetron sputtering deposition. Various substrate temperatures and 500 °C annealing on the electrical and optical properties of as-deposited AZO film were investigated by Hall measurement and spectrometer. The minimum resistivity of the as-deposited AZO film was 1.0×10^{-3} ohm cm at the substrate temperature of 300 °C. After annealing, the resistivity of all films was improved. The optimum resistivity of AZO thin film is 5.6×10^{-4} ohm cm. The average transmittance of AZO thin films in the visible range was decreased with increased substrate temperature. It was found that the minimum resistivity and maximum average transmittance of 82% in the visible range were at substrate temperature of 300 °C and after 500 °C annealing.

TF-ThP15 Photo-functional Properties for Fe-Added Titanium Dioxide Thin Films Prepared by Reactive Magnetron Sputtering. *S. Arahara, I. Takano, M. Sato*, Kogakuin University, Japan

Since the photoinduced decomposition of water on TiO₂ electrodes was discovered, semiconductor based on photocatalyst has attracted extensive interest. TiO₂ is anticipated as one of materials which are alternative for existing solar cell technology type based on a silicon type. TiO₂ shows relatively high reactivity and chemical stability under UV light whose energy exceeds the band gap of 3.2 eV in the anatase crystalline phase. The sun can provide an abundant source of photons. However, UV light accounts for the only small fraction (~5 %) of the sun's energy compared to the visible region (45 %). Many techniques have been examined to achieve this purpose, including the doping of TiO₂ with transition metals (such as Cr, Fe, Ni, V).

In this study, TiO₂ film has been prepared by reactive magnetron sputtering using a Ti target in an Ar/O₂ gas mixture. Fe addition was performed by Fe sputtering onto those TiO₂ films. Composition and microstructure of these films were investigated by X-ray photoelectron spectroscopy and X-ray diffraction, respectively. Chromatic change of a methylene blue solution was applied to a photocatalytic property. Light irradiation to the TiO₂ film in a methylene blue solution was carried out using a commercial sterilizing lamp as ultraviolet light and artificial sun light as visible light. Transmittance of a methylene blue solution was measured by a spectrophotometer. Furthermore, photocurrent between the TiO₂ film and a platinum electrode was measured by a volt-ampere characteristic using an unresisted ammeter in a KCl solution of 0.5 mol/l.

The crystal structure of TiO₂ turned from a rutile type into an anatase type with increase of O₂ gas flow rate. Photocatalytic characteristic of an anatase type showed the higher value under ultraviolet light, while the difference in the crystallographic structure was not observed under visible light. The effect of adding Fe was obtained at the Fe-added sample basing TiO₂ prepared with O₂ gas flow rate of 1.5 and 2.0 sccm. It was considered that the charge separation between an electron and a hole was enhanced by adding Fe to the TiO₂ surface. The optimum thickness of the Fe film was about 0.1 nm.

TF-ThP16 Control of Reflectivity at Substrate/Resist Interface of Nanometer-scaled Devices by Inorganic Bottom Anti-Reflection Coating (BARC). *S.-Y. Kim*, Korea Polytechnic College IV, Republic of Korea, *N.-H. Kim*, Chonnam National University, Republic of Korea

As the device has become highly integrated, the more accurate critical dimension (CD) was demanded. High contrast resist was also required for the exposure threshold effect. However in this case, the reflectivity between

substrate and resist became higher; therefore, the CD swing curve was intensified which was directly influenced by the change of resist thickness. Lastly, the resist notching phenomenon was appeared, which was caused by the reflectivity owing to the shape of sub-layer. It is very important to control the reflectivity between substrate and resist for the precise CD control. The bottom anti-reflective coating (BARC) is one of the most widely used methods. The conventional inorganic BARC has been employed in the metal pattern process of μ m-scaled devices with oxynitride. Because the more accurate CD control is necessary for the nm-scaled devices, the resist thickness, the conditions of reflectivity and absorption coefficient, and metal stack as a sub-layer were changed. The standing wave was also observed in the resist profile after metal pattern process of nm-scaled devices. Therefore, the optimization of inorganic BARC was investigated for the application to the nm-scaled devices with the changes of resist thickness and sub-layer. The reflectivity in the interface between BARC (oxynitride) and resist was under the control of thickness, refractive index, and absorption coefficient. The refractive index and absorption coefficient were investigated by a function of the SiH₄/N₂O gas flow rate, which is the main control factor of the refractive index and absorption coefficient, in oxynitride deposition. Computational simulation was performed in order to obtain the reflectivity in the interface of BARC and resist with changes of the optical factors. The optimum thickness, refractive index, and absorption coefficient were obtained for the minimum reflectivity of oxynitride. The simulated results were successfully applied to the experiments, which was confirmed by the cross-sectional SEM. There is no standing wave in this optimum condition.

TF-ThP17 Ar/O₂ Plasma Treatment Effects on Structural, Optical and Electrical Properties of Sputtering-deposited CdS Thin Films. *S.-H. Ryu, K.D. Myung, J.-S. Park*, Chosun University, Republic of Korea, *N.-H. Kim*, Chonnam National University, Republic of Korea, *W.-S. Lee*, Chosun University, Republic of Korea

CdS thin film has been widely used in the heterostructured solar cell applications as a window layer, which is a well-known n-typed semiconductor material. The sputtering method was employed for a large-area preparation of CdS thin film by the author in the previous study. It was good quality and had the high transmittance through it. In this study, the sputtering-deposited CdS thin films were treated by the plasmas under the various conditions with some process parameters including RF power, gas flow rate and treatment time with Ar or O₂ gases. Surface morphology and structure of them were analyzed by AFM and XRD. The effects of each plasma treatment on the electrical and optical properties of CdS thin film were investigated by UV-Visible spectrophotometer and Hall effect measurement. The roles of morphology and structure of plasma-treated CdS thin films were compared by the optical and electrical characteristics. The improved cell parameters of CdTe / the plasma-treated CdS thin film solar cells, including short-circuit current density (J_{sc}), open-circuit voltage (V_{oc}), fill factor (FF), and efficiency, were also obtained at the condition for the good properties of the plasma-treated CdS thin film. Acknowledgement: This work was supported by National Research Foundation of Korea(NRF) grant funded by the Korean Government(MEST) (20 10-0016048).

TF-ThP18 Photodissolution and Photodiffusion Effects of Silver on Electrical Characteristics of CdTe Thin Film for CdTe/CdS Solar Cells. *J.-S. Park, C.-H. Lim, S.-H. Ryu*, Chosun University, Republic of Korea, *N.-H. Kim*, Chonnam National University, Republic of Korea, *W.-S. Lee*, Chosun University, Republic of Korea

The maximum efficiency of CdTe/CdS solar cell was just 16.8% although the CdTe thin films shows the excellent absorbance above 99% with only about 2 μ m of active thickness. The enhanced electrical characteristics of CdTe thin film are required for the improvement of the efficiency. Doping of polycrystalline CdTe thin film is thought to be one of the effective methods to control the conductivity of CdTe thin film. The group I elements including copper are generally known as substitutional acceptors in CdTe thin films, which increase the p-doping of CdTe thin films. However, there have been many reports on the degradation of solar cell by the high diffusivity of copper. In this study, silver was employed to dope the sputtering-deposited CdTe thin film. Silver was deposited on the 1 μ m-thickness of CdTe thin film by the sputtering method with 10 nm-thickness. He-Ne laser (632.8 nm) was exposed with a small energy by a change of exposure time. The remained silver layer was removed with HNO₃+3HCl and H₂SO₄+H₂O₂ solutions. The photodissolution and photodiffusion effects of silver on the CdTe thin films were investigated by analyzing the electrical and optical properties of CdTe thin films including absorption coefficient, carrier mobility, resistivity and carrier density. AES depth profile was employed to examine the Ag-doped CdTe thin film with a change of He-Ne laser exposure time. Acknowledgement: This work was supported by National Research Foundation of Korea(NRF) grant funded by the Korean Government(MEST) (2010-0016048).

TF-ThP19 Surface and Interface Characterization of ALD and PVD Thin Films for Microelectronic Applications, L. Zhang, K.G. Lloyd, G. Blackman, DuPont Corporate Center for Analytical Sciences, J. Thompson, DuPont CR&D, L. Bao, J. Ryley, DuPont Engineering, D. Reardon, DuPont CR&D, M.A. Plummer, J.R. Marsh, DuPont Corporate Center for Analytical Sciences

Surface and interface properties of thin films are critical for the growth and commercialization of microelectronics and Photovoltaics (PV) products. During the development of these thin film materials, chemical and structural characterization of surfaces at each film layer and interfaces between different layers are essential to aid product development and manufacture process for optimum products.

This presentation will focus on the applications of applying integrated methods/techniques to support thin film construction using Atomic Layer Deposition (ALD) and Physical Vapor Deposition (PVD) methods, including the study of surface composition and morphology, surface treatment, inter-layer diffusion, and film stoichiometry.

TF-ThP20 , H.A. Shukur, I. Takano, Kogakuin University, Japan

Titanium dioxide (TiO_2) has considerable properties such as photocatalytic effect, dye-sensitized photovoltaic effect, photoinduced hydrophilicity and transparent electrode. Among all these properties photocatalytic property has been interested by many researchers because of its promised application such as antifouling effect and ability to decompose environmental pollution materials. However, TiO_2 has a high band gap (3.0 ~ 3.2 eV) so that the most photocatalytic effect occurs under UV irradiation. In order to improve TiO_2 behavior under visible light, there is many researchers have used various methods such as gas or metal doping.

In this study N^+ ion implantation was used to improve the optical properties of TiO_2 films, which were prepared by reactive magnetron sputtering on glass substrate (corning #1737). The substrate was sputtered by Ar ions in order to clean the surface before the TiO_2 thin film formation. Titanium (Ti) was sputtered from Ti target in an Ar / O_2 gas and the substrate was heated at 200 °C. The total film thickness was around 145nm with a deposition rate of 0.025nm/sec. N^+ ion was irradiated to TiO_2 thin film at 15keV in acceleration voltage and $40\mu\text{A}/\text{cm}^2$ in ion current density with a various irradiation doses from 2.5×10^{15} to 250×10^{15} ions/ cm^2 . Film thickness of the samples was measured by Avantes optical spectrometers system (AvaSpe-2048). The structure was determined by X-ray diffraction (XRD: MAC Science High quality XG M18XCE) with $\text{CuK}\alpha$ (0.154nm) radiation at an incident angle of 0.3° , and the composition was characterized by X-ray photoelectron spectroscopy. The photocatalytic property was measured by a methylene blue immersion test. The spectrophotometer (SHIMADZU UV-2550) was used to measure the difference in light absorption at a wave length of 665nm and also was used to measure the optical band gap for ion irradiated films.

N^+ ion implanted TiO_2 films showed a narrower optical band gap than unirradiation films, i.e. N^+ was substituted for O and created a new energy level. Optical band gap was changed from 3.58 to 3.5 eV at sample of 12.5×10^{15} ions/ cm^2 ion irradiation dose, this sample was showed a maximum photocatalytic activity for visible light.

TF-ThP21 , F.J. De Moure-Flores, K.E. Nieto-Zepeda, J.G. Quiñones-Galvan, A. Hernandez-Hernandez, M. Olvera, M.A. Melendez-Lira, CINVESTAV-IPN, Mexico

We propose the addition of fluorine in SnO_2 to increase n-type doping be used as transparent electrode in photovoltaic heterostructure. The thin films were deposited on glass substrates (at different temperatures) by RF magnetron sputtering using a $\text{SnO}_2:\text{F}$ target employing an argon atmosphere. The thin films were thermal annealed using a nitrogen flux. We present results of the structural and chemical characterization obtained through X-ray diffraction, atomic force microscopy (AFM), scanning electron microscopy (SEM) and energy dispersive X-ray microanalysis (EDX). The electrical, optical and structural properties were determined before and after heat treatment; the results are discuss in terms of growth details.

Authors Index

Bold page numbers indicate the presenter

— A —

Abdulagatov, A.I.: TF-MoA2, **6**; TF-ThP5, 48; TF-TuA7, 18; TF-TuP19, 22
Abe, Y.: TF-TuP2, 20
Abraham, D.W.: TF2-TuM1, **11**; TF2-TuM6, 12
Abrikosov, I.A.: TF-ThM1, 38
Adams, D.P.: TF-ThP2, 48
Adams, M.L.C.: TF+EN-MoM6, 5
Agarwal, S.: TF-TuA2, 17
Agrawal, R.: EN+TF-WeM1, 24
Alexeenko, A.: TF-ThM6, 39
Alexis, F.A.: TF+EM-WeM10, 28
Allara, D.L.: TF-ThA2, 44
Alling, B.: TF-ThM1, **38**
Allred, D.D.: EL+AS+EM+MS+TF-ThP4, 47
Anass, B.: TF+EM-WeM5, 27
Anderson, T.J.: EN+TF-WeM6, 25; TF-TuA10, 18
Anderson, V.R.: TF-MoA2, **6**; TF-ThP5, 48; TF-TuA7, **18**
Annelies, D.A.: TF+EM-WeM10, 28
Anthis, J.: TF-TuA12, 19
Antrazi, S.: TF-ThA2, 44
Antunez de Mayolo, E.: EL+AS+EM+MS+TF-ThP2, **47**
Arahara, S.: TF-ThP15, **50**
Armini, S.: TF+EM-WeM10, 28
Arwin, H.: EL+AS+EM+MS+TF-ThA4, 40; EL+AS+EM+MS+TF-ThP2, 47
Attygalle, D.: EL+AS+EM+MS+TF-ThA11, 41
Atuchin, V.: EL+AS+EM+MS+TF-ThP3, **47**
Aubuchon, J.: TF+EM-WeM10, 28
Avoiris, P.: GR+EM+MS+TF+MI-WeM5, 26
Ayyaswamy, V.: TF-ThM6, **39**

— B —

Bachmann, J.: TF-WeM1, **30**
Back, T.C.: TF-ThA7, 45
Bae, G.-Y.: EN+SS+TF-ThA10, 43
Baker, L.: TF-TuA9, **18**
Banerjee, P.: EN+SS+TF-ThA10, **43**; TF1-TuM10, 11
Banerjee, S.: GR+TF-TuM12, 9
Banerjee, S.K.: GR+EM+MS+TF+MI-WeM9, 26
Bao, L.: TF-ThP19, 51
Baraket, M.: GR+TF-TuA8, **16**
Bartelt, N.C.: GR+AS+TF-ThM11, 36; GR+AS+TF-ThM5, 35; GR+AS+TF-ThM6, 35; GR+SS+TF+EM-MoM2, 1
Bauer, J.: TF+SE-WeM3, 28
Baxter, J.B.: EN+TF-WeM4, **24**
Beard, M.C.: EL+AS+EM+MS+TF-ThA8, 41
Beckord, S.: GR+AS+TF-ThM2, 35
Beebe, T.P.: EN+TF-WeM4, 24
Beechem, T.E.: GR+EM+MS+TF+MI-WeM6, 26
Beerbom, M.M.: EN+TF-TuA10, 15
Behm, R.J.: GR+AS+TF-ThM2, 35; GR+TF-TuA7, 16
Bennett, W.D.: TF-WeA1, 33
Bent, S.F.: EN+TF-WeM5, **24**
Bersch, E.J.: TF+EM-WeM6, **27**
Beyer, A.: GR+TF-TuM3, 8
Beyer, G.: TF+EM-WeM10, 28
Biedermann, L.B.: GR+EM+MS+TF+MI-WeM6, 26
Birch, J.: EL+AS+EM+MS+TF-ThA4, 40
Bjelkevig, C.: GR+TF-TuA3, 15
Blackman, G.: TF-ThP19, 51
Blanc, R.: TF2-TuM5, 12
Bonner, J.: TF-WeM5, 31
Bonvalot, M.: TF+EM-MoM4, **2**
Borysiuk, J.: GR+SS+TF+EM-MoM5, 1
Bose, R.K.: TF-MoA9, 7
Bostwick, A.: GR+AS+TF-ThM6, 35
Brar, V.W.: GR+AS+TF+MI-ThA1, 43
Brett, M.J.: SE+TF-WeA9, 32; TF+SE-WeM6, 29; TF-ThP4, 48

Bright, V.M.: TF-WeM9, **31**
Brillson, L.J.: TF+EM-WeM12, 28
Broenstrup, G.: TF+EN-MoM5, 5
Bronneberg, A.C.: EN+TF-TuA1, **14**
Bruley, J.: TF1-TuM6, 10
Büenfeld, M.: GR+TF-TuA4, 16
Bui, H.P.: EN+TF-WeM4, 24
Bulkin, P.: EL+AS+EM+MS+TF-ThA6, 40
Burst, J.: EN+SS+TF-ThA6, **42**; TF-ThP6, 49
Byun, J.S.: EL+AS+EM+MS+TF-ThP1, 47

— C —

Caballero-Briones, F.: EN+TF-TuA12, 15
Cabarcos, O.M.: TF+EM-MoM9, 3; TF-ThA2, **44**
Cahen, D.: EN+TF-WeM3, 24
Camara, N.: GR+SS+TF+EM-MoM10, 2
Camassel, J.: GR+SS+TF+EM-MoM10, 2
Campbell, P.M.: GR+SS+TF+EM-MoM1, 1; GR+SS+TF+EM-MoM8, 1
Campbell, S.A.: EN+SS+TF-ThA9, 43; TF-TuP10, 21
Cansizoglu, M.F.: TF+SE-WeM5, **29**
Cao, Y.: TF1-TuM11, 11
Carbonell, L.: TF+EM-WeM10, 28
Carroll, M.S.: EN+TF-TuA8, 14
Cartier, E.: TF1-TuM6, 10
Castillo, H.A.: TF-TuP3, **20**
Castner, D.G.: TF-WeA3, 33
Cavalero, R.: GR+EM+MS+TF+MI-WeM1, 25
Cavanagh, A.S.: TF-MoA2, **6**; TF-ThP5, 48; TF-TuA7, 18
Cavanaugh, A.S.: TF-TuA9, 18
Cederberg, J.G.: EN+TF-TuA8, 14
Cerón Gutiérrez, S.: TF-TuP5, 20
Chabal, Y.J.: TF-TuA12, 19
Chambers, S.A.: TF-ThA6, 45
Chandril, S.: TF-ThA10, 45
Chang, J.P.: TF1-TuM5, 10
Chang, L.S.: TF-TuP16, 22
Chang, Y.Y.: TF-TuP13, **21**
Chang, Z.C.: TF-ThP1, 48
Chaudhari, V.U.: EN+TF-WeM6, 25
Chen, F.Z.: TF-TuP15, 22
Chen, H.: GR+AS+TF-ThM1, **35**
Chen, H.P.: TF-TuP15, 22
Chen, M.: TF-ThA8, 45; TF-ThP8, **49**
Chen, W.: MI+TF-ThM4, 37
Chen, W.-C.: TF-TuP18, 22
Chen, Y.: GR+TF-TuM5, **8**
Cheng, S.-L.: TF+EM-WeM9, 27
Cheng, Y.J.: TF-TuP4, 20
Cheong, W.-S.: TF-TuP9, 21
Chevolleau, T.: TF2-TuM4, 12
Chhowalla, M.: GR+TF-TuM4, 8
Chiam, S.Y.: EN+TF-TuA7, **14**
Chiang, P.H.: TF+SE-WeM10, 29
Chiang, S.: GR+SS+TF+EM-MoM10, **2**
Chim, W.K.: EN+TF-TuA7, 14
Chintalapalle, R.V.: TF-WeA10, 34
Chirita, V.: TF-ThM2, **38**; TF-ThM5, 38
Chiu, P.K.: TF-TuP15, 22
Chivers, J.: EN+SS+TF-ThA11, **43**
Cho, C.H.: TF1-TuM1, 9
Cho, K.I.: TF-TuP9, 21
Cho, W.H.: TF-TuP15, 22; TF-TuP20, 22
Choi, S.G.: EL+AS+EM+MS+TF-ThA8, **41**
Christiansen, S.H.: TF+EN-MoM5, 5
Christou, Y.: TF+EM-MoM10, 3
Chung, H.J.: GR+TF-TuM11, **9**
Chung, J.G.: TF+EM-WeM5, 27
Chung, S.M.: TF-TuP9, **21**
Ciobanu, C.V.: GR+AS+TF-ThM12, **36**; GR+TF-TuA11, 17
Clark, R.D.: TF+EM-WeM6, 27
Clavero, C.: MI+TF-ThM3, 36; MI+TF-ThM4, 37
Cockburn, A.: TF+EM-WeM10, 28

Coetsee, E.: TF+EN-MoM8, 5
Cohen, A.: TF-ThA6, 45
Cohen, S.R.: EN+TF-WeM3, 24
Collins, R.W.: EL+AS+EM+MS+TF-ThA11, 41
Colombo, L.: GR+EM+MS+TF+MI-WeM11, 26; GR+EM+MS+TF+MI-WeM9, 26
Consiglio, S.A.: TF+EM-WeM6, 27
Coss, B.E.: TF1-TuM11, 11
Coutts, T.: EN+SS+TF-ThA6, 42
Creatore, A.M.: EN+TF-TuA1, 14
Crommie, M.F.: GR+AS+TF+MI-ThA1, 43
Culbertson, J.C.: GR+SS+TF+EM-MoM8, 1
Curtis, C.J.: EN+TF-WeM9, 25
Cyganik, P.: TF-WeA4, **33**

— D —

Dahal, L.R.: EL+AS+EM+MS+TF-ThA11, **41**
Dai, M.Z.: EL+AS+EM+MS+TF-ThA3, 40
Daineka, D.: EL+AS+EM+MS+TF-ThA9, **41**
Davies, T.E.: GR+TF-TuA11, 17
Davis, J.: TF-ThP12, 50
de Heer, W.A.: GR+AS+TF+MI-ThA3, 44; GR+AS+TF+MI-ThA4, 44; GR+SS+TF+EM-MoM9, 2
de la Cruz, W.H.: TF-TuP3, 20
De Martino, A.: EL+AS+EM+MS+TF-ThA6, 40
de Moure Flores, F.: TF-TuP5, 20
De Moure-Flores, F.J.: TF-ThP21, **51**
Decker, R.T.: GR+AS+TF+MI-ThA1, **43**
Demirel, M.C.: TF+SE-WeM1, **28**
Deniz, D.: SE+TF-WeA11, **33**
Devine, C.: TF-TuA3, 17; TF-WeM5, **31**
Dewdney, J.: TF+EM-MoM11, 4
Dhlamini, M.S.: TF+EN-MoM8, 5
Di, M.: TF+EM-WeM6, 27
Dickey, E.C.: EL+AS+EM+MS+TF-ThA10, 41; TF+EM-MoM9, 3; TF-ThA2, 44
Diebold, A.C.: GR+AS+TF+MI-ThA8, **44**; TF+EM-WeM6, 27
Ding, L.: EL+AS+EM+MS+TF-ThP6, 48
Dingemans, G.: TF+EN-MoM6, 5
Dolo, J.J.: TF+EN-MoM8, 5
Dowben, P.A.: GR+TF-TuA3, 15
Driscoll, J.: TF-ThA1, 44
Droubay, T.: TF-ThP11, 49
Dubon, O.: GR+AS+TF-ThM11, 36
Dubourdieu, C.: TF1-TuM6, **10**
Duensing, B.A.: EL+AS+EM+MS+TF-ThA7, 41
Dussarrat, C.: TF+EN-MoM3, 4

— E —

Ebnonnasir, A.: GR+AS+TF-ThM12, 36
Eda, G.: GR+TF-TuM4, 8
Eddy, Jr., C.R.: GR+SS+TF+EM-MoM8, 1
Egdell, R.G.: EN+SS+TF-ThA3, **42**
Eita, M.: EL+AS+EM+MS+TF-ThP2, 47
Elam, J.W.: TF+EN-MoM1, 4; TF-TuA4, 17; TF-TuA8, 18; TF-WeM4, 30
Elsayed-Ali, H.: TF+EM-MoM6, 3
Engelhard, M.H.: TF-WeA1, 33
Engstfeld, A.K.: GR+AS+TF-ThM2, **35**
Engstrom, J.R.: TF1-TuM3, 9
Enriquez, H.: GR+SS+TF+EM-MoM10, 2
Epaminonda, P.: TF+EM-MoM10, 3
Er, A.O.: TF+EM-MoM6, **3**
Evans, P.J.: TF-ThP12, 50

— F —

Fairchild, S.B.: TF-ThA7, 45
Fallah, B.: GR+EM+MS+TF+MI-WeM9, 26
Fang, F.: EN+TF-TuA9, **14**
Felmetsger, V.: TF-ThP7, **49**
Feng, H.: TF+EN-MoM1, 4
Ferekides, C.S.: EN+TF-TuA10, 15
Fernández-Rossier, J.: GR+EM+MS+TF+MI-WeM3, **26**

First, P.N.: GR+AS+TF+MI-ThA3, 44;
GR+AS+TF+MI-ThA4, 44; GR+SS+TF+EM-
MoM6, 1; GR+SS+TF+EM-MoM9, 2
Fischer, D.A.: GR+TF-TuM12, 9
Fisher, E.R.: TF-WeM11, 31
Fitz-Gerald, J.M.: TF+EM-MoM8, 3
Fitzpatrick, R.: TF-TuA1, 17; TF-TuP19, 22
Fitzsimmons, M.: MI+TF-ThM2, 36
Fleischauer, M.D.: SE+TF-WeA9, 32; TF-ThP4,
48
Ford, G.M.: EN+TF-WeM1, 24
Fowlkes, J.D.: TF+EM-MoM3, 2
Franceschetti, A.: EL+AS+EM+MS+TF-ThA8, 41
Frank, M.M.: TF1-TuM6, 10
Franz, G.: TF-WeM6, 31
Frazier, R.M.: TF-ThA8, 45; TF-ThP8, 49
Friedman, A.L.: GR+SS+TF+EM-MoM8, 1
Fuhrmann, B.: TF+SE-WeM3, 28

— **G** —
Gaddam, S.: GR+TF-TuA3, 15
Gai, Z.: MI+TF-ThM1, 36
Gall, D.: SE+TF-WeA3, 32
Garimalla, M.: MI+TF-ThM11, 37
Gartsman, K.: EN+TF-WeM3, 24
Gaskill, D.K.: GR+SS+TF+EM-MoM1, 1;
GR+SS+TF+EM-MoM8, 1
Gaspar, D.J.: TF-WeA1, 33
Gatineau, J.: TF+EN-MoM3, 4
Gauntt, B.D.: TF+EM-MoM9, 3; TF-ThA2, 44
George, S.M.: TF-MoA10, 7; TF-MoA2, 6; TF-
ThP5, 48; TF-TuA1, 17; TF-TuA7, 18; TF-
TuA9, 18; TF-TuP19, 22
Gerlach, J.W.: TF+SE-WeM3, 28
Gessert, T.: EN+SS+TF-ThA6, 42; TF-ThP6, 49
Ghosh, A.W.: GR+TF-TuA1, 15
Gibbs, Z.M.: TF-MoA2, 6; TF-TuA1, 17; TF-
TuA7, 18
Gibson, K.D.: TF-WeA7, 33
Gilinsky, A.: TF-ThP3, 48
Ginley, D.S.: EN+TF-WeM9, 25
Gladfelter, W.L.: EN+SS+TF-ThA9, 43; TF-
TuP10, 21
Godfrey, T.: TF-MoA8, 6
Godfroid, T.: EN+SS+TF-ThA1, 42
Godignon, Ph.: GR+SS+TF+EM-MoM10, 2
Gözlhäuser, A.: GR+TF-TuA4, 16; GR+TF-TuM3,
8
Gong, B.: TF-MoA1, 6; TF-MoA8, 6; TF-TuA3,
17
Gonon, P.: TF2-TuM4, 12
Gordan, O.D.: EL+AS+EM+MS+TF-ThP6, 48;
EN+TF-TuA2, 14
Gordon, R.G.: TF+EM-WeM12, 28
Gougousi, T.: TF-TuP6, 20
Gourvest, E.: TF2-TuM5, 12
Grampeix, H.: TF2-TuM4, 12
Granados, B.: TF-TuA11, 18
Granberg, H.: EL+AS+EM+MS+TF-ThP2, 47
Gravey, V.: TF+EM-WeM10, 28
Green, E.: GR+SS+TF+EM-MoM6, 1
Greene, J.: TF+EM-MoM5, 3; TF-WeM4, 30
Gregorczyk, K.: TF+EN-MoM3, 4
Groner, M.: TF-TuP19, 22
Gross, M.E.: TF-WeA1, 33
Guisbiers, G.: EN+SS+TF-ThA1, 42
Gullapalli, S.K.: TF-TuP11, 21; TF-WeA10, 34
Guo, Q.: EN+TF-WeM1, 24
Gupta, A.: TF1-TuM9, 10
Gupta, S.: MI+TF-ThM9, 37
Gutmann, S.: EN+TF-TuA10, 15

— **H** —
Hall, R.A.: TF-MoA10, 7
Han, S.: TF-TuP21, 22
Han, S.M.: EN+TF-TuA8, 14
Harish Kumar, N.: MI+TF-ThM12, 37
Haspert, L.C.: TF1-TuM10, 11
Hauffman, T.: TF-WeA8, 33
Hellberg, C.S.: GR+SS+TF+EM-MoM1, 1

Hendel, R.: TF+EM-WeM1, 26
Henn-Lecordier, L.: TF+EN-MoM3, 4; TF1-
TuM10, 11
Heo, J.: GR+TF-TuM11, 9
Hernández Hernández, A.: TF-TuP5, 20
Hernandez-Hernandez, A.: TF-ThP21, 51
Hernández-Rosas, J.: TF-ThP3, 48
Herron, S.M.: EN+TF-WeM5, 24
Hersam, M.C.: GR+TF-TuA9, 16
Hersh, P.: EN+TF-WeM9, 25
Hillhouse, H.W.: EN+TF-WeM1, 24
Hirano, T.: EN+SS+TF-ThA2, 42
Hite, J.K.: GR+SS+TF+EM-MoM8, 1
Höche, T.: TF+SE-WeM3, 28
Hoffbauer, M.A.: EN+TF-TuA11, 15
Hoffmann, B.: TF+EN-MoM5, 5
Hofmann, T.: EL+AS+EM+MS+TF-ThP5, 48;
TF+SE-WeM9, 29
Hollander, M.J.: GR+EM+MS+TF+MI-WeM1, 25
Holloway, P.H.: EN+TF-TuA3, 14
Hong, K.: TF-ThP10, 49; TF-ThP13, 50
Horn, K.: GR+AS+TF-ThM6, 35
Horn, M.W.: TF+EM-MoM9, 3; TF-ThA2, 44
Hoshi, Y.: EN+SS+TF-ThA8, 43
Hoster, H.E.: GR+AS+TF-ThM2, 35; GR+TF-
TuA7, 16
Howe, B.: TF+EM-MoM5, 3
Howell, S.W.: GR+EM+MS+TF+MI-WeM6, 26
Hsiao, C.-L.: EL+AS+EM+MS+TF-ThA4, 40
Hsiao, C.N.: TF-ThP1, 48; TF-ThP14, 50; TF-
TuP15, 22; TF-TuP18, 22; TF-TuP20, 22
Hsu, H.C.: TF-TuP18, 22
Hu, Y.: GR+SS+TF+EM-MoM9, 2
Huang, Z.: EL+AS+EM+MS+TF-ThA11, 41
Huber, T.H.: TF-WeM6, 31
Hubin, A.: TF-WeA8, 33
Hughes, K.J.: TF1-TuM3, 9
Hughes, Z.: GR+EM+MS+TF+MI-WeM1, 25
Hultman, L.: TF+EM-MoM5, 3; TF-ThM1, 38;
TF-ThM2, 38; TF-ThM5, 38
Hwang, C.-S.: TF-TuP9, 21
Hwang, G.S.: GR+TF-TuA12, 17
Hwang, H.J.: TF1-TuM1, 9
Hwang, S.Y.: EL+AS+EM+MS+TF-ThP1, 47

— **I** —
Issacson, S.: TF1-TuM3, 9

— **J** —
Jackson, T.N.: EL+AS+EM+MS+TF-ThA10, 41
Jaing, C.C.: TF-ThP1, 48; TF-TuP20, 22
Järrendahl, K.: EL+AS+EM+MS+TF-ThA4, 40
Jaye, C.: GR+TF-TuM12, 9
Jen, S.U.: TF+SE-WeM10, 29
Jena, D.: TF1-TuM11, 11
Jeon, H.T.: TF1-TuM4, 10
Jernigan, G.G.: GR+SS+TF+EM-MoM1, 1
Jia, Q.: TF-ThA1, 44
Jiang, W.: TF-WeA12, 34
Jones Jr., E.D.: TF-ThP2, 48
Joo, J.: TF-ThP10, 49; TF-ThP13, 50; TF-WeA11,
34
Joseph, E.A.: TF2-TuM6, 12
Jourde, D.: TF2-TuM5, 12
Jousseau, V.: TF2-TuM4, 12
Jun, S.: GR+TF-TuA11, 17
Jung, C.-T.: TF-TuP4, 20
Jung, C.Y.: GR+EM+MS+TF+MI-WeM2, 25
Jung, S.: GR+TF-TuM10, 9; GR+TF-TuM9, 8
Jung, U.J.: TF1-TuM1, 9
Jung, Y.W.: EL+AS+EM+MS+TF-ThP1, 47
Jur, J.S.: TF-MoA1, 6; TF-MoA8, 6; TF-WeM5,
31

— **K** —
Kalidindi, N.R.: TF-TuP11, 21
Kalinin, S.V.: TF-ThA3, 45; TF-TuP17, 22
Kalinkin, A.V.: EL+AS+EM+MS+TF-ThP3, 47
Kalugin, N.G.: GR+TF-TuM1, 8
Kamineni, V.K.: GR+AS+TF+MI-ThA8, 44
Kang, C.G.: TF1-TuM1, 9

Kang, Y.C.: TF-ThP9, 49
Kanjolia, R.: TF-TuA12, 19
Kappes, B.B.: GR+AS+TF-ThM12, 36; GR+TF-
TuA11, 17
Karabacak, T.: TF+SE-WeM4, 29; TF+SE-WeM5,
29
Karuppanan, K.B.: MI+TF-ThM11, 37; TF-TuP11,
21; TF-WeA9, 34
Kawamura, M.: TF-TuP2, 20
Kayani, A.: TF-WeA12, 34
Keenan, C.: TF-ThA10, 45
Kelber, J.A.: GR+TF-TuA3, 15
Kellock, A.: TF1-TuM6, 10
Kellogg, G.L.: GR+SS+TF+EM-MoM2, 1
Kessels, E.W.M.M.: TF+EN-MoM6, 5; TF-TuA9,
18
Khare, C.: TF+SE-WeM3, 28
Khudhayer, W.J.: TF+SE-WeM4, 29
Killelea, D.R.: TF-WeA7, 33
Kim, D.-J.: GR+EM+MS+TF+MI-WeM2, 25
Kim, H.: TF1-TuM4, 10
Kim, H.K.: GR+TF-TuM4, 8
Kim, H.-S.: TF+EN-MoM1, 4
Kim, J.: TF1-TuM11, 11
Kim, J.G.: TF2-TuM3, 11; TF-TuP8, 20
Kim, N.-H.: TF-ThP16, 50; TF-ThP17, 50; TF-
ThP18, 50
Kim, S.: GR+EM+MS+TF+MI-WeM9, 26
Kim, S.Y.: EL+AS+EM+MS+TF-ThP1, 47
Kim, S.-Y.: TF-ThP16, 50
Kim, Y.D.: EL+AS+EM+MS+TF-ThP1, 47
Kimura, K.: SE+TF-WeA7, 32
King, J.S.: EN+TF-WeM5, 24
Kisielowski, C.: GR+TF-TuA4, 16
Kislov, N.: TF+EM-MoM4, 4
Kiyono, R.: TF-TuP2, 20
Kjerstad, A.C.: TF+SE-WeM9, 29
Klein, T.M.: TF1-TuM9, 10
Klimov, N.N.: GR+TF-TuM10, 9; GR+TF-TuM9,
8
Ko, D.-H.: TF2-TuM11, 13
Kochubey, V.A.: EL+AS+EM+MS+TF-ThP3, 47
Kodambaka, S.: GR+AS+TF-ThM12, 36;
GR+AS+TF-ThM5, 35
Kotru, S.: TF-ThA8, 45; TF-ThP8, 49
Kravchenko, I.I.: MI+TF-ThM1, 36
Krishnan, K.M.: TF+EM-MoM1, 2
Krishnan, R.: EN+TF-WeM6, 25
Kruchinin, V.N.: EL+AS+EM+MS+TF-ThP3, 47
Krukowski, S.K.: GR+SS+TF+EM-MoM5, 1
Kubista, K.D.: GR+AS+TF+MI-ThA3, 44;
GR+AS+TF+MI-ThA4, 44
Kuchibatla, S.: TF-WeA12, 34
Kuo, S.-Y.: TF-TuP18, 22
Kupfer, H.: EN+TF-TuA2, 14
Kweon, K.E.: GR+TF-TuA12, 17
Kwon, J.: TF-TuA12, 19

— **L** —
LaBella, M.: GR+EM+MS+TF+MI-WeM1, 25
Lacis, J.W.: TF-TuP6, 20
Lad, R.J.: SE+TF-WeA11, 33
LaForge, J.M.: TF+SE-WeM6, 29
Lai, F.-I.: TF-TuP18, 22
Lalany, A.: TF-ThP4, 48
Landin, J.: EL+AS+EM+MS+TF-ThA4, 40
Laptev, P.: TF-ThP7, 49
Lau, J.W.: MI+TF-ThM5, 37
Lau, K.K.S.: TF-MoA9, 7
Lederman, D.: MI+TF-ThM10, 37; MI+TF-ThM2,
36; TF-ThA10, 45
Lee, B.H.: TF1-TuM1, 9
Lee, C.T.: TF-ThP1, 48; TF-ThP14, 50; TF-TuP20,
22
Lee, D.S.: TF2-TuM11, 13
Lee, E.H.: TF+EM-WeM5, 27
Lee, H.: TF1-TuM4, 10
Lee, J.: TF1-TuM4, 10; TF-TuA10, 18
Lee, J.C.: TF+EM-WeM5, 27
Lee, J.H.: TF+EM-WeM5, 27

- Lee, K.: GR+EM+MS+TF+MI-WeM9, 26; TF-TuA3, 17
- Lee, K.-M.: TF2-TuM3, 11; TF-TuP8, 20
- Lee, M.-Y.: EL+AS+EM+MS+TF-ThA10, 41
- Lee, N.-E.: GR+EM+MS+TF+MI-WeM2, 25; TF+EM-WeM11, 28
- Lee, S.: TF-ThP10, 49; TF-TuP7, 20
- Lee, S.-B.: EN+SS+TF-ThA10, 43
- Lee, S.-H.: GR+TF-TuM11, 9; TF2-TuM3, 11; TF-TuP8, 20
- Lee, S.Y.: TF1-TuM1, 9
- Lee, T.: TF-ThP10, 49
- Lee, V.: GR+TF-TuM12, 9
- Lee, W.-J.: EN+SS+TF-ThA10, 43
- Lee, W.-S.: TF-ThP17, 50; TF-ThP18, 50
- Lee, Y.: TF-MoA10, 7
- Lee, Y.-G.: TF1-TuM1, 9
- Leisch, J.: EN+TF-WeM9, 25
- Leonhardt, D.: EN+TF-TuA8, 14
- Leusink, G.J.: TF+EM-WeM6, 27
- Lhostis, S.: TF2-TuM5, 12
- Li, J.: TF-ThA2, 44
- Li, N.: TF1-TuM9, 10
- Li, W.: EN+TF-WeM3, 24
- Li, Y.: TF-ThA1, 44
- Libera, J.E.: TF+EN-MoM1, 4
- Licitra, C.: TF2-TuM4, 12
- Lievens, P.: TF-WeA4, 33
- Lim, C.-H.: TF-ThP18, 50
- Lim, S.K.: TF1-TuM1, 9
- Lin, W.-T.: TF-TuP18, 22
- Lin, Y.W.: TF-TuP15, 22
- Lin, Z.: EL+AS+EM+MS+TF-ThA8, 41
- Lindsay, M.: TF-ThP12, 50
- Liou, B.H.: TF-ThP14, 50; TF-TuP20, 22
- Liou, D.R.: TF-ThP14, 50
- Liu, Y.: TF+EM-WeM12, 28
- Liu, Z.Y.: TF-TuA9, 18
- Lloyd, K.G.: TF-ThP19, 51
- Lock, E.H.: GR+TF-TuA8, 16
- López-López, M.: TF-ThP3, 48
- Lorenz, N.: TF+EM-WeM3, 27
- Lu, J.: MI+TF-ThM4, 37; TF+EN-MoM1, 4
- Lu, T.-M.: SE+TF-WeA10, 32
- Lucovsky, G.: TF-ThM3, 38; TF-TuP12, 21
- Lukaszew, R.A.: MI+TF-ThM3, 36; MI+TF-ThM4, 37
- Luo, B.: EN+SS+TF-ThA9, 43; TF-TuP10, 21
- Lusk, M.T.: EL+AS+EM+MS+TF-ThA8, 41
- Luther, J.M.: EL+AS+EM+MS+TF-ThA8, 41
- Lysaght, P.: GR+TF-TuM12, 9
- M —
- Mackus, A.J.M.: TF-TuA9, 18
- Magnusson, R.: EL+AS+EM+MS+TF-ThA4, 40
- Maitrejean, S.: TF2-TuM5, 12
- Manciu, F.S.: TF-TuP11, 21
- Mandoc, M.M.: TF+EN-MoM6, 5
- Mane, A.U.: TF-TuA8, 18; TF-WeM4, 30
- Mannequin, C.: TF2-TuM4, 12
- Marsh, J.R.: TF-ThP19, 51
- Marsillac, S.X.: EL+AS+EM+MS+TF-ThA11, 41
- Martin, R.M.: TF2-TuM6, 12
- Martinotti, D.: GR+SS+TF+EM-MoM10, 2
- Masumdar, E.: TF-ThA9, 45
- Matias, V.: TF-ThA1, 44
- Matson, D.W.: TF-WeA1, 33
- Mattevi, C.: GR+TF-TuM4, 8
- May, R.A.: EL+AS+EM+MS+TF-ThP5, 48
- Mayer, J.: GR+TF-TuA4, 16
- McCandless, B.: EN+TF-TuA9, 14
- McCarty, K.F.: GR+AS+TF-ThM11, 36; GR+AS+TF-ThM5, 35; GR+AS+TF-ThM6, 35
- McDonnell, S.: GR+EM+MS+TF+MI-WeM11, 26; TF1-TuM11, 11
- McPeak, K.M.: EN+TF-WeM4, 24
- Mejía-García, C.: TF-ThP3, 48
- Meléndez Lira, M.A.: TF-TuP5, 20
- Melendez-Lira, M.A.: TF-ThP21, 51
- Mertens, S.: TF+EM-WeM10, 28
- Mewes, T.: MI+TF-ThM3, 36; MI+TF-ThM4, 37
- Mi, Z.: GR+TF-TuA3, 15
- Michallon, P.: TF2-TuM5, 12
- Michely, T.: GR+AS+TF-ThM3, 35
- Miedaner, A.: EN+TF-WeM9, 25
- Miller, D.L.: GR+AS+TF+MI-ThA3, 44; GR+AS+TF+MI-ThA4, 44; GR+SS+TF+EM-MoM6, 1
- Miller, S.: TF1-TuM12, 11
- Minami, T.: EN+SS+TF-ThA2, 42
- Minton, T.: TF-TuP19, 22
- Miyata, T.: EN+SS+TF-ThA2, 42
- Montgomery, E.: EL+AS+EM+MS+TF-ThP5, 48; TF+SE-WeM9, 29
- Moon, H.K.: TF+EM-WeM11, 28
- Morales, C.: TF+EM-MoM11, 4
- Moriwaka, H.: SE+TF-WeA7, 32
- Mortensen, D.: EL+AS+EM+MS+TF-ThP4, 47
- Mudavakkat, V.H.: TF-WeA9, 34
- Munbodh, K.: MI+TF-ThM2, 36
- Murai, Y.: TF-ThP12, 50
- Murata, Y.: GR+AS+TF-ThM12, 36; GR+AS+TF-ThM5, 35
- Murray, P.T.: TF-ThA7, 45
- Muscat, A.J.: TF1-TuM12, 11; TF-TuA11, 18
- Musgrave, C.: TF-MoA3, 6
- Myers, T.H.: TF-ThA10, 45
- Myers-Ward, R.L.: GR+SS+TF+EM-MoM8, 1
- Myung, K.D.: TF-ThP17, 50
- N —
- Na, H.D.: TF2-TuM3, 11; TF-TuP8, 20
- Nachimuthu, P.: TF-ThP11, 49; TF-WeA12, 34
- Nah, J.: GR+EM+MS+TF+MI-WeM9, 26
- Nakajima, K.: SE+TF-WeA7, 32
- Nampoori, H.V.: TF-ThA8, 45; TF-ThP8, 49
- Nandasiri, M.: TF-WeA12, 34
- Narayanan, V.: TF1-TuM6, 10
- Narita, S.: TF-TuP14, 21
- Natarajarathinam, A.: MI+TF-ThM9, 37
- Nekuda, J.A.: EN+TF-WeM9, 25
- Nelson, F.J.: GR+AS+TF+MI-ThA8, 44
- Neumayer, D.: GR+EM+MS+TF+MI-WeM5, 26
- Newell, D.B.: GR+TF-TuM10, 9; GR+TF-TuM9, 8
- Nie, S.: GR+AS+TF-ThM11, 36; GR+AS+TF-ThM6, 35; GR+SS+TF+EM-MoM2, 1
- Niensch, K.: TF-WeM1, 30
- Nieto Zepeda, K.: TF-TuP5, 20
- Nieto-Zepeda, K.E.: TF-ThP21, 51
- Nikiforov, M.: TF-TuP17, 22
- Nishi, Y.: TF+EM-WeM9, 27
- Nishida, K.: TF-TuP2, 20
- Nobis, F.: EN+TF-TuA2, 14
- Noh, J.H.: TF-TuP17, 22
- Noirfalise, X.: EN+SS+TF-ThA1, 42
- Nolen, J.: TF-WeM4, 30
- Nomoto, J.-I.: EN+SS+TF-ThA2, 42
- Norman, A.G.: EL+AS+EM+MS+TF-ThA8, 41
- Nottbohm, C.T.: GR+TF-TuM3, 8
- Noufi, R.: EN+TF-WeM6, 25
- Novikova, T.: EL+AS+EM+MS+TF-ThA6, 40
- Nozik, A.J.: EL+AS+EM+MS+TF-ThA8, 41
- Nsimama, P.D.: TF+EN-MoM8, 5
- Ntwaeaborwa, O.M.: TF+EN-MoM8, 5
- Nyakiti, L.O.: GR+SS+TF+EM-MoM1, 1
- O —
- Odysseos, A.: TF+EM-MoM10, 3
- O'Hayre, R.P.: EN+TF-WeM9, 25
- Ohta, T.: GR+EM+MS+TF+MI-WeM6, 26; GR+SS+TF+EM-MoM2, 1
- Oldham, C.: TF-MoA8, 6; TF-WeM5, 31
- Olvera, M.: TF-ThP21, 51
- Opila, R.: EN+TF-TuA9, 14; TF+EM-WeM3, 27
- Otte, A.F.: GR+SS+TF+EM-MoM9, 2
- Oughaddou, H.: GR+SS+TF+EM-MoM10, 2
- Owen, T.: TF-WeM4, 30
- P —
- Pal, S.: TF+EM-MoM11, 4
- Palacios-Padrós, A.: EN+TF-TuA12, 15
- Pan, J.S.: EN+TF-TuA7, 14
- Pan, W.: GR+EM+MS+TF+MI-WeM6, 26
- Pangan-Okimoto, K.: EN+TF-WeM5, 24
- Pannier, A.K.: EL+AS+EM+MS+TF-ThA7, 41
- Park, J.H.: EN+SS+TF-ThA7, 43
- Park, J.S.: TF+EM-WeM5, 27
- Park, J.-S.: GR+EM+MS+TF+MI-WeM2, 25
- Park, J.-S.: TF-ThP17, 50
- Park, J.-S.: TF-ThP18, 50
- Park, J.Y.: TF-ThP9, 49
- Park, S.H.: TF-TuP9, 21
- Park, T.J.: TF1-TuM11, 11
- Parsons, G.N.: TF-MoA1, 6; TF-MoA8, 6; TF-TuA3, 17; TF-WeM5, 31
- Pascher, H.: TF-ThP3, 48
- Pasquarelli, R.M.: EN+TF-WeM9, 25
- Payzant, E.A.: EN+TF-WeM6, 25
- Pellin, M.J.: TF+EN-MoM1, 4
- Peng, Q.: TF-MoA1, 6; TF-TuA3, 17; TF-TuA8, 18
- Perebeinos, V.: GR+EM+MS+TF+MI-WeM5, 26
- Perez, F.A.: MI+TF-ThM10, 37; MI+TF-ThM2, 36
- Perkins, F.K.: GR+TF-TuA8, 16
- Perng, Y.-C.: TF1-TuM5, 10
- Petrach, R.V.: GR+TF-TuM2, 8
- Petrov, I.: GR+AS+TF-ThM12, 36; TF+EM-MoM5, 3
- Petrova, V.: GR+AS+TF-ThM12, 36
- Phillips, M.: GR+SS+TF+EM-MoM6, 1
- Pinna, N.: TF-MoA6, 6
- Pirkle, A.: GR+EM+MS+TF+MI-WeM11, 26
- Plummer, M.A.: TF-ThP19, 51
- Podraza, N.J.: EL+AS+EM+MS+TF-ThA10, 41
- Pokharel, S.: GR+TF-TuA3, 15
- Popov, V.: EL+AS+EM+MS+TF-ThA6, 40
- Popovitch-Biro, R.: EN+TF-WeM3, 24
- Prathiba, G.: MI+TF-ThM12, 37
- Profijt, H.B.: TF+EN-MoM6, 5
- Q —
- Qian, L.: EN+TF-TuA3, 14
- Qiao, L.: TF-ThA6, 45
- Quickel, T.E.: TF1-TuM5, 10
- Quiñones Galván, J.G.: TF-TuP5, 20
- Quiñones-Galván, J.G.: TF-ThP21, 51
- R —
- Rack, P.D.: TF+EM-MoM3, 2; TF-TuP17, 22
- Rai, V.R.: TF-TuA2, 17
- Ramana, C.V.: EL+AS+EM+MS+TF-ThP3, 47; MI+TF-ThM11, 37; TF-TuP11, 21; TF-WeA9, 34
- Rauschenbach, B.: TF+SE-WeM3, 28
- Reardon, D.: TF-ThP19, 51
- Rebholz, C.: TF+EM-MoM10, 3
- Reichertz, L.A.: EN+TF-TuA11, 15
- Ren, H.: TF+EM-WeM9, 27
- Retterer, S.T.: MI+TF-ThM1, 36
- Richter, F.: EN+TF-TuA2, 14
- Rincon, V.C.: TF-ThA8, 45; TF-ThP8, 49
- Rissom, Th.: EN+TF-WeM3, 24
- Robinson, J.: GR+EM+MS+TF+MI-WeM1, 25
- Robinson, J.A.: GR+TF-TuA8, 16
- Roca i Cabarrocas, P.: EL+AS+EM+MS+TF-ThA9, 41
- Rochat, N.: TF2-TuM4, 12
- Rodenhausen, K.B.: EL+AS+EM+MS+TF-ThA7, 41
- Rodriguez, M.A.: TF-ThP2, 48
- Rogers, B.: EN+SS+TF-ThA6, 42
- Romero, M.J.: EN+TF-TuA8, 14
- Roos, M.: GR+TF-TuA7, 16
- Rosaz, G.M.: TF+EM-MoM4, 2
- Ross, A.J.: GR+EM+MS+TF+MI-WeM6, 26
- Rossnagel, S.M.: TF1-TuM6, 10; TF-WeA11, 34
- Rotenberg, E.: GR+AS+TF-ThM6, 35
- Ruan, M.: GR+AS+TF+MI-ThA3, 44; GR+AS+TF+MI-ThA4, 44

Rubloff, G.W.: EN+SS+TF-ThA10, 43; TF+EN-MoM3, 4; TF1-TuM10, 11
 Rutter, G.M.: GR+AS+TF+MI-ThA3, 44;
 GR+AS+TF+MI-ThA4, 44; GR+TF-TuM10, 9;
 GR+TF-TuM9, 8
 Ryley, J.: TF-ThP19, 51
 Ryu, M.K.: TF+EM-WeM5, 27
 Ryu, S.-H.: TF-ThP17, 50; TF-ThP18, 50

— S —

Saint John, D.B.: EL+AS+EM+MS+TF-ThA10, 41
 Salupo, C.: EL+AS+EM+MS+TF-ThA11, 41
 Sammann, E.: TF+EM-MoM5, 3
 Sampathkumaran, U.: TF-WeM4, 30
 Sandström, P.: EL+AS+EM+MS+TF-ThA4, 40
 Sanghavi, R.: TF-ThP11, 49
 Sangiovanni, D.G.: TF-ThM2, 38; TF-ThM5, 38
 Sanz, F.: EN+TF-TuA12, 15
 Sardela, M.: TF+EM-MoM5, 3
 Sasaki, K.: TF-TuP2, 20
 Sato, M.: TF-ThP15, 50
 Schaeckers, M.: TF+EM-WeM10, 28
 Schäfer, P.: EN+TF-TuA2, 14
 Schall, J.D.: GR+TF-TuM2, 8
 Schamberger, F.: TF-WeM6, 31
 Schlaf, R.: EN+TF-TuA10, 15
 Schmidt, D.: EL+AS+EM+MS+TF-ThP5, 48;
 TF+SE-WeM9, 29
 Schöche, S.: TF+SE-WeM9, 29
 Schoeller, A.E.: SE+TF-WeA9, 32
 Schubert, E.B.: EL+AS+EM+MS+TF-ThP5, 48;
 TF+SE-WeM9, 29
 Schubert, M.: EL+AS+EM+MS+TF-ThA1, 40;
 EL+AS+EM+MS+TF-ThA7, 41;
 EL+AS+EM+MS+TF-ThP5, 48; TF+SE-
 WeM9, 29
 Scott, M.: EN+SS+TF-ThA6, 42; TF-ThP6, 49
 Seal, S.: TF-WeA12, 34
 Seebauer, E.G.: TF-WeM3, 30
 Seghete, D.: TF-ThP5, 48; TF-TuA9, 18
 Seidel, F.: EL+AS+EM+MS+TF-ThP6, 48
 Sellers, M.C.K.: TF-WeM3, 30
 Semonin, O.E.: EL+AS+EM+MS+TF-ThA8, 41
 Senecal, K.: TF-MoA8, 6
 Seo, S.: GR+TF-TuM11, 9
 Sestak, M.N.: EL+AS+EM+MS+TF-ThA11, 41
 Seyller, T.: GR+SS+TF+EM-MoM3, 1
 Shah, K.: TF+EM-WeM10, 28
 Shaikh, A.U.: TF+SE-WeM4, 29
 Shearer, J.C.: TF-WeM11, 31
 Shen, S.: TF+EM-WeM12, 28
 Sheng, J.J.: EN+TF-TuA8, 14
 Shiao, M.H.: TF-ThP1, 48
 Shih, H.C.: TF-TuP16, 22
 Shih, M.H.: TF-TuP16, 22
 Shimizu, H.: EN+SS+TF-ThA8, 43
 Shin, H.-B.: EL+AS+EM+MS+TF-ThA10, 41
 Shin, J.H.: TF-TuP9, 21
 Shin, S.H.: EL+AS+EM+MS+TF-ThP1, 47
 Shohet, J.L.: TF+EM-WeM9, 27
 Shukur, H.A.: TF-ThP20, 51
 Shutthanandan, S.V.: TF-ThA6, 45
 Shutthanandan, V.: TF-ThP11, 49; TF-WeA12, 34
 Sibener, S.J.: TF-WeA7, 33
 Singh, D.: TF+SE-WeM11, 30
 Singh, J.: TF+SE-WeM11, 30
 Sivakov, V.A.: TF+EN-MoM5, 5
 Sivasubramani, P.: TF1-TuM11, 11
 Skidmore, S.: TF+EM-MoM11, 4
 Skuza, J.R.: MI+TF-ThM3, 36; MI+TF-ThM4, 37
 Snyder, D.: GR+EM+MS+TF+MI-WeM1, 25
 Snyders, R.: EN+SS+TF-ThA1, 42
 Sohn, H.-C.: TF2-TuM3, 11; TF-TuP8, 20
 Solinsky, M.: EL+AS+EM+MS+TF-ThA7, 41
 Solowan, M.H.: GR+AS+TF+MI-ThA1, 43
 Soma, D.: SE+TF-WeA8, 32
 Song, J.D.: EL+AS+EM+MS+TF-ThP1, 47
 Song, L.Y.: EL+AS+EM+MS+TF-ThA3, 40
 Song, T.B.: EN+TF-WeM6, 25
 Song, Y.J.: GR+SS+TF+EM-MoM9, 2

Soukiassian, P.: GR+SS+TF+EM-MoM10, 2
 Spagnola, J.C.: TF-MoA1, 6; TF-MoA8, 6
 Spila, T.: TF+EM-MoM5, 3
 Srikanth, H.: TF+EM-MoM11, 4
 Stair, P.C.: TF+EN-MoM1, 4
 Starodub, E.: GR+AS+TF-ThM5, 35; GR+AS+TF-
 ThM6, 35
 Steiner, M.A.: TF+EM-MoM8, 3
 Steirer, K.: EN+TF-WeM9, 25
 Stojak, K.: TF+EM-MoM11, 4
 Stroschio, J.A.: GR+AS+TF+MI-ThA3, 44;
 GR+AS+TF+MI-ThA4, 44; GR+SS+TF+EM-
 MoM9, 2; GR+TF-TuM10, 9; GR+TF-TuM9,
 8
 Su, C.Y.: TF-ThP1, 48
 Suendo, V.: EL+AS+EM+MS+TF-ThA9, 41
 Sung, Y.H.: TF2-TuM11, 13
 Sutter, E.: GR+AS+TF-ThM9, 35
 Sutter, P.: GR+AS+TF-ThM9, 35
 Suzuki, M.: SE+TF-WeA7, 32
 Swart, H.C.: TF+EN-MoM8, 5
 Sweet, W.J.: TF-MoA1, 6
 Swensen, J.S.: TF-WeA1, 33
 Swerts, J.: TF+EM-WeM10, 28

— T —

Tadisa, Z.R.: MI+TF-ThM9, 37
 Takano, I.: TF-ThP15, 50; TF-ThP20, 51; TF-
 TuP14, 21
 Talkenberg, F.: TF+EN-MoM5, 5
 Tang, A.: EN+TF-TuA3, 14
 Tang, K.S.: TF-ThP1, 48; TF-TuP20, 22
 Tanto, B.: SE+TF-WeA10, 32
 Tao, B.: TF-ThA1, 44
 Tarasevich, B.J.: TF-WeA1, 33
 Taschuk, M.T.: TF+SE-WeM6, 29
 Tedesco, J.L.: GR+SS+TF+EM-MoM1, 1;
 GR+SS+TF+EM-MoM8, 1
 Ten Eyck, G.A.: SE+TF-WeA10, 32
 Terblans, J.J.: TF+EN-MoM8, 5
 Terlinden, N.M.: TF+EN-MoM6, 5
 Terryn, H.: TF-WeA8, 33
 Thevuthasan, S.: TF-ThP11, 49; TF-WeA12, 34
 Thompson, J.: TF-ThP19, 51
 Thompson, P.E.: GR+SS+TF+EM-MoM1, 1
 Thürmer, K.: GR+AS+TF-ThM6, 35;
 GR+SS+TF+EM-MoM2, 1
 Tinkey, H.: GR+SS+TF+EM-MoM6, 1
 Tiwald, T.E.: EL+AS+EM+MS+TF-ThA7, 41
 Tökei, Z.: TF+EM-WeM10, 28
 Tolbert, S.: TF1-TuM5, 10
 Torrance, D.B.: GR+SS+TF+EM-MoM6, 1;
 GR+SS+TF+EM-MoM9, 2
 Tourwé, E.: TF-WeA8, 33
 Tran, B.P.: EN+TF-WeM5, 24
 Triani, G.: TF-ThP12, 50
 Trotter, D.C.: GR+EM+MS+TF+MI-WeM6, 26
 Trugman, D.T.: TF-ThA1, 44
 Trumbull, K.: GR+EM+MS+TF+MI-WeM1, 25
 Tsai, D.P.: TF-TuP15, 22
 Tsotsos, C.: TF+EM-MoM10, 3
 Tucker, R.T.: SE+TF-WeA9, 32; TF-ThP4, 48
 Turchanian, A.: GR+TF-TuA4, 16; GR+TF-TuM3,
 8
 Tutuc, E.: GR+EM+MS+TF+MI-WeM9, 26
 Twigg, M.E.: GR+SS+TF+EM-MoM8, 1

— U —

Ueda, O.: EN+SS+TF-ThA2, 42

— V —

Vallée, C.: TF2-TuM4, 12; TF2-TuM5, 12
 Valyukh, S.: EL+AS+EM+MS+TF-ThA4, 40
 van de Sanden, M.C.M.: EN+TF-TuA1, 14;
 TF+EN-MoM6, 5
 van Duin, A.C.T.: GR+TF-TuA11, 17
 Van Elshocht, S.: TF+EM-WeM10, 28
 van Hest, M.F.A.M.: EN+TF-WeM9, 25
 Vandalon, V.: TF-TuA2, 17
 Vandervelde, T.: EN+SS+TF-ThA11, 43
 Vandeweert, E.: TF-WeA4, 33

Varga, T.: TF-ThP11, 49; TF-WeA12, 34
 Vélez, J.M.: TF-TuP3, 20
 Vemuri, R.S.: EL+AS+EM+MS+TF-ThP3, 47;
 TF-TuP11, 21; TF-WeA10, 34
 Venkatesh, S.: MI+TF-ThM12, 37
 Vertegel, A.A.: TF-TuP17, 22
 Vervaecke, F.: TF-WeA4, 33
 Vitiello, J.: TF2-TuM5, 12
 Vizzini, S.: GR+SS+TF+EM-MoM10, 2
 Vogt, B.D.: EL+AS+EM+MS+TF-ThA3, 40
 von Huth, P.: EN+TF-WeM3, 24

— W —

Wägberg, L.: EL+AS+EM+MS+TF-ThP2, 47
 Wagner, F.T.: TF-TuA9, 18
 Wallace, R.M.: GR+EM+MS+TF+MI-WeM11,
 26; TF1-TuM11, 11
 Walter, A.L.: GR+AS+TF-ThM6, 35
 Walton, S.G.: GR+TF-TuA8, 16
 Walukiewicz, W.: EN+TF-TuA11, 15
 Wang, A.: TF1-TuM9, 10
 Wang, D.Y.: TF-TuP16, 22
 Wang, J.: TF+EM-MoM11, 4; TF+EN-MoM4, 4
 Wang, L.: MI+TF-ThM3, 36; MI+TF-ThM4, 37;
 TF-WeA1, 33
 Wang, S.J.: EN+TF-TuA7, 14
 Wang, W.: TF-ThP5, 48
 Wang, Y.C.: GR+AS+TF+MI-ThA1, 43
 Wangperawong, A.: EN+TF-WeM5, 24
 Weber, D.H.: GR+TF-TuA4, 16
 Weiland, C.: TF+EM-WeM3, 27
 Weimann, T.: GR+TF-TuA4, 16
 Weiss, S.: EN+SS+TF-ThA6, 42
 Weller, T.: TF+EM-MoM11, 4
 Wen, J.-G.: TF+EM-MoM5, 3
 Wendelken, J.F.: MI+TF-ThM1, 36
 Wheeler, V.D.: GR+SS+TF+EM-MoM1, 1
 Wiemer, C.: TF2-TuM9, 12
 Williamson, T.L.: EN+TF-TuA11, 15
 Williford, R.E.: TF-WeA1, 33
 Winter, A.: TF-ThP3, 48
 Winter, R.: TF-WeM4, 30
 Witters, T.: TF+EM-WeM10, 28
 Wofford, J.M.: GR+AS+TF-ThM11, 36
 Wolak, M.A.: EN+TF-TuA10, 15
 Wong, L.M.: EN+TF-TuA7, 14
 Woo, S.: TF1-TuM4, 10
 Wu, B.: TF-TuP19, 22
 Wu, I.-T.: TF+EN-MoM4, 4
 Wu, J.: TF-TuP4, 20
 Wu, K.: TF-TuP12, 21
 Wu, W.H.: TF-TuP13, 21
 Wu, Y.: TF+EM-MoM3, 2
 Wyczawska, S.: TF-WeA4, 33

— X —

Xiao, J.: GR+TF-TuA3, 15
 Xie, Y.-H.: GR+AS+TF-ThM12, 36
 Xing, H.: TF1-TuM11, 11
 Xiong, J.: TF-ThA1, 44
 Xue, J.: EN+TF-TuA3, 14

— Y —

Yang, H.: GR+TF-TuM11, 9
 Yang, J.: EN+TF-TuA3, 14
 Yang, W.: TF-ThP10, 49; TF-ThP13, 50; TF-
 WeA11, 34
 Yanguas-Gil, A.: TF-TuA4, 17
 Yasuda, Y.: EN+SS+TF-ThA8, 43
 Yazyev, O.V.: GR+AS+TF+MI-ThA6, 44
 Ye, D.-X.: SE+TF-WeA8, 32
 Yen, C.C.: TF-TuP16, 22
 Yoon, B.: TF-MoA10, 7; TF-MoA2, 6
 Yoon, J.J.: EL+AS+EM+MS+TF-ThP1, 47
 Yoon, O.J.: GR+EM+MS+TF+MI-WeM2, 25
 Yu, K.M.: EN+TF-TuA11, 15
 Yuan, H.: EN+SS+TF-ThA9, 43; TF-TuP10, 21;
 TF-WeA7, 33
 Yun, J.: TF-TuP21, 22

— Z —

Zahn, D.R.T.: EL+AS+EM+MS+TF-ThP6, 48;
EN+TF-TuA2, 14
Zeller, D.J.: TF-TuP12, **21**
Zettl, A.: GR+AS+TF+MI-ThA1, 43
Zhai, J.: TF-ThA1, 44
Zhang, F.: TF1-TuM5, **10**
Zhang, L.: TF-ThP19, **51**

Zhang, X.: GR+TF-TuM3, **8**
Zhang, X.G.: MI+TF-ThM1, 36
Zhang, Y.: TF2-TuM6, 12; TF-ThA1, 44
Zhang, Z.: GR+AS+TF-ThM1, 35
Zheng, Y.: EN+TF-TuA3, 14
Zhernenkov, M.: MI+TF-ThM2, 36
Zhitenev, N.B.: GR+TF-TuM10, 9; GR+TF-TuM9,
8

Zhou, R.: EN+TF-TuA3, 14
Zhu, W.: GR+AS+TF-ThM1, 35
Zhu, W.J.: GR+EM+MS+TF+MI-WeM5, **26**
Zhu, Z.H.: TF-WeA1, 33
Zhuo, M.: TF-ThA1, 44
Zorn, G.: TF-WeA3, **33**
Zou, G.: TF-ThA1, 44